THE UNIVERSITY OF QUEENSLAND

AUSTRALIA

Development of Cathode Materials for Intermediate Temperature Solid Oxide Fuel Cells

Mengran Li

Bachelor of Chemical Engineering

A thesis submitted for the degree of Doctor of Philosophy at

The University of Queensland in 2016

School of Chemical Engineering

Abstract

A solid oxide fuel cell (SOFC) is a promising energy device that can generate electricity by converting chemical energy of nearly all types of fuels with very high efficiency. However, its high operating temperature (> 850°C) is the main impediment to deploying this technology, because high temperature can lead to sealing issues, slow start-up/shut-down procedures, poor thermal cycling stability, poor fuel cell durability, as well as high material and operational cost. Lowering the operating temperature down to intermediate temperature (IT, 500 °C – 750 °C) is an effective and significant strategy to solve these issues, but it makes the kinetics of electrolyte and electrodes especially the cathode sluggish. Despite slow kinetics of electrolyte have been significantly alleviated by using novel electrolyte materials and thin film fabrication technology, low electroactivity of IT-SOFC cathode still remains a major challenge. Besides, the susceptibility of cathodes containing alkaline-earth elements to CO_2 is another concern on long-term cathode stability, especially at low temperature. Therefore, developing a robust cathode material with high electroactivity is significant for commercialising SOFC technology, and have received growing research interest and efforts in recent years.

This thesis is mainly focused on developing highly active and stable cathode materials based on $SrCoO_{3-\delta}$ perovskite oxide for IT-SOFC. The factors affecting catalysis on oxygen reduction reaction (ORR), and the CO_2-poisoning mechanisms on the $SrCoO_{3-\delta}$-based cathodes at intermediate temperature were investigated. In this thesis, we developed and evaluated $SrCoO_{3-\delta}$ doped with high-valence elements such as P, Nb, and Ta as cathodes for SOFC by studying their crystal structures, compositions, microstructures and electrochemical properties as well as electroactivity in ORR at intermediate temperature.

In the first part of the experimental chapters, we mainly worked on developing $SrCoO_{3-\delta}$-based cathode materials and studying the effects of high fixed valence dopants (P, Ta, and Nb) on $SrCoO_{3-\delta}$ perovskite cathode for IT-SOFC. We successfully doped P and Ta into $SrCoO_{3-\delta}$ oxide separately, and found these dopants at certain doping level can stabilise the beneficial perovskite structure at both room temperature and intermediate temperature. The study on P-doped $SrCoO_{3-\delta}$ reveals that the stabilising effect of P is a result of the high-valence that prevents oxygen vacancy ordering and phase distortions. The electrical conductivity of $SrCoO_{3-\delta}$ can be enhanced by small amount of P or Ta (≤ 5 mol%) due to the stabilized perovskite structure and high valence of P and Ta, but can be adversely affected for higher doping level as shown in study on $SrCo_{1-x}Ta_xO_{3-\delta}$. Additionally, $SrCoO_{3-\delta}$ doped with <20 mol% Ta shows superior electroactivity on ORR at IT, with a cathode polarisation resistance as low as 0.089~0.11 $\Omega\cdot cm^2$ at 550°C for $SrCo_{0.95}Ta_{0.05}O_{3-\delta}$. However, the high fixed valence can

decrease oxygen vacancy content, so high doping level (e.g. 40mol%) of Ta can seriously deteriorate cathode electroactivity at intermediate temperature.

In the second part, we investigated other non-geometry factors that have an effect on cathode electroactivity. We doped 20mol% of Nb and Ta separately into $SrCoO_{3-\delta}$ oxides, and compared their ORR-related properties. The reason we chose Nb and Ta as dopants is that these dopants have the same valence state and very similar ionic radii. These similarities allow us to explore other factors that may affect ORR activity by constraining their geometry factor. This comparative study shows that lower electronegativity of Ta than Nb can reduce the average valence of neighbouring Co, thus creating more oxygen vacancies and leading to higher electroactivity. Moreover, we developed a highly active ORR catalyst by co-doping Nb and Ta into $SrCoO_{3-\delta}$, showing a remarkably low polarisation resistance of ~0.16 $\Omega\cdot cm^2$ at 500 °C. The outstanding cathode performance is likely attributed to an optimised balance of oxygen vacancy content, oxygen ionic mobility and surface electron transfer ability.

The focus of the third part of experimental chapters is to address the susceptibility of $SrCoO_{3-\delta}$-derived cathode materials to CO_2 at intermediate temperature. We incorporated Sm-doped ceria (SDC) into $SrCo_{0.85}Ta_{0.15}O_{3-\delta}$ cathode by either mechanical mixing or wet impregnation, and significantly improved the CO_2 tolerance of $SrCo_{0.85}Ta_{0.15}O_{3-\delta}$ by over 5 times in the presence of 10% CO_2 at 550 °C as compared to pure $SrCo_{0.85}Ta_{0.15}O_{3-\delta}$. The CO_2 resistance improvement of SDC is a result of the low CO_2 reactivity and adsorption on SDC. More importantly, this strategy prevails for other cathode materials containing alkaline-earth elements, such as benchmark IT-SOFC $Ba_{0.5}Sr_{0.5}Co_{0.8}Fe_{0.2}O_{3-\delta}$.

Declaration by author

This thesis is composed of my original work, and contains no material previously published or written by another person except where due reference has been made in the text. I have clearly stated the contribution by others to jointly-authored works that I have included in my thesis.

I have clearly stated the contribution of others to my thesis as a whole, including statistical assistance, survey design, data analysis, significant technical procedures, professional editorial advice, and any other original research work used or reported in my thesis. The content of my thesis is the result of work I have carried out since the commencement of my research higher degree candidature and does not include a substantial part of work that has been submitted to qualify for the award of any other degree or diploma in any university or other tertiary institution. I have clearly stated which parts of my thesis, if any, have been submitted to qualify for another award.

I acknowledge that an electronic copy of my thesis must be lodged with the University Library and, subject to the policy and procedures of The University of Queensland, the thesis be made available for research and study in accordance with the Copyright Act 1968 unless a period of embargo has been approved by the Dean of the Graduate School.

I acknowledge that copyright of all material contained in my thesis resides with the copyright holder(s) of that material. Where appropriate I have obtained copyright permission from the copyright holder to reproduce material in this thesis.

Publications during candidature

Mengran Li, Wei Zhou, Xiaoyong Xu, Zhonghua Zhu, $SrCo_{0.85} Fe_{0.1} P_{0.05} O_{3-\delta}$ Perovskite as A Cathode for Intermediate-temperature Solid Oxide Fuel Cells. *Journal of Materials Chemistry A* **2013,** 1, (43), 13632-13639.

Mengran Li, Wei Zhou, Zhonghua Zhu, Comparative Studies of $SrCo_{1-x}Ta_xO_{3-\delta}$ (x=0.05–0.4) Oxides as Cathodes for Low-Temperature Solid-Oxide Fuel Cells. *ChemElectroChem* **2015,** 2, (9), 1331-1338.

Mengran Li, Wei Zhou, Vanessa K. Peterson, Mingwen Zhao, Zhonghua Zhu, A Comparative Study of $SrCo_{0.8}Nb_{0.2}O_{3-\delta}$ and $SrCo_{0.8}Ta_{0.2}O_{3-\delta}$ as Low-temperature Solid Oxide Fuel Cell Cathodes: Effect of Non-Geometry Factors on the Oxygen Reduction Reaction. *Journal of Materials Chemistry A* **2015**, 3, 24064-24070.

Mengran Li, Wei Zhou, Zhonghua Zhu, Recent Development on Perovskite-type Cathode Materials based on $SrCoO_{3-\delta}$ Parent Oxide for Intermediate-temperature Solid Oxide Fuel Cells. *Asia-Pacific Journal of Chemical Engineering* **2016,** 11, (3), 370-381.

Conference

Mengran Li, Wei Zhou, Xiaoyong Xu, Zhonghua Zhu, A Novel Phosphorous Doped Perovskite cathode for Intermediate-temperature Solid Oxide Fuel Cell, APEnergy2014, 5-8 Feb 2014, Brisbane, Australia. (Oral presentation).

Publications included in this thesis

Mengran Li, Wei Zhou, Zhonghua Zhu, Recent Development on Perovskite-type Cathode Materials based on $SrCoO_{3-\delta}$ Parent Oxide for Intermediate-temperature Solid Oxide Fuel Cells. *Asia-Pacific Journal of Chemical Engineering* **2016,** 11, (3), 370-381. –Included in Chapter 2.

Contributor	Statement of contribution
Author Mengran Li	Structuring (50%) Writing (70%)
Author Wei Zhou	Structuring (30%) Writing (10%)
Author Zhonghua Zhu	Structuring (20%) Writing (20%)

Mengran Li, Wei Zhou, Xiaoyong Xu, Zhonghua Zhu, $SrCo_{0.85}Fe_{0.1}P_{0.05}O_{3-\delta}$ Perovskite as A Cathode for Intermediate-temperature Solid Oxide Fuel Cells. *Journal of Materials Chemistry A* **2013,** 1, (43), 13632-13639.-Incorporated as Chapter 4.

Contributor	Statement of contribution
Author Mengran Li	concept and design (60%) analysis and interpretation of data (70%) drafting and writing (70%)
Author Wei Zhou	concept and design (30%) analysis and interpretation of data (15%) drafting and writing (20%)
Author Xiaoyong Xu	analysis and interpretation of data (10%)
Author Zhonghua Zhu	concept and design (10%) analysis and interpretation of data (5%) drafting and writing (10%)

Mengran Li, Wei Zhou, Zhonghua Zhu, Comparative Studies of $SrCo_{1-x}Ta_xO_{3-\delta}$ (x=0.05–0.4) Oxides as Cathodes for Low-Temperature Solid-Oxide Fuel Cells. *ChemElectroChem* **2015,** 2, (9), 1331-1338.-Incorporated as Chapter 5.

Contributor	Statement of contribution
Author Mengran Li	concept and design (70%) analysis and interpretation of data (80%) drafting and writing (70%)
Author Wei Zhou	concept and design (20%) analysis and interpretation of data (20%) drafting and writing (20%)
Author Zhonghua Zhu	concept and design (10%) drafting and writing (10%)

Mengran Li, Wei Zhou, Vanessa K. Peterson, Mingwen Zhao, Zhonghua Zhu, A Comparative Study of $SrCo_{0.8}Nb_{0.2}O_{3-\delta}$ and $SrCo_{0.8}Ta_{0.2}O_{3-\delta}$ as Low-temperature Solid Oxide Fuel Cell Cathodes: Effect of Non-Geometry Factors on the Oxygen Reduction Reaction. *Journal of Materials Chemistry A* **2015**, 3, 24064-24070.-Incorporated as Chapter 6.

Contributor	Statement of contribution
Author Mengran Li	concept and design (60%) analysis and interpretation of data (70%) drafting and writing (70%)
Author Wei Zhou	concept and design (20%) analysis and interpretation of data (15%) drafting and writing (10%)
Author Vanessa K. Peterson	analysis and interpretation of data (8%) drafting and writing (10%)
Author Mingwen Zhao	analysis and interpretation of data (2%) drafting and writing (3%)
Author Zhonghua Zhu	concept and design (10%) analysis and interpretation of data (5%) drafting and writing (7%)

Contributions by others to the thesis

Contributions by Vanessa K. Peterson, Mingwen Zhao and Xiaoyong Xu in concept, analysis, interpretation and drafting & writing.

Contributions by Wei Zhou and Zhonghua Zhu in experiment design, analysis, concept, interpretation, drafting and writing in the advisory capacity.

Statement of parts of the thesis submitted to qualify for the award of another degree

None

Acknowledgements

I would like to express my sincere gratitude to Prof. John Zhu and Prof. Wei Zhou for their immense time contribution as well as their invaluable guidance, advice, support and friendship during my PhD study. Besides, I really appreciate the significant technical assistance and help from Dr. Xiaoyong Xu, Rijia Lin, Dr. Fengli Liang, Dr. Ying Yang and other group members including Dr. Li Wang, Dr. Xuegang Tang, Dr. Taiwo Odedairo, Dr. Jiuling Chen, Jie Zhao, Dr. Byron Villacorta Hernandez, Yisu Yang, Linzhou Zhuang and Sathia Aruliah. I am very thankful for enormous support and help from Dr. Vanessa K. Peterson, Prof. Mingwen Zhao, Prof. Zongping Shao and Prof. Ian Gentle. I feel very grateful to my parents and my lovely girlfriend Liuying Fan for their great support, encouragement, and love.

I greatly appreciate the financial support from UQ tuition fee waiving scholarship for my tuition fee, financial funding from Australian Research Council (DP130102151) for my research project, and Chinese Scholarship Council scholarship, TUAP and 3M scholarship for my living.

I also thank the Centre for Microscopy and Microanalysis staffs for the training and technical support. Particularly, I would like to express my gratitude to Ying Yu, Dr. Zhi Zhang, Dr. Barry Wood, Anya Yago, Kim Sewell and Ron Rasch.

Besides, I would also like to thank the technical support from UQ professional staffs, especially from Des Cameron, Tim Wogan, David Kallman, Peter Khan, Liam Bull, Henry Lorek, Steven Kimball, Daniel Epstein, Keith Lane and Robin Berlyn. Many thanks to Siu Bit Iball, June Nicholson, Anne Tan, Stephen Coombs, Vicki Thompson, Maureen Pollard and Marion Dunstan.

Keywords

Cathode, perovskite, solid oxide fuel cells, oxygen reduction reaction, stability

Australian and New Zealand Standard Research Classifications (ANZSRC)

ANZSRC code: 090402 Catalytic Process Engineering, 40%

ANZSRC code: 091201, Ceramics, 40%

ANZSRC code: 030299, Inorganic Chemistry not elsewhere classified, 20%

Fields of Research (FoR) Classification

FoR code: 0904, Chemical Engineering

FoR code: 0302, Inorganic Chemistry

Table of Contents

List of Figures

List of Tables

List of Abbreviations

AE - Alkaline Earth

ASR - Area Specific Resistance

BSCF - (Ba, Sr)(Co, Fe)$O_{3-\delta}$

ECR - Electrical Conductivity Relaxation

EDS or EDX - Energy Dispersive X-ray Spectroscopy

EIS - Electrochemical Impedance Spectroscopy

GDC - Gadolinium Doped Ceria

HADDF - High Angle Annular Dark Field

HF - High Frequency

IT - Intermediate Temperature

LF - Low Frequency

LSCF - (La, Sr)(Co, Fe)$O_{3-\delta}$

LT - Low Temperature

NPD - Neutron Powder Diffraction

ORR - Oxygen Reduction Reaction

RP - Ruddlesden Popper

SC - $SrCoO_{3-\delta}$

SCFP - $SrCo_{0.85}Fe_{0.1}P_{0.05}O_{3-\delta}$

SCNT - $SrCo_{0.8}Nb_{0.1}Ta_{0.1}O_{3-\delta}$

SCNx - $SrCo_{1-0.01x}Nb_{0.01x}O_{3-\delta}$

SCTx - $SrCo_{1-0.01x}Ta_{0.01x}O_{3-\delta}$

SDC - Samarium Doped Ceria

SEM - Scanning Electron Microscopy

SOFC - Solid Oxide Fuel Cell

SSNC - Sr(Sc, Nb, Co)$O_{3-\delta}$

TEM - Transmission Electron Microscopy

TGA - Thermogravimetric Analysis

TM - Transition Metal

TPB - Three Phase Boundary

TPD - Temperature Programmed Desorption

XPS - X-ray Photoelectron Spectroscopy

XRD - X-Ray Diffraction

Chapter 1 Introduction

1.1 Background

In recent years, direct energy conversion through fuel cells has become a significant and interesting topic for electrochemical research and technology development.[1] Fuel cell is a device that generates electricity by converting chemical energy in fuels directly into useful electrical energy and heat via electrochemical reactions.[2] Fuel cells have higher chemical to electricity efficiencies and much lower pollutions than conventional electricity generators such as heat engines, because their electrochemical reaction can inherently avoid the efficiency-limiting combustion step (the Carnot cycle). For most of fuel cells such as polymer electrolyte fuel cells, relatively pure hydrogen is the only direct fuel that can be applied to anode.[3] However, the formidable challenges for large-scale hydrogen production and storage significantly impede the deployment of most of the fuel cells. Nevertheless, a solid oxide fuel cell (SOFC) shows a good compatibility with commercially available hydrocarbon fuels, with an outstanding system efficiency due to its oxygen-ion-conducting electrolyte and high operating temperature. Therefore, SOFC appears to be a promising fuel cell technology that can use the currently available hydrocarbon resources and deliver high fuel efficiency and low pollutants at the same time.

A SOFC is an all-solid device that can convert nearly all types of fuels with higher efficiency and less pollution as compared to other conventional electricity generators. The SOFC electrolyte is a dense solid ceramic film that renders oxygen ions possible to transport in a solid-state conduction way. The solid dense electrolyte can also completely prevent fuels and air from cross-over, thereby making SOFC possible to apply different fuels including natural gas, methanol, jet fuel, and “dry” hydrocarbons. Other fuels, such as coal, diesel, and ethanol, can also be applied into SOFC by being pre-converted into syngas (H_2 and CO). Besides the fuel adaptability of SOFC, another reason SOFC stands out is its higher efficiency as compared to the commercialized technologies based on hydrocarbon infrastructures: a sole SOFC application can achieve an efficiency of 45~65% based on low heating value (LHV) ,[4] and an efficiency over 85 % LHV can be achieved if SOFC is integrated with combined heat and power (CHP)[5].

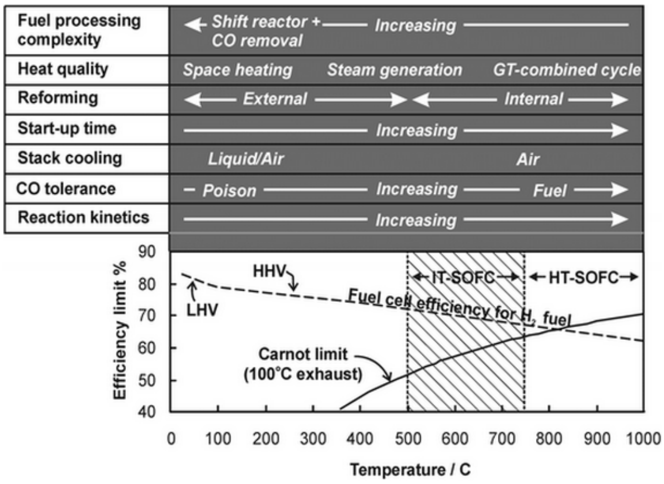

Figure 1-1 The fuel cell issues affected by the operating temperature with H_2 as the fuel.[6] *LHV* or *HHV* accounts for theoretical efficiency based on lower heating value or higher heating value respectively.

The high operating temperature brings both advantages and challenges to SOFC technology. Figure 1-1 summarises temperature-related performance for a H_2-fueled fuel cell. High-temperature SOFCs (HT-SOFCs) work at temperature from 850 °C to 1000 °C. The high operating temperature is beneficial for improving the electrode reaction kinetics, reducing the electrolyte ohmic resistance, and improving fuel adaptability. On the other hand, high temperature results in high system cost, poor sealing, slow start-ups/shutdown procedures and poor long-term performance degradation. These challenges become the main obstacles hindering the SOFC development and practical deployment. Additionally, the ceramic-made configuration of HT-SOFC required to withstand high temperature significantly lowers the volumetric power density, and renders the HT-SOFC impossible for portable applications, such as micro combined heat and power (CHP) unit and auxiliary power unit (APU). As a consequence, lowering the operating temperature into intermediate-temperature (IT) range (500 °C ~ 750 °C)[7] is considered as an effective approach to address these challenges, and attracts immense research interests these years.

However, low temperature results in slow kinetics of SOFC's electrolyte and electrodes, where thermally activated processes occur to facilitate fuel cell operation. Accordingly, there are two main routes to achieve sufficient power at reduced temperature: one is to apply novel electrolyte materials or thinner electrolyte to reduce ohmic resistances; the other is to enhance the kinetics of electrodes, especially the cathode, to decrease electrode polarisation resistances. Given significant progress that have been achieved on electrolyte improvement, the sluggish kinetics of oxygen reduction at cathode becomes the controlling step for the overall fuel cell performance at intermediate temperature. What is more, low operating temperature makes the cathode materials, especially those cathodes containing alkaline earth elements, susceptible to CO_2 poisoning in the air.

There are still challenges hitherto in improving the cathode electroactivity and stability at IT range. Therefore, the development of robust cathode materials with high electro-catalytic activity towards ORR is significant to pave the way for commercialization of fuel cells and make contributions to a dispersed and robust energy infrastructure.

1.2 Scope and research contributions

This project is focused on developing a robust cathode material showing high ORR activity for IT-SOFCs, and on studying catalysis mechanisms on ORR and CO_2 poisoning. Correspondingly, the objectives to be achieved by this project are specified as follows:

- To develop stable and high-performance cathode materials based on $SrCoO_{3-\delta}$ (SC) perovskite oxide for IT-SOFC by doping highly charged elements in to cobalt sites.
- To investigate the effects of highly charged dopants on electroactivity of single-doped SC cathodes by studying their properties related to ORR activity, such as crystallography, oxygen defects, conductivities and etc.
- To develop novel SC-based perovskite oxides by co-doping highly-charged elements, and to investigate the effects of co-doping on ORR through studying their ORR-related properties and calculating their electronic structures using first principles.
- To improve the tolerance of SC-based cathodes against CO_2 at reduced temperature, and to probe mechanisms behind the CO_2 poisoning effects on these cathode materials.

SC has been proved to be one of the most promising candidates for IT-SOFC cathodes. Therefore, in this thesis we worked on the development and evaluation of cathodes using SC as the parent oxide, and investigated the effects of dopants on cathode performance at the same time. Investigations on CO_2 poisoning were also conducted, and strategy was explored in attempt to improve CO_2 tolerance of the IT-SOFC cathode. Based on the specific objectives as listed above, the thesis consists of nine chapters. The results and discussions of the research are presented in chapter 4-8, some of which have been published or submitted for journal publications.

1.3 Structure of thesis

Chapter 1 provides some background of IT-SOFCs, and describes the scope and specific research objectives of this thesis.

Chapter 2 provides an overview of SOFC and recent progress on cathode development for IT-SOFCs in different aspects such as their crystallography, factors affecting ORR activity, specific cathode materials developed, and the strategies to address cathode instability in the presence of CO_2.

In chapter 3, we summarize the general methods used in this project to develop and evaluate cathode materials for IT-SOFC, including sample syntheses, sample preparations, powder characterization, electrochemical measurements and first principle calculations.

In chapter 4, a phosphorus-doped perovskite, $SrCo_{0.85}Fe_{0.1}P_{0.05}O_{3-\delta}$ (SCFP) was evaluated as a cathode for IT-SOFCs. It is found that the dopant P can stabilize the benign perovskite phase of Sr (Co, Fe) $O_{3-\delta}$ and suppress oxygen vacancy ordering mainly because of its high valence. The area specific resistance (ASR) of SCFP is about 0.097 $\Omega\cdot cm^2$ at 589°C, which is comparable to the benchmark cathode $Ba_{0.5}Sr_{0.5}Co_{0.8}Fe_{0.2}O_{3-\delta}$ (BSCF). Besides, the performance stability SCFP is also significantly improved by the incorporation of the P dopant.

A comparative study of $SrCo_{1-x}Ta_xO_{3-\delta}$ (x=0.05-0.4) was conducted in chapter 5 to investigate the effects of Ta^{5+} on the electrocatalytic activity on oxygen reduction. It is found that not only the beneficial perovskite phase of $SrCoO_{3-\delta}$ can be stabilized by doping Ta, but the cathode performance can be further improved for relatively small content of Ta dopant, which may arise from the optimised cobalt ions induced by the Ta^{5+} that enhances the oxygen surface exchange kinetics.

Chapter 6 is focused on studying the non-geometry factors on catalyzing activity of cathodes. We designed two isostructural $SrCoO_{3-\delta}$-based cathodes doped with same level of Nb^{5+} and Ta^{5+}, which are in very similar ionic size but different electronegativity. By comparing the activity-related properties between these two cathodes, we found that relatively lower electronegativity imparted by Ta^{5+} will slightly reduce the cobalt oxidation state and the work function, which will enhance the charge-transfer process of the surface exchange, and therefore improve the cathode performance.

Chapter 7 introduces a novel perovskite cathode $SrCo_{0.8}Nb_{0.1}Ta_{0.1}O_{3-\delta}$ that was developed and exhibited superior electrochemical activity in reducing oxygen with the lowest ASR ever reported of ~0.16 and ~0.68 $\Omega\cdot cm^2$ at 500 °C and 450 °C respectively. The outstanding activity is proved to be related to the improved oxygen-ion migration in the lattice and the oxygen surface exchange as a result of the co-doping Nb and Ta. We believe this co-doping will be a promising strategy to design next-generation of cathodes for IT-SOFCs.

Chapter 8 mainly works on improving cathode resistance against CO_2 poisoning. Therefore, $Sm_{0.2}Ce_{0.8}O_{2-\delta}$ (SDC) was introduced into our previously studied $SrCo_{0.85}Ta_{0.15}O_{3-\delta}$ (SCT15) through mechanical mixing and infiltration method. The stability of the composite cathode in the presence of CO_2 is improved by over 4 times as compared to pure SCT15 mainly because of the high tolerance of SDC.

In chapter 9, the findings from all the work as presented in the previous chapters are summarized, and also some future directions are recommended.

1.4 References

1. Doyle, M.; Rajendran, G.; Vielstich, W.; Gasteiger, H. A.; Lamm, A., Handbook of Fuel Cells Fundamentals, Technology and Applications. *Fuel Cell Technology and Applications* **2003,** 3, (Part 1).

2. O'Hayre, R. P.; Cha, S.-W.; Colella, W.; Prinz, F. B., *Fuel Cell Fundamentals*. John Wiley & Sons New York: 2006.

3. Steele, B. C.; Heinzel, A., Materials for Fuel-Cell Technologies. *Nature* **2001,** 414, (6861), 345-352.

4. Handbook, F. C., EG&G Technical Services, Inc. Under Contract No. *DEAM26-99FT40575, US Department of Energy, Office of Fossil Energy, National Energy Technology Laboratory, Morgantown, West Virginia, USA* **2004**.

5. Maru, H. C.; Singhal, S.; Stone, C.; Wheeler, D. *1- 10 kW Stationary Combined Heat and Power Systems Status and Technical Potential: Independent Review*; National Renewable Energy Laboratory (NREL), Golden, CO.: 2010.

6. Brett, D. J. L.; Atkinson, A.; Brandon, N. P.; Skinner, S. J., Intermediate Temperature Solid Oxide Fuel Cells. *Chemical Society Reviews* **2008,** 37, (8), 1568-1578.

7. Steele, B. C. H., Material Science and Engineering: The Enabling Technology for the Commercialisation of Fuel Cell Systems. *Journal of Materials Science* 36, (5), 1053-1068.

Chapter 2 Literature review

In this review, working principles and components of SOFC are briefly introduced, followed by a review on reaction mechanisms and crystal structures of the IT-SOFC cathode. This chapter is mainly focused on recent advances in developing IT-SOFC cathodes, with an emphasis on the development of single-phase cathode materials and research progresses on the susceptibility of cathodes to CO_2.

2.1 Overview of the SOFC

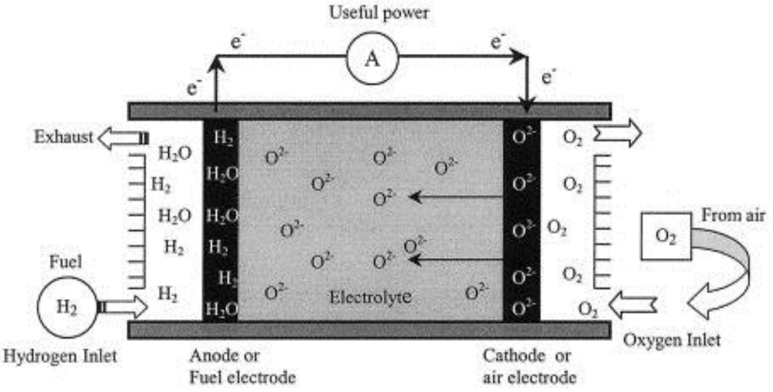

Figure 2-1 A schematic of working principles on a typical SOFC.[1]

A solid oxide fuel cell has three main components: two porous electrodes sandwiching a dense electrolyte. Figure 2-1 shows the working mechanisms of a typical SOFC based on oxygen-ion conducting electrolyte. Fuels such as H_2 and CO are applied to the anode and oxidized to produce water and CO_2; oxygen in air is reduced to O^{2-} at the cathode and transported to the anode via the electrolyte; the liberated electrons from oxidation reaction at the anode do useful electrical work when they travel to the cathode through an external circuit. Obviously, there is no fuel combustion in the SOFC, so that the Carnot cycle can be inherently prevented, which is why SOFC has higher electricity efficiency than conventional power generators.

The electrolyte, anode and cathode of a SOFC are made of different types of materials, so an overview is given as follows on the typical materials for these three components.

2.1.1 Electrolyte materials

An electrolyte is an oxygen-ion conductor with low electronic conductivity, and is responsible for both transporting oxygen ions and preventing cross-over of electrons and gases. The internal ohmic resistance of a SOFC cell is mainly contributed by the electrolyte.

Zirconia (ZrO_2)-based materials are one of the widely used electrolyte materials especially for HT-SOFC, such as yttria-stabilised or scandia-stabilised zirconia (YSZ or ScZ respectively) due to their high ionic conductivity and high mechanical and thermodynamic stability at elevated temperature.

The ScZ shows higher ionic conductivity than YSZ at lower temperature.[2, 3] However, at high temperature a highly resistant secondary phase can be formed between zirconia and lanthanide or strontium from cathode, so a barrier is normally required to prevent such unwanted chemical interactions.

δ-phase Bi_2O_3 (a fluorite-type structure) is another promising electrolyte material showing high ionic conductivity of ~1 S/cm at 800°C.[4] The challenge concerning this material is its structure instability: the δ-phase is only stable between 730°C and 804°C, which is its melting point. Therefore yttria[5] or erbia[6] was incorporated into bismuth oxide to partially substitute Bi to stabilise its δ-phase. However, the instability for stabilised bismuth oxides under anode conditions, due to the susceptibility of Bi to being reduced, still remains to be resolved.

$(La,Sr)(Ga,Mg)O_{3-\delta}$ (LSGM) is a perovskite-structured electrolyte suitable for IT-SOFC. Though the substitutions of Sr and Mg increase the concentration of oxygen vacancies, they also reduce Ga valence and lead to formation of unwanted secondary phases under reducing environment.[7-9] Chemical incompatibility with Ni is also another challenge for LSGM electrolyte[10].

The Gd or Sm stabilised ceria are regarded as one of the most promising electrolyte materials for IT-SOFC because of its high oxide ionic conductivity and compatibility with cobalt-based electrodes. There are two main challenges for ceria-based electrolyte: one is their poor sinterability; the other is their high electronic conductivity under reducing conditions especially at high temperature.[11-13] Numerous approaches have been developed to improve the sinterability, such as doping ideal elements or introducing sintering aids. For example, researchers improved the electrolyte performance by incorporating Mg[14] or Y[15] into Gd-doped ceria, and Y[16] into Sm-doped ceria. Some sintering aids, such as transition metal oxides can lower the maximum temperature for electrolyte densification. For instance, 1% of cobalt oxide can decrease the densification temperature of $Ce_{0.9}Gd_{0.1}O_{1.95}$ down to 950 °C.[17]

Goodenough *et al.*[18-20] developed new electrolyte materials based on $Sr(Si,Ge)O_{2.9}$ that also show superior oxygen-ion conductivity at IT range. Meanwhile, the techniques such as slurry coating were also explored to fabricate electrolyte with reduced thickness in order to boost the fuel cell performance at reduced temperature.[21-25] The thin electrolyte film can shorten the oxygen-ion travel distance, thereby lowering ohmic resistance at low temperature. By applying the electrolyte materials with superior ionic conductivity through novel thin film fabrication technique, it is possible to achieve the target ionic conductivity (~0.01 S/cm)[26] for sufficient fuel cell power output at intermediate temperature.

2.1.2 Anode materials

An anode is an electrocatalyst to oxidise the fuels electrochemically, and a good IT-SOFC anode should have:

- High electronic (typically ~100S/cm) and ionic conductivity
- High electrocatalytic activity
- High stability in reducing and oxidising environment at high temperature
- Good chemical and thermal compatibility with other contacting components

The conventional anode is a cermet of a metal that is percolated in a porous electrolyte material. This anode structure allows electrons travel through the electrolyte matrix, and optimises the active three phase boundaries, where the electrochemical reaction takes place.

Ni/YSZ cermet meets most of the anode requirements due to its high electronic conductivity, relative high ionic conductivity and high activity on hydrogen oxidation. The cermet can be easily fabricated by co-sintering YSZ and NiO, followed by reduction by hydrogen. Little chemical interaction occurs between YSZ and NiO.[27] The doped zirconia can also be replaced with other electrolyte materials such as ceria-based electrolyte. However, there are challenges for such kind of anode: Ni can be adversely affected by sulphur in the fuel, and carbon choking when the fuel is hydrocarbon. One approach to prevent carbon choking is to tune water content in the fuel or to reduce the operating temperature. Another way is to replace Ni with less active transition metals such as Cu, which does not catalyse carbon deposition.

Recently, oxides with mixed electronic and ionic conductivities under reducing environment have been found to possess higher catalytic activity than ceria for fuel oxidation. Therefore, researchers studied different oxide structures as SOFC anodes, and perovskite oxides were reported to show better performance than other structures.[28] The perovskite anodes that are widely studied are titanates and chromites because of their high stability in reducing atmosphere. Unfortunately, no promising material has been found so far showing comparable performance to Ni, regarding to hydrogen oxidation and hydrocarbon reforming.

2.1.3 Cathode materials

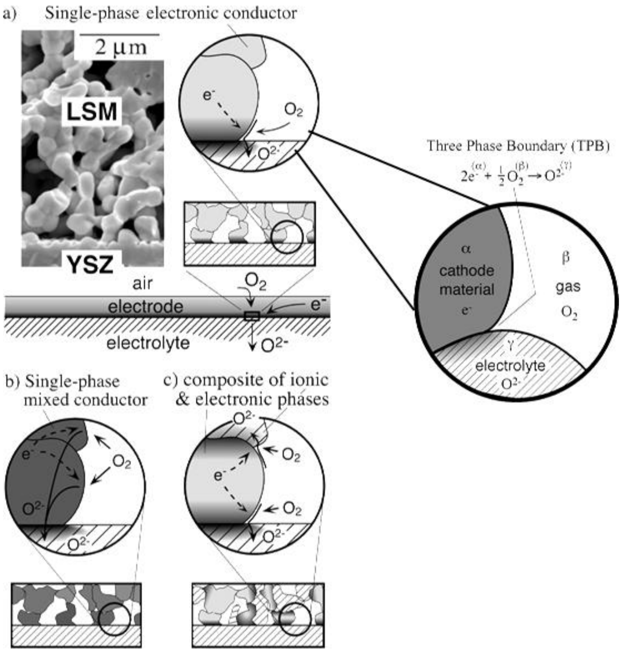

Figure 2-2 A schematic of active region for electrochemical oxygen reduction for (a) single phase pure electronic conductive cathode such as (La,Sr)MnO_3 (LSM) and (b) single phase cathode with mixed conductivities and (c) composite cathodes with mixed conductivities.[29]

The function of a cathode is to catalyse the ORR electrochemically. Conventional cathodes for HT-SOFC are usually sole electronically conductive materials, such as (La, Sr)MnO_3 (LSM). The lack of ionic conductivity of cathodes limits the active regions for ORR only to the three phase boundaries (TPBs) among cathode, electrolyte and gaseous oxygen (Figure 2-2 (a)), which results in a drastic increase of cathode polarization resistance at intermediate temperature. Consequently, improving both electronic and ionic conductivities (MIECs) of a cathode can extend the active sites throughout the cathode surface and significantly improve the electro-activity of cathode at IT range. One principal strategy is to design a single-phase material with MIECs, such as (La,Sr)(Co,Fe)$O_{3-\delta}$ (LSCF) as shown in Figure 2-2 (b) ; another is to develop a composite cathode by combining the electronically and ionically conductive phases together (Figure 2-2 (c)). In addition to sufficient ORR activity, a good cathode for IT-SOFC should also have matched thermal expansion coefficients, good chemical compatibility with electrolyte and current collectors, high long-term durability at elevated temperature, and high tolerance against contaminants such as Cr, B and CO_2. Though plenty of materials have been developed and evaluated as IT-SOFC cathodes, it still remains challenging to develop a suitable cathode candidate that meets all the requirements. The sluggish kinetics and instability of cathode are currently major challenges limiting the development of IT-SOFC technology. For this reason, the research advances on developing cathode materials are reviewed in the following sections.

2.2 Reaction mechanisms of SOFC cathode

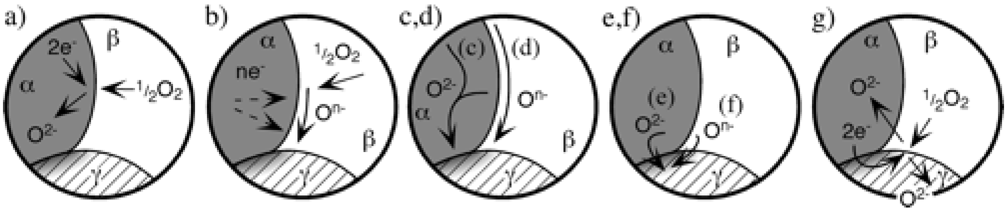

Figure 2-3 A simplified diagram for a few mechanisms considered to dominate ORR in cathodes. α, β and γ stand for electronic phase, gas phase and ionic phase respectively. a) Oxygen molecule is directly incorporated into the electronic phase bulk if α is mixed conductive; b) oxygen is adsorbed and/or partially reduced on the electronic phase surface; c) the partially reduced oxygen or d) the reduced oxygen transport to α/γ interface through surface or bulk respectively; e) Charge transfer of O^{2-} or f) partially reduced oxygen across the α/γ interface; g) one or multiple mechanisms wherein electroactive oxygen species are generated and transported at electrolyte. [29]

A typical SOFC cathode is a porous solid electrocatalyst applied onto a solid electrolyte membrane, and its function is to electrochemically catalyse ORR as described as follows:

$$\frac{1}{2}O_2(g)+2e^- \rightarrow O^{-2} \tag{2.1}$$

To achieve such function, a high quality cathode is required to possess (a) sufficient electronic conductivity (ideally > 100 S cm^{-1} in air); (b) optimized microstructure that allows easy oxygen diffusion to the cathode surface; (c) high electroactivity on ORR; (d) high stability for long-term SOFC operation; and (e) a matched thermal expansion coefficient (TEC) and chemical compatibility with other components such as electrolyte and current collectors.

Figure 2-3 introduces a few ORR mechanisms that might dominate the ORR rate in cathodes. In general, the O_2 molecules are adsorbed onto one or multiple solid surfaces, and subsequently are completely or partially reduced into electroactive species. Simultaneously, the oxygen species are traveling through the surface, interface or inside the cathode bulk into the electrolyte to form the electrolytic O^{2-}. Unfortunately, there is no single mechanism that is suitable for all the cathode materials, and the cathode performance are also significantly affected by the material types, microstructures, cathode fabrication processes, and cathode testing conditions.

The conventional cathode for high-temperature SOFC, such as (La,Sr)MnO_3, is typically a good electronic conductor but with negligible oxygen ion conductivity, so that the ORR is restricted at the TPBs. Such ORR active region confinement is generally considered to be the main reason for the slow ORR of conventional cathodes at reduced temperature. Ionic conducting phases can be incorporated into the conventional cathodes to increase the size of TPBs and therefore enhance cathode electroactivity at intermediate temperature.[30-33] Another strategy is to replace these pure electronic conductive cathodes with single-phase materials with MIECs that can extend the ORR active region throughout the cathode surface, thereby improving cathode performance at reduced temperature. There are many structures of materials having mixed conductivities, such as Ruddlesden-popper type structure, double perovskite structure, and perovskite structures. Among those structures, perovskite structured materials (ABO_3) receive immense research interest mainly because of their relatively high mixed conductivities at intermediate temperature. Therefore, a discussion mainly on the mixed conductivities of perovskite structure is presented in the following section.

2.2.1 Electronic conductivity

As illustrated by the ORR equation, electrons are directly involved in the electrochemical reduction of adsorbed oxygen species, so electronic conductivity is important for electroactivity of cathode. More specifically, the electronic conduction facilitates the availability of electrons at cathode surface for the surface exchange process, thereby of significance for the surface exchange kinetics.[34]

In the ABO_3 perovskite oxide, where B-site cations are usually reducible trivalent transition metals (TMs), the oxygen octahedral symmetry for B-site cations is beneficial for high electronic conductivity due to a semiconducting or metallic band structure brought about by the B-site cations. The couples of TMs with different valences (e.g. TM^{3+}/TM^{4+}) at B-sites can serve as hopping sites for electrons or holes, which are the charge carriers for the n-type or p-type electronic conduction respectively. In certain cases, such hopping sites can be generated by incorporating aliovalent cations into the oxides. For example, $La_{0.4}Sr_{0.6}Co_{0.2}Fe_{0.8}O_{3-\delta}$ has relatively higher electrical conductivity than $La_{0.6}Sr_{0.4}Co_{0.2}Fe_{0.8}O_{3-\delta}$ at lower temperature: the charge imbalance due to partial doping divalent Sr^{2+} into La^{3+}-sites can be easily compensated by transformation of B-site Co/Fe from +3 to +4 at lower temperature, and these TM^{+3}/TM^{+4} couples provide additional sites for hopping holes.[35] Charge disproportionation of B-site cations can also increase the hopping sites, and this defect reaction is driven by entropy and depend on the stability of electron configuration.[36] Sr doped $LaFeO_{3-\delta}$ is one example: Fe^{4+} cations can separate into Fe^{3+}/Fe^{5+} couples, which can increase the electronic conductivity.

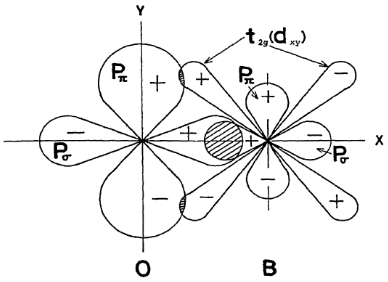

Figure 2-4 Schematic diagram for covalent bonds between the oxygen ion p_π-orbitals and B-cation t_{2g} (d) orbitals.[37]

For many perovskite cathodes, hopping mechanism dominates the electronic conduction. The covalence bond of B-cations with oxygen should be closely related to the electronic properties of the oxides. Figure 2-4 shows a schematic graph of the interaction between an oxygen ion and a B-site cation. The p_σ of the anion strongly interact with the cationic one, which is the major part of the B-O covalent bond and forces the t_{2g} orbitals towards anionic p_π orbitals. As a result, overlap between t_{2g} and p_π may exist to allow the transfer of t_{2g} electrons to the neighbouring t_{2g} orbitals through the p_π orbitals, therefore leading to mobility of electrons or holes along B-O-B bond.[37]

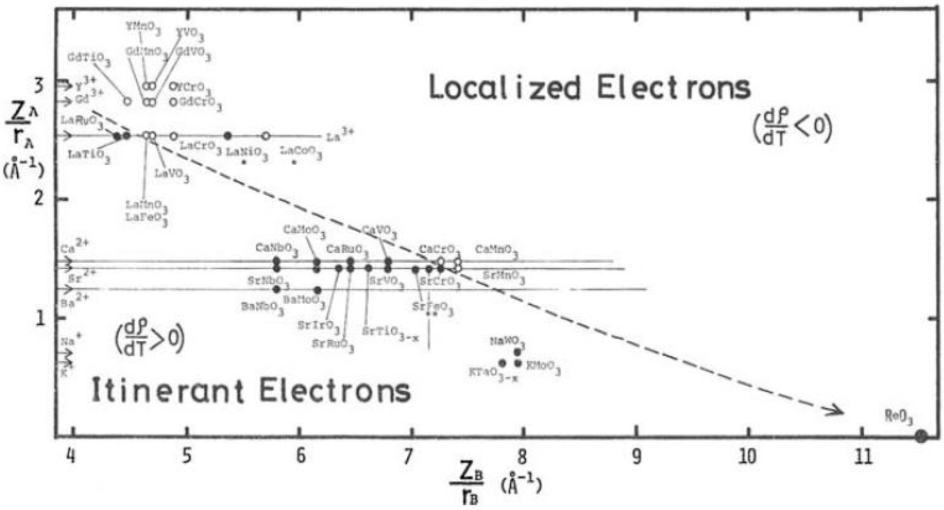

Figure 2-5 Potential map of perovskite oxides.[37]

Kamata *et al.*[37] categorized the electronic conduction behaviour of perovskite oxides into two main types: itinerate electrons and localised electrons. (Figure 2-5) In the potential map, Z and r refer to cation's valence and the Shannon's radius respectively. Lowering both values of the two variables (Z_A/r_A and Z_B/r_B) can increase the itinerant electrons of the perovskite oxides because low values of Z/r means low Coulomb-potential, which causes spread and overlap of the orbitals. Therefore, the electrical properties of the perovskite can be tuned by changing the integral overlap of the orbitals.

Taking advantage of the potential map, one can evaluate the electrical conductivity of any simple perovskite oxide. For relatively complicated perovskite oxides, the potential Z/r can be gained as a weighted average. Besides the potential of the cations, the degree of the distortion from ideal perovskite structure also affects the overlap of orbitals, and the tilting of the structure is reported to narrow the conduction band and enlarge the band gap.[38]

2.2.2 Ionic conductivity

As another significant property of IT-SOFC cathode, ionic conduction of most perovskite oxides is normally driven by oxygen vacancy gradient. For some materials such as Ruddlesden-Popper structured oxides[39-41], oxygen mobiles through an interstitial mechanism. In the vacancy-driven cases, an oxygen ion hops from an occupied oxygen site to the neighbouring vacancy site. Through interstitial mechanism, the oxygen ion at one interstitial site migrates to a neighbouring interstitial site. Since oxygen vacancy mechanism is more common and effective for oxygen ion conduction, this review attempts to mainly summarize the progress of the understanding on vacancy-driven oxygen ionic conduction.

Formation of oxygen vacancy

Oxygen vacancy is important in the vacancy mechanism, and its concentration affects the ionic conducting kinetics. The oxygen vacancy is a result of temperature (intrinsic defects) or impurities and/ or partial substitution of other cations (extrinsic defects). Taking (La, Sr) (Co, Fe) $O_{3-\delta}$ as an example, the charge neutrality can be ionically compensated by forming oxygen vacancies especially at higher temperature.[35] Low-valence dopant are found effective in lowering the oxygen vacancy formation energy especially in fluorite-structured ceria or MgO because they can lower the energy of unpaired electrons at the oxygen vacancies by creating a hole at the top of valence band to let the unpaired electrons to fill in.[42] Besides the cationic valence, the size of dopant also has an impact on the energy of vacancy formation. For instance, doping Ba^{2+} into Sr (Co, Fe) $O_{3-\delta}$ reduces the oxygen vacancy formation energy by 0.3 eV likely due to the relatively large size of Ba^{2+} that causes lattice expansion and thereby leads to formation of lower-valence Co. What is more, higher density of state of B-site cations close to the fermi level is also beneficial for oxygen vacancy formation due to its ease of valence transformation. For this reason, a higher level of Co in (Ba, Sr) (Co, Fe) $O_{3-\delta}$ leads to a lower oxygen vacancy formation energy as compared to the analogues with more Fe content.[43, 44]

However, the oxygen vacancy formation usually accompanies with diminishing charge carriers due to the following reaction as denoted using Kroger-Vink notation:

$$2B_B^{\times} + O_O^{\times} \rightarrow V_O^{\bullet\bullet} + 2B_B' + \frac{1}{2}O_2 \qquad (2.2)$$

Where “$\bullet$” and “ $/$ ” stands for unit positive and negative charge respectively, and “$\times$” represents neutrality. Therefore, the electronic conductivity can be negatively affected by the increasing level of oxygen vacancies. On the other hand, too large oxygen deficiency may destabilize the perovskite structure: distortion of cubic perovskite structure or formation of brownmillerite-type structure with ordering oxygen vacancies can severely deteriorate the ionic conductivity.[45, 46]

Oxygen vacancy mobility

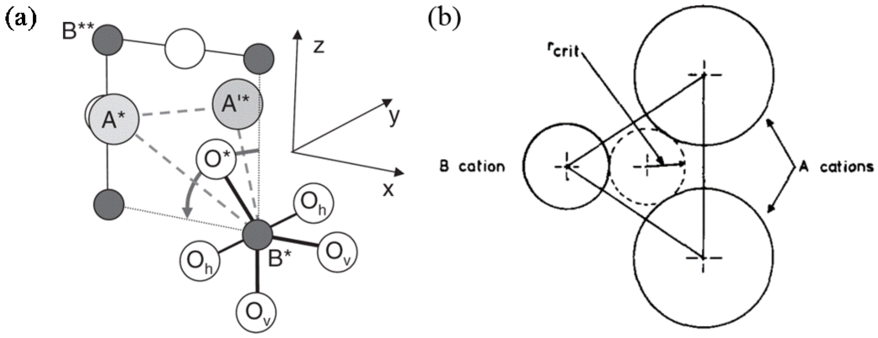

Figure 2-6 A schematic illustrating (a) a transition state of an oxygen O* migrate through the "saddle point" formed by one B-site cation (B*) and two A-site cations A* and A'* in a perovskite oxide; [44] **(b) the critical radius for the saddle point configuration.**[47]

Geometry also influences the ionic conductivities. Higher symmetry usually facilitates faster ionic conduction because it allows oxygen vacancies migrate isotropically to the neighbouring equivalent sites. During the transport along the edge of octahedral BO_6, oxygen ions have to pass through a space established by two A-site cations and one cation at B-site. That space is normally called as "saddle point". (Figure 2-6) Larger space of saddle point makes it easier for oxygen ion migrate through. Critical radius r_{cr} is the parameter, derived from a rigid hard-sphere model, that characterises the size of saddle point, which is defined as:[47]

$$r_{cr} = \frac{a_0\left(\frac{3}{4}a_0 - \sqrt{2}r_B\right) + {r_B}^2 - {r_A}^2}{2\left(r_A - r_B\right) + \sqrt{2}a_0} \tag{2.3}$$

$$a_0 \approx {V_{cell}}^{\frac{1}{3}} = 2.37r_B + 2.47 - 2(t^{-1} - 1) \tag{2.4}$$

where a_0 is the lattice constant of the pseudo cubic structure, and t is the tolerance factor. Critical radius r_{cr} can be increased by increasing B-site ionic radius r_B and/or decreasing A-site cation radius r_A.

However, typical r_{cr} for perovskite oxides is normally less than 1.05 Å,[48] much smaller than an oxygen ion, with an ionic radius of 1.4 Å, making it impossible for an oxygen ion to travel through. This size mismatch can be ascribed to the hard-sphere model that the r_{cr} is defined upon neglecting the effects from lattice relaxation. Consequently, Cherry *et al.* took the lattice relaxation into account to study the oxygen ion migration in the perovskite oxides, and suggested that an evenly distributed relaxation among cations while oxygen ion is migrating through the saddle point is important for lowering the energy barriers for oxygen ion migration.[49] In addition, smaller activation energy for oxygen ion migration is reported for materials with higher lattice polarizability.[50]

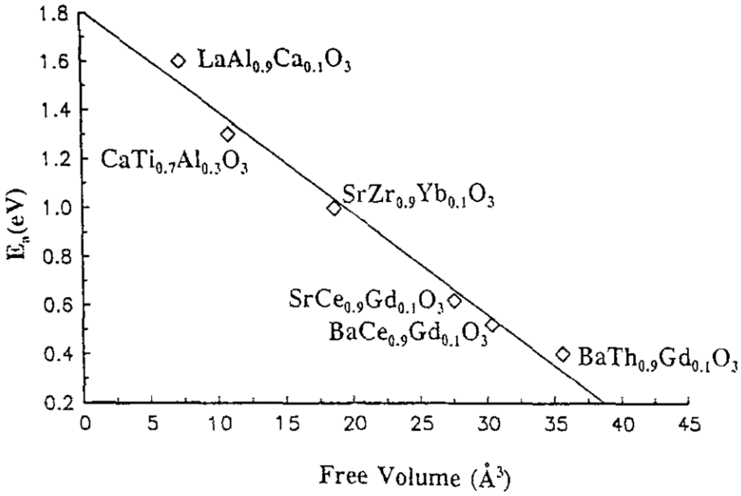

Figure 2-7 Relationship between activation energy for ionic conduction in perovskite oxides as a function of free volume.[51]

Lattice free volume V_f, which defined as the volume unoccupied by the ions in the unit cell, is also considered to influence the oxygen ion migration. A significant correlation as shown in Figure 2-7 was reported by Cook *et al.* between activation energy for oxygen ion migration and the free volume: larger V_f makes it easier for the migration of oxygen ions. Hayashi *et al.*[52] introduced a more universal parameter- the specific free volume (i.e. lattice free volume divided by total unit cell volume)- for easier comparison of different perovskite oxides. However, some exceptions were also reported such as $La_{0.9}Sr_{0.1}M_{0.9}Mg_{0.1}O_{2.9}$ (M=Al^{3+}, Ga^{3+}, Sc^{3+}, In^{3+})[53] : the oxide containing In^{3+} is predicted to be the optimal for oxygen conduction but the highest ionic conductivity is observed for Ga^{3+} containing oxide. Mogensen *et al.* argued the importance of lattice strain and structural distortion from cubic structure to the oxygen ionic conductivity, and claimed that a stress-free structure with cubic symmetry plays a significant role in fast oxygen migration.[48] Further experiment results also demonstrated that the deviation from such ideal perovskite phase degrades ionic conductivity.[54]

Moreover, the ionic conductivity can also be improved by lowering down the bonding strength between cation and oxygen.[54, 55] It is easy to understand that weak bonding strength of cations to oxygen ions renders easier oxygen ion migration. For perovskite oxides, this bond strength can be characterized by the average metal-oxygen bond energy (ABE) as given by[50]:

$$ABE = \frac{1}{12m}\left(\Delta H_{A_mO_n} - m\Delta H_A - \frac{n}{2}D_{(O_2)}\right) + \frac{1}{6x}\left(\Delta H_{B_xO_y} - x\Delta H_B - \frac{y}{2}D_{(O_2)}\right) \quad (2.5)$$

Where $\Delta H_{A_mO_n}$ and $\Delta H_{B_xO_y}$ refer to the heats of formation for A_mO_n and B_xO_y respectively; ΔH_A and ΔH_B stand for the heats of sublimations of A and B metals respectively; $D_{(O_2)}$ is the dissociation energy of the O_2. The activation energy of oxygen-ion migration was found for certain perovskite ionic conducting materials correlates linearly with their calculated ABEs.[50]

Unfortunately, designing optimal material for cathode of SOFC usually ends up with making compromise. For example, substitution of aliovalent cations can increase oxygen vacancies but sometime sacrifices the symmetry of the structure and number of charge carriers. The valence state of the B-cations should be minimised to achieve low average metal-oxygen bonding energy, but the concentration of the charge carriers is consequently reduced so that deteriorate electronic conductivity. Though no approaches are perfect for cathode material design, the aforementioned factors more or less provide us some hints for IT-SOFC cathode development.

2.2.3 Controlling steps for ORR

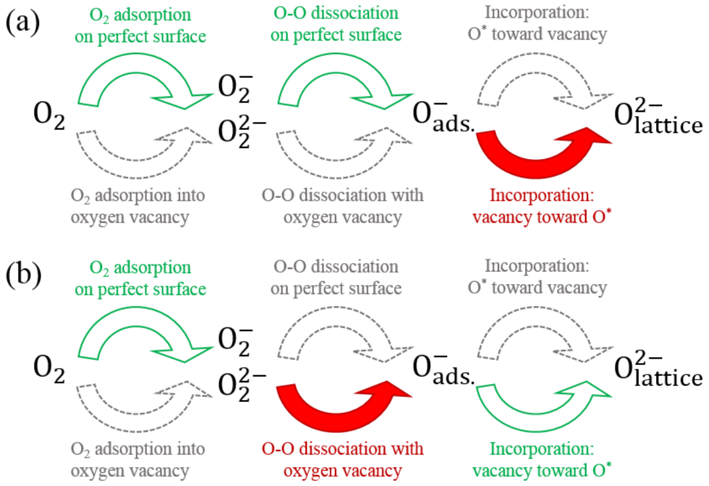

Figure 2-8 A schematic of possible pathways for incorporation of O_2 into perovskite oxides, with red standing for the rate-controlling step, green for fast process and dotted grey for slower step than other alternative step. Main mechanism for (a) perovskite oxides with few oxygen vacancies and (b) perovskites with high vacancy content.[56]

Recognizing which process that determines the ORR kinetics is significant for understanding the cathode reaction mechanism as well as for cathode activity improvement for IT-SOFC. For different cathode materials, the rating-controlling step may be different. An example is presented in Figure 2-8, the rate-determining step is the oxygen incorporation process for perovskite oxides containing very few oxygen vacancies such as (La, Sr)MnO_3 because of the scarce of vacancy on the surface. Interestingly, it is the vacancy that reaches the adsorbed oxygen species due to the observed high migration energy barrier for adsorbed oxygen species (~ 2 eV).[56] Nevertheless, the ORR kinetics of perovskites with sufficient oxygen deficiency, such as (La, Sr) (Co, Fe) $O_{3-\delta}$ and (Ba, Sr) (Co, Fe) O_{3-}

$_{\delta}$, are usually controlled by the oxygen dissociation step where oxygen vacancy gets involved. The rate of this vacancy-involved dissociation is limited by the encounter between the surface vacancy and the adsorbed oxygen molecules. Because of the adequate amount of movable vacancies, the oxygen reduction is no more limited by the oxygen incorporation step and the ORR activity is relatively high at lower temperature.

Electronic versus ionic conductivity

As mentioned in previous sections, mixed electronic and ionic conductivities are required especially for single-phase cathode materials for IT-SOFC, but these two conductivities cannot get along well with each other in most cases: increasing ionic conductivity can degrade the electronic conductivity mainly because oxygen vacancies can diminish charge carriers for electronic conduction. Consequently, which conductivity dominating the ORR catalytic rate has to be understood to optimize the cathode performance at reduced temperature.

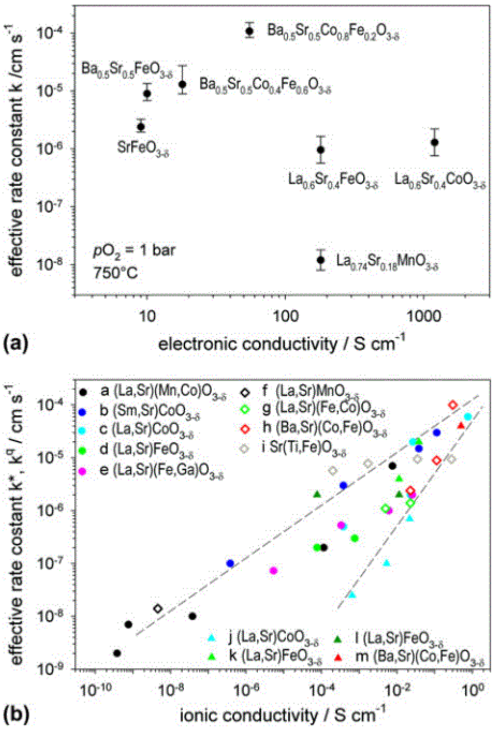

Figure 2-9 (a) Effective rate constant k of several perovskite oxides with mixed conductivities as a function of electronic conductivity under 1 bar oxygen partial pressure at 750 °C; (b) rate constants for bulk samples (circles for k*; triangles for $k^* = k_{chem}/w_o$ from chemical relaxation experiment where $w_o = 0.5\ (\partial \ln pO_2 / \partial \ln c_O)$) and dense films (diamond for k^q) against ionic conductivity under similar condition.[56]

Correlations between ORR rate constant and the conductivities are given in Figure 2-9, and it is obvious in Figure 2-9(a) that the electronic conductivity has little impact on cathode electroactivity, though electron transfer is involved in the reaction. For example, poor electronic conductor $Ba_{0.5}Sr_{0.5}Co_{0.8}Fe_{0.2}O_{3-\delta}$ shows much higher effective rate constant than that of $La_{0.74}Sr_{0.18}MnO_{3-\delta}$

which has higher electronic conductivity. In contrast, however, a clear trend can be seen for rate constants versus ionic conductivity: faster ionic conduction leads to higher oxygen exchange rate. (Figure 2-9(b)) Maier *et al.* also found that the content and mobility of oxygen vacancies are both the key factors for the oxygen incorporation process on the (Ba, Sr) (Co, Fe) $O_{3-\delta}$ surface.[57] Besides, an obvious relationship is also recognised between oxygen surface exchange coefficient and oxygen bulk diffusivity by many researchers.[34, 57-59] This correlation can be ascribed to the oxygen vacancies that is involved in both the rate-determining steps in surface exchange and the bulk oxygen ion conduction. A linear free enthalpy relationship derived by Maier *et al.*[59] also provides a quantified basis for such correlation. In addition, higher surface exchange kinetics are also reported for electron-rich materials than electron-poor materials with similar diffusivity, implying certain significance of electron conducting for the oxygen surface exchange.[34] However, the ionic conductivity is still the factor more important than electronic conductivity limiting the ORR activity.

Oxygen p-band center

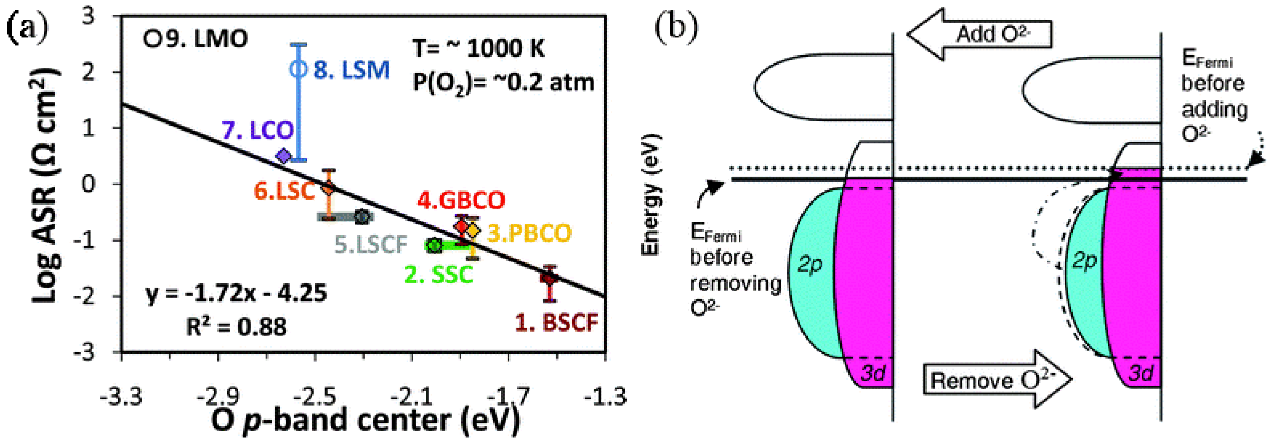

Figure 2-10 (a) The area specific resistance (ASR) of perovskite cathode materials from experiments as a function of O p-band centre; (b) a schematic illustration of relationship between ORR energetics and the O p-band centre based on the rigid band model.[60]

Ease of adding and removing an oxygen ion was also considered to be a vital limiting factor for cathode electroactivity. Morgan *et al.* used O p-band center to quantify this property and claimed that this variable can be a universal predictor for ORR activity, which is supported by the strong correlation of experimental ORR-related properties (including polarization resistance, surface exchange coefficient and B-site oxygen adsorption energy) versus the O p-band center.[60] (Figure 2-10) This clear trend can be explained by the number of electrons moving between Fermi level and the oxygen O p band when oxygen is added or removed as illustrate in Figure 2-10(b): the lower O p-band center, the easier for the electron interchange and thereby faster for oxygen addition and removal.

2.2.4 Conclusions of Section 2.2

In summary, the cathode materials such as perovskite oxides with both electronic and ionic conductivity exhibit higher electroactivity towards ORR at intermediate temperature, because such mixed conductivities help extend the reaction active region throughout the cathode surface. For electronic conduction, the charge carriers usually hop among reducible transition metal couples (e.g. TM^{3+}/TM^{4+}) via the overlaps between p_π and t_{2g} orbitals, so increasing the hopping sites or enlarging the orbital overlaps can improve the electronic conduction. For ionic conduction, high concentration and high mobility of oxygen vacancies are both important. The oxygen vacancy formation energy can be reduced by lowering the valence of B-site cations or increasing the density of states close to the Fermi level. The oxygen mobility can be affected by factors such as lattice geometry, lattice relaxation and strength of metal-oxygen bond. In many cases, increasing the ionic conductivity has to sacrifice the electronic conductivity due to the decreased amount of electrons when oxygen vacancies are formed. As compared to electronic conductivity, ionic conductivity is the major factor limiting the ORR activity, though electronic conduction shows somehow indirect positive effects on the surface exchange kinetics when comparing samples with similar oxygen diffusivity.

2.3 Crystallography of cathode materials

Crystallography is vital for a SOFC cathode because it usually determines the electroactivity and stability of the cathode. There are many types of crystal structures that have the potential to be cathode candidates for IT-SOFC, such as perovskite oxides, Ruddlesden-Popper oxides, double perovskite oxides, pyrochlore-type oxides and tetrahedrally coordinated materials. The following provides a very brief introduction about the perovskite oxides, Ruddlesden-popper oxides and double perovskite oxides because they are common candidates for IT-SOFC cathodes.

2.3.1 Ruddlesden-popper (RP) oxides

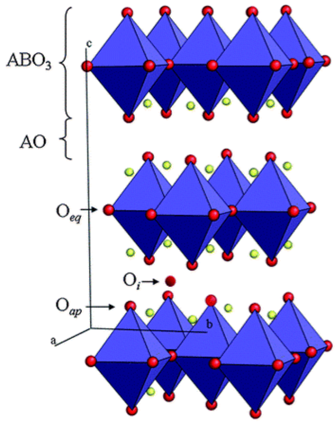

Figure 2-11 A schematic structure of a Ruddlesden-popper oxide containing *n* ABO_3 perovskite phases inserted between two AO rock-salt phase layers, and the oxygen atoms highlighted by the arrow are oxygen in equatorial (O_{eq}) , apical (O_{ap}) and interstitial site (O_i).[61]

A typical RP structure is presented in Figure 2-11, and materials in this structure has a general formula given as $A_{n+1}B_nO_{3n+1}$ (typically n=1,2,3), wherein several consecutive ABO_3 perovskite layers are alternated with AO rock-salt layers which stacks along c-axis. The RP structure is mainly in a tetragonal symmetry belonging to *I4/mmm* space group, with rare-earth or alkaline-earth cations at A-sites and transition metal elements at B-sites. For SOFC applications, RP materials for n=1 such as $Ln_2NiO_{4+\delta}$ (Ln = lanthanides) are alternative cathode materials due to their relatively high ionic conductivity, [62-64] and are also usually named as K_2NiF_4 structured materials.

The ionic conduction in RP lattice is generally considered to undergo an interstitial mechanism, where an oxygen accommodated at an interstitial site in the AO layers[65] jumps to other neighbouring interstitial site.[39] Interstitial oxygen ions can be formed by oxygen intercalation, accompanying with oxidisation of the lattice, as illustrated by:

$$\frac{1}{2}O_2 \leftrightarrow O_i'' + 2h^{\bullet} \tag{2.6}$$

Where O_i'' and $h^{\bullet}$ stand for an interstitial oxygen ion and a hole respectively. This oxygen intercalation can be realized chemically or electrochemically,[66-68] and the intercalated oxygen is located in a double tetrahedron consisting four O_{ap} and four A-site cations in the A_2O_2 layers. Though distortion of BO_6 octohedra occurs due to adding interstitial oxygen ions especially for $La_2NiO_{4+\delta}$, it is found more favourable for lattice relaxation by intercalating oxygen ions as compared to the stoichiometric one, where orthorhombic distortion is required to reduce lattice strain caused by parameter mismatch between different layers.[69]

The oxygen ions were found to diffuse anisotropically in the RP lattice: the conduction along the a-b plane is much faster than that along c axis. For example, the oxygen diffusivity (~ 10^{-7} cm^2 s^{-1} at 900°C) of $La_2CuO_{4+\delta}$ in the a-b plane is 100 times higher than that along the c- axis.[70] Similarly, a $La_2NiO_{4+\delta}$ film shows faster oxygen-ion diffusion (by three orders of magnitude) and surface exchange kinetic (by two orders of magnitude) as compared to those along c-axis.[71] The anisotropic ionic conduction behaviour arises from the layered structure of RP: a-b plane (i.e. A_2O_2) has higher content of interstitial sites for oxygen and lower migration activation energy as compared to c-axis.[70] Lattice relaxation, atomic volumetric change and oxygen polarizability were found to play significant roles in the interstitial oxygen migration,[69] but the charge transfer has a negligible effect on the migration. [69, 72]

2.3.2 Perovskite

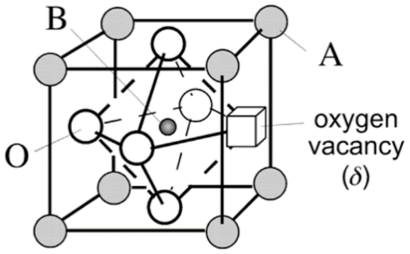

Figure 2-12 An atomic structure of a basic cubic perovskite oxide ABO_3 with an oxygen vacancy.[29]

A perovskite-structured oxide, as shown in Figure 2-12, is typically in a cubic structure with a general formula ABO_3. A-site cations are relatively larger cations with 12-fold coordination, such as rare-earth or alkaline-earth elements, and B-site cations are usually 6-fold coordinated cations in smaller size such as TMs like Mn, Fe, Co or Ni. The perovskite structures can be influenced by the sizes of A and B cations: the degree to which the structure deviates from the ideal perovskite can be measured by tolerance factor (t) as given by the following equation[73]:

$$t = \frac{r_A + r_O}{\sqrt{2}\left(r_B + r_O\right)} \tag{2.7}$$

where r stands for the ionic radius of A, B and oxygen ions. Different t values can point to different crystal structures as summarized in Table 2-1.

Table 2-1 The effects of cations on Goldschmidt factors and the corresponding possible crystalline structures to different values of Goldschmidt factors.

Tolerance Factor	Effects	Possible structures
t>1	The cations at A-sites are too large to stay at their interstices.	Hexagonal perovskite polytypes.
t=0.9~1	Cations and anions fit their sites.	Cubic structure
t=0.71~0.9	The cations at A-sits are too small.	Orthorhombic or rhombohedral
t<0.71	The size of A-cations is the same to B-cations	Some close-packed structure including corundum structure, ilmenite structure, and etc.

The radii of the ions were also studied by Goldschmidt[73], Zacharisasen[74], Pauling[75], Ahrens[76], and Shannon, [77-79] but the results differ from each other. Nowadays, the set of radii given by Shannon is widely accepted for the calculation of the tolerance factor since Shannon took into account the effect of coordination numbers on the radii of the ions. Though the perovskite phase still exist even when the calculated tolerance factor is not close to unity (for example $La_{1-x}Sr_xCoO_{3-\delta}$[80]), Goldschmidt's tolerance factor is an easy and practical tool to roughly predict perovskite formation and the crystal structure evolution as a function of concentration changes of the constituent ions.

Based on the type of B-site cations, the perovskite cathodes can be mainly categorized into Mn-based (e.g. LSM), [81-83] Fe-based (e.g. $SrFeO_{3-\delta}$), [84-94] Ni-based (e.g. $LaNiO_{3-\delta}$), Co-based (e.g. $(La, Sr)CoO_{3-\delta}$), [95-99] or mixed-TMs-based (e.g. $La(Ni, Fe)O_{3-\delta}$ and $Sr(Co, Fe)O_{3-\delta}$)[100-104] materials. As compared to other crystal structures, perovskite is relatively stable tolerating high level oxygen vacancies, thereby rendering fast bulk oxygen-ion conduction. The oxygen octahedral symmetry around reducible TMs usually makes it possible for rapid electron conduction. More details on the mixed conductivities are discussed in previous sections. (see Section 2.2.1 and 2.2.2) Because of their outstanding mixed conductivities, perovskite materials are regarded as one of the most promising candidates for the IT-SOFC cathodes.

2.3.3 Double perovskite

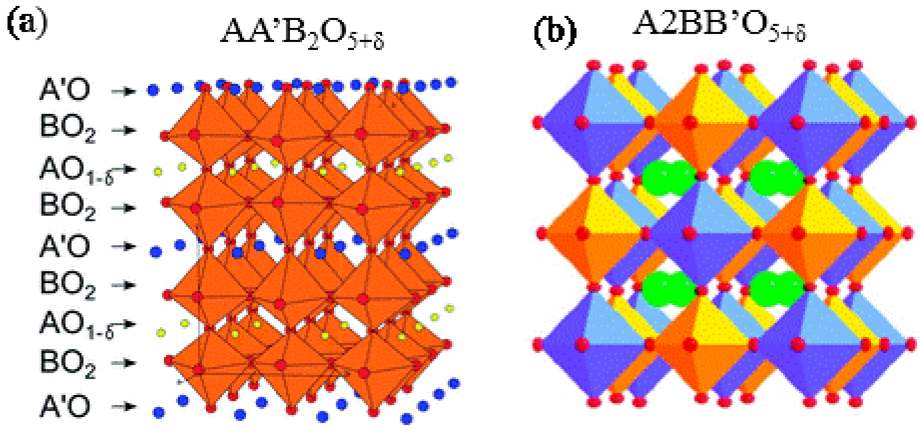

Figure 2-13 A schematic of (a) A-site cation ordering double perovskite oxide $AA'B_2O_{5+\delta}$,[105] and (b) B-site cation ordering double perovskite oxide $A_2BB'O_{5+\delta}$ with a rock-salt type B-cation sublattice.[106]

Another type of mixed conductor under wide investigations for SOFC applications is the double perovskite structured oxides. Double perovskite materials are a group of perovskite-related materials containing either ordered A-site ($AA'B_2O_{5+\delta}$) or B-site cations ($A_2BB'O_{5+\delta}$). (Figure 2-13) For an A-site ordering double perovskite, cations at A- and A’- sites are normally rare and alkaline earth elements respectively, and B-site cations are transition metals. A-site cation ordering is a result of the significant size difference between the two different A-site cations (A and A’).[61] For double perovskite oxides with ordered B-site cations, the crystallographic ordering, such as the common rock-salt ordering, is dominated by charge (primary factor) and size difference (secondary factor) of the B-site cations, and it is found that ordering B-cation sublattice is favoured when charge difference is larger than two.[107] Besides difference of cations at the same sites, the A/B cation mismatch also has an impact on the cation sublattice arrangement and phase stability, which can be characterises by the tolerance factor as defined by Eq (2.7).[107]

Some double perovskite oxides also show fast kinetics of oxygen surface exchange and diffusivity at reduced temperature, such as $LnBaCo_2O_{5+\delta}$ (Ln = Pr, Nd, Sm and Gd) and $PrBa_{0.5}Sr_{0.5}$(Co, Fe) $O_{5+\delta}$.[108-111] For example, $GdBaCo_2O_{5+\delta}$ shows an oxygen exchange coefficient of 2.8×10^{-7} cm s^{-1} and diffusivity of 4.8×10^{-10} cm^2 s^{-1} at 575 °C, with the respective activation energy of 0.81(4) eV and 0.60(4) eV, which are even lower than those of some benchmark simple perovskite cathodes such as (La, Sr) (Co, Fe) $O_{3-\delta}$.[108] Far higher ionic conductivity (by orders of magnitude) was also observed for double perovskite $GdBaMn_2O_{5+\delta}$ when compared with simple perovskite $Ga_{0.5}Ba_{0.5}MnO_{3-\delta}$,which is ascribed to the reduced oxygen bonding strength by the ordering GaO and BaO planes and the disorder-free trajectories for oxygen ion migration.[112] Similarly, Kim and Liu *et al* studied A-site ordering $PrBa_{0.5}Sr_{0.5}$(Co, Fe) $O_{5+\delta}$ double perovskite material using DFT simulations, and reported that pore channels in the lattice, especially the zigzag path through CoO plane, are the reason for its enhanced oxygen surface exchange and diffusion processes.[109]

2.3.4 Conclusions of Section 2.3

In conclusion, crystallography plays an important role in facilitating ORR-beneficial mixed conductivities. There are several types of mixed conductors having the potential to become IT-SOFC cathode, such as Ruddlesden-popper type, double perovskite and perovskite oxides. Most of these materials are composed of rare /alkaline earth elements, transition metals and oxygen ions. The structures of these materials are significantly affected by the sizes and electronic configurations of the cations. Mechanisms for these materials are different: interstitial mechanism dominates the ionic conduction in RP-type materials, and vacancy mechanism drives ionic conduction for the other two structures. Materials in simple perovskite structure are regarded as one of the most promising candidates for IT-SOFC cathodes, and some benchmark cathodes such as (La, Sr) (Co, Fe) $O_{3-\delta}$, $Sm_{0.5}Sr_{0.5}CoO_{3-\delta}$ and (Ba, Sr) (Co, Fe) $O_{3-\delta}$, are simple perovskite oxides. Therefore, this review also attempts to summarize the progress on developing some key perovskite cathode materials for IT-SOFC applications in the following section.

2.4 Materials for perovskite cathodes

As aforementioned in Section 2.2, the sluggish kinetics of conventional HT-SOFC cathode materials at intermediate temperature can be enhanced by either being replaced with single-phase mixed conductors or incorporated other phases with high ionic conductivity and enhanced redox properties. Correspondingly, this section attempts to give a review on recent advances in developing single-phase and composite perovskite cathode materials. More details are discussed on the perovskite cathode materials based on $SrCoO_{3-\delta}$ parent oxide, since this group of materials are recently reported to exhibit outstanding ORR electroactivity at very low temperature.

2.4.1 Single perovskite cathode materials based on different B-site cations

Depending on the B-site cation types, the perovskite oxides can be categorized into Mn-based, Co-based, Fe-based, Ni-based and mixed transition metal-based cathodes. As B-site cation is a dominant factor affecting the cathode performance, a brief review on these types is given as follows:

Manganese-based perovskite oxides

Perovskite-related manganites, such as (La, Sr) MnO_3, are a sort of materials that have the potential to be cathodes at high operating temperature (> 800 °C) because of their high electronic conductivity, fast kinetics towards ORR and relative low TEC that is compatible with commonly used electrolyte, such as yttria-stabilised zirconia (YSZ). [113]

Most of $LnMnO_3$-based cathodes are electronic conductors with very low oxygen ion conductivity. The insufficiency of oxygen vacancies is the main reason for the slow ionic conduction in Mn-based materials. Doping divalent alkaline-earth elements is not an effective way to create oxygen vacancies in the Mn-based lattice[28, 114] because the introduced charge imbalance by divalent dopants result in formation of more Mn^{4+}, which provides more holes for the electronic conduction.[115] Nevertheless, doping cations with fixed valence, such as Sc^{3+}, into B-site was found helpful in promoting oxygen vacancies and thus improve their cathode performance.[116, 117]

Another challenge of manganite cathodes is the reactivity of A-site cations with YSZ at high operating temperature. The formed secondary phases formed at cathode-YSZ interface, such as $SrZrO_3$ and $La_2Zr_2O_7$, are electronically insulated, leading to high polarisation resistance and high ohmic loss of cathodes by hindering surface diffusion of electrochemically active oxygen to TPBs and the formation of activated oxygen. [118] However, the chemical compatibility of Mn-based materials can be improved by creating A-site deficiency, doping low content of alkaline earth elements or Al^{3+} or reducing the size of lanthanide. [119-123] Although perovskite manganite oxides especially for (La, Sr) MnO_3 are still considered to be state-of-the-art cathode materials for HT-SOFC, they fail in meeting the requirements for an IT-SOFC cathode due to its inherent poor ionic conduction.

Iron-based perovskite oxides

Iron-based perovskite oxides, such as $SrFeO_{3-\delta}$, have been extensively studied and evaluated as cathode alternatives for IT-SOFC cathodes because they are more cost effective exhibit higher electroactivity in oxygen reduction than conventional Mn-based cathodes.[124-126] For instance, Petitjean *et al.* compared the bulk oxygen tracer diffusivity between $La_{0.8}Sr_{0.2}MnO_3$ and

$La_{0.8}Sr_{0.2}FeO_{3-\delta}$, and observed that the bulk oxygen diffusion of the latter is faster than the former by nearly six orders of magnitude.[127] The better catalytic activity of Fe-based perovskite is primarily ascribed to its available oxygen vacancies and therefore high ionic conduction. As compared to Co-based perovskite cathodes, iron-based perovskites stand out with having better matched thermal expansion coefficient with commonly used electrolytes such as doped ceria and doped zirconia at elevated temperature.[124, 128, 129]

Perovskite oxides derived from $LaFeO_{3-\delta}$ are widely studied as IT-SOFC cathodes. However, $LaFeO_{3-\delta}$ itself has poor electronic and ionic conductivity due to few oxygen vacancies and the absence of Fe^{3+}/Fe^{4+} hopping sites.[128] Therefore, doping divalent cation (eg. Sr^{2+}, Ba^{2+}) can improve both the electronic and ionic conductivity by creating anion vacancies and Fe^{4+} in the lattice.[130-132] Partial B-site cation substitution can improve the ORR-related properties of $(La, Sr)FeO_{3-\delta}$. For example, partially replacing Fe with Nb^{5+} can increase the electrical conductivity and thereby the electroactivity on ORR at IT range.[133] Cu is also a dopant that can improve the activity towards ORR at intermediate temperature, which may be attributed to the enhanced oxygen ion mobility by Cu and the optimised microstructure by lowering the cathode fabrication temperature.[134, 135] Moreover, replacing La with other rare earth elements such as Sm, Pr and Nd also show promising ORR activity, with an ASR of 0.085, 0.05 and 0.071 $\Omega\cdot cm^2$ at 700 °C for $Ln_{0.5}Sr_{0.5}Fe_{0.8}Cu_{0.2}O_{3-\delta}$ (Ln = Sm, Pr and Nd) respectively.[136-138] Xia *et al.* studied Bi^{3+} -doped $LaFeO_{3-\delta}$ as cathode for IT-SOFC, and found that the cathode performance is significantly improved as a result of more oxygen vacancies promoted by Bi^{3+}.[139]

$SrFeO_{3-\delta}$ is also a common parent oxide for Fe-based perovskite cathodes due to its sufficient oxygen vacancies for ionic conduction.[140] However, the structure of the $SrFeO_{3-\delta}$ is not stable, and phase transformation occurs at different temperature, and sometimes several phases coexist such as cubic perovskite structure and vacancy-ordering phases.[140, 141] Doping is an effective to stabilize the beneficial perovskite structure of $SrFeO_{3-\delta}$. For example, a cubic perovskite structure can be achieved by doping Bi^{3+} into Sr^{2+} site of $SrFeO_{3-\delta}$,[91, 126, 142] and the polarisation resistance of $(Sr, Bi) FeO_3$ is greatly improved at reduced temperature, owing to the low ABE, increased oxygen vacancy content and high ionic mobility brought by Bi^{3+}.[126] Substitution of Ba^{2+} is also found beneficial for stabilizing the cubic perovskite phase and enhancing cathode performance, and an example is the a polarisation resistance of 0.137 and 0.23 $\Omega\cdot cm^2$ were achieved by $Ba_{0.5}Sr_{0.5}Fe_{0.8}Cu_{0.2}O_{3-\delta}$ and $Ba_{0.5}Sr_{0.5}Fe_{0.8}Zn_{0.2}O_{3-\delta}$ at 750 °C, respectively.[143, 144] Besides, B-site cation substitution is another effective strategy to improve cathode electroactivity. Doping Ti, Nb, Mo and co-doping Sc and Nb are reported to stabilize the perovskite structure of $SrFeO_3$ and good for activity enhancement on oxygen reduction at lower temperature.[145-148]

Nickel-based perovskite oxides

$LaNiO_{3-\delta}$-based perovskite cathodes are also common cathodes for IT-SOFC. A phase transition is easy to occur from perovskite phase to a K_2NiF_4-type structure (i.e. $La_2NiO_{4+\delta}$) at temperature over ~ 850 ºC. Correspondingly, Chiba *et al.* evaluated $LaNiO_{3-\delta}$ oxide doped with different B-site dopants, such as Al, Cr, Mn, Fe, Co and Ga, as SOFC cathode, and observed that doping Fe is effective in stabilizing the perovskite phase and increasing the electronic conductivity up to 580 S cm^{-1} at 800 °C for $LaNi_{0.6}Fe_{0.4}O_{3-\delta}$.[149] $LaNi_{0.6}Fe_{0.4}O_{3-\delta}$ shows the highest electrochemical activity, with an ASR value of 5.5 $\Omega \cdot cm^2$ at 600 ºC, which is a result of increased ionic conductivity brought by Fe.[150] However, $LaNiO_{3-\delta}$-based cathodes are chemically incompatible with YSZ electrolyte at temperature over 1000 ºC, and the formed electronically insulating $La_2Zr_2O_7$ can lead to detriment of cathode performance. Another challenge for La (Ni, Fe) $O_{3-\delta}$ is its susceptibility to volatile Cr species coming from the metallic components of fuel cell stack. It is found that Cr can be gradually incorporated into the lattice and expel nickel out of the lattice, thereby degrading the electronic conductivity and cathode performance especially at higher temperature.[151]

Cobalt-based perovskite oxides

The perovskite cathodes containing Co usually exhibit high electronic and ionic conductivities, and superior electrocatalytic activity towards ORR at intermediate temperature. For this reason, Co-based perovskite oxides receive enormous research interest and work in IT-SOFC cathode development. Perovskite cathodes derived from $SrCoO_{3-\delta}$ are one of the most promising candidates for high performance IT-SOFC. Several benchmarked cathode materials are developed based on $SrCoO_{3-\delta}$ such as (Sm, Sr) $CoO_{3-\delta}$, (La, Sr) (Co, Fe) $O_{3-\delta}$, and $Ba_{0.5}Sr_{0.5}Co_{0.8}Fe_{0.2}O_{3-\delta}$. Recently, a few novel $SrCoO_{3-\delta}$-based cathodes have been developed, showing superior electroactivity at very low temperature. For instance, a highly active cathode material $SrSc_{0.125}Nb_{0.025}Co_{0.8}O_{3-\delta}$ shows an ASR as low as 0.11 $\Omega \cdot cm^2$ at 550 °C. One of the challenges for $SrCoO_{3-\delta}$-based perovskite cathodes is their mismatched TEC with commonly used electrolyte materials (like doped ceria). Taking $Ba_{0.5}Sr_{0.5}Co_{0.8}Fe_{0.2}O_{3-\delta}$ for an example, it has a TEC of 24×10^{-6} K^{-1} that is over twice higher than that of the electrolyte, and the mismatched thermal expansion can cause thermal stress in the cathode.[152] The high TEC is normally related to the reduction of cobalt ions, where the electrons in d-orbitals change from low-spin stats to high-spin states at elevated temperature.[153] However, the mismatched TEC can be effectively alleviated by mixing Co-containing perovskite cathodes with low-TEC electrolyte materials. Besides, the Co-based cathodes containing alkaline-earth elements are also susceptible to the acidic contaminates in the air, such as CO_2, boron and volatile Cr species, and the cathode performance can be severely deteriorated by these contaminates. As this project mainly focuses on developing high-performance cathode materials based on $SrCoO_{3-\delta}$, a review with more details is given in the following section.

2.4.2 $SrCoO_{3-\delta}$-based perovskite oxides

The reason for using pristine $SrCoO_{3-\delta}$ as a parent oxide is its potential of high mixed conductivities as demonstrated by the observed high permeability of $La_{1-x}Sr_xCo_{1-y}Fe_yO_{3-\delta}$ oxygen permeation membranes when the composition approaches pure $SrCoO_{3-\delta}$.[154] The oxygen vacancies are likely formed to compensate the charge imbalance introduced by the low valence of Sr, so ionic conductivity can be enhanced by these oxygen vacancies. However, the crystal structure of $SrCoO_{3-\delta}$ is not stable: the $SrCoO_{3-\delta}$ at below 900 °C is in an ordered 2H-type $BaNiO_3$ structure, showing oxygen permeability over 5 times lower than that of $SrCoO_{3-\delta}$ in the disordered cubic perovskite phase at above 900 °C.[155] Partially doping cations into A-sites or/and B-sites turns out effective to stabilize the benign perovskite structure at reduced temperature, and also to improve the electrode activity and stability of $SrCoO_{3-\delta}$ cathode. Therefore, in the following discussion, we focus on the advances of the doped $SrCoO_{3-\delta}$ perovskite cathode materials, particularly the cathode activity and stability.

A-site doping on $SrCoO_{3-\delta}$ perovskite

Improved cathode performance can be achieved by creating cation deficiency or by doping A-site of $SrCoO_{3-\delta}$ perovskite with other similar size cations such as rare-earth and other alkaline-earth elements.

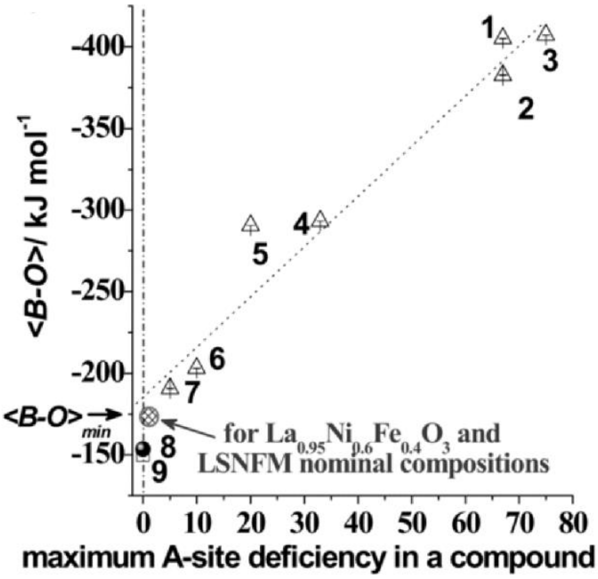

Figure 2-14 Relationship between the highest level of A-site deficiency and the average B-O bond energy. 1. $La_{1/3}TaO_3$; 2. $La_{1/3}NbO_3$; 3. $Na_{0.25}WO_3$; 4. $La_{2/3}(Ti^{4+}_{0.5}Ti^{3+}_{0.5})O_{3-\delta}$; 5. $La_{0.2}Sr_{0.6}Ti_{0.8}Nb_{0.2}O_3$; 6. $La_{0.9}(Mn^{4+}_{0.5}Mn^{3+}_{0.5})O_{3+\delta}$; 7. $La_{0.55}Sr_{0.4}Co^{3+}_{0.2}Fe^{3+}_{0.8}O_3$; 8. $LaNiO_{3-\delta}$; 9. $LaCoO_{3-\delta}$.[156]

Introducing small amount of A-site deficiency can create more oxygen vacancies, and enhance the ionic conductivity. For example, 5 mol% of Sr deficiency increases the oxygen vacancy content of $SrCo_{0.9}Nb_{0.1}O_{3-\delta}$ from 0.240 to 0.345, leading to a lower ASR of about 0.147 $\Omega\cdot cm^2$ at 550 °C.[157, 158] Electroactivity improvement was also reported for (La or Pr, Sr) (Co, Fe) $O_{3-\delta}$ cathodes with relatively low A-site deficiency.[159, 160] However, the electronic conductivity is sacrificed by introducing A-site deificency.[44,45] The reduction in conductivity is likely caused by the additionally formed oxygen vacancies, which suppresses charge change of B-site cations and consequently reduces the hopping sites for charge carriers. The TEC can also be reduced by introducing deficiency at A-site. A TEC of 9.3×10^{-6} K^{-1} is achieved for 20 mol% of A-site deficiency for (Ba, Sr) (Co, Fe) $O_{3-\delta}$ cathode, and the TEC value is much lower than that of the original one (27.5×10^{-6} K^{-1}).[161] However, excessive A-site deficiency may lead to loss of B-site cations in the lattice, and therefore deteriorates the cathode activity.[160] In order to probe the maximum possible A-site deficiency content, Konysheva *et al.* studied the relationship between maximum deficiency at A-site and the B-site bond energy with oxygen (Figure 2-14), and suggested a method to estimate the highest tolerable A-site deficiency in a perovskite compound by evaluating whether the B-O bond energy is close to -170 kJ mol^{-1}.[156]

What is more, the A-site can be substituted with other rare earth elements such as La and Sm. Tu *et al.* evaluated the $SrCo_{0.8}Fe_{0.2}O_{3-\delta}$ cathodes doped with different lanthanide elements, and found that Nd-doped SC exhibit the best ORR activity.[162] Sm-doped SC cathode also shows promising cathode performance,[163] exhibiting an ASR of 0.085 $\Omega\cdot cm^2$ at 700 °C.[164] Doping lanthanide such as Pr into Sr can create more oxygen vacancies on the surface as compared to pure SC, thereby benefiting the oxygen surface exchange kinetics.[164] However, studies on $La_{1-x}Sr_xCo_{0.2}Fe_{0.8}O_{3-\delta}$ ($x \leq 0.4$) reveals that both overall oxygen vacancy content and electrical conductivity decrease as La content increases, owing to relatively high valence of La^{3+} that mitigates the ionic compensation (good for oxygen vacancy formation) and suppresses the charge disproportion of B-site cations (good for forming polaron hopping sites).[165]

Other alkaline earth elements such as Ba can also be incorporated into the A-site of $SrCoO_{3-\delta}$ perovskite cathodes. There is enormous research work on the (Ba, Sr) (Co, Fe)$O_{3-\delta}$ perovskite cathode because of its superior ORR activity at intermediate temperature, with an ASR of 0.055-0.071 $\Omega\cdot cm^2$ at 600 °C.[43, 60, 166-168] A more detailed review on (Ba, Sr) (Co, Fe)$O_{3-\delta}$ cathode was given by Shao *et al.*[169], so a brief discussion is given in this section. The outstanding electrode activity of (Ba, Sr) (Co, Fe)$O_{3-\delta}$ can be attributed to the fast oxygen exchange kinetics and high ionic conductivity.[170, 171] The Ba dopant with < 70 mol% doping level can stabilize the beneficial cubic perovskite phase of $SrCo_{0.8}Fe_{0.2}O_{3-\delta}$.[167, 172] Lower valence states are more preferable for Ba-doped $SrCoO_{3-\delta}$-based perovskite due to the relatively larger ionic radius of Ba than that of Sr.[172] Such low valence B-site cation preference, however, is a main reason for the lower electrical conductivity for Ba-doped SC cathode.[173] A major concern for the (Ba, Sr) (Co, Fe)$O_{3-\delta}$ application is its structure instability at intermediate temperature: a slow phase transformation occurs from cubic perovskite phase to hexagonal phase with lower mixed conductivities, and the electrochemical performance is affected by this phase transition.[174-176] The unwanted phase transition is likely caused by a gradual change of B-site valence that affects the ionic sizes of B-site and therefore makes tolerance factor larger than one.[174]

B-site doping on $SrCoO_{3-\delta}$ perovskite

Reducible dopants

In SC-based perovskite oxides, cobalt ions can be partially replaced with other reducible cations, such as Fe, Ni and Mn,[177-180] and these materials can be also regarded as the aforementioned mixed TMs-based perovskite cathode. Fe is one of the most common dopant that can be incorporated into SC oxide, and some benchmark IT-SOFC cathodes, such as LSCF[181] and BSCF[166, 169], are based on the Fe-doped SC. Doping Fe can stabilize the cubic perovskite phase of SC[182-186] and is effective in reducing the very high TEC of $SrCoO_{3-\delta}$ cathodes[181, 187] For some materials such as $SrCo_{0.8}Fe_{0.2}O_{3-\delta}$ (SCF20), however, a phase transition occurs from cubic perovskite phase to brownmillerite structure with very low ionic conductivity at below 800 °C especially under low oxygen partial pressure.[155, 188-190] Therefore, other cations, such as Cr[191], Zr[192] and P[193], are also doped into SCF20 to suppress such unwanted phase deformation by retarding too much oxygen loss from the lattice at high temperature. Unfortunately, the electrical conductivity of materials like LSCF and BSCF can be degraded by the Fe dopant.[194-196] Tai *et al.* attributed this electrical conductivity deterioration, particularly in $La_{0.8}Sr_{0.2}Co_{1-y}Fe_yO_{3-\delta}$, to a charge carrier trapping effect induced by Fe: a portion of hopping polarons are trapped in the Fe-sites and need a long time to overcome the energy barrier to hop back to the neighbouring Co-sites, where most of the polarons are migrating.[195] Besides, the charge compensation, as a result of the divalent Sr, is found more preferable on Fe (from +3 to +4) rather than on Co, and the charge disproportional ability of Co is also retarded by doping Fe, which also contributes to the lower conductivity for Fe-doped analogues.[195] Doping Fe also has a negative effect on oxygen vacancies: higher Fe content results in less oxygen vacancies, [197] and the calculated energies for both oxygen vacancy formation and migration also increase with Fe doping level particularly for $Ba_{0.5}Sr_{0.5}$ (Co, Fe) $O_{3-\delta}$ materials[43].

Fixed valence dopants

High valence cations with good solid solubility are also found effective in improving structure stability because of their high electrostatic repulsion between B cations.[182] TMs, such as Sc^{3+},Sn^{4+}, Ti^{4+}, Nb^{5+}, Sb^{5+} and Mo^{6+}, are a group of elements with fixed valence and similar size of cobalt (which means good for the solubility). Incorporating up to 20 mol% of these TMs into $SrCoO_{3-\delta}$ is proved beneficial for SC structural stability by other researchers.[186, 198-210] Moreover, some oxyanions such as phosphate, sulphate and silicate can also have some beneficial effect on stabilizing the cubic structure.[193, 211, 212] For some of these dopants such as Sc^{3+}, Mo^{6+} and Sb^{5+}, the crystal structure of $SrCoO_{3-\delta}$ at room temperature may be influenced by their substitution level[202, 203, 206, 213]: tetragonal structure (P4/mmm) is obtained if the doping content lower than 10 mol %; higher doping level will lead to the cubic perovskite structure.

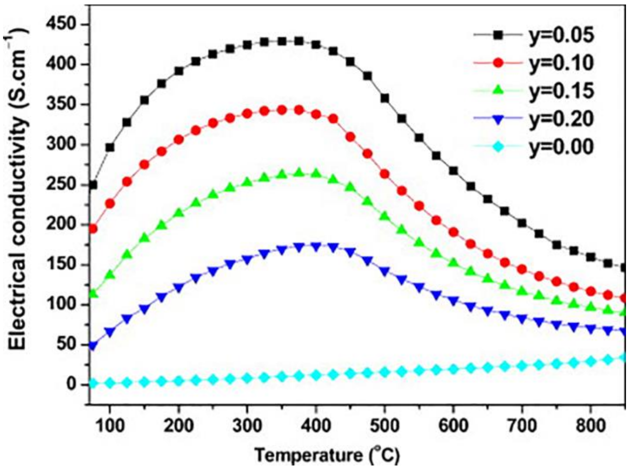

Figure 2-15 Electrical conductivity of $SrCo_{1-y}Ti_yO_{3-\delta}$ as a function of temperature.[214]

The fixed valence dopant content also has an impact on $SrCoO_{3-\delta}$'s electrical conductivity. The electrical conductivity of SC is improved by small doping level of fixed valence dopants probably due to the stabilized perovskite phase, but is degraded by higher level of dopants, which may hamper the electron hopping process along the (Co, TM)-O- (Co, TM) bond due to their fixed valences.[203] Taking Sr (Co, Ti) $O_{3-\delta}$ as an example, SC with 5 mol% Ti exhibits a maximum electrical conductivity of 430 S cm^{-1}, which is more than 20 times higher than that of pure SC, but the electrical conductivity decreases with the concentration of Ti^{4+} when the doping level is over 5 mol%, shown as Figure 2-15.[214] Similar trend was also reported for SC doped with Sc[213], Nb[201] and Mo[203]. Another property also affected by doping content is the oxygen vacancy, which is important to drive the ionic conduction. The oxygen vacancy will diminish with the substitutional content of high valence dopant for the reason that more oxygen ions are required to compensate the charge imbalance[182, 202], and too high dopant content will seriously deteriorate the cathode performance.

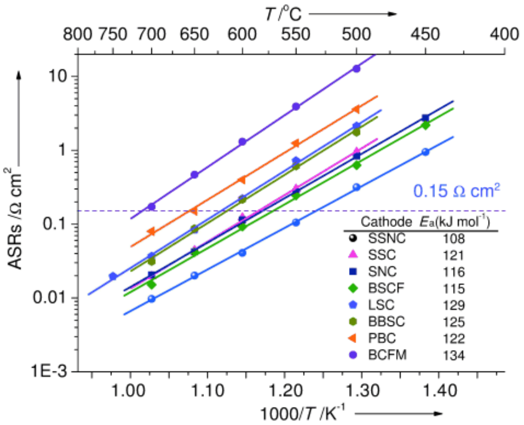

Figure 2-16 Temperature dependence of $Ba_{0.9}Co_{0.7}Fe_{0.2}Mo_{0.1}O_{3-\delta}$ (BCFM), $PrBaCo_2O_{5+\delta}$ (PBC), $La_{0.6}Sr_{0.4}CoO_{3-\delta}$ (LSC), $Ba_2Bi_{0.1}Sc_{0.2}Co_{1.7}O_{6-\delta}$ (BBSC), $SrSc_{0.2}Co_{0.8}O_{3-\delta}$ (SSC), $SrNb_{0.1}Co_{0.9}O_{3-\delta}$ (SNC) and $SrSc_{0.175}Nb_{0.025}Co_{0.8}O_{3-\delta}$ (SSNC) cathodes. [215]

Many $SrCoO_{3-\delta}$-derived cathodes doped with fixed valence TMs were reported to be highly active to reduce oxygen at intermediate temperature. For example, Shao *et al.* developed a Sc-doped SC cathode doped showing an ASR of 0.206 Ω·cm^2 at 550 °C, [199] and another Nb-doped $SrCoO_{3-\delta}$ with an ASR of 0.096 and 0.243 Ω·cm^2 at 600 °C and 550 °C, respectively.[198] Both of these cathodes also show relatively low TECs because of the dopants. What is more, a much higher ORR activity was then reported by Zhou *et al.*[215] for the cathode composition $SrSc_{0.175}Nb_{0.025}Co_{0.8}O_{3-\delta}$ (SSNC), reducing the ASR down to 0.11 Ω·cm^2 at 550°C. (Figure 2-16) The electrocatalytic activities of these materials are comparable to or even surpass that of the benchmark $Ba_{0.5}Sr_{0.5}Co_{0.8}Fe_{0.2}O_{3-\delta}$ cathode especially at below 550 °C.

Further cathode activity enhancement can be achieved by co-doping of Sc^{3+} and Nb^{5+}, and the simulation results showed that such co-doping facilitates lattice migration of oxygen vacancy by significantly reducing the migration energy barrier for paths between dopant neighbouring cobalt octahedral.[215]

One challenge to study the effects of these dopants on ORR is that the electrochemical oxygen reduction is a complex process involving different factors such as crystal structure, lattice geometry and cathode microstructure. For doped- $SrCoO_{3-\delta}$ materials, the interruption especially from lattice geometry cannot be avoided because of different ionic sizes and valences of the dopants in the cathode composition. Moreover, there are still many dopants remaining unexplored to incorporate into $SrCoO_{3-\delta}$ oxides for IT-SOFC cathode applications.

2.4.3 Composite cathode materials

Incorporating ionic conductors

As aforementioned in Section 2.2, the cathode performance at reduced temperature can be improved by compositing the cathode materials. One strategy is to develop composite cathodes by taking advantages of the merits of different constituents. An introduction of ionic conducting phases to the conventional electronic conducting cathodes is macroscopically accepted to bestow the mixed conductivities that are benign for cathode performance, and is also usually accompanied by a remarkably increased oxygen surface exchange coefficient (k). One example is a cathode composed of $La_{0.8}Sr_{0.2}MnO_3$ (LSM) with ~50 wt% of ionic conductor $Gd_{0.2}Ce_{0.8}O_{2-\delta}$ (GDC) showing an improved electrocatalytic activity about 7-times higher than the pure LSM, and the better cathode performance is claimed to arise from the fast ionic conduction and surface exchange rate at GDC.[33] Another example is a nanostructured assembly of (La, Sr)$MnO_{3-\delta}$ and highly ionic conductive $Bi_{1.6}Er_{0.4}O_3$ (ESB) exhibiting an improved area specific resistance (ASR) of 0.078 $\Omega\cdot cm^2$ at 600 °C thanks to the combination of both superior oxygen dissociative adsorption on (La, Sr)$MnO_{3-\delta}$ and the excellent surface exchange kinetics on the ESB.[32] Obviously, the authors for these examples both attributed the enhanced k to their ionic conducting phase, while some researchers believe that it is probably caused by a catalytic "spillover" effect[30] from the electronic conductive constituent facilitating the injection oxygen ions into the ionic conductive one. The "spillover" effect is evidenced by the two-orders of magnitude k enhancement of partial coated GDC with $La_{0.8}Sr_{0.2}Co_{0.2}Fe_{0.8}O_{3-\delta}$ (LSCF) as compared to the pure GDC.[216]

Introducing nano-scale redox electrocatalysts

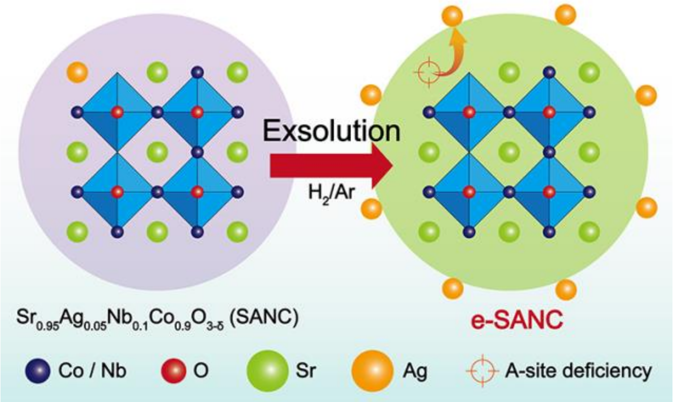

Figure 2-17 A schematic of silver exsolving process from bulk to the surface.[217]

Another effective route is to incorporate nano-scale redox catalysts. The reduced electrocatalyst dimensions will dramatically extend the ORR active TPBs due to an increase of interfaces between cathode and ionic conductors. There are many methods to achieve such nanostructured cathode, such as wet impregnation[218, 219], vapour deposition[220-222], electrospinning[223] and etc. A novel approach worth to be mentioned is the recently reported exsolving process, through which a nano-size Ag decorated $Sr_{0.95}Co_{0.9}Nb_{0.1}O_{3-\delta}$ (SCN0.95) was developed to exhibit extremely high cathode performance, with the lowest polarization resistances ever reported of 0.214 and 0.641 $\Omega\cdot cm^2$ at 550 °C and 450 °C.[217] Figure 2-17 is a simple scheme illustrating the exsolution process: nano metallic Ag particles is exsolved by 1 h diluted 10% H_2/Ar reduction at 320 °C from the original single-phase $Sr_{0.95}Ag_{0.05}Co_{0.9}Nb_{0.1}O_{3-\delta}$ (SACN) as synthesized via solid state reaction with $AgNbO_3$ serving as the silver source.[217] The superior ORR activity of such cathode is attributed to the fast oxygen surface exchange rate and the strong adhesion of Ag to the SCN0.95 backbone.[217]

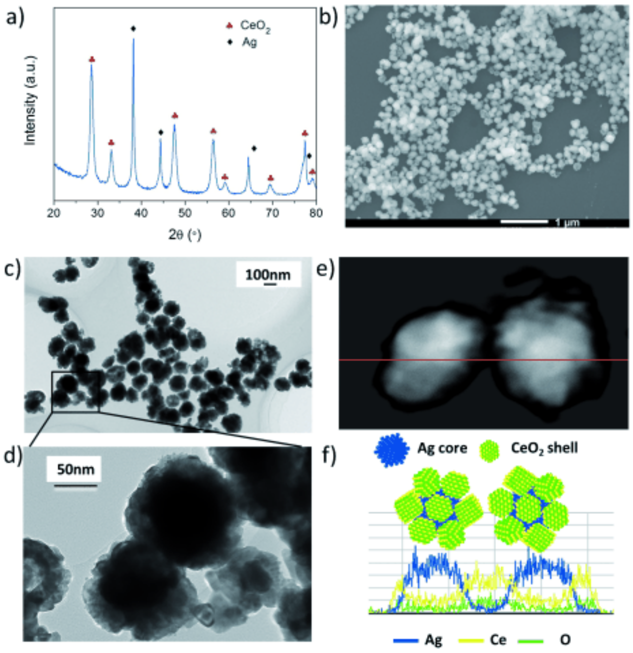

Figure 2-18 a) XRD profiles and b) a scanning electron microscopy (SEM) image of the Ag@CeO_2 core-shell nano spheres. c,d) Transmission electron microscopy (TEM) images and e,f) linear EDS scanning of the sample particles.[224]

Particle coarsening, which results in loss of effective active sites, is a major concern for the nano-size ORR catalyst during high-temperature cathode sintering and long-term operation. An effective strategy addressing this issue is to use the ionic conducting constituent to suppress the particle agglomeration. The aforementioned nano dual-phase (La, Sr)$MnO_{3-\delta}$-ESB cathode is synthesized by in-situ assembling the LSM and ESB phases, and such dual phase structure is demonstrated to suppress the grain growth during sintering.[32] Zhu *et al.* reported a highly active composite cathode by decorating the $SrSc_{0.175}Nb_{0.025}Co_{0.8}O_{3-\delta}$ cathode with Ag@CeO_2 core-shell nano spheres (Figure 2-18), where the CeO_2 shell is found effective to prevent the Ag core from coarsening during treatment at 800°C, and high cathode performance stability was achieved at 600 °C.[224] Moreover, the particle growth is also effectively confined for the nanoscale cathode by co-loading LSM and YSZ nanoparticles.[31]

In some situations, however, this compositing method seems to be ineffective, especially for the cathodes possessing sufficiently high MIECs itself such as $Ba_{0.5}Sr_{0.5}Co_{0.8}Fe_{0.2}O_{3-\delta}$ (BSCF), which is reported to deliver a higher power density than the one simply mixed with $Sm_{0.15}Ce_{0.75}O_{2-\delta}$ (SDC).[166] Nevertheless, the cathode development strategy prevails in most cases, and will also be very effective in mitigating the usually mismatched TEC of most cobalt-containing cathodes.

2.4.4 Conclusions of Section 2.4

In summary, cathode performance can be improved by using single phase perovskite cathodes with high mixed conductivities or/and developing composite cathodes combining advantages of different constitutes.

Some main categories of single phase perovskite oxides based on Mn, Fe, Ni and Co are reviewed for IT-SOFC applications. More details on the development $SrCoO_{3-\delta}$ – derived perovskite cathode materials are given in this section because of their superior electroactivity on oxygen reduction at low temperature relative to other perovskite materials. For these perovskite cathode materials, preserving the benign perovskite structure is of significance for achieving high ORR activity, doping different cations or deficiency into either A-site or B-site is effective not only in stabilizing the perovskite phase but also in promoting ORR-related properties such as mixed conductivity, surface exchange kinetics and oxygen diffusivities. Besides the structure stability, challenges also exist in the chemical and thermal incompatibility of cathodes with commonly used electrolyte materials such as YSZ and doped ceria. For example, Mn-based cathodes are easy to react with YSZ at high temperature, and cathodes containing Co show excessively high TEC when compared with doped ceria. However, the seriousness of these issues can be somehow alleviated by lowering the cathode operating temperature. The susceptibility of cathode materials containing alkaline earth elements to contaminates in air is another challenge for long-term operation of perovskite cathode materials. In the section 2.5, the corresponding research progress is reviewed.

Developing composite cathode materials is one of the most common strategy for activity enhancement for intermediate temperature operation. Mechanically mixing ionic conducting materials (eg. electrolyte materials) with electronically conducting oxides (usually conventional cathodes) can bestow mixed conductivities, increase ORR active regions and therefore lower cathode polarisation resistance at low temperature. Recently, novel compositing approaches are developed to further improve the composite cathode activity by reducing the cathode particle dimensions and strengthening the contact between electronic and ionic conductors. Moreover, introducing efficient redox electrocatalysts by impregnation, vapour deposition and exsolving are also proved effective in activity enhancement. Another advantage of a composite cathode is its significantly reduced TEC, which makes the Co-containing well match with the commonly used electrolytes.

2.5 Instability of $SrCoO_{3-\delta}$-based perovskite cathodes

Applications are limited for some highly active $SrCoO_{3-\delta}$-based perovskite cathodes because of their crystal structural instability and/ or susceptibility to contaminates such as Cr, boron and CO_2. As aforementioned, the BSCF perovskite phase is gradually transformed to the hexagonal phase that have lower mixed conductivities, and the oxygen flux performance degrades by nearly 50% for only 240 hours operation at 750°C.[225] Cr volatile species, which are from Fe-Cr alloy interconnects, can deposit on cathode surface and severely degrade the $SrCoO_{3-\delta}$-based cathode performance such as LSCF and BSCF at intermediate temperature.[226-229] It is found that the Cr poisoning effect is related to the surface segregation of Sr and/or Ba, and $SrCrO_4$, $BaCrO_4$ and $BaCr_2O_4$ are easy to be formed at temperature higher than 500 °C.[229] Moreover, the ORR kinetics and the microstructure of $SrCoO_{3-\delta}$-based perovskite cathodes are also negatively affected by boron which comes from glass sealants.[230-232] The boron can deposit onto the cathode surface and lead to significant Ba and Sr surface segregation. However, higher tolerance to boron is observed for cathodes with low content of La^{3+} , which is likely due to higher activity La_2O_3 with boron than SrO and BaO.[230, 232]

Since work on cathode instability in the presence of Cr and B have been extensively and profoundly done and reviewed, [233-237] the susceptibility to CO_2 attack at intermediate temperature still remains challenging for AE-containing perovskite cathodes. This review therefore attempts to review recent studies on addressing the susceptibility of most alkaline-earth-containing cathodes to even small content of CO_2 in air (~ 300 ppm) at intermediate temperature (< 800 °C).

2.5.1 CO_2 poisoning mechanisms

In the presence of CO_2, the oxygen surface exchange will be drastically slowed down for cathodes containing alkaline earth elements, such as (Ba, Sr) (Co, Fe) $O_{3-\delta}$[238-241] and (Sm, Sr) Co $O_{3-\delta}$[242]. The susceptibility of cathodes to CO_2 is mainly related to the basic surface as a result of their basic alkaline earth elements.[242-244] CO_2 and O_2 were reported to compete for the limited active oxygen vacancies on the cathode surface,[245] and long-term exposure to CO_2 will lead to carbonate formation on the surface and further unrecoverable crystal structure damage down to the bulk.[246] The alkaline earth cations usually play a significant role in the oxygen reduction catalysis, so reducing their concentration normally lowers the electrocatalytic activity on ORR in the absence of CO_2. For this reason, two approaches seem to be useful to improve the CO_2 tolerance without sacrifice of the superior electrocatalytic activity of the IT-SOFC cathodes: one is to improve ORR activity for alkaline earth-free cathodes; another is to enhance the CO_2 resistance for alkaline earth-containing cathodes by tuning their surface chemistry or other material properties. Very recently, the former has been summarized and reviewed[247], such as $LaNiO_{3-\delta}$, $La_2NiO_{4+\delta}$ and etc., so a brief discussion on the latter one will be given in this review.

2.5.2 Strategies to improve CO_2 tolerance

Tuning single phase cathodes

As aforementioned, it is mainly the basicity that makes the cathode easy to be poisoned by the acidic CO_2. So by incorporating relatively acidic elements, the CO_2 tolerance of the cathode will be improved. Cheng *et al.* studied the CO_2 tolerance of $Ba_{1-x}Sr_xCo_{0.8}Fe_{0.2}O_{3-\delta}$ cathodes in exposure to 1% CO_2/O_2, and reported higher resistances against CO_2 for cathodes with higher content of Sr, which is relatively more acidic than Ba. [243] Similarly, improved redox stability of SSNC relative to (Ba, Sr) (Co, Fe) $O_{3-\delta}$ when exposed to CO_2 was claimed to be partly related to the absence of Ba and relatively higher acidity of Nb than Fe.[248] Moreover, incorporation of Ta into Sr(Co,Fe)$O_{3-\delta}$ oxygen permeable membrane increases the material acidity, and therefore also significantly improves its performance stability in CO_2-containing atmosphere.[249]

Additionally, the alkaline earth phase segregation to the cathode surface is another issue related to the formation of carbonates on cathode surface and a heterogeneous phase near the surface.[240, 246, 250] Therefore, suppressing such segregation should be effective alleviating the CO_2 poisoning of cathode. One way as proposed by Yildiz *et al*.[251] is to restrain the alkaline earth segregation by reducing the size mismatch between dopant and host, so that a much more stable single cell performance was achieved by replacing Sr with smaller-size Ca into Pr (Ba, Sr)$Co_2O_{5+\delta}$ (PBSCO) layered perovskite cathode at 550 °C. [252] The alkaline earth phase segregation may be also promoted by the oxygen defects.[251, 253, 254] For example, much less carbonates are formed on $SrNb_{0.1}$(Co, Fe)$O_{3-\delta}$ cathodes with smaller oxygen nonstoichiometry than the analogues with more oxygen defects.[244] Moreover, the ABE is also recently regarded as an effective descriptor to predict the CO_2 tolerance for alkaline earth-containing perovskite materials: the stronger ABE of cathode material, the higher resistance against CO_2.[244, 248, 250] However, the electrocatalytic activity for ORR is usually sacrificed by the reduced level of oxygen vacancies or increase of ABEs. A trade-off still cannot be avoided between CO_2 resistance and the ORR activity for the cathodes containing AEs.

Composite cathodes

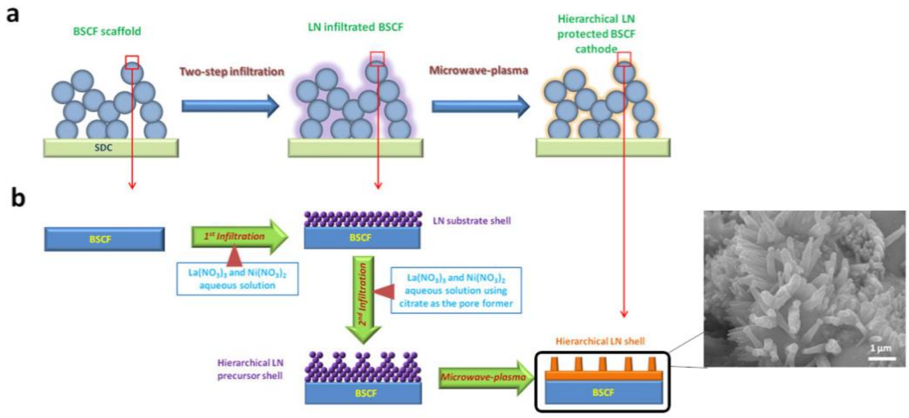

Figure 2-19 A schematic of the route to fabricate the dense hierarchical LN shell on BSCF surface.[242]

An attracting advantage of composite cathodes is that they exhibit combined merits from different constituents. So the resistance of cathodes against CO_2 attack can be improved by introducing an additional phase with high CO_2 tolerance. An example is the BSCF cathode protected by a hierarchical shell developed from CO_2-resistant $La_2NiO_{4+\delta}$ (LN), which does not only show enhanced cathode performance without CO_2 but also complete resistance against CO_2.[242] As shown in Figure 2-19, a microwave-induced plasma technique was in use to facilitate the formation and densification of the hierarchical LN shell without any phase interactions between pristine BSCF and LN coating. The poor oxygen surface exchange kinetics of the original LN is enhanced due to the hierarchical LN morphology, which therefore further improve the ORR activity of (Ba, Sr) (Co, Fe) $O_{3-\delta}$.[242] Moreover, the dense shell, facilitated by the microwave plasma treatment, provides superior protection for pristine (Ba, Sr) (Co, Fe) $O_{3-\delta}$ from CO_2, such hybrid cathode showing nearly no redox deterioration resulted from CO_2 and the ability to be fully recovered when CO_2 is removed.[242] However, one drawback for this method is the difficulties in applying the microwave plasma treatment in an industrial scale. Though very few work has been done in this field, we believe it is a very promising strategy to mitigating the susceptibility of alkaline earth-containing perovskite cathode while still maintaining or even enhancing its electrocatalytic activity in the absence of CO_2.

2.5.3 Conclusions of Section 2.5

To sum up, susceptibility of $SrCoO_{3-\delta}$-based perovskite cathode materials to the contaminates in the air such as Cr, boron and CO_2 can detrimentally affect the cathode performance especially for long-term SOFC operation. At lower temperature, the $SrCoO_{3-\delta}$-based perovskite cathodes becomes less tolerate against even very low content of CO_2 in the air. The CO_2 poisoning is mainly ascribed to the existence of basic alkaline earth elements, which play a significant role in efficiently catalyzing oxygen reduction for perovskite cathode materials. Strategies are explored to improve the resistance of $SrCoO_{3-\delta}$-based cathode materials, such as increasing the global acidity of the oxides by doping more acidic cations or suppressing the surface segregation of the basic phases. Unfortunately, these approaches developed so far have to sacrifice the ORR activity of the cathodes in the absence of CO_2. Another way is to introduce a CO_2-resistant ORR catalyst hierarchical shell covering the whole surface of the pristine $SrCoO_{3-\delta}$-based perovskite cathode to prevent the contact between CO_2 and the pristine cathode. Because only a few studies were carried out on cathode in exposure to CO_2, more work require to be probe the CO_2-poisoning mechanisms and explore effective ways to further improve cathode tolerance while still maintaining sufficiently high ORR activity at low temperature.

2.6 Summary

In this chapter, an overview of the SOFC is provided, followed by a review on the progresses in understanding the reaction mechanisms for ORR as well as the development of cathodes for intermediate-temperature solid oxide fuel cells. At reduced temperature, conventional cathodes with poor ionic conductivity usually applied in high-temperature solid oxide fuel cells show very slow catalyzing kinetics mainly due to their very limited active regions for oxygen reduction. The cathode performance at low temperature can be improved by introducing ionic conductors to electronic conducting electrodes or by using single phase cathode materials with mixed electronic and ionic conductivities. The mixed conductivities can extend the reaction active regions throughout the whole cathode surface, thereby significantly lowering the cathode polarization resistance.

For electronic conduction, the charge carriers (either electrons or holes) usually hop among reducible transition metal couples (e.g. TM^{3+}/TM^{4+}), so the electronic conductivity can be enhanced by increasing concentration of charge carriers or the overlap between orbitals of cations and oxygen ions. The mechanisms for oxygen ion conduction are different for different types of oxides. For example, interstitial mechanism dominates oxygen ion diffusion for Ruddlesden-popper oxides, and vacancy mechanism prevails for ionic conduction in perovskite and double-perovskite structured materials. The ionic conductivity can be improved by lowering the formation energy for oxygen vacancies or interstitial oxygen ions and/or increasing the oxygen ion mobility. The electronic and ionic conductivities show different functions in the ORR on cathode: electronic conductivity ensures that electrons are available on cathode surface for oxygen exchange processes; ionic conduction is involved in the limiting steps of oxygen reduction. For this reason, ionic conductivity is more dominant factor than electronic conductivity for cathode electroactivity.

There are several types of mixed conducting oxides that have the potential to become alternative candidates for IT-SOFC cathodes, such as Ruddlesden-popper, perovskite and double perovskite oxides. The crystal structure of a cathode is very important for cathode activity, because it determines the capability of tolerating defects such as oxygen vacancies and the mobility of the oxygen ions and electronic charge carriers. Among those structures, simple perovskite shows outstanding mixed conductivities and therefore regarded as one of the most promising candidates for IT-SOFC cathodes. For this reason, more details are discussed on single-phase perovskite cathode materials. $SrCoO_{3-\delta}$-based perovskite cathodes show the most promising activity at reduced temperatures, and some benchmark cathodes are all derived from $SrCoO_{3-\delta}$. Developing composite cathode is also an effective way to enhance cathode performance at low temperature. Several novel approaches developed recently are reviewed. What is more, the mismatched TEC of $SrCoO_{3-\delta}$, as a result of significant increase of ionic size of Co when being reduced, can be effectively alleviated by compositing these cathodes with electrolyte materials.

One of the challenges is the instability of perovskite phase at intermediate temperature under different conditions. Doping is an effective approach to stabilize the benign perovskite structure of $SrCoO_{3-\delta}$. Besides, doping strategies are also found useful to improve other properties related to cathode electroactivity, such as promoting oxygen vacancies for fast ionic conduction. However, great amount of work still requires to be carried out to study the specific effects of the dopant on electroactivity and how they interact with the pristine lattice, which is very important for rational design next generation of cathodes for IT-SOFC. Another challenge for $SrCoO_{3-\delta}$ – based perovskite cathodes is their susceptibility to the poisoning from contaminates in the air such as volatile Cr species, boron and CO_2. Only a few research investigated the CO_2 poisoning on perovskite cathodes at intermediate temperature. Although some progresses have been achieved in understanding the CO_2 – poisoning mechanisms and in improving resistance of alkaline-earth containing perovskite cathodes, it is still required substantial efforts for stability improvement on the highly ORR active cathodes based on $SrCoO_{3-\delta}$

2.7 References

1. Stambouli, A. B.; Traversa, E., Solid oxide fuel cells (SOFCs): A Review of An Environmentally Clean and Efficient Source of Energy. *Renewable and Sustainable Energy Reviews* **2002,** 6, (5), 433-455.

2. Badwal, S.; Foger, K., Solid Oxide Electrolyte Fuel Cell Review. *Ceramics International* **1996,** 22, (3), 257-265.

3. Badwal, S.; Ciacchi, F.; Milosevic, D., Scandia–zirconia Electrolytes for Intermediate Temperature Solid Oxide Fuel Cell Operation. *Solid State Ionics* **2000,** 136, 91-99.

4. Jacobson, A. J., Materials for Solid Oxide Fuel Cells. *Chemistry of Materials* **2009,** 22, (3), 660-674.

5. Takahashi, T.; Iwahara, H.; Arao, T., High Oxide Ion Conduction in Sintered Oxides of the System Bi_2O_3-Y_2O_3. *Journal of Applied Electrochemistry* **1975,** 5, (3), 187-195.

6. Verkerk, M.; Keizer, K.; Burggraaf, A., High oxygen ion conduction in sintered oxides of the Bi_2O_3-Er_2O_3 System. *Journal of Applied Electrochemistry* **1980,** 10, (1), 81-90.

7. Djurado, E.; Labeau, M., Second Phases in Doped Lanthanum Gallate Perovskites. *Journal of the European Ceramic Society* **1998,** 18, (10), 1397-1404.

8. Stevenson, J. W.; Armstrong, T. R.; Pederson, L. R.; Li, J.; Lewinsohn, C.; Baskaran, S., Effect of A-site Cation Nonstoichiometry on the Properties of Doped Lanthanum Gallate. *Solid State Ionics* **1998,** 113, 571-583.

9. Yamaji, K.; Horita, T.; Ishikawa, M.; Sakai, N.; Yokokawa, H., Chemical stability of the $La_{0.9}Sr_{0.1}Ga_{0.8}Mg_{0.2}O_{2.85}$ Electrolyte in A Reducing Atmosphere. *Solid State Ionics* **1999,** 121, (1-4), 217-224.

10. Huang, P.; Horky, A.; Petric, A., Interfacial Reaction Between Nickel Oxide and Lanthanum Gallate during Sintering and its Effect on Conductivity. *Journal of the American Ceramic Society* **1999,** 82, (9), 2402-2406.

11. Wang, S.; Kobayashi, T.; Dokiya, M.; Hashimoto, T., Electrical and Ionic Conductivity of Gd - Doped Ceria. *Journal of the Electrochemical Society* **2000,** 147, (10), 3606-3609.

12. Wang, S.; Inaba, H.; Tagawa, H.; Hashimoto, T., Nonstoichiometry of $Ce_{0.8}Gd_{0.2}O_{1.9-x}$. *Journal of the Electrochemical Society* **1997,** 144, (11), 4076-4080.

13. Wang, S.; Kato, T.; Nagata, S.; Honda, T.; Kaneko, T.; Iwashita, N.; Dokiya, M., Ni/Ceria Cermet as Anode of Reduced-Temperature Solid Oxide Fuel Cells. *Journal of the Electrochemical Society* **2002,** 149, (7), A927-A933.

14. Wang, F.-Y.; Chen, S.; Wang, Q.; Yu, S.; Cheng, S., Study on Gd and Mg Co-doped Ceria Electrolyte for Intermediate Temperature Solid Oxide Fuel Cells. *Catalysis Today* **2004,** 97, (2), 189-194.

15. Guan, X.; Zhou, H.; Wang, Y.; Zhang, J., Preparation and properties of Gd^{3+} and Y^{3+} Co-doped Ceria-based Electrolytes for Intermediate Temperature Solid Oxide Fuel Cells. *Journal of Alloys and Compounds* **2008,** 464, (1), 310-316.

16. Sha, X.; Lü, Z.; Huang, X.; Miao, J.; Jia, L.; Xin, X.; Su, W., Preparation and Properties of Rare Earth Co-doped $Ce_{0.8}Sm_{0.2-x}Y_xO_{1.9}$ Electrolyte Materials for SOFC. *Journal of Alloys and Compounds* **2006,** 424, (1), 315-321.

17. Han, M.-F.; Zhou, S.; Liu, Z.; Lei, Z.; Kang, Z.-C., Fabrication, Sintering and Electrical Properties of Cobalt Oxide Doped $Gd_{0.1}Ce_{0.9}O_{2-\delta}$. *Solid State Ionics* **2011,** 192, (1), 181-184.

18. Martinez-Coronado, R.; Singh, P.; Alonso-Alonso, J.; Goodenough, J. B., Structural Investigation of the Oxide-ion Electrolyte with $SrMO_3$ (M = Si/Ge) Structure. *Journal of Materials Chemistry A* **2014,** 2, (12), 4355-4360.

19. Singh, P.; Goodenough, J. B., Monoclinic $Sr_{1-x}Na_xSiO_{3-0.5x}$: New Superior Oxide Ion Electrolytes. *Journal of the American Chemical Society* **2013,** 135, (27), 10149-10154.

20. Wei, T.; Singh, P.; Gong, Y.; Goodenough, J. B.; Huang, Y.; Huang, K., $Sr_{3-3x}Na_{3x}Si_3O_{9-1.5x}$ (x = 0.45) as a Superior Solid Oxide-Ion Electrolyte for Intermediate Temperature-Solid Oxide Fuel Cells. *Energy & Environmental Science* **2014,** 7, (5), 1680-1684.

21. Lee, J. G.; Park, J. H.; Shul, Y. G., Tailoring Gadolinium-Doped Ceria-Based Solid Oxide Fuel Cells to Achieve 2 W Cm^{-2} at 550 °C. *Nature Communications* **2014,** 5.

22. Su, P.-C.; Chao, C.-C.; Shim, J. H.; Fasching, R.; Prinz, F. B., Solid Oxide Fuel Cell with Corrugated Thin Film Electrolyte. *Nano Letters* **2008,** 8, (8), 2289-2292.

23. Hui, R.; Wang, Z.; Yick, S.; Maric, R.; Ghosh, D., Fabrication of Ceramic Films for Solid Oxide Fuel Cells via Slurry Spin Coating Technique. *Journal of Power Sources* **2007,** 172, (2), 840-844.

24. Leng, Y. J.; Chan, S. H.; Jiang, S. P.; Khor, K. A., Low-temperature SOFC with Thin Film GDC Electrolyte Prepared In Situ by Solid-state Reaction. *Solid State Ionics* **2004,** 170, (1–2), 9-15.

25. Lutgard C. De Jonghe; Craig P. Jacobson; Visco, S. J., Supported Electrolyte Thin Film Symthesis of Solid Oxide Fuel Cells. *Annual Review of Materials Research* **2003,** 33, (1), 169-182.

26. Steele, B. C.; Heinzel, A., Materials for Fuel-Cell Technologies. *Nature* **2001,** 414, (6861), 345-352.

27. Gerk, C.; Willert-Porada, M. In *Development of Graded Composite Electrodes for the SOFC*, Materials science forum, 1999; Trans Tech Publ: 1999; pp 806-813.

28. Ralph, J.; Schoeler, A.; Krumpelt, M., Materials for Lower Temperature Solid Oxide Fuel Cells. *Journal of Materials Science* **2001,** 36, (5), 1161-1172.

29. Adler, S. B., Factors Governing Oxygen Reduction in Solid Oxide Fuel Cell Cathodes†. *Chemical Reviews* **2004,** 104, (10), 4791-4844.

30. Steele, B. C. H.; Hori, K. M.; Uchino, S., Kinetic Parameters Influencing the Performance of IT-Sofc Composite Electrodes. *Solid State Ionics* **2000,** 135, (1–4), 445-450.

31. Zhang, X.; Liu, L.; Zhao, Z.; Tu, B.; Ou, D.; Cui, D.; Wei, X.; Chen, X.; Cheng, M., Enhanced Oxygen Reduction Activity and Solid Oxide Fuel Cell Performance with a Nanoparticles-Loaded Cathode. *Nano Letters* **2015,** 15, (3), 1703-1709.

32. Lee, K. T.; Lidie, A. A.; Yoon, H. S.; Wachsman, E. D., Rational Design of Lower-Temperature Solid Oxide Fuel Cell Cathodes Via Nanotailoring of Co-Assembled Composite Structures. *Angewandte Chemie International Edition* **2014,** 53, (49), 13463-13467.

33. Perry Murray, E.; Barnett, S. A., $(La,Sr)MnO_3$–$(Ce,Gd)O_{2-x}$ Composite Cathodes for Solid Oxide Fuel Cells. *Solid State Ionics* **2001,** 143, (3–4), 265-273.

34. De Souza, R. A.; Kilner, J. A., Oxygen Transport in $La_{1-x}Sr_xMn_{1-y}Co_yO_{3\pm\delta}$ perovskites: Part II. Oxygen surface exchange. *Solid State Ionics* **1999,** 126, (1–2), 153-161.

35. Stevenson, J.; Armstrong, T.; Carneim, R.; Pederson, L.; Weber, W., Electrochemical Properties of Mixed Conducting Perovskites $La_{1-x}M_xCo_{1-y}Fe_yO_{3-\delta}$ (M= Sr, Ba, Ca). *Journal of the Electrochemical Society* **1996,** 143, (9), 2722-2729.

36. Van Roosmalen, J.; Cordfunke, E.; Helmholdt, R.; Zandbergen, H., The Defect Chemistry of $LaMnO_{3\pm\delta}$: 2. Structural Aspects of $LaMnO_{3+\delta}$. *Journal of Solid State Chemistry* **1994,** 110, (1), 100-105.

37. Kamata, K.; Nakamura, T.; Sata, T., State of d-electrons in Perovskite-type Compounds ABO_3. *Bull. Tokyo Inst. Technol* **1974,** 120, 73-79.

38. Eng, H. W.; Barnes, P. W.; Auer, B. M.; Woodward, P. M., Investigations of the Electronic Structure of d_0 Transition Metal Oxides belonging to the Perovskite Family. *Journal of Solid State Chemistry* **2003,** 175, (1), 94-109.

39. Chroneos, A.; Yildiz, B.; Tarancon, A.; Parfitt, D.; Kilner, J. A., Oxygen Diffusion in Solid Oxide Fuel Cell Cathode and Electrolyte Materials: Mechanistic Insights from Atomistic Simulations. *Energy & Environmental Science* **2011,** 4, (8), 2774-2789.

40. Parfitt, D.; Chroneos, A.; Kilner, J. A.; Grimes, R. W., Molecular Dynamics Study of Oxygen Diffusion in $Pr_2NiO_{4+\delta}$. *Physical Chemistry Chemical Physics* **2010,** 12, (25), 6834-6836.

41. Kushima, A.; Parfitt, D.; Chroneos, A.; Yildiz, B.; Kilner, J. A.; Grimes, R. W., Interstitialcy Diffusion of Oxygen in Tetragonal $La_2CoO_{4+\delta}$. *Physical Chemistry Chemical Physics* **2011,** 13, (6), 2242-2249.

42. Hu, Z.; Metiu, H., Effect of Dopants on the Energy of Oxygen-Vacancy Formation at the Surface of Ceria: Local or Global? *The Journal of Physical Chemistry C* **2011,** 115, (36), 17898-17909.

43. Kotomin, E. A.; Mastrikov, Y. A.; Kuklja, M. M.; Merkle, R.; Roytburd, A.; Maier, J., First Principles Calculations of Oxygen Vacancy Formation and Migration in Mixed Conducting $Ba_{0.5}Sr_{0.5}Co_{1-y}Fe_yO_{3-\delta}$ Perovskites. *Solid State Ionics* **2011,** 188, (1), 1-5.

44. Merkle, R.; Mastrikov, Y. A.; Kotomin, E. A.; Kuklja, M. M.; Maier, J., First Principles Calculations of Oxygen Vacancy Formation and Migration in $Ba_{1-x}Sr_xCo_{1-y}Fe_yO_{3-\delta}$ Perovskites. *Journal of The Electrochemical Society* **2011,** 159, (2), B219-B226.

45. van Doorn, R. H. E.; Burggraaf, A. J., Structural Aspects of the Ionic Conductivity of $La_{1-x}Sr_xCoO_{3-\delta}$. *Solid State Ionics* **2000,** 128, (1–4), 65-78.

46. Berastegui, P.; Hull, S.; García-García, F. J.; Eriksson, S. G., The Crystal Structures, Microstructure and Ionic Conductivity of $Ba_2In_2O_5$ and $Ba(In_xZr_{1-x})O_{3-x/2}$. *Journal of Solid State Chemistry* **2002,** 164, (1), 119-130.

47. Kilner, J. A.; Brook, R. J., A Study of Oxygen Ion Conductivity in Doped Non-stoichiometric Oxides. *Solid State Ionics* **1982,** 6, (3), 237-252.

48. Mogensen, M.; Lybye, D.; Bonanos, N.; Hendriksen, P.; Poulsen, F., Factors controlling the oxide ion conductivity of fluorite and perovskite structured oxides. *Solid State Ionics* **2004,** 174, (1), 279-286.

49. Cherry, M.; Islam, M. S.; Catlow, C., Oxygen Ion Migration in Perovskite-type Oxides. *Journal of Solid State Chemistry* **1995,** 118, (1), 125-132.

50. Sammells, A. F.; Cook, R. L.; White, J. H.; Osborne, J. J.; MacDuff, R. C., Rational selection of advanced solid electrolytes for intermediate temperature fuel cells. *Solid State Ionics* **1992,** 52, (1), 111-123.

51. Cook, R. L.; Osborne, J. J.; White, J. H.; MacDuff, R. C.; Sammells, A. F., Investigations on $BaTh_{0.9}Gd_{0.1}O_3$ as an Intermediate Temperature Fuel Cell Solid Electrolyte. *Journal of The Electrochemical Society* **1992,** 139, (2), L19-L20.

52. Cook, R. L.; Sammells, A. F., On the Systematic Selection of Perovskite Solid Electrolytes for Intermediate Temperature Fuel Cells. *Solid State Ionics* **1991,** 45, (3), 311-321.

53. Lybye, D.; Poulsen, F. W.; Mogensen, M., Conductivity of A-and B-site Doped $LaAlO_3$, $LaGaO_3$, $LaScO_3$ and $LaInO_3$ Perovskites. *Solid State Ionics* **2000,** 128, (1), 91-103.

54. Boivin, J.; Mairesse, G., Recent Material Developments in Fast Oxide Ion Conductors. *Chemistry of Materials* **1998,** 10, (10), 2870-2888.

55. Pouchard, M.; Hagenmuller, P., Solid Electrolytes: General Principles, Characterization, Materials, Applications. In *Solid Electrolytes as a Materials Problem*, Hagenmuller, P.; Van Gool, W., Eds. Elsevier: 1978.

56. Wang, L.; Merkle, R.; Mastrikov, Y. A.; Kotomin, E. A.; Maier, J., Oxygen Exchange Kinetics on Solid Oxide Fuel Cell Cathode Materials—General Trends and Their Mechanistic Interpretation. *Journal of Materials Research* **2012,** 27, (15), 2000-2008.

57. Wang, L.; Merkle, R.; Maier, J., Surface Kinetics and Mechanism of Oxygen Incorporation Into $Ba_{1-x}Sr_xCo_yFe_{1-y}O_{3-\delta}$ SOFC Microelectrodes. *Journal of The Electrochemical Society* **2010,** 157, (12), B1802-B1808.

58. Ramanarayanan, T. In *Proceedings of the Second International Symposium on Ionic and Mixed Conducting Ceramics*, 1994; The Electrochemical Society: 1994.

59. Merkle, R.; Maier, J.; Bouwmeester, H. J. M., A Linear Free Energy Relationship for Gas-Solid Interactions: Correlation between Surface Rate Constant and Diffusion Coefficient of Oxygen Tracer Exchange for Electron-Rich Perovskites. *Angewandte Chemie International Edition* **2004,** 43, (38), 5069-5073.

60. Lee, Y.-L.; Kleis, J.; Rossmeisl, J.; Shao-Horn, Y.; Morgan, D., Prediction of Solid Oxide Fuel Cell Cathode Activity with First-Principles Descriptors. *Energy & Environmental Science* **2011,** 4, (10), 3966-3970.

61. Tarancon, A.; Burriel, M.; Santiso, J.; Skinner, S. J.; Kilner, J. A., Advances in Layered Oxide Cathodes for Intermediate Temperature Solid Oxide Fuel Cells. *Journal of Materials Chemistry* **2010,** 20, (19), 3799-3813.

62. V. Kharton, V.; P. Viskup, A.; N. Naumovich, E.; M. B. Marques, F., Oxygen Ion Transport in La_2NiO_4-based Ceramics. *Journal of Materials Chemistry* **1999,** 9, (10), 2623-2629.

63. Skinner, S. J.; Kilner, J. A., Oxygen Diffusion and Surface Exchange in $La_{2-x}Sr_xNiO_{4+\delta}$. *Solid State Ionics* **2000,** 135, (1–4), 709-712.

64. Kharton, V. V.; Viskup, A. P.; Kovalevsky, A. V.; Naumovich, E. N.; Marques, F. M. B., Ionic Transport in Oxygen-Hyperstoichiometric Phases with K_2NiF_4-type Structure. *Solid State Ionics* **2001,** 143, (3–4), 337-353.

65. Jorgensen, J. D.; Dabrowski, B.; Pei, S.; Richards, D. R.; Hinks, D. G., Structure of the Interstitial Oxygen Defect in $La_2NiO_{4+\delta}$. *Physical Review B* **1989,** 40, (4), 2187-2199.

66. Nemudry, A.; Rudolf, P.; Schöllhorn, R., Room Temperature Topotactic Oxidation of Lanthanum Cobalt Oxide $La_2CoO_{4.0}$. *Solid State Ionics* **1998,** 109, (3–4), 213-222.

67. Buttrey, D. J.; Ganguly, P.; Honig, J. M.; Rao, C. N. R.; Schartman, R. R.; Subbanna, G. N., Oxygen Excess in Layered Lanthanide Nickelates. *Journal of Solid State Chemistry* **1988,** 74, (2), 233-238.

68. Demourgues, A.; Wattiaux, A.; Grenier, J. C.; Pouchard, M.; Soubeyroux, J. L.; Dance, J. M.; Hagenmuller, P., Electrochemical Preparation and Structural Characterization of $La_2NiO_{4+\delta}$ Phases ($0 \leqslant \delta \leqslant 0.25$). *Journal of Solid State Chemistry* **1993,** 105, (2), 458-468.

69. Frayret, C.; Villesuzanne, A.; Pouchard, M., Application of Density Functional Theory to the Modeling of the Mixed Ionic and Electronic Conductor $La_2NiO_{4+\delta}$: Lattice Relaxation, Oxygen Mobility, and Energetics of Frenkel Defects. *Chemistry of Materials* **2005,** 17, (26), 6538-6544.

70. Claus, J.; Borchardt, G.; Weber, S.; Hiver, J.-M.; Scherrer, S., Combination of EBSP Measurements and SIMS to Study Crystallographic Orientation Dependence of Diffusivities in a Polycrystalline Material: Oxygen Tracer Diffusion in $La_{2-x}Sr_xCuO_{4\pm\delta}$. *Materials Science and Engineering: B* **1996,** 38, (3), 251-257.

71. Burriel, M.; Garcia, G.; Santiso, J.; Kilner, J. A.; Chater, R. J.; Skinner, S. J., Anisotropic Oxygen Diffusion Properties in Epitaxial Thin Films of $La_2NiO_{4+\delta}$. *Journal of Materials Chemistry* **2008,** 18, (4), 416-422.

72. Chroneos, A.; Parfitt, D.; Kilner, J. A.; Grimes, R. W., Anisotropic Oxygen Diffusion in Tetragonal $La_2NiO_{4+\delta}$: Molecular Dynamics Calculations. *Journal of Materials Chemistry* **2010,** 20, (2), 266-270.

73. Goldschmidt, V.; Barth, T.; Holmsen, D.; Lunde, G.; Zachariasen, W., Geoçhemische Verteilungsgesetze Der Elemente; Vi. Tíber Die Krystallstrukturen Vom Rutiltypus. In mit Bemerkungen zur Geochemie Zweiwertiger und vierwertiger Element, Skrifter Norske Videnskaps-Akad. Oslo I. Mat.-Naturv. Kl: 1926.

74. Zachariasen, W., A Set of Empirical Crystal Radii for Ions with Inert Gas Configuration. *Z. Kristallogr* **1931,** 80, 137-153.

75. Pauling, L., The Sizes of Ions and the Structure of Ionic Crystals. *Journal of the American Chemical Society* **1927,** 49, (3), 765-790.

76. Ahrens, L. H., The Use of Ionization Potentials Part 1. Ionic Radii of the Elements. *Geochimica et Cosmochimica Acta* **1952,** 2, (3), 155-169.

77. Shannon, R. t.; Prewitt, C. T., Effective Ionic Radii in Oxides and Fluorides. *Acta Crystallographica Section B: Structural Crystallography and Crystal Chemistry* **1969,** 25, (5), 925-946.

78. Shannon, R.; Prewitt, C., Effective Ionic Radii and Crystal Chemistry. *Journal of Inorganic and Nuclear Chemistry* **1970,** 32, (5), 1427-1441.

79. Shannon, R., Revised effective ionic radii and systematic studies of interatomic distances in halides and chalcogenides. *Acta Crystallographica Section A: Crystal Physics, Diffraction, Theoretical and General Crystallography* **1976,** 32, (5), 751-767.

80. Richter, J.; Holtappels, P.; Graule, T.; Nakamura, T.; Gauckler, L., Materials Design for Perovskite SOFC Cathodes. *Monatshefte für Chemie - Chemical Monthly* **2009,** 140, (9), 985-999.

81. Liang, F.; Chen, J.; Jiang, S. P.; Chi, B.; Pu, J.; Jian, L., High Performance Solid Oxide Fuel Cells with Electrocatalytically Enhanced (La, Sr)MnO_3 Cahodes. *Electrochemistry Communications* **2009,** 11, (5), 1048-1051.

82. Sakaki, Y.; Takeda, Y.; Kato, A.; Imanishi, N.; Yamamoto, O.; Hattori, M.; Iio, M.; Esaki, Y., $Ln_{1-x}Sr_xMnO_3$ (Ln= Pr, Nd, Sm and Gd) as the Cathode Material for Solid Oxide Fuel Cells. *Solid State Ionics* **1999,** 118, (3), 187-194.

83. Dong, F.; Chen, D.; Ran, R.; Park, H.; Kwak, C.; Shao, Z., A Comparative Study of $Sm_{0.5}Sr_{0.5}Mo_{3-\delta}$ (M = Co and Mn) as Oxygen Reduction Electrodes for Solid Oxide Fuel Cells. *International Journal of Hydrogen Energy* **2012,** 37, (5), 4377-4387.

84. Huang, Y.; Vohs, J. M.; Gorte, R. J., Fabrication of Sr-Doped $LaFeO_3$ YSZ Composite Cathodes. *Journal of The Electrochemical Society* **2004,** 151, (4), A646-A651.

85. Orikasa, Y.; Nakao, T.; Oishi, M.; Ina, T.; Mineshige, A.; Amezawa, K.; Arai, H.; Ogumi, Z.; Uchimoto, Y., Local Structural Analysis for Oxide Ion Transport in $La_{0.6}Sr_{0.4}Feo_{3-\delta}$ Cathodes. *Journal of Materials Chemistry* **2011,** 21, (36), 14013-14019.

86. Simner, S. P.; Anderson, M. D.; Pederson, L. R.; Stevenson, J. W., Performance Variability of La(Sr)FeO_3 Sofc Cathode with Pt, Ag, and Au Current Collectors. *Journal of the Electrochemical Society* **2005,** 152, (9), A1851-A1859.

87. Jiang, S.; Zhou, W.; Sunarso, J.; Ran, R.; Shao, Z., A Cobalt-Free Layered Oxide as an Oxygen Reduction Catalyst for Intermediate-Temperature Solid Oxide Fuel Cells. *International Journal of Hydrogen Energy* **2015,** 40, (45), 15578-15584.

88. Yang, G.; Shen, J.; Chen, Y.; Tadé, M. O.; Shao, Z., Cobalt-Free $Ba_{0.5}Sr_{0.5}Fe_{0.8}Cu_{0.1}Ti_{0.1}O_{3-\delta}$ as a Bi-Functional Electrode Material for Solid Oxide Fuel Cells. *Journal of Power Sources* **2015,** 298, 184-192.

89. Jiang, S.; Sunarso, J.; Zhou, W.; Shen, J.; Ran, R.; Shao, Z., Cobalt-Free $SrNb_xFe_{1-x}O_{3-\delta}$ (X = 0.05, 0.1 and 0.2) Perovskite Cathodes for Intermediate Temperature Solid Oxide Fuel Cells. *Journal of Power Sources* **2015,** 298, 209-216.

90. Yang, G.; Su, C.; Chen, Y.; Dong, F.; Tade, M. O.; Shao, Z., Cobalt-Free $SrFe_{0.9}Ti_{0.1}O_{3-\delta}$ as a High-Performance Electrode Material for Oxygen Reduction Reaction on Doped Ceria Electrolyte with Favorable CO_2 Tolerance. *Journal of the European Ceramic Society* **2015,** 35, (9), 2531-2539.

91. Niu, Y.; Sunarso, J.; Zhou, W.; Liang, F.; Ge, L.; Zhu, Z.; Shao, Z., Evaluation and Optimization of $Bi_{1-x}Sr_xFeO_{3-\delta}$ Perovskites as Cathodes of Solid Oxide Fuel Cells. *International Journal of Hydrogen Energy* **2014,** 39, (27), 15156.

92. Dong, F.; Chen, Y.; Ran, R.; Chen, D.; Tade, M. O.; Liu, S.; Shao, Z., $BaNb_{0.05}Fe_{0.95}O_{3-\delta}$ as a New Oxygen Reduction Electrocatalyst for Intermediate Temperature Solid Oxide Fuel Cells. *Journal of Materials Chemistry A* **2013,** 1, (34), 9781-9791.

93. Jiang, S.; Zhou, W.; Niu, Y.; Zhu, Z.; Shao, Z., Phase Transition of a Cobalt-Free Perovskite as a High-Performance Cathode for Intermediate-Temperature Solid Oxide Fuel Cells. *ChemSusChem* **2012,** 5, (10), 2023-2031.

94. Niu, Y.; Sunarso, J.; Liang, F.; Zhou, W.; Zhu, Z.; Shao, Z., A Comparative Study of Oxygen Reduction Reaction on Bi- and La-Doped $SrFeO_{3-\delta}$ Perovskite Cathodes. *Journal of The Electrochemical Society* **2011,** 158, (2), B132-B138.

95. Lee, K.; Manthiram, A., Comparison of $Ln_{0.6}Sr_{0.4}CoO_{3-\delta}$ (Ln= La, Pr, Nd, Sm, and Gd) as Cathode Materials for Intermediate Temperature Solid Oxide Fuel Cells. *Journal of the Electrochemical Society* **2006,** 153, (4), A794-A798.

96. Xia, C.; Rauch, W.; Chen, F.; Liu, M., $Sm_{0.5}Sr_{0.5}CoO_3$ Cathodes for Low-Temperature SOFCs. *Solid State Ionics* **2002,** 149, (1–2), 11-19.

97. Srdić, V. V.; Omorjan, R. P.; Seydel, J., Electrochemical Performances of $(La,Sr)CoO_3$ Cathode for Zirconia-Based Solid Oxide Fuel Cells. *Materials Science and Engineering: B* **2005,** 116, (2), 119-124.

98. Chen, D.; Yang, G.; Ciucci, F.; Tade, M. O.; Shao, Z., 3D Core-Shell Architecture from Infiltration and Beneficial Reactive Sintering as Highly Efficient and Thermally Stable Oxygen Reduction Electrode. *Journal of Materials Chemistry A* **2014,** 2, (5), 1284-1293.

99. Wang, F.; Chen, D.; Shao, Z., Composition and Microstructure Optimization and Operation Stability of Barium Deficient $Ba_{1-x}Co_{0.7}Fe_{0.2}Nb_{0.1}O_{3-\delta}$ Perovskite Oxide Electrodes. *Electrochimica Acta* **2013,** 103, 23-31.

100. Orui, H.; Watanabe, K.; Chiba, R.; Arakawa, M., Application of $LaNi(Fe)O_3$ as SOFC Cathode. *Journal of The Electrochemical Society* **2004,** 151, (9), A1412-A1417.

101. Zhen, Y. D.; Tok, A. I. Y.; Jiang, S. P.; Boey, F. Y. C., $La(Ni,Fe)O_3$ as a Cathode Material with High Tolerance to Chromium Poisoning for Solid Oxide Fuel Cells. *Journal of Power Sources* **2007,** 170, (1), 61-66.

102. Liu, H.; Zhu, X.; Cong, Y.; Zhang, T.; Yang, W., Remarkable Dependence of Electrochemical Performance of $SrCo_{0.8}Fe_{0.2}O_{3-\delta}$ on A-Site Nonstoichiometry. *Physical Chemistry Chemical Physics* **2012,** 14, (20), 7234-7239.

103. Qian, B.; Chen, Y.; Tade, M. O.; Shao, Z., $BaCo_{0.6}Fe_{0.3}Sn_{0.1}O_{3-\Delta}$ Perovskite as a New Superior Oxygen Reduction Electrode for Intermediate-to-Low Temperature Solid Oxide Fuel Cells. *Journal of Materials Chemistry A* **2014,** 2, (36), 15078-15086.

104. Shen, J.; Chen, Y.; Yang, G.; Zhou, W.; Tadé, M. O.; Shao, Z., Impregnated $LaCo_{0.3}Fe_{0.67}Pd_{0.03}O_{3-\delta}$ as a Promising Electrocatalyst for “Symmetrical” Intermediate-Temperature Solid Oxide Fuel Cells. *Journal of Power Sources* **2016,** 306, 92-99.

105. Druce, J.; Tellez, H.; Burriel, M.; Sharp, M. D.; Fawcett, L. J.; Cook, S. N.; McPhail, D. S.; Ishihara, T.; Brongersma, H. H.; Kilner, J. A., Surface Termination and Subsurface Restructuring of Perovskite-based Solid Oxide Electrode Materials. *Energy & Environmental Science* **2014,** 7, (11), 3593-3599.

106. Deng, Z. Q.; Smit, J. P.; Niu, H. J.; Evans, G.; Li, M. R.; Xu, Z. L.; Claridge, J. B.; Rosseinsky, M. J., B Cation Ordered Double Perovskite $Ba_2CoMo_{0.5}Nb_{0.5}O_{6-\delta}$ As a Potential SOFC Cathode. *Chemistry of Materials* **2009,** 21, (21), 5154-5162.

107. Anderson, M. T.; Greenwood, K. B.; Taylor, G. A.; Poeppelmeier, K. R., B-cation Arrangements in Double Perovskites. *Progress in Solid State Chemistry* **1993,** 22, (3), 197-233.

108. Tarancon, A.; Skinner, S. J.; Chater, R. J.; Hernandez-Ramirez, F.; Kilner, J. A., Layered Perovskites as Promising Cathodes for Intermediate Temperature Solid Oxide Fuel Cells. *Journal of Materials Chemistry* **2007,** 17, (30), 3175-3181.

109. Choi, S.; Yoo, S.; Kim, J.; Park, S.; Jun, A.; Sengodan, S.; Kim, J.; Shin, J.; Jeong, H. Y.; Choi, Y., Highly Efficient and Robust Cathode Materials for Low-Temperature Solid Oxide Fuel Cells: $PrBa_{0.5}Sr_{0.5}Co_{2-x}Fe_xO_{5+\delta}$. *Scientific reports* **2013,** 3.

110. Kim, G.; Wang, S.; Jacobson, A. J.; Reimus, L.; Brodersen, P.; Mims, C. A., Rapid Oxygen Ion Diffusion and Surface Exchange Kinetics in $PrBaCo_2O_{5+x}$ with A Perovskite Related Structure and Ordered A Cations. *Journal of Materials Chemistry* **2007,** 17, (24), 2500-2505.

111. Pelosato, R.; Cordaro, G.; Stucchi, D.; Cristiani, C.; Dotelli, G., Cobalt based Layered Perovskites as Cathode Material for Intermediate Temperature Solid Oxide Fuel Cells: A Brief Review. *Journal of Power Sources* **2015,** 298, 46-67.

112. Taskin, A. A.; Lavrov, A. N.; Ando, Y., Achieving Fast Oxygen Diffusion in Perovskites by Cation Ordering. *Applied Physics Letters* **2005,** 86, (9), 091910.

113. Sun, C. W.; Hui, R.; Roller, J., Cathode Materials for Solid Oxide Fuel Cells: A Review. *Journal of Solid State Electrochemistry* **2010,** 14, (7), 1125-1144.

114. Minh, N. Q.; Takahashi, T., *Science and Technology of Ceramic Fuel Cells*. Elsevier: 1995.

115. Ralph, J. M.; Schoeler, A. C.; Krumpelt, M., Materials for Lower Temperature Solid Oxide Fuel Cells. *Journal of Materials Science* 36, (5), 1161-1172.

116. Gu, H.; Zheng, Y.; Ran, R.; Shao, Z.; Jin, W.; Xu, N.; Ahn, J., Synthesis and Assessment of $La_{0.8}Sr_{0.2}Sc_yMn_{1-y}O_{3-\delta}$ as Cathodes for Solid-Oxide Fuel Cells on Scandium-stabilized Zirconia Electrolyte. *Journal of Power Sources* **2008,** 183, (2), 471-478.

117. Yue, X.; Yan, A.; Zhang, M.; Liu, L.; Dong, Y.; Cheng, M., Investigation on Scandium-doped Manganate $La_{0.8}Sr_{0.2}Mn_{1-x}Sc_xO_{3-\delta}$ Cathode for Intermediate Temperaturesolid Oxide Fuel Cells. *Journal of Power Sources* **2008,** 185, (2), 691-697.

118. Tsipis, E.; Kharton, V., Electrode Materials and Reaction Mechanisms in Solid Oxide Fuel Cells: A Brief Review. *Journal of Solid State Electrochemistry* **2008,** 12, (11), 1367-1391.

119. Yokokawa, H.; Sakai, N.; Kawada, T.; Dokiya, M., Thermodynamic Analysis of Reaction Profiles Between $LaMO_3$ (M = Ni , Co , Mn) and ZrO_2. *Journal of The Electrochemical Society* **1991,** 138, (9), 2719-2727.

120. Stochniol, G.; Syskakis, E.; Naoumidis, A., Chemical Compatibility between Strontium-Doped Lanthanum Manganite and Yttria-Stabilized Zirconia. *Journal of the American Ceramic Society* **1995,** 78, (4), 929-932.

121. Kostogloudis, G. C.; Ftikos, C., Chemical Compatibility of $RE_{1-x}Sr_xMnO_{3\pm\delta}$ (RE = La, Pr, Nd, Gd, $0 \leqslant x \leqslant 0.5$) with Yttria stabilized Zirconia Solid Electrolyte. *Journal of the European Ceramic Society* **1998,** 18, (12), 1707-1710.

122. Sakaki, Y.; Takeda, Y.; Kato, A.; Imanishi, N.; Yamamoto, O.; Hattori, M.; Iio, M.; Esaki, Y., $Ln_{1-x}Sr_xMnO_3$ (Ln=Pr, Nd, Sm and Gd) as the Cathode Material for Solid Oxide Fuel Cells. *Solid State Ionics* **1999,** 118, (3–4), 187-194.

123. Holc, J.; Kuščer, D.; Hrovat, M.; Bernik, S.; Kolar, D., Electrical and Microstructural Characterisation of $(La_{0.8}Sr_{0.2})(Fe_{1-x}Al_x)O_3$ and $(La_{0.8}Sr_{0.2})(Mn_{1-x}Al_x)O_3$ as Possible SOFC Cathode Materials. *Solid State Ionics* **1997,** 95, (3–4), 259-268.

124. Simner, S. P.; Bonnett, J. F.; Canfield, N. L.; Meinhardt, K. D.; Shelton, J. P.; Sprenkle, V. L.; Stevenson, J. W., Development of Lanthanum Ferrite SOFC Cathodes. *Journal of Power Sources* **2003,** 113, (1), 1-10.

125. Niu, Y.; Sunarso, J.; Zhou, W.; Liang, F.; Ge, L.; Zhu, Z.; Shao, Z., Evaluation and Optimization of $Bi_{1-x}Sr_xFeO_{3-\delta}$ Perovskites as Cathodes of Solid Oxide Fuel Cells. *International Journal of Hydrogen Energy* **2011,** 36, (4), 3179-3186.

126. Niu, Y.; Zhou, W.; Sunarso, J.; Ge, L.; Zhu, Z.; Shao, Z., High Performance Cobalt-free Perovskite Cathode for Intermediate Temperature Solid Oxide Fuel Cells. *Journal of Materials Chemistry* **2010,** 20, (43), 9619-9622.

127. Petitjean, M.; Caboche, G.; Siebert, E.; Dessemond, L.; Dufour, L. C., $(La_{0.8}Sr_{0.2})(Mn_{1-y}Fe_y)O_{3\pm\delta}$ Oxides for IT-SOFC Cathode Materials: Electrical and Ionic Transport Properties. *Journal of the European Ceramic Society* **2005,** 25, (12), 2651-2654.

128. Simner, S. P.; Bonnett, J. F.; Canfield, N. L.; Meinhardt, K. D.; Sprenkle, V. L.; Stevenson, J. W., Optimized Lanthanum Ferrite-Based Cathodes for Anode-Supported SOFCs. *Electrochemical and Solid-State Letters* **2002,** 5, (7), A173-A175.

129. Ullmann, H.; Trofimenko, N.; Tietz, F.; Stöver, D.; Ahmad-Khanlou, A., Correlation between Thermal Expansion and Oxide Ion Transport in Mixed Conducting Perovskite-type Oxides for SOFC Cathodes. *Solid State Ionics* **2000,** 138, (1–2), 79-90.

130. Chiba, R.; Yoshimura, F.; Sakurai, Y., Properties of $La_{1-y}Sr_yNi_{1-x}Fe_xO_3$ as a Cathode Material for a Low-temperature Operating SOFC. *Solid State Ionics* **2002,** 152–153, (0), 575-582.

131. Wærnhus, I.; Sakai, N.; Yokokawa, H.; Grande, T.; Einarsrud, M.-A.; Wiik, K., Mass Transport in $La_{1-x}Sr_xFeO_3$(x=0 and 0.1) measured by SIMS. *Solid State Ionics* **2004,** 175, (1–4), 69-71.

132. Ding, X.; Gao, X.; Zhu, W.; Wang, J.; Jiang, J., Electrode Redox Properties of $Ba_{1-x}La_xFeO_{3-\delta}$ as Cobalt Free Cathode Materials for Intermediate-Temperature SOFCs. *International Journal of Hydrogen Energy* **2014,** 39, (23), 12092-12100.

133. Yu, T.; Mao, X.; Ma, G., Performance of Cobalt-free Perovskite $La_{0.6}Sr_{0.4}Fe_{1-x}Nb_xO_{3-\delta}$ Cathode Materials for Proton-conducting IT-SOFC. *Journal of Alloys and Compounds* **2014,** 608, 30-34.

134. Coffey, G.; Hardy, J.; Marina, O.; Pederson, L.; Rieke, P.; Thomsen, E., Copper doped Lanthanum Strontium Ferrite for Reduced Temperature Solid Oxide Fuel Cells. *Solid State Ionics* **2004,** 175, (1–4), 73-78.

135. Alifanti, M.; Kirchnerova, J.; Delmon, B.; Klvana, D., Methane and Propane Combustion over Lanthanum Transition-metal Perovskites: Role of Oxygen mobility. *Applied Catalysis A: General* **2004,** 262, (2), 167-176.

136. Ling, Y.; Zhao, L.; Lin, B.; Dong, Y.; Zhang, X.; Meng, G.; Liu, X., Investigation of Cobalt-free Cathode Mterial $Sm_{0.5}Sr_{0.5}Fe_{0.8}Cu_{0.2}O_{3-\delta}$ for Itermediate Temperature Solid oxide Fuel Cell. *International Journal of Hydrogen Energy* **2010,** 35, (13), 6905-6910.

137. Lu, J.; Yin, Y.-M.; Ma, Z.-F., Preparation and Characterization of New Cobalt-free Cathode $Pr_{0.5}Sr_{0.5}Fe_{0.8}Cu_{0.2}O_{3-\delta}$ for IT-SOFC. *International Journal of Hydrogen Energy* **2013,** 38, (25), 10527-10533.

138. Yin, J.-W.; Yin, Y.-M.; Lu, J.; Zhang, C.; Minh, N. Q.; Ma, Z.-F., Structure and Properties of Novel Cobalt-Free Oxides $Nd_xSr_{1-x}Fe_{0.8}Cu_{0.2}O_{3-\delta}$ ($0.3 \leqslant x \leqslant 0.7$) as Cathodes of Intermediate Temperature Solid Oxide Fuel Cells. *The Journal of Physical Chemistry C* **2014,** 118, (25), 13357-13368.

139. Li, M.; Wang, Y.; Wang, Y.; Chen, F.; Xia, C., Bismuth Doped Lanthanum Ferrite Perovskites as Novel Cathodes for Intermediate-Temperature Solid Oxide Fuel Cells. *ACS Applied Materials & Interfaces* **2014,** 6, (14), 11286-11294.

140. Takeda, Y.; Kanno, K.; Takada, T.; Yamamoto, O.; Takano, M.; Nakayama, N.; Bando, Y., Phase Relation in the Oxygen Nonstoichiometric System, $SrFeO_x$ ($2.5 \leqslant x \leqslant 3.0$). *Journal of Solid State Chemistry* **1986,** 63, (2), 237-249.

141. Mizusaki, J.; Okayasu, M.; Yamauchi, S.; Fueki, K., Nonstoichiometry and Phase Relationship of the $SrFeO_{2.5}$-$SrFeO_3$ system at High Temperature. *Journal of Solid State Chemistry* **1992,** 99, (1), 166-172.

142. Li, J.; Duan, Y.; He, H.; Song, D., Crystal Structure, Electronic Structure, and Magnetic Properties of Bismuth-Strontium Ferrites. *Journal of Alloys and Compounds* **2001,** 315, (1–2), 259-264.

143. Zhao, L.; He, B.; Zhang, X.; Peng, R.; Meng, G.; Liu, X., Electrochemical Performance of Novel Cobalt-free Oxide $Ba_{0.5}Sr_{0.5}Fe_{0.8}Cu_{0.2}O_{3-\delta}$ for Solid Oxide Fuel Cell Cathode. *Journal of Power Sources* **2010,** 195, (7), 1859-1861.

144. Wei, B.; Lü, Z.; Huang, X.; Liu, M.; Li, N.; Su, W., Synthesis, Electrical and Electrochemical Properties of $Ba_{0.5}Sr_{0.5}Zn_{0.2}Fe_{0.8}O_{3-\delta}$ Perovskite Oxide for IT-SOFC Cathode. *Journal of Power Sources* **2008,** 176, (1), 1-8.

145. Chen, G.; Wang, Y.; Sunarso, J.; Liang, F.; Wang, H., A New Scandium and Niobium Co-doped Cobalt-free Perovskite Cathode for Intermediate-Temperature Solid Oxide Fuel Cells. *Energy* **2016,** 95, 137-143.

146. Yi, J.; Schroeder, M.; Martin, M., CO2-Tolerant and Cobalt-Free $SrFe_{0.8}Nb_{0.2}O_{3-\delta}$ Perovskite Membrane for Oxygen Separation. *Chemistry of Materials* **2013,** 25, (6), 815-817.

147. Yu, X.; Long, W.; Jin, F.; He, T., Cobalt-free Perovskite Cathode Materials $SrFe_{1-x}Ti_xO_{3-\delta}$ and Performance Optimization for Intermediate-Temperature Solid Oxide Fuel Cells. *Electrochimica Acta* **2014,** 123, 426-434.

148. Zhou, Q.; Zhang, L.; He, T., Cobalt-free Cathode Material $SrFe_{0.9}Nb_{0.1}O_{3-\delta}$ for Intermediate-Temperature Solid Oxide Fuel Cells. *Electrochemistry Communications* **2010,** 12, (2), 285-287.

149. Chiba, R.; Yoshimura, F.; Sakurai, Y., An Investigation of $LaNi_{1-x}Fe_xO_3$ as a Cathode Material for Solid Oxide Fuel Cells. *Solid State Ionics* **1999,** 124, (3–4), 281-288.

150. Kharton, V.; Viskup, A.; Naumovich, E.; Tikhonovich, V., Oxygen Permeability of $LaFe_{1-x}Ni_xO_{3-\delta}$ Solid Solutions. *Materials research bulletin* **1999,** 34, (8), 1311-1317.

151. Stodolny, M. K.; Boukamp, B. A.; Blank, D. H. A.; van Berkel, F. P. F., Impact of Cr-poisoning on the Conductivity of $LaNi_{0.6}Fe_{0.4}O_3$. *Journal of Power Sources* **2011,** 196, (22), 9290-9298.

152. Wei, B.; Lü, Z.; Li, S.; Liu, Y.; Liu, K.; Su, W., Thermal and Electrical Properties of New Cathode Material $Ba_{0.5}Sr_{0.5}Co_{0.8}Fe_{0.2}O_{3-\delta}$ for Solid Oxide Fuel Cells. *Electrochemical and Solid-State Letters* **2005,** 8, (8), A428-A431.

153. McIntosh, S.; Vente, J. F.; Haije, W. G.; Blank, D. H.; Bouwmeester, H. J., Oxygen Stoichiometry and Chemical Expansion of $Ba_{0.5}Sr_{0.5}Co_{0.8}Fe_{0.2}O_{3-\delta}$ Measured by in Situ Neutron Diffraction. *Chemistry of Materials* **2006,** 18, (8), 2187-2193.

154. Teraoka, Y.; Zhang, H.-M.; Furukawa, S.; Yamazoe, N., Oxygen Permeation through Perovskite-Type Oxides. *Chemistry Letters* **1985,** 14, (11), 1743-1746.

155. Kruidhof, H.; Bouwmeester, H. J. M.; v. Doorn, R. H. E.; Burggraaf, A. J., Influence of Order-Disorder Transitions on Oxygen Permeability through Selected Nonstoichiometric Perovskite-Type Oxides. *Solid State Ionics* **1993,** 63–65, 816-822.

156. Konysheva, E. Y.; Xu, X.; Irvine, J. T. S., On the Existence of A-Site Deficiency in Perovskites and Its Relation to the Electrochemical Performance. *Advanced Materials* **2012,** 24, (4), 528-532.

157. Zhu, Y.; Chen, Z.-G.; Zhou, W.; Jiang, S.; Zou, J.; Shao, Z., An A-Site-Deficient Perovskite Offers High Activity and Stability for Low-Temperature Solid-Oxide Fuel Cells. *ChemSusChem* **2013,** 6, (12), 2249-2254.

158. Zhu, Y.; Lin, Y.; Shen, X.; Sunarso, J.; Zhou, W.; Jiang, S.; Su, D.; Chen, F.; Shao, Z., Influence of Crystal Structure on the Electrochemical Performance of A-Site-Deficient $Sr_{1-s}Nb_{0.1}Co_{0.9}O_{3-\delta}$ Perovskite Cathodes. *RSC Advances* **2014,** 4, (77), 40865-40872.

159. Hansen, K. K., A-Site Deficient $(Pr_{0.6}Sr_{0.4})_{1-s}Fe_{0.8}Co_{0.2}O_{3-\delta}$ Perovskites as Solid Oxide Fuel Cell Cathodes. *Journal of The Electrochemical Society* **2009,** 156, (10), B1257-B1260.

160. Hansen, K. K.; Hansen, K. V., A-Site Deficient $(La_{0.6}Sr_{0.4})_{1-s}Fe_{0.8}Co_{0.2}O_{3-\delta}$ Perovskites as SOFC Cathodes. *Solid State Ionics* **2007,** 178, (23–24), 1379-1384.

161. Zhou, W.; Ran, R.; Shao, Z.; Jin, W.; Xu, N., Evaluation of A-Site Cation-Deficient $(Ba_{0.5}Sr_{0.5})_{1-x}Co_{0.8}Fe_{0.2}O_{3-\delta}$ (x>0) Perovskite as a Solid-Oxide Fuel Cell Cathode. *Journal of Power Sources* **2008,** 182, (1), 24-31.

162. Tu, H. Y.; Takeda, Y.; Imanishi, N.; Yamamoto, O., $Ln_{0.4}Sr_{0.6}Co_{0.8}Fe_{0.2}o_{3-\delta}$ (Ln=La, Pr, Nd, Sm, Gd) for the Electrode in Solid Oxide Fuel Cells. *Solid State Ionics* **1999,** 117, (3–4), 277-281.

163. Zhang, G.; Dong, X.; Liu, Z.; Zhou, W.; Shao, Z.; Jin, W., Cobalt-Site Cerium Doped $Sm_xSr_{1-x}CoO_{3-\delta}$ Oxides as Potential Cathode Materials for Solid-Oxide Fuel Cells. *Journal of Power Sources* **2010,** 195, (11), 3386-3393.

164. Kim, J. H.; Baek, S.-W.; Lee, C.; Park, K.; Bae, J., Performance Analysis of Cobalt-Based Cathode Materials for Solid Oxide Fuel Cell. *Solid State Ionics* **2008,** 179, (27–32), 1490-1496.

165. Tai, L. W.; Nasrallah, M. M.; Anderson, H. U.; Sparlin, D. M.; Sehlin, S. R., Structure and Electrical Properties of $La_{1-x}Sr_xCo_{1-y}Fe_yO_3$. Part 2. The System $La_{1-x}Sr_xCo_{0.2}Fe_{0.8}O_3$. *Solid State Ionics* **1995,** 76, (3–4), 273-283.

166. Shao, Z.; Haile, S. M., A High-Performance Cathode for the Next Generation of Solid-Oxide Fuel Cells. *Nature* **2004,** 431, (7005), 170-173.

167. Wei, B.; Lü, Z.; Huang, X.; Miao, J.; Sha, X.; Xin, X.; Su, W., Crystal Structure, Thermal Expansion and Electrical Conductivity of Perovskite Oxides $Ba_xSr_{1-x}Co_{0.8}Fe_{0.2}O_{3-\delta}$ ($0.3 \leqslant x \leqslant 0.7$). *Journal of the European Ceramic Society* **2006,** 26, (13), 2827-2832.

168. Su, C.; Xu, X.; Chen, Y.; Liu, Y.; Tadé, M. O.; Shao, Z., A Top-Down Strategy for the Synthesis of Mesoporous $Ba_{0.5}Sr_{0.5}Co_{0.8}Fe_{0.2}O_{3-\delta}$ as a Cathode Precursor for Buffer Layer-Free Deposition on Stabilized Zirconia Electrolyte with a Superior Electrochemical Performance. *Journal of Power Sources* **2015,** 274, 1024-1033.

169. Zhou, W.; Ran, R.; Shao, Z., Progress in Understanding and Development of $Ba_{0.5}Sr_{0.5}Co_{0.8}Fe_{0.2}O_{3-\delta}$ -Based Cathodes for Intermediate-Temperature Solid-Oxide Fuel Cells: A Review. *Journal of Power Sources* **2009,** 192, (2), 231-246.

170. Bucher, E.; Egger, A.; Ried, P.; Sitte, W.; Holtappels, P., Oxygen Nonstoichiometry and Exchange Kinetics of $Ba_{0.5}Sr_{0.5}Co_{0.8}Fe_{0.2}O_{3-\delta}$. *Solid State Ionics* **2008,** 179, (21), 1032-1035.

171. Chen, D.; Shao, Z., Surface Exchange and Bulk Diffusion Properties of $Ba_{0.5}Sr_{0.5}Co_{0.8}Fe_{0.2}O_{3-\delta}$ Mixed Conductor. *International Journal of Hydrogen Energy* **2011,** 36, (11), 6948-6956.

172. Shao, Z.; Xiong, G.; Tong, J.; Dong, H.; Yang, W., Ba Effect in Doped $Sr(Co_{0.8}Fe_{0.2})O_{3-\delta}$ on the Phase Structure and Oxygen Permeation Properties of the Dense Ceramic Membranes. *Separation and Purification Technology* **2001,** 25, (1–3), 419-429.

173. Patra, H.; Rout, S. K.; Pratihar, S. K.; Bhattacharya, S., Thermal, Electrical and Electrochemical Characteristics of $Ba_{1-x}Sr_xCo_{0.8}Fe_{0.2}O_{3-\Delta}$ Cathode Material for Intermediate Temperature Solid Oxide Fuel Cells. *International Journal of Hydrogen Energy* **2011,** 36, (18), 11904-11913.

174. Švarcová, S.; Wiik, K.; Tolchard, J.; Bouwmeester, H. J. M.; Grande, T., Structural Instability of Cubic Perovskite $Ba_xSr_{1-x}Co_{1-y}Fe_yO_{3-\delta}$. *Solid State Ionics* **2008,** 178, (35–36), 1787-1791.

175. Mueller, D. N.; De Souza, R. A.; Weirich, T. E.; Roehrens, D.; Mayer, J.; Martin, M., A Kinetic Study of the Decomposition of the Cubic Perovskite-Type Oxide $Ba_xSr_{1-x}Co_{0.8}Fe_{0.2}O_{3-\delta}$ (BSCF) (x= 0.1 and 0.5). *Physical Chemistry Chemical Physics* **2010,** 12, (35), 10320-10328.

176. Efimov, K.; Xu, Q.; Feldhoff, A., Transmission Electron Microscopy Study of $Ba_{0.5}Sr_{0.5}Co_{0.8}Fe_{0.2}O_{3-\delta}$ Perovskite Decomposition at Intermediate Temperatures. *Chemistry of Materials* **2010,** 22, (21), 5866-5875.

177. Hjalmarsson, P.; Søgaard, M.; Mogensen, M., Electrochemical Behaviour of $(La_{1-x}Sr_x)_sCo_{1-y}Ni_yO_{3-\delta}$ as Porous SOFC Cathodes. *Solid State Ionics* **2009,** 180, (26–27), 1395-1405.

178. Fu, Y.-P.; Subardi, A.; Hsieh, M.-Y.; Chang, W.-K., Electrochemical Properties of $La_{0.5}Sr_{0.5}Co_{0.8}M_{0.2}O_{3-\delta}$ (M=Mn, Fe, Ni, Cu) Perovskite Cathodes for IT-SOFCs. *Journal of the American Ceramic Society* **2016**, n/a-n/a.

179. Liu, Z.; Cheng, L.-z.; Han, M.-F., A-Site Deficient $Ba_{1-x}Co_{0.7}Fe_{0.2}Ni_{0.1}O_{3-\delta}$ Cathode for Intermediate Temperature SOFC. *Journal of Power Sources* **2011,** 196, (2), 868-871.

180. Chen, W.; Wen, T.; Nie, H.; Zheng, R., Study of $Ln_{0.6}Sr_{0.4}Co_{0.8}Mn_{0.2}O_{3-\delta}$ (Ln=La, Gd, Sm or Nd) as the Cathode Materials for Intermediate Temperature SOFC. *Materials Research Bulletin* **2003,** 38, (8), 1319-1328.

181. Petric, A.; Huang, P.; Tietz, F., Evaluation of La–Sr–Co–Fe–O Perovskites for Solid Oxide Fuel Cells and Gas Separation Membranes. *Solid State Ionics* **2000,** 135, (1–4), 719-725.

182. Nagai, T.; Ito, W.; Sakon, T., Relationship between Cation Substitution and Stability of Perovskite Structure in $SrCoO_{3-\delta}$-Based Mixed Conductors. *Solid State Ionics* **2007,** 177, (39–40), 3433-3444.

183. Grunbaum, N.; Mogni, L.; Prado, F.; Caneiro, A., Phase Equilibrium and Electrical Conductivity of $SrCo_{0.8}Fe_{0.2}O_{3-\delta}$. *Journal of Solid State Chemistry* **2004,** 177, (7), 2350-2357.

184. Porras-Vazquez, J. M.; Slater, P. R., Synthesis of Oxyanion-Doped Barium Strontium Cobalt Ferrites: Stabilization of the Cubic Perovskite and Enhancement in Conductivity. *Journal of Power Sources* **2012,** 209, (0), 180-183.

185. Wang, Z.; Zhao, H.; Xu, N.; Shen, Y.; Ding, W.; Lu, X.; Li, F., Electrical Conductivity and Structural Stability of $SrCo_{1-x}Fe_xO_{3-\delta}$. *Journal of Physics and Chemistry of Solids* **2011,** 72, (1), 50-55.

186. Chen, Y.; Qian, B.; Shao, Z., Tin and Iron Co-Doping Strategy for Developing Active and Stable Oxygen Reduction Catalysts from $SrCoO_{3-\delta}$ for Operating Temperature Below 800 °C. *Journal of Power Sources* **2015,** 294, 339-346.

187. Qiu, L.; Ichikawa, T.; Hirano, A.; Imanishi, N.; Takeda, Y., $Ln_{1-x}Sr_xCo_{1-y}Fe_yO_{3-\delta}$ (Ln=Pr, Nd, Gd; X=0.2, 0.3) for the Electrodes of Solid Oxide Fuel Cells. *Solid State Ionics* **2003,** 158, (1–2), 55-65.

188. Qiu, L.; Lee, T. H.; Liu, L. M.; Yang, Y. L.; Jacobson, A. J., Oxygen Permeation Studies of $SrCo_{0.8}Fe_{0.2}O_{3-\delta}$. *Solid State Ionics* **1995,** 76, (3–4), 321-329.

189. Liu, L.; Lee, T.; Qiu, L.; Yang, Y.; Jacobson, A., A Thermogravimetric Study of the Phase Diagram of Strontium Cobalt Iron Oxide, $SrCo_{0.8}Fe_{0.2}O_{3-\delta}$. *Materials research bulletin* **1996,** 31, (1), 29-35.

190. Harrison, W.; Lee, T.; Yang, Y.; Scarfe, D.; Liu, L.; Jacobson, A., A Neutron Diffraction Study of Two Strontium Cobalt Iron Oxides. *Materials research bulletin* **1995,** 30, (5), 621-630.

191. Tikhonovich, V. N.; Zharkovskaya, O. M.; Naumovich, E. N.; Bashmakov, I. A.; Kharton, V. V.; Vecher, A. A., Oxygen Nonstoichiometry of $Sr(Co,Fe)O_{3-\delta}$-Based Perovskites: I. Coulometric Titration of $SrCo_{0.85}Fe_{0.10}Cr_{0.05}O_{3-\delta}$ by the Two-Electrode Technique. *Solid State Ionics* **2003,** 160, (3–4), 259-270.

192. Yang, L.; Tan, L.; Gu, X.; Jin, W.; Zhang, L.; Xu, N., A New Series of Sr (Co, Fe, Zr) $O_{3-\delta}$ Perovskite-Type Membrane Materials for Oxygen Permeation. *Industrial & Engineering Chemistry Research* **2003,** 42, (11), 2299-2305.

193. Li, M.; Zhou, W.; Xu, X.; Zhu, Z., $SrCo_{0.85}Fe_{0.1}P_{0.05}O_{3-\delta}$ Perovskite as a Cathode for Intermediate-Temperature Solid Oxide Fuel Cells. *Journal of Materials Chemistry A* **2013,** 1, (43), 13632-13639.

194. Chen, Z.; Ran, R.; Zhou, W.; Shao, Z.; Liu, S., Assessment of Ba0. 5Sr0. 5Co1− yFeyO3− δ (y= 0.0–1.0) for prospective application as cathode for IT-SOFCs or oxygen permeating membrane. *Electrochimica Acta* **2007,** 52, (25), 7343-7351.

195. Tai, L. W.; Nasrallah, M. M.; Anderson, H. U.; Sparlin, D. M.; Sehlin, S. R., Structure and Electrical Properties of $La_{1-x}Sr_xCo_{1-y}Fe_yO_3$. Part 1. The System $La_{0.8}Sr_{0.2}Co_{1-y}Fe_yO_3$. *Solid State Ionics* **1995,** 76, (3–4), 259-271.

196. Lv, H.; Wu, Y.-j.; Huang, B.; Zhao, B.-y.; Hu, K.-a., Structure and Electrochemical Properties of $Sm_{0.5}Sr_{0.5}Co_{1-x}Fe_xO_{3-\delta}$ Cathodes for Solid Oxide Fuel Cells. *Solid State Ionics* **2006,** 177, (9–10), 901-906.

197. Chen, Z.; Ran, R.; Zhou, W.; Shao, Z.; Liu, S., Assessment of $Ba_{0.5}Sr_{0.5}Co_{1-y}Fe_yO_{3-\delta}$ (y= 0.0–1.0) for Prospective Application as Cathode for IT-SOFCs or Oxygen Permeating Membrane. *Electrochimica Acta* **2007,** 52, (25), 7343-7351.

198. Zhou, W.; Jin, W. Q.; Zhu, Z. H.; Shao, Z. P., Structural, Electrical and Electrochemical Characterizations of $SrNb_{0.1}Co_{0.9}O_{3-\delta}$ as a Cathode of Solid Oxide Fuel Cells Operating Below 600°C *International Journal of Hydrogen Energy* **2010,** 35, (3), 1356-1366.

199. Zhou, W.; Shao, Z.; Ran, R.; Cai, R., Novel $SrSc_{0.2}Co_{0.8}O_{3-\delta}$ as a Cathode Material for Low Temperature Solid-Oxide Fuel Cell. *Electrochemistry Communications* **2008,** 10, (10), 1647-1651.

200. Gao, Z.; Mao, Z.; Wang, C.; Liu, Z., Novel $SrTi_xCo_{1-x}O_{3-\delta}$ Cathodes for Low-Temperature Solid Oxide Fuel Cells. *International Journal of Hydrogen Energy* **2011,** 36, (12), 7229-7233.

201. Wang, F.; Zhou, Q.; He, T.; Li, G.; Ding, H., Novel $SrCo_{1-y}Nb_yO_{3-\delta}$ Cathodes for Intermediate-Temperature Solid Oxide Fuel Cells. *Journal of Power Sources* **2010,** 195, (12), 3772-3778.

202. Li, M.; Zhou, W.; Zhu, Z., Comparative Studies of $SrCo_{1-X}Ta_xo_{3-\delta}$ (X=0.05–0.4) Oxides as Cathodes for Low-Temperature Solid-Oxide Fuel Cells. *ChemElectroChem* **2015,** 2, (9), 1331-1338.

203. Aguadero, A.; Pérez-Coll, D.; Alonso, J. A.; Skinner, S. J.; Kilner, J., A New Family of Mo-Doped $SrCoO_{3-\delta}$ Perovskites for Application in Reversible Solid State Electrochemical Cells. *Chemistry of Materials* **2012,** 24, (14), 2655-2663.

204. Zhou, Q.; Wei, T.; Shi, Y.; Guo, S.; Li, Y.; Su, J.; Ren, H.; Zhu, Y., Evaluation and Optimization of $SrCo_{0.9}Ta_{0.1}O_{3-\delta}$ Perovskite as Cathode for Solid Oxide Fuel Cells. *Current Applied Physics* **2012,** 12, (4), 1092-1095.

205. Aguadero, A.; Calle, C. d. l.; Alonso, J. A.; Escudero, M. J.; Fernández-Díaz, M. T.; Daza, L., Structural and Electrical Characterization of the Novel $Srco_{0.9}Sb_{0.1}O_{3-\delta}$ Perovskite: Evaluation as a Solid Oxide Fuel Cell Cathode Material. *Chemistry of Materials* **2007,** 19, (26), 6437-6444.

206. Aguadero, A.; Pérez-Coll, D.; de la Calle, C.; Alonso, J. A.; Escudero, M. J.; Daza, L., SrCo1−xSbxO3−δ perovskite oxides as cathode materials in solid oxide fuel cells. *Journal of Power Sources* **2009,** 192, (1), 132-137.

207. Chen, D.; Chen, C.; Gao, Y.; Zhang, Z.; Shao, Z.; Ciucci, F., Evaluation of Pulsed Laser Deposited $SrNb_{0.1}Co_{0.9}O_{3-\delta}$ Thin Films as Promising Cathodes for Intermediate-Temperature Solid Oxide Fuel Cells. *Journal of Power Sources* **2015,** 295, 117-124.

208. Huang, C.; Chen, D.; Lin, Y.; Ran, R.; Shao, Z., Evaluation of $Ba_{0.6}Sr_{0.4}Co_{0.9}Nb_{0.1}O_{3-\delta}$ Mixed Conductor as a Cathode for Intermediate-Temperature Oxygen-Ionic Solid-Oxide Fuel Cells. *Journal of Power Sources* **2010,** 195, (16), 5176-5184.

209. Zhang, Z.; Chen, Y.; Tade, M. O.; Hao, Y.; Liu, S.; Shao, Z., Tin-Doped Perovskite Mixed Conducting Membrane for Efficient Air Separation. *Journal of Materials Chemistry A* **2014,** 2, (25), 9666-9674.

210. Zeng, P.; Ran, R.; Chen, Z.; Zhou, W.; Gu, H.; Shao, Z.; Liu, S., Efficient Stabilization of Cubic Perovskite $SrCoO_{3-\delta}$ by B-Site Low Concentration Scandium Doping Combined with Sol–Gel Synthesis. *Journal of Alloys and Compounds* **2008,** 455, (1–2), 465-470.

211. Hancock, C. A.; Porras-Vazquez, J. M.; Keenan, P. J.; Slater, P. R., Oxyanions in Perovskites: From Superconductors to Solid Oxide Fuel Cells. *Dalton Transactions* **2015,** 44, (23), 10559-10569.

212. Porras-Vazquez, J. M.; Slater, P. R., Synthesis and Characterization of Oxyanion-Doped Cobalt Containing Perovskites. *Fuel Cells* **2012,** 12, (6), 1056-1063.

213. Chen, D.; Chen, C.; Zhang, Z.; Baiyee, Z. M.; Ciucci, F.; Shao, Z., Compositional Engineering of Perovskite Oxides for Highly Efficient Oxygen Reduction Reactions. *ACS Applied Materials & Interfaces* **2015,** 7, (16), 8562-8571.

214. Shen, Y.; Wang, F.; Ma, X.; He, T., $SrCo_{1-y}Ti_yO_{3-\delta}$ as Potential Cathode Materials for Intermediate-Temperature Solid Oxide Fuel Cells. *Journal of Power Sources* **2011,** 196, (18), 7420-7425.

215. Zhou, W.; Sunarso, J.; Zhao, M.; Liang, F.; Klande, T.; Feldhoff, A., A Highly Active Perovskite Electrode for the Oxygen Reduction Reaction Below 600 °C. *Angewandte Chemie International Edition* **2013,** 52, (52), 14036-14040.

216. Sirman, J. D.; Kilner, J. A., Surface Exchange Properties of Ce0.9Gd0.1 O 2 − x Coated with La1 − x Sr x Fe y Co1 − y O 3 − δ. *Journal of the Electrochemical Society* **1996,** 143, (10), L229-L231.

217. Zhu, Y.; Zhou, W.; Ran, R.; Chen, Y.; Shao, Z.; Liu, M., Promotion of Oxygen Reduction by Exsolved Silver Nanoparticles on a Perovskite Scaffold for Low-Temperature Solid Oxide Fuel Cells. *Nano Letters* **2016,** 16, (1), 512-518.

218. Jiang, S. P., A Review of Wet Impregnation—an Alternative Method for the Fbrication of High Performance and Nano-Structured Electrodes of Solid Oxide Fuel Cells. *Materials Science and Engineering: A* **2006,** 418, (1–2), 199-210.

219. Vohs, J. M.; Gorte, R. J., High-Performance SOFC Cathodes Prepared by Infiltration. *Advanced Materials* **2009,** 21, (9), 943-956.

220. Liu, Y.; Zha, S.; Liu, M., Novel Nanostructured Electrodes for Solid Oxide Fuel Cells Fabricated by Combustion Chemical Vapor Deposition (CVD). *Advanced Materials* **2004,** 16, (3), 256-260.

221. Zhou, W.; Ge, L.; Chen, Z.-G.; Liang, F.; Xu, H.-Y.; Motuzas, J.; Julbe, A.; Zhu, Z., Amorphous Iron Oxide Decorated 3D Heterostructured Electrode for Highly Efficient Oxygen Reduction. *Chemistry of Materials* **2011,** 23, (18), 4193-4198.

222. Suzuki, M.; Sasaki, H.; Otoshi, S.; Kajimura, A.; Sugiura, N.; Ippommatsu, M., High Performance Solid Oxide Fuel Cell Cathode Fabricated by Electrochemical Vapor Deposition. *Journal of the Electrochemical Society* **1994,** 141, (7), 1928-1931.

223. Lee, J. G.; Park, J. H.; Shul, Y. G., Tailoring gadolinium-doped ceria-based solid oxide fuel cells to achieve 2 W cm−2 at 550 °C. *Nat Commun* **2014,** 5.

224. Liang, F.; Zhou, W.; Zhu, Z., A Highly Stable and Active Hybrid Cathode for Low-Temperature Solid Oxide Fuel Cells. *ChemElectroChem* **2014,** 1, (10), 1627-1631.

225. Shao, Z.; Yang, W.; Cong, Y.; Dong, H.; Tong, J.; Xiong, G., Investigation of the Permeation Behavior and Stability of a $Ba_{0.5}Sr_{0.5}Co_{0.8}Fe_{0.2}O_{3-\delta}$ Oxygen Membrane. *Journal of Membrane Science* **2000,** 172, (1–2), 177-188.

226. Konysheva, E.; Penkalla, H.; Wessel, E.; Mertens, J.; Seeling, U.; Singheiser, L.; Hilpert, K., Chromium Poisoning of Perovskite Cathodes by the Ods Alloy Cr5Fe1Y2O3 and the High Chromium Ferritic Steel Crofe22APU. *Journal of The Electrochemical Society* **2006,** 153, (4), A765-A773.

227. Chen, X.; Zhang, L.; Jiang, S. P., Chromium Deposition and Poisoning on $(La_{0.6}Sr_{0.4-X}Ba_X)(Co_{0.2}Fe_{0.8})O_3$ $(0 \leqslant X \leqslant 0.4)$ Cathodes of Solid Oxide Fuel Cells. *Journal of The Electrochemical Society* **2008,** 155, (11), B1093-B1101.

228. Kim, Y.-M.; Chen, X.; Jiang, S. P.; Bae, J., Chromium Deposition and Poisoning at $Ba_{0.5}Sr_{0.5}Co_{0.8}Fe_{0.2}O_{3-\delta}$ Cathode of Solid Oxide Fuel Cells. *Electrochemical and Solid-State Letters* **2011,** 14, (4), B41-B45.

229. Kim, Y.-M.; Chen, X.; Jiang, S. P.; Bae, J., Effect of Strontium Content on Chromium Deposition and Poisoning in $Ba_{1-x}Sr_xCo_{0.8}Fe_{0.2}O_{3-\delta}$ $(0.3 \leqslant X \leqslant 0.7)$ Cathodes of Solid Oxide Fuel Cells. *Journal of The Electrochemical Society* **2011,** 159, (2), B185-B194.

230. Chen, K.; Ai, N.; Jiang, S. P., Chemical Compatibility between Boron Oxides and Electrolyte and Cathode Materials of Solid Oxide Fuel Cells. *Fuel Cells* **2013**, n/a-n/a.

231. Zhao, L.; Hyodo, J.; Chen, K.; Ai, N.; Amarasinghe, S.; Ishihara, T.; Ping Jiang, S., Effect of Boron Deposition and Poisoning on the Surface Exchange Properties of Lscf Electrode Materials of Solid Oxide Fuel Cells. *Journal of the Electrochemical Society* **2013,** 160, (6), F682-F686.

232. Chen, K.; Hyodo, J.; O'Donnell, K. M.; Rickard, W.; Ishihara, T.; Jiang, S. P., Effect of Volatile Boron Species on the Electrocatalytic Activity of Cathodes of Solid Oxide Fuel Cells: III. $Ba_{0.5}Sr_{0.5}Co_{0.8}Fe_{0.2}O_{3-\delta}$ Electrodes. *Journal of The Electrochemical Society* **2014,** 161, (12), F1163-F1170.

233. Jiang, S. P.; Chen, X., Chromium Deposition and Poisoning of Cathodes of Solid Oxide Fuel Cells – a Review. *International Journal of Hydrogen Energy* **2014,** 39, (1), 505-531.

234. Jiang, S. P.; Zhen, Y., Mechanism of Cr Deposition and Its Application in the Development of Cr-Tolerant Cathodes of Solid Oxide Fuel Cells. *Solid State Ionics* **2008,** 179, (27–32), 1459-1464.

235. Zhen, Y.; Tok, A. I. Y.; Boey, F. Y. C.; Jiang, S. P., Development of Cr-Tolerant Cathodes of Solid Oxide Fuel Cells. *Electrochemical and Solid-State Letters* **2008,** 11, (3), B42-B46.

236. Zhou, X.-D.; Templeton, J. W.; Zhu, Z.; Chou, Y.-S.; Maupin, G. D.; Lu, Z.; Brow, R. K.; Stevenson, J. W., Electrochemical Performance and Stability of the Cathode for Solid Oxide Fuel Cells: III. Role of Volatile Boron Species on LSM/YSZ and LSCF. *Journal of The Electrochemical Society* **2010,** 157, (7), B1019-B1023.

237. Jiang, S. P., Challenges in the Development of Reversible Solid Oxide Cell Technologies: A Mini Review. *Asia-Pacific Journal of Chemical Engineering* **2016,** 11, (3), 386-391.

238. Yan, A.; Cheng, M.; Dong, Y.; Yang, W.; Maragou, V.; Song, S.; Tsiakaras, P., Investigation of a Ba0. 5Sr0. 5Co0. 8Fe0. 2O3Ād based cathode IT-SOFC: I. The effect of CO2 on the cell performance. *Applied Catalysis B: Environmental* **2006,** 66, 64-71.

239. Yan, A.; Liu, B.; Dong, Y.; Tian, Z.; Wang, D.; Cheng, M., A Temperature Programmed Desorption Investigation on the Interaction of $Ba_{0.5}Sr_{0.5}Co_{0.8}Fe_{0.2}O_{3-\delta}$ Perovskite Oxides with CO_2 in the abence and presence of H_2O and O_2. *Applied Catalysis, B: Environmental* **2008,** 80, (1–2), 24-31.

240. Yan, A.; Maragou, V.; Arico, A.; Cheng, M.; Tsiakaras, P., Investigation of a $Ba_{0. 5}Sr_{0. 5}Co_{0. 8}Fe_{0. 2}O_{3-\delta}$ Based Cathode Sofc. II. The Effect of CO_2 on the Chemical Stability. *Applied catalysis. B, Environmental* **2007,** 76, (3-4), 320-327.

241. Bucher, E.; Egger, A.; Caraman, G. B.; Sitte, W., Stability of the Sofc Cathode Material $(Ba, Sr)(Co, Fe)O_{3-\delta}$ in CO_2-Containing Atmospheres. *Journal of the Electrochemical Society* **2008,** 155, (11), B1218-B1224.

242. Zhou, W.; Liang, F.; Shao, Z.; Zhu, Z., Hierarchical CO_2-Protective Shell for Highly Efficient Oxygen Reduction Reaction. *Scientific Reports* **2012,** 2, 327.

243. Yan, A.; Yang, M.; Hou, Z.; Dong, Y.; Cheng, M., Investigation of $Ba_{1-x}Sr_xCo_{0.8}Fe_{0.2}O_{3-\delta}$ as Cathodes for Low-Temperature Solid Oxide Fuel Cells Both in the absence and presence of CO_2. *Journal of Power Sources* **2008,** 185, (1), 7684.

244. Zhu, Y.; Sunarso, J.; Zhou, W.; Shao, Z., Probing CO_2 Reaction Mechanisms and Effects on the $SrNb_{0.1}Co_{0.9-x}Fe_xO_{3-\delta}$ Cathodes for Solid Oxide Fuel Cells. *applied Catalysis, B: Environmental* **2015,** 172–173, 52-57.

245. Yáng, Z.; Harvey, A. S.; Gauckler, L. J., Influence of CO_2 on $Ba_{0.2}Sr_{0.8}Co_{0.8}Fe_{0.2}O_{3-\delta}$ at Elevated Temperatures. *Scripta Materialia* **2009,** 61, (11), 1083-1086.

246. Yi, J.; Schroeder, M.; Weirich, T.; Mayer, J., Behavior of Ba(Co, Fe, Nb)$O_{3-\delta}$ Perovskite in CO_2-Containing Atmospheres: Degradation Mechanism and Materials Design. *Chemistry of Materials* **2010,** 22, (23), 6246-6253.

247. Chen, Y.; Zhou, W.; Ding, D.; Liu, M.; Ciucci, F.; Tade, M.; Shao, Z., Advances in Cathode Materials for Solid Oxide Fuel Cells: Complex Oxides without Alkaline Earth Metal Elements. *Advanced Energy Materials* **2015,** 5, (18), n/a-n/a.

248. Zhang, Y.; Yang, G.; Chen, G.; Ran, R.; Zhou, W.; Shao, Z., Evaluation of the CO_2 Poisoning Effect on a Highly Active Cathode $SrSc_{0.175}Nb_{0.025}Co_{0.8}O_{3-\delta}$ in the Oxygen Reduction Reaction. *ACS Applied Materials & Interfaces* **2016,** 8, (5), 3003-3011.

249. Chen, W.; Chen, C.-s.; Winnubst, L., Ta-Doped $SrCo_{0.8}Fe_{0.2}O_{3-\delta}$ Membranes: Phase Stability and Oxygen Permeation in CO_2 Atmosphere. *Solid State Ionics* **2011,** 196, (1), 30-33.

250. Yi, J.; Weirich, T. E.; Schroeder, M., CO_2 Corrosion and Recovery of Perovskite-Type $BaCo_{1-x-y}Fe_xNb_yO_{3-\delta}$ Membranes. *Journal of Membrane Science* **2013,** 437, (0), 49-56.

251. Lee, W.; Han, J. W.; Chen, Y.; Cai, Z.; Yildiz, B., Cation Size Mismatch and Charge Interactions Drive Dopant Segregation at the Surfaces of Manganite Perovskites. *Journal of the American Chemical Society* **2013,** 135, (21), 7909-7925.

252. Choi, S.; Park, S.; Shin, J.; Kim, G., The Effect of Calcium Doping on the Improvement of Performance and Durability in a Layered Perovskite Cathode for Intermediate-Temperature Solid Oxide Fuel Cells. *Journal of Materials Chemistry A* **2015,** 3, (11), 6088-6095.

253. Ding, H.; Virkar, A. V.; Liu, M.; Liu, F., Suppression of Sr Surface Segregation in $La_{1-x}Sr_xCo_{1-y}Fe_yO_{3-\delta}$: A First Principles Study. *Physical Chemistry Chemical Physics* **2013,** 15, (2), 489-496.

254. Finsterbusch, M.; Lussier, A.; Schaefer, J. A.; Idzerda, Y. U., Electrochemically Driven Cation Segregation in the Mixed Conductor $La_{0.6}Sr_{0.4}Co_{0.2}Fe_{0.8}O_{3-\delta}$. *Solid State Ionics* **2012,** 212, 77-80.

Chapter 3 Experimental details

3.1 Sample syntheses

The perovskite oxides can be synthesized through solid state reaction route. Generally, the first step is to weigh stoichiometric amounts of precursors (normally metal oxides), and then ball mill these precursors for a certain time in ethanol. For alkaline-earth elements as A-site cations, carbonates are normally used, and $NH_4H_2PO_4$ is used as the source of P dopant. The second step is to pelletize and sinter the well-ground dry precursor mixtures at high temperature, the maximum of which normally does not exceed two thirds of the lowest melting point of the precursors. In most cases, an intermediate grinding using pestle and mortar is required for better dispersion of the precursors. An example of synthesizing $SrCo_{0.8}Ta_{0.2}O_{3-\delta}$ is given as follows:

Stoichiometric mixtures of $SrCoO_3$ (≥ 99.9%, Aldrich), Co_3O_4((≥ 99.9%, ≤ 10μm, Aldrich), and Ta_2O_5 (≥ 99.9%, Aldrich) are ball-milled using ethanol as media for 24 h, followed by drying, pelletizing and sintering at 1200 °C for 10 h in stagnant air. Subsequently, the sintered pellets are ground into powders using pestle and mortar, and the following step is to pelletize the powders for 1200 °C sintering for another 10 h.

3.2 Sample preparation

Sample fabrication for four-probe dc electrical conductivity measurement

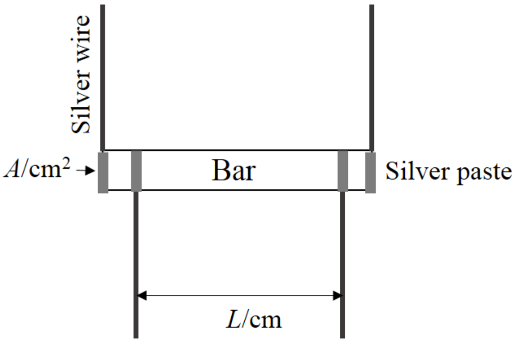

Figure 3-1 A schematic of sample configuration for 4-probe dc electrical conductivity testing method. *L* is the length of effective length the sample, and *A* represents the cross section area of the bar.

The targeted powder sample is first ball milled in ethanol media for 2 h at 400 rpm, and then dried and sieved to obtain the fine powder with similar grain sizes. The following step is to pelletize the powder into a bar, and sinter it to dense at high temperature for 5 h in stagnant air, and polish the bar when it is cooled down. Thereafter, the bar undergoes the density measurement, where the bar volume is tested using the Archimedes method: the bar, hung by a very fine thread, is placed into water, and the weight increase of the water system is actually the weight of water having the same volume to the bar. Finally, the bar should be dried, and be applied with silver paste and wire as the current collectors. A schematic of the fabricated bar is shown in Figure 3-1.

Symmetrical cell preparation

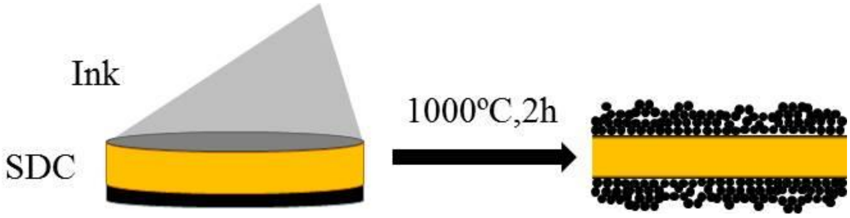

Figure 3-2 A schematic of preparing a symmetrical cell using spray coating.

A symmetrical cell is used for electrochemical impedance spectroscopy (EIS) testing. A symmetrical cell consists of a dense electrolyte disk and two layers of porous targeted cathode sample deposited on both sides of the electrolyte disk. (Figure 3-2) The dense electrolyte disk is prepared by pressing electrolyte powder into a disk, which is then sintered to dense at 1400 °C for 5 h. The porous cathode layer is fabricated by nitrogen-borne spray coating a cathode ink onto both sides of the dense electrolyte disk followed by calcination at high temperature for 2 h. The cathode ink is prepared by suspending the cathode powders in the solvent added with a binder to ensure good suspension. Finally, the silver paste is applied onto the cathode layer, and silver wires are attached onto both silver pastes for current collection.

Anode-support single cell preparation

The anode-support single cell can be fabricated by co-pressing the anode and electrolyte into a pellet and subsequently sintering it at high temperature until electrolyte is dense. Another way is to press the anode material into a pellet and sinter the pellet at relatively low temperature, followed by coating an electrolyte layer onto surface of the anode substrate and then sintering at high temperature. The anode material can be prepared by ball milling commercial NiO, electrolyte material and pore former in a weight ratio of 6:4:1, respectively, in the ethanol media. The cathode is fabricated onto the dense electrolyte following similar procedure as described in symmetrical cell, but the valid area is smaller than the anode substrate. Silver paste is applied onto both cathode and anode layers, and two silver wires are attached to each electrode. The completed button cell is then sealed onto an alumina tube using silver paste, which is then cured and densified at 260 °C for 2 h.

3.3 Powder characterizations

We perform the thermogravimetric analysis (TGA) to study the oxygen content change as a function of temperature by measuring the mass change of the powder sample while gradually increasing the temperature. During the measurement, the moisture should be removed by keeping the sample at >

100 °C for a while before carried out TGA. The loss of mass at >200 °C is mainly due to the loss of oxygen from the lattice, so we can study the oxygen content change of the sample. The kinetics of oxygen surface exchange can be reflected by how fast the sample respond to change of oxygen partial pressure. Therefore, monitoring mass change of the sample after a sudden change of atmosphere (e.g. from air to N_2) in the furnace is effective to characterize how fast oxygen is exchanged at the surface of sample. Moreover, the adsorption behavior and the reactivity of sample with CO_2 can be studied using the TGA method.

The desorption behavior of a sample can be characterized using temperature-programed desorption method. This technique uses a mass spectroscopy to monitor the amount of specific molecules such as O_2 and CO_2 coming out from samples while the sample is being heated up. Helium is usually the sweep gas to carry the desorbed gas from sample to the mass spectroscopy.

Powder x-ray diffraction (XRD) and neutron powder diffraction (NPD) can study the crystalline structures of the samples at room temperature. XRD investigations are conducted in Centre for Microscopy & Microanalysis (CMM), and XRD scans the powder sample from 10° to 90° at rate of 2°/min, using Cu as radiation source, with a voltage of 40 kV, current of 40 mA and step size of 0.1°. Dr. Vanessa K. Peterson at ANSTO helped us with performing the NPD analysis and refinement. High resolution NPD data were collected using ECHIDNA[1] at the ANSTO with a neutron wavelength of 1.6219(2) Å, determined using the $La^{11}B_6$ NIST standard reference material 660b. NPD data were collected from samples in a 6 mm vanadium can for 6 h over the angular range (2θ) 4 to 164°. GSAS-II[2] was employed to perform Rietveld analysis of the NPD data using a $Pm\bar{3}m$ cubic perovskite starting structure.[3] High-resolution electron transmission microscopy (HR-TEM, Tecnai F20) in conjunction with selected area electron diffraction was also used for phase identification.

We also studied the surface chemistry and compositions of the samples. Dr. Barry Wood in CMM helped us analyze the binding energies of dopants at the surface of the doped $SrCoO_{3-\delta}$ samples using high resolution scanning of x-ray photoelectron spectroscopy (XPS). The binding energies of the dopants can reflect the oxidation states of the dopants. Energy-dispersive X-ray Spectroscopy (EDS) of SEM and TEM were also performed to identify the compositions of the samples.

3.4 Electrochemical characterizations

Electrical conductivity test

We performed the four-probe dc conductivity technique to measure the electrical conductivity of samples using a PGSTAT302 Autolab workstation. During the test, the bar samples as prepared following the procedures described in Section 3.2 were connected with the four electrodes of workstation. The workstation scanned the sample from ΔV V to 0 V at a rate of 0.01V/s, and measured the current I going through the sample. Therefore, the conductivity σ can be calculated using the following equation:

$$\sigma = \frac{I}{V} \times \frac{L}{A} \tag{3.1}$$

Where L and A are the dimensions of the bar sample as indicated in Figure 3-1.

Surface exchange coefficient and diffusivity test

We measured the surface exchange coefficient and bulk diffusivity of samples using electrical conductivity relaxation (ECR) method. The ECR is conducted by recording the changes of the electrical conductivity with time after a step change in the ambient atmosphere with O_2 from 0.21 to 0.0998 atm. The change of the electrical conductivities against time were fitted using ECRTOOL[4] to obtain these two parameters.

Oxygen permeability test

Oxygen permeability of a membrane can indicate how fast the oxygen ion conducts in the sample. Following similar steps for dense bar preparation, dense membranes of samples can be fabricated. The membrane is thereby sealed onto one end of the alumina tube using silver paste as the sealant, which is subsequently cured at 260 °C for 1 h. The following step is to heat the membrane up to high temperature, while helium being applied as sweep gas into the alumina tube and flowing air outside the alumina tube. The oxygen will permeate from the side exposed to air to the side swept by helium, and the exit helium gas mixture is analysed by a gas chromatograph. The recorded oxygen permeability can be converted into overall resistance to oxygen permeation using the following equation:

$$R_{overall} = \frac{RT}{16F^2} \frac{1}{SJ_{O_2}} \left[\ln\left(\frac{P'_{O_2}}{P''_{O_2}} \right) \right] \tag{3.2}$$

Where R stands for real gas constant, F for Faraday constant, S for valid permeable area of the membrane, J_{O_2} for oxygen permeation flux, P'_{O_2} for partial pressure near the side of membrane exposed to air and P''_{O_2} for the oxygen partial pressure at the other side. By assuming that bulk ionic conduction dominates the overall oxygen membrane permeation, we can estimate the ionic conductivity of the sample by:

$$\sigma_{ionic} = \frac{1}{R_{ionic}} \times \frac{S}{L} \approx \frac{1}{R_{overall}} \times \frac{S}{L} \tag{3.3}$$

Where L represents the thickness of the membrane.

Cathode polarisation resistance measurement

We measured cathode polarisation resistance by using electrochemical impedance spectroscopy (EIS) method. The targeted cathodes are evaluated in a configuration of symmetrical cell under open circuit condition. A Nyquist plot is obtained during EIS test, and the intercept difference of the arc with the real axis is the combined polarisation resistance R_c of cathodes on both sides of electrolyte disk. The ASR is calculated by:

$$ASR = R_c \times \frac{A}{2} \tag{3.4}$$

The ORR mechanism was studied by fitting the EIS impedance spectra at different pO_2 to the R_e (R_1CPE_1) (R_2CPE_2) equivalent circuit model by using the LEVM software. R_e represents the ohmic resistance of the electrolyte; (R_1CPE_1) and (R_2CPE_2) stand for the two ORR processes at high frequency and low frequency respectively. The physical meaning of the ORR processes are determined by a m parameter given as follows^5:

$$\frac{1}{R_p} \propto P_{O_2}^{m} \tag{3.5}$$

Where R_p is the polarisation resistance of different ORR processes, and P_{O_2} is the oxygen partial pressure of the atmosphere in which we measure the polarisation resistance of the cathode.

Single cell test

We sealed the single button cells onto one end of the alumina tube with silver paste, with the cathode side outside the tube, and densified the silver paste at 260 °C. Subsequently, the sealed single cell was heated in a tube furnace up to 600 °C, followed by reducing the anode with flowing hydrogen. After the reduction is completed, we used the linear sweep voltammetry potentiostatic to obtain the i-V curve with scanning rate of 0.1V s^{-1} to determine its power density by:

$$P = \frac{i \times V}{A} \tag{3.6}$$

Where P stands for the power density of single cell and A for valid area of the single cell.

Meanwhile, we can also study resistances arising from electrolyte and electrodes through EIS method. A Nyquist plot can be achieved, and the first intercept of arc with real axis indicates the ohmic resistance of the single cell, which is mainly contributed by the electrolyte. The intercept difference between the two intercepts of arc with real axis reflect the overall polarization resistance of electrodes.

Long-term stability test on single cell can be carried out by measuring either current with applied constant voltage or voltage while applying constant current as a function of time.

3.5 First-principles calculations

Prof. Mingwen Zhan in Shan Dong University helped us with the simulations to probe ORR mechanisms of our targeted cathode materials. The first-principles calculations were performed with the Vienna ab initio simulation package (VASP)[6, 7] using density-functional theory (DFT). Ion-electron interactions were treated using projector-augmented-wave potentials[8] and a generalized gradient approximation (GGA) in the form of Perdew-Burke-Ernzerhof was adopted to describe electron-electron interactions.[9] The GGA+U calculations were performed with the simplified spherically-averaged approach applied to d electrons, where the coulomb (U) and exchange (J) parameters are combined into the single parameter U_{eff} ($U_{eff} = U - J$). Electron wave functions were expanded using plane waves with an energy cut-off of 520 eV. The Kohn-Sham equation was solved self-consistently with a convergence of 10^{-5}. The stoichiometry of the simulated systems was set to $SrCo_{0.75}Nb_{0.25}O_3$, $SrCo_{0.75}Ta_{0.25}O_3$, and $SrCo_{0.75}Nb_{0.125}Ta_{0.125}O_3$ respectively due to computational limitation, and the Nb and Ta in SCNT are regarded as ordered instead of randomly distributed for simplification.

3.6 References

1. Liss, K.-D.; Hunter, B.; Hagen, M.; Noakes, T.; Kennedy, S., Echidna—the new high-resolution powder diffractometer being built at OPAL. *Physica B: Condensed Matter* **2006,** 385, 1010-1012.

2. Toby, B. H.; Von Dreele, R. B., GSAS-II: the Genesis of a Modern Open-source All Purpose Crystallography Software Package. *Journal of Applied Crystallography* **2013,** 46, (2), 544-549.

3. Aguadero, A.; Calle, C. d. l.; Alonso, J. A.; Escudero, M. J.; Fernández-Díaz, M. T.; Daza, L., Structural and Electrical Characterization of the Novel $Srco_{0.9}Sb_{0.1}O_{3-\delta}$ Perovskite: Evaluation as a Solid Oxide Fuel Cell Cathode Material. *Chemistry of Materials* **2007,** 19, (26), 6437-6444.

4. Ciucci, F., Electrical conductivity relaxation measurements: Statistical investigations using sensitivity analysis, optimal experimental design and ECRTOOLS. *Solid State Ionics* **2013,** 239, (0), 28-40.

5. Takeda, Y.; Kanno, R.; Noda, M.; Tomida, Y.; Yamamoto, O., Cathodic polarization phenomena of perovskite oxide electrodes with stabilized zirconia. *Journal of The Electrochemical Society* **1987,** 134, (11), 2656-2661.

6. Kresse, G.; Hafner, J., *Ab initio* molecular dynamics for liquid metals. *Physical Review B* **1993,** 47, (1), 558-561.

7. Kresse, G.; Furthmüller, J., Efficient Iterative Schemes for *ab initio* Total-energy Calculations using A Plane-wave Basis Set. *Physical Review B* **1996,** 54, (16), 11169-11186.

8. Kresse, G.; Joubert, D., From Ultrasoft Pseudopotentials to the Projector Augmented-wave Method. *Physical Review B* **1999,** 59, (3), 1758-1775.

9. Perdew, J. P.; Burke, K.; Ernzerhof, M., Generalized Gradient Approximation Made Simple. *Physical Review Letters* **1996,** 77, (18), 3865-3868.

Chapter 4 P-doped SC perovskite cathode for IT-SOFC

Introduction

As mentioned in Section 2.4.2 and Section 2.6, the instability of perovskite phase limits the application of the $SrCoO_{3-\delta}$ derivatives as IT-SOFC cathodes, because the phase deviations result in the degradation of ionic conductivity (Section 2.2.2) and thereby cathode performance especially for long-term operation. Some researchers reported that doping some non-metal ions such as P, S and Si can stabilize the perovskite structure of $SrCoO_{3-\delta}$ at elevated temperature. Therefore, we systematically studied a P-doped Sr (Co, Fe) $O_{3-\delta}$ perovskite oxide as a cathode for IT-SOFC, and attempted to probe the effects of P dopants on the properties related to ORR.

Contribution

We successfully incorporated 5 mol% of P into the Sr (Co, Fe) $O_{3-\delta}$ oxide, and found that P dopant can stabilise the perovskite structure at both room and elevated temperature. The stabilizing effect of P is mainly due to its high valence state, which can slow down the rate of oxygen loss from lattice and prevent oxygen vacancies from becoming ordered, especially in the atmosphere at low oxygen partial pressure. High valence state of P is also beneficial for electronic conduction even at low oxygen partial pressure by increasing electronic holes for hopping process. Because of the improvement brought by P dopant, the P-doped Sr (Co, Fe) $O_{3-\delta}$ shows improved ORR activity and cathode stability. From our experimental results, we concluded that high valence is beneficial for electroactivity and stability of perovskite cathode at intermediate temperature. We published this work in the Journal of Material Chemistry A: Li, M.; Zhou, W.; Xu, X.; Zhu, Z., $SrCo_{0.85}Fe_{0.1}P_{0.05}O_{3-\delta}$ perovskite as a cathode for intermediate-temperature solid oxide fuel cells. *Journal of Materials Chemistry A* **2013,** 1, (43), 13632-13639.

$SrCo_{0.85}Fe_{0.1}P_{0.05}O_{3-\delta}$ Perovskite as a Cathode for Intermediate Temperature Solid Oxide Fuel Cell

Mengran Li, Wei Zhou, Xiaoyong Xu and Zhonghua Zhu**

Abstract: In this chapter, phosphorous doped perovskite, $SrCo_{0.85}Fe_{0.1}P_{0.05}O_{3-\delta}$ (SCFP), is evaluated as the cathode for intermediate temperature solid oxide fuel cells. It is observed that the phosphorous as dopant can prevent Sr-Co-Fe-O system from oxygen vacancy ordering and stabilise the crystallite structure of the oxide at 3C perovskite phase at high temperature as proved by XRD, TGA, O_2-TPD and electrical conductivity characterizations. The SCFP shows excellent chemical compatibility with $Sm_{0.2}Ce_{0.8}O_{1.9}$ (SDC) electrolyte even at 1200 °C. The oxygen reduction reaction (ORR) activity is investigated on a dense SDC pellet in a symmetrical cell configuration, and the area specific resistances (ASRs) of SCFP is as low as 0.097 $\Omega\cdot cm^2$ at 589 °C, which is comparable to the performance of the benchmark cathode BSCF. The stabilised structure for SCFP also improves the stability of the ORR activity at high temperature.

Keywords: SOFC; cathode; perovskite; ORR; stability

4.1 Introduction

Intermediate temperature solid oxide fuel cells (IT-SOFCs) are of great interest these years due to their relatively low temperature (500~750 °C)[1], making it possible for enhanced durability, rapid start-up, and improved sealing and the utilization of cheap metallic interconnectors[2]. However, lowering the operating temperature may result in slow kinetics of oxygen reduction at the cathodes.[3-6] Perovskite oxide is regarded as one of the most promising cathode materials[7] mainly due to its high rate of ionic and electronic conductivity and its fast kinetics of oxygen reduction reaction (ORR).[8] Among this kind of materials, a series of promising cathodes based on strontium cobaltite ($SrCoO_{3-\delta}$) were developed because of $SrCoO_{3-\delta}$'s high oxide ionic conductivity at intermediate temperature[9]. The crystallite structure of $SrCoO_{3-\delta}$ varies with different conditions of the synthesis such as oxygen partial pressure, temperature and preparation methods.[10-14]

In order to stabilise its phase at cathode-preferable 3C perovskite structure, doping into $SrCoO_{3-\delta}$ has been tested and $SrCo_{0.8}Fe_{0.2}O_{3-\delta}$ was reported to exhibit high performance as cathode for IT-SOFC.[15] However, this material was found to be still unstable in its phase, and unwanted oxygen vacancy ordering was observed during a phase transition from cubic to a brownmillerite-type structure at high temperature below 800°C with low oxygen level (pO_2<0.1atm).[16-20]

In order to improve the stability of $SrCo_{0.8}Fe_{0.2}O_{3-\delta}$, some research demonstrated that partial replacement of Co on B-sites or Sr on A-sites would preserve the perovskite cubic phase. For example, low level of chromium doped $SrCo_{0.85}Fe_{0.1}Cr_{0.05}O_{3-\delta}$ could keep cubic phase at low oxygen partial pressure (10^{-3}~10^{-5} tm) due to the stabilization of oxygen octahedral of Cr^{4+} cations.[21] Certain level of zirconium as dopant can suppress oxygen losing at high temperature and thus stabilize the phase.[22] The substitution of strontium on A-site by cations with relative large ionic radii like Ba[23] can also enhance the phase stability.

Recently, it was reported that the partial substitution of cations at B-sites with phosphorus, boron, silicon, and sulphur may boost the performance of cobaltite and manganite perovskite cathodes, including the enhancement on stability, electrical conductivities, tolerance to CO_2 and electrochemical performance.[24-26] Hancock et al reported that the phosphorus doped $SrCo_{0.8}Fe_{0.2}O_{3-\delta}$[25] has enhanced a beneficial effect on electrical conductivity. In addition, it was also found that the phosphorus doped in $BaIn_2O_5$ could prevent oxygen vacancies from being ordered.[27, 28] It can be noted that phosphorous seems to be another effective alternatives to solve stability issue of $SrCo_{0.8}Fe_{0.2}O_{3-\delta}$ as a cathode for IT-SOFC.

Herein, the incorporation of phosphorous in SCFP perovskite as the cathode was demonstrated. The stability of SCFP was studied by focusing on the effect of phosphorous on oxygen vacancy ordering at high temperature. The ORR activity and the corresponding stability of SCFP cathode was evaluated on a symmetrical cell configuration with $Sm_{0.2}Ce_{0.8}O_{1.9}$ as its electrolyte.

4.2 Experimental

SCFP was synthesized by a solid-state reaction method using $SrCoO_3$ (≥99.9%, Aldrich), Co_3O_4 (≤10μm, Aldrich), $NH_4H_2PO_4$ (≥98%, Sigma-Aldrich) and Fe_2O_3 as raw materials which were first weighed according to the stoichiometry of the oxide and ball milled at rate of 350 rpm for 1 hour. The powders were then pelletized to be sintered at 1200 ºC in air for 12h, followed by ball milling and then pelletizing to sinter for at 1200 °C another 12 h. $SrCo_{0.85}Fe_{0.15}O_{3-\delta}$ (SCF0.15) and $SrCo_{0.85}Fe_{0.1}O_{3-\delta}$ (SCF0.1) were synthesized through the same procedure as SCFP. The samples for the structure determination at 600 °C were prepared by quenching the powders to room temperature after calcination at 600ºC 24h. SCFP and SCF0.15 bars (18 mm×5mm×1.6mm) were prepared for the electrical conductivity test. These bars were sintered to dense at 1150 °C in air for 5h. Thereafter, silver pastes were used as electrodes printed onto the bars. The SCFP or SCF0.15 powders were made into ink by mixing with ethanol, terpineol and ethyl cellulose via ball milling. Symmetrical cells were fabricated by spraying SCFP or SCF0.15 ink followed by calcination at 1000 °C or 850 °C in air for 2 h. Then the silver paste was painted onto electrodes as the current collectors.

X-ray diffractometer (XRD) was utilized to identify the crystallite structure of synthesized powders at room temperature. Scanning electron microscopy (SEM) was used to characterize the microstructures of the prepared electrodes. The electrical conductivity test was carried out by 4-probe dc technique using silver paste as the electrodes. An oxygen programmed desorption (O_2-TPD) technique was used to study the oxygen desorption properties of the prepared powders with temperature ramping from 25 °C to 900 °C at a rate of 5 °C/min; the oxygen released was monitored by BelMass mass spectroscopy. Iodometry titration technique was used to determine the non-stoichiometry of SCFP and SCF0.15 at room temperature. Thermogravimetric analysis (TGA) was used to investigate oxygen desorption of the samples and to grab the oxygen non-stoichiometry of SCFP and SCF0.15 at high temperature. PGSTAT302 Autolab workstation was used to test the conductivity tests and the electrochemical impedance spectroscopy (EIS) of the cathode, where all the flows of gas are at a rate of 80 mL/min.

4.3 Results and discussion

4.3.1 Powder properties

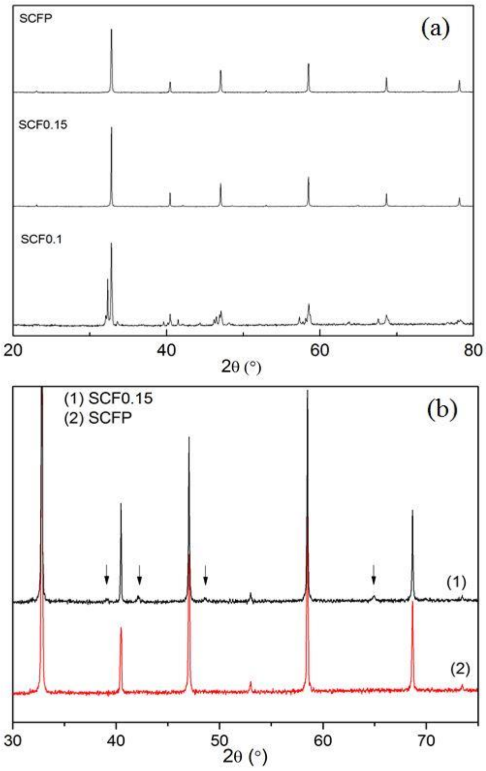

Figure 4-1 (a) X-ray diffraction profiles of SCFP, SCF0.15 and SCF0.1 at room temperature; (b) difference of XRD profiles of SCFP and SCF0.15 at room temperature for clarity.

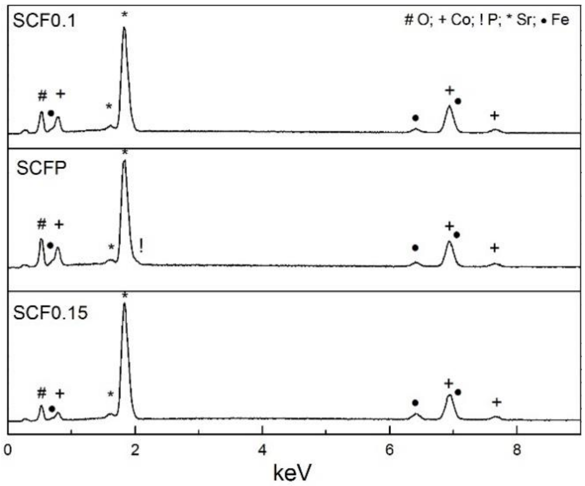

Figure 4-2 Electron dispersion spectroscopy (EDS) spectra for SCF0.1, SCFP and SCF0.15

Table 4-1 Comparison of cation ratios of samples calculated from EDS

	Sr	**Co**	**Fe**	**P**
SCF0.1	1	0.88	0.12	0
SCFP	1	0.83	0.10	0.08
SCF0.15	1	0.85	0.16	0

Figure 4-1(a) shows the XRD patterns of SCFP, SCF0.15 and SCF0.1 at room temperature. The structure parameters of SCFP and SCF0.15 are obtained by Le Bail refinement, revealing that SCFP has a 3C cubic perovskite structure belonging to a space group Pm-3m with a=3.86559Å, while the pattern of SCF0.15 is indexed in a I4mm tetragonal structure with a=b=10.94329 Å, c=7.73222 Å. The difference between SCFP and SCF0.15 is shown in Figure 4-1(b).

SCF0.1 was also synthesized to study whether the phosphorus was indeed incorporated into SCFP. The possibility that SCFP may be a B-site nonstoichiometric perovskite can be excluded by the XRD patterns of SCF0.1, which differs from SCFP structure. The composition of SCFP obtained by EDS is similar to the target material as prepared, which further proves the incorporation of phosphorus (Figure 4-2 and Table 4-1). The difference of stoichiometry may be due to the uncertainty of EDS and the possibility that some of Sr and Co may evaporate away during calcination at high temperature.

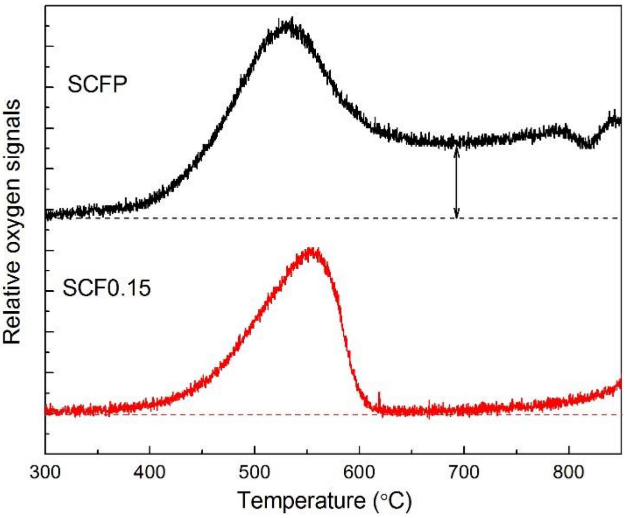

Figure 4-3 O_2-temperature programmed desorption (TPD) of SCFP with Ar as the sweep gas.

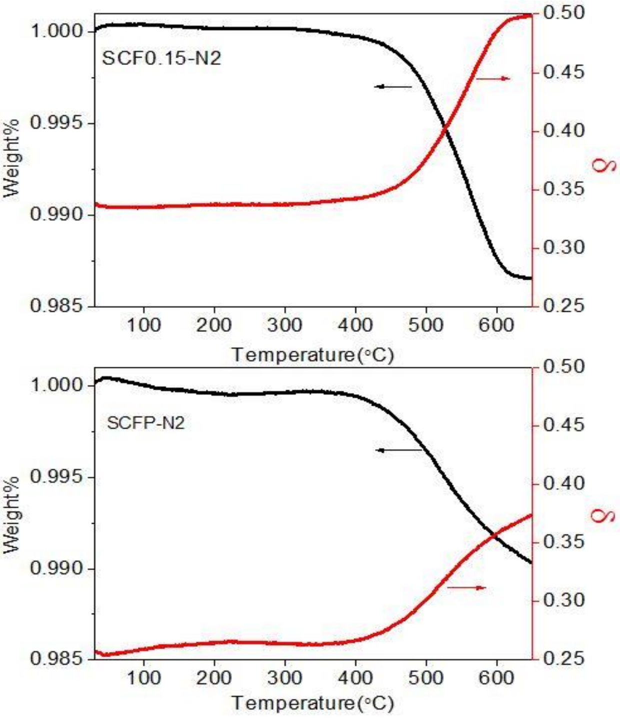

Figure 4-4 Thermogravimetric analysis profile and nonstoichiometry δ as a function of temperature under flowing N_2.

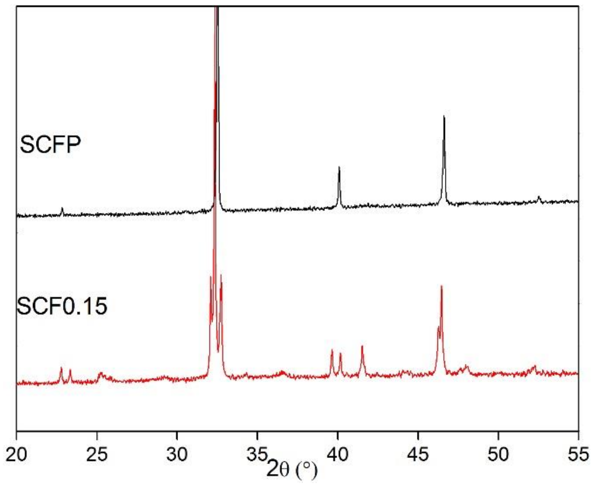

Figure 4-5 X-ray diffraction profile of SCFP and SCF0.15 quenching in N_2 at 650 °C.

The oxygen desorption properties of SCFP and SCF0.15 were studied through O_2-TPD under Argon from room temperature to 900 °C as shown in Figure 4-3. Oxygen started to desorb at approximately 400 °C from both samples. However, the oxygen was observed to release SCFP until 900 °C, while in SCF0.15 the oxygen release rate was found to decrease rapidly and a plateau was formed at the baseline of the signal at 600 °C. This indicates that a phase-transition may occur in SCF0.15 from oxygen vacancy disordered structure to ordered brownmillerite-type oxide at that temperature, which is quite similar to the results obtained in literature.[29] In comparison, the ordering was prevented by the incorporation of phosphorous at high temperature and low oxygen atmosphere, which can be proved by the XRD profiles exhibited in Figure 4-5. It is likely that this stabilization effect may be ascribed to the high valence state of the phosphorous (+5). High valence state may hinder the loss of oxygen anions in the lattice at high temperature to balance the charge in the structure, and this was further demonstrated by the results of TGA indicating that more loss of weight occurring in SCF0.15 than SCFP. Another effect of high valence state of phosphorous is to raise the electrostatic repulsion at B-sites and thus destabilize the formation of hexagonal phases with face-shared oxygen octahedral. The cubic structure was consequently remained at high temperature for SCFP. Several research groups also reported that the substitution of Nb^{5+} and Sb^{5+} into B-sites have the similar effect to Sr-Co-O based materials.[30, 31]

An estimate of the concentration of oxygen vacancies (or non-stoichiometry of oxygen, denoted by δ) was carried out based on TGA. The results of TGA (Figure 4-4) indicates that the δ values of both materials start to increase at approximately 400 °C, which is consistent well with the results of O_2-TPD discussed above. The estimated non-stoichiometry of SCF0.15 at about 650 °C reaches ~ 0.5, which is similar to that of brownmillerite structure of $SrCo_{0.8}Fe_{0.2}O_{2.5}$ [32], implying that SCF0.15 become oxygen-vacancy-ordered at N_2 atmosphere at 650 °C.

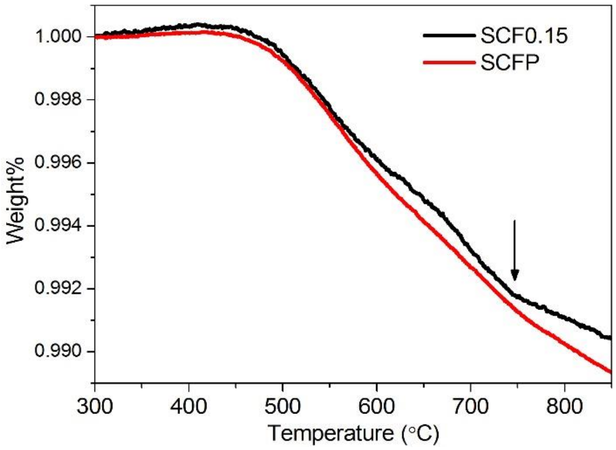

Figure 4-6 TGA profile of SCFP and SCF0.15 in flowing air.

The properties of releasing oxygen of the ceramic materials in air were also investigated. A slight flattened curve for SCF0.15 was observed after ~750 °C (Figure 4-6), indicating that the oxygen releasing rate was slowed down. It may be ascribed to the formation of oxygen ordering structure at the surface of SCF0.15 particles, which slows down oxygen ionic conduction in the lattice and therefore decreases the rate of oxygen release.

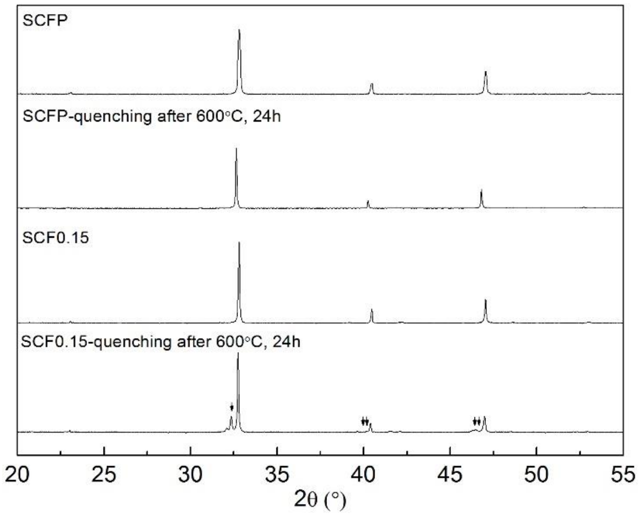

Figure 4-7 XRD profiles of SCFP and SCF0.15 with or without quenching at 600 °C after 24 h and the peaks denoted by arrows belong to brownmillerite-type structure. Higher angles are not shown for clarity.

The structure of the cathodes at typical working temperature for IT-SOFCs (~ 600 °C) in air atmosphere was then investigated by quenching the powders annealed at 600 °C for 24 h to retain their structure at high temperature. As can be seen from the results of XRD (Figure 4-7), the peaks of both materials shifted to lower 2θ values, implying that cell parameters of both materials increased as a result of the reduction of cobalt and iron cations and/or increased cation-cation repulsion caused by the removal of bridging oxygen ions. SCFP structure still remained at cubic phase at 600 °C in air, but the patterns of XRD for SCF0.15 shows the formation of ordering oxygen vacancy phase.

Therefore, it can be concluded that a transition from cubic to brownmillerite-type structure ($Sr_2Co_{1.6}Fe_{0.4}O_5$) will occur in SCF0.15 in the atmosphere with or without oxygen at 600 °C, and incorporating certain level of phosphorus could stabilize its phase, thus preventing the oxygen vacancy from being ordered.

4.3.2 Compatibility with electrolyte

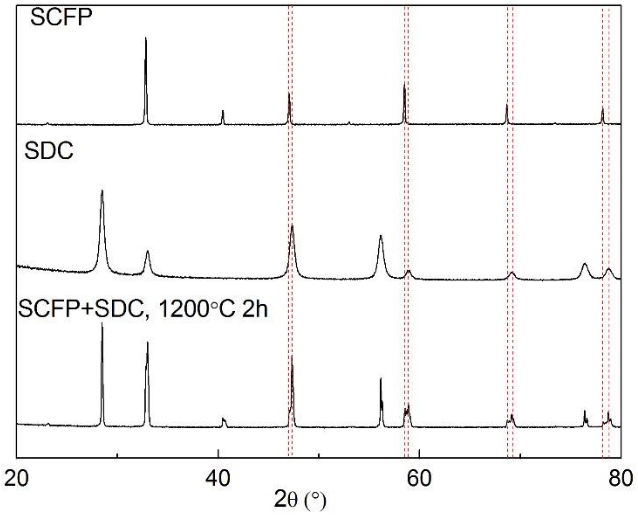

Figure 4-8 XRD profiles of SCFP, SDC and SCFP with SDC (mixture ratio 1:1) sintered at 1200 °C for 2 h.

The chemical compatibility of SCFP and SDC electrolyte was also investigated. As shown in Figure 4-8, in comparison to the patterns of SCFP and SDC, there are no extra peaks or any changes of peak positions observed in SDC and SCFP mixture calcined at 1200 ºC for 2 h, implying that SCFP can be chemically well compatible with SDC at a temperature higher than the temperature (1000 ºC) used for the cathode fabrication. Therefore, it can be concluded that little reaction between SCFP and SDC will occur during the cathode fabrication process.

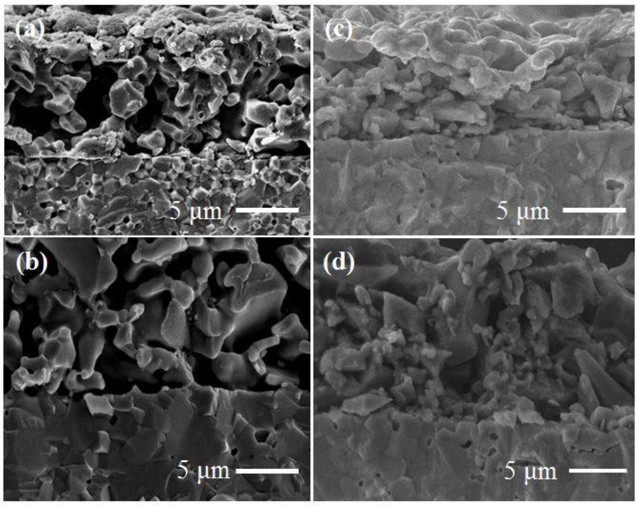

Figure 4-9 SEM micrograph of the cross section of SCFP cathodes with SDC electrolyte calcined at (a) 1000 °C and (c) 850 °C; micrograph of SCF0.15 cathodes with SDC electrolyte calcined at (b) 1000 °C and (d) 850 °C.

The SEM images show the cross section of the interface between cathode and electrolyte after being calcined at 1000ºC or 850ºC, revealing the adherence of cathodes to SDC electrolyte is similar for the cathodes fabricated at 850ºC and 1000ºC (Figure 4-9). However, better interconnection between particles was found in the cathodes with higher temperature calcination.

4.3.3 Electrochemical performance

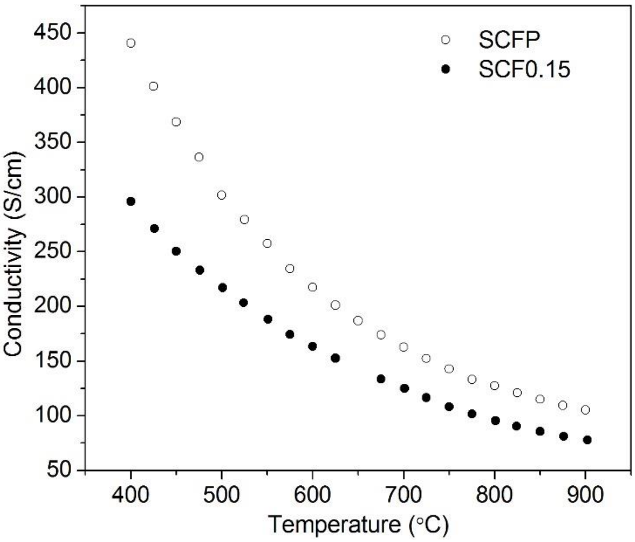

Figure 4-10 Electrical conductivity of SCFP and SCF0.15 as a function of temperature in air.

It is shown from the Figure 4-10 that the electrical conductivities of both SCFP and SCF0.15 decrease with increasing temperature in a range of temperature from 400 °C to 900 °C. Jung *et al.*[33] studied systematically the effects of temperature and oxygen partial pressure on the electrical conductivity of $Ba_{0.5}Sr_{0.5}Co_xFe_{1-x}O_{3-\delta}$ $(0 \leq x \leq 1)$ and concluded that the decreasing conductivity at over 673 K with $pO_2 \geq 0.01$atm resulted from the reduction of p-type carriers due to the loss of oxygen at high temperature. The results of O-TPD and TGA have shown that the formation of oxygen vacancy started in both SCFP and SCF0.15 at about 400 °C, and electrons were generated according to the equation as follows[33]:

$$O_O \rightarrow V_O^{\bullet\bullet} + 2e' + \frac{1}{2}O_2(g) \tag{4.1}$$

Meanwhile, additional amount of Co^{3+} and Fe^{3+} were formed at B-sites, both decreasing the concentration of p-carriers and thus lowering the conductivity. The conductivity of SCFP was enhanced as compared with SCF0.15, and the difference becomes larger at lower temperature. Firstly, the high valence of P, as discussed before, may suppress the loss of oxygen and therefore mitigate the adverse effects on p-type conduction. Meanwhile, the valence 5+ is beneficial for the hopping process.

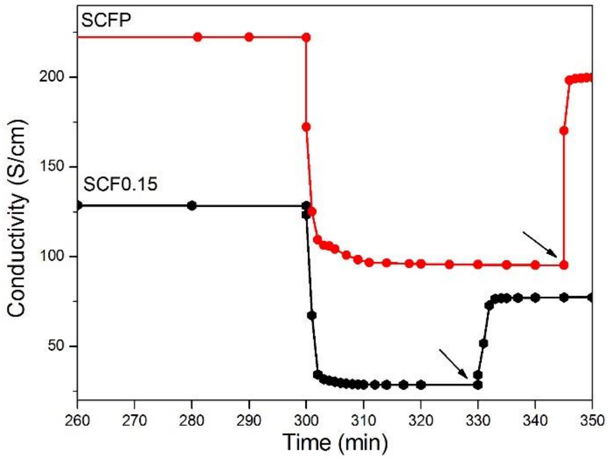

Figure 4-11 Electrical conductivity of SCFP and SCF0.15 as a function of time at 600 °C in air for 5 h, and subsequently replace air with N_2 for a certain time, and then change the gas back to air. The point denoted by the arrow is the time when N_2 is replaced by air.

Further study was carried out on the changes of conductivities of these composites at 600 °C when being fed with N_2 instead of air after heating in air for 5 h, and the then switching nitrogen to air after conductivities reaching steady state in N_2. As shown in Figure 4-11, the electrical conductivity of both samples remained nearly unchanged in air for 5h, and decreased with the time because of the loss of oxygen from the perovskite lattice. This confirms that the two materials belong to p-type conductors.

It was observed that the conductivity of SCF0.15 dropped immediately to about 32 S cm^{-1} in only 4 min after the nitrogen was fed in, while a gradual decrease of the conductivity was shown in SCFP, taking about 20min to reach the bottom of the conductivity with a value of around 98 S cm^{-1}. However, when N_2 is replaced by air, it is found that the conductivity of SCFP increased more quickly than

SCF0.15. Furthermore, the conductivity of SCF0.15 is only recovered by half of its initial conductivity.

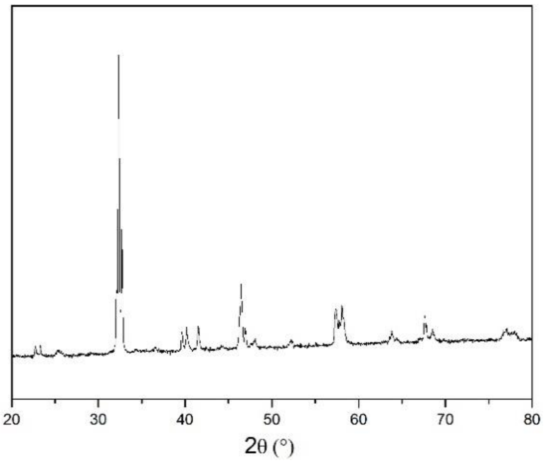

Figure 4-12 XRD pattern of SCF0.15 quenching in N_2 after 5 min exposure to N_2 at 600 °C.

The steep conductivity decrease for SCF0.15 may be ascribed to either the fast oxygen surface exchange rate or the phase transition to ordered structure. The XRD result of SCF0.15 in Figure 4-12 indicates that the structure of SCF0.15 has been transformed into ordered structure during 5 min of being fed with N_2 at 600 °C, which implies that structure transformation, rather than fast surface exchange, is the cause of the fast decrease of electrical conductivity. Moreover, the formation of brownmillerite phase in SCF0.15 leads to the decrease of conductivity to a much lower level which is similar to the values obtained for ordered $SrCo_{0.8}Fe_{0.2}O_{3-\delta}$ at the same temperature.[18] The slow recover of SCF0.15 conductivity provides another evidence for the change of structure in SCF0.15. In contrast, however, the incorporation of P will suppress such structure distortion, and improve the electrical conductivity of SCFP at high temperature in a reducing atmosphere.

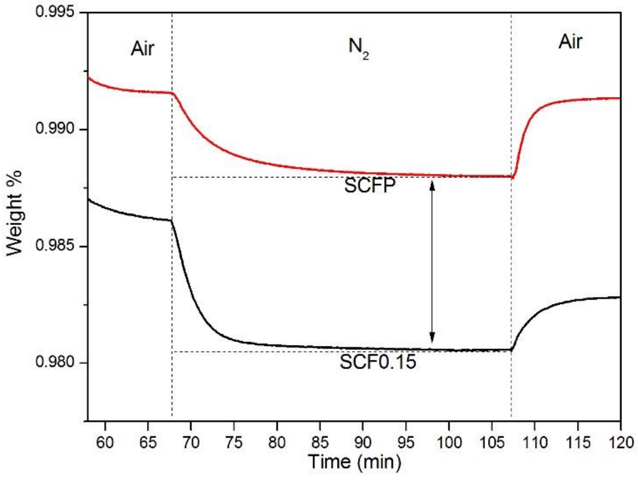

Figure 4-13 TGA profiles of SCFP and SCF0.15 as a function of time at 600 °C in air, then in N_2 and finally in air.

Furthermore, TGA was conducted at similar conditions to the conductivity test discussed above. It is observed from Figure 4-13 that the weight of SCF0.15 drop fast in the first 5min but then reach the plateau with a very slow rate. In contrast, SCFP gradually decreases its weight until steady state, but the time they spent are about the same as denoted in the figure. Combined with the result shown in Figure 4-12, the fast weight drop of SCF0.15 can be attributed to the formation of brownmillerite-type structure, which results in higher oxygen escaping rate. Once most of SCF0.15 changed their structure, the oxygen releasing rate became very slow. The different oxygen releasing profile from the decreasing conductivity behaviour in Figure 4-11 for SCF0.15 further proves that the initial fast conductivity drop of SCF0.15 is due to the formation of ordered structure. When the flowing gas was switched back to air, it can be seen from Figure 4-13 that SCFP increases its weight more quickly than SCF0.15, and nearly recovers back to initial weight in air at 600 °C. The XRD patterns of both samples after TGA analysis are also presented in Figure S4-1, and indicate that SCFP is still in a cubic phase while SCF0.15 has been distorted to ordered structure. This suggests again that P benefits the stabilization of 3C perovskite phase thus a relative high electrical conductivity was achieved under low oxygen partial pressure.

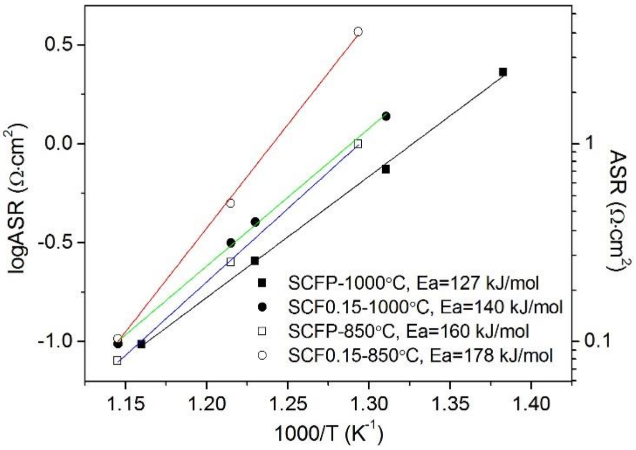

Figure 4-14 Temperature dependence of the area specific resistances for SCFP and SCF0.15 cathodes fabricated at 1000 °C and 850 °C.

Figure 4-14 presents the ASR values of the SCFP and SCF0.15 cathodes at various temperatures. The ASR value corresponds to the difference between the intercepts of high and low frequency impedance spectra achieved from EIS. The ASRs of the SCFP cathode, as determined by two-electrode impedance method, are 0.097 and 0.255 $\Omega\cdot cm^2$ at 589 °C and 540 °C respectively, in contrast to 0.19 and 0.7 $\Omega\cdot cm^2$ for SCF0.15. The lower ASR value reflects higher ORR activity of the cathode. The ASRs of SCFP cathode are enhanced by over 50% especially at low temperatures (< 550 °C) as compared to SCF0.15. The better performance of SCFP is a result of a combination of factors including stable cubic structure, high electrical conductivity and smaller grain sizes as shown in Figure S 4-2. What is more, the activity of SCFP is much higher than those of Sr-Co-Fe-O system doped with La[34], and Sr-Co-O with dopants as Sb[31], Mo[34] and Ce[35] at B-site. Moreover, its good performance is comparable to BSCF cathode[23], which is currently one of the most promising cathodes for IT-SOFC.

The ORR activity of the cathodes calcined at 850 °C was also studied. It can be shown from the Figure 11 that the activation energies of both cathodes fabricated at 850 °C are higher than the corresponding ones fabricated at 1000ºC. The high activation energy is probably due to the poor connection among particles of cathodes as shown by the SEM images in Figure 4-9 which leads to the poor performance at lower operating temperatures (< 600 °C). Furthermore, even in the case of low fabrication temperature, the performance of SCFP is still better than that of SCF0.15 at the same operating temperatures.

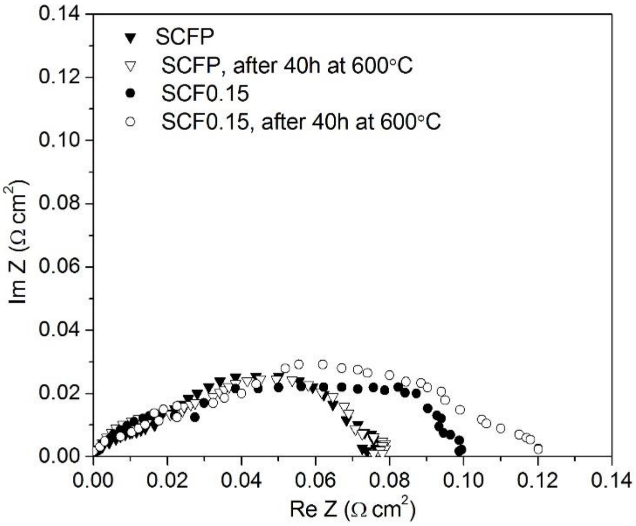

Figure 4-15 Nyquist impedance spectra for SCFP and SCF0.15 operated at 600 °C temperature before and after 40 h with fabrication temperature of 850 °C.

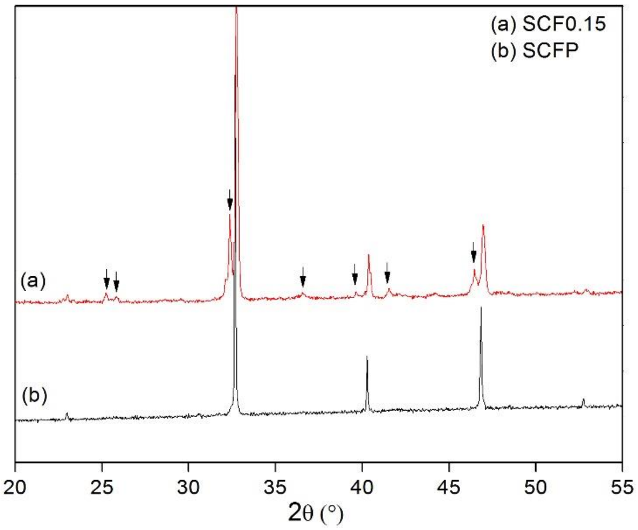

Figure 4-16 Difference of XRD patterns of SCFP and SCF0.15 quenching in air after heating at 600 °C for 40 h, and peaks denoted by arrows belong to brownmillerite-type structure.

The stabilities of the cathodes were also investigated. Figure 4-15 shows the comparison of performance of ORR at 600 °C before and after 40 h operation for SCFP and SCF0.15 cathodes in symmetrical cell configuration. There is nearly no deterioration of performance for SCFP after 40 h operation, but the ASR of SCF0.15 increases by about 20% after 40 h operation at 600 °C, indicating the much better stability of ORR performance was achieved by SCFP compared with SCF0.15 at the same condition. As discussed above, a partial phase transition may occur to brownmillerite structure with ordering oxygen vacancies, which hinders oxygen ion conduction, in the cathode of SCF0.15 during long time operation in air at 600 °C. This partial phase transition is demonstrated by the XRD results of SCFP and SCF0.15 quenched in air after heating at 600 °C for 40 h, which are presented in Figure 4-16. In contrast, P dopant can suppress this phase transition, thus renders SCFP maintain a stable ORR performance at 600 °C for a long time. Figure S 4-2 shows the topographies of SCF0.15 and SCFP cathodes before and after 40h heat treatment at 600°C in air, and slight grain coarsening can be observed for both of materials; therefore it is believed that the grain coarsening has insignificant impacts on the performance degradation with comparison to the phase transformation in SCF0.15.

4.4 Conclusions

$SrCo_{0.85}Fe_{0.1}P_{0.05}O_{3-\delta}$ and $SrCo_{0.85}Fe_{0.15}O_{3-\delta}$ were prepared using the conventional solid state reaction. It is observed that the incorporation of phosphorous can prevent Sr-Co-Fe-O perovskite from oxygen vacancy ordering at temperature higher than 600 °C both in air and atmosphere with lower oxygen level. An enhancement of electrical conductivity was noticed by around 150 S cm^{-1} in SCFP at 400 °C when compared with SCF0.15. ASRs of both cathodes implied that SCFP is better than SCF0.15 especially at low operating temperature with a value of 0.097 $\Omega\cdot cm^2$ at 589 °C, while SCF0.15 only has 0.19 $\Omega\cdot cm^2$ at the same temperature. These results indicate that the incorporation of phosphorus helps stabilize 3C perovskite phase both at room temperature and high operating temperature, and thus improve the ORR activity and the stability of cathode for IT-SOFC.

Acknowledgement

This work is financial supported by Australian Research Council and author Mengran Li acknowledges additional financial support from the top-up assistance program (TUAP) scholarship and the scholarship from China Scholarship Council.

4.5 Supplementary Information

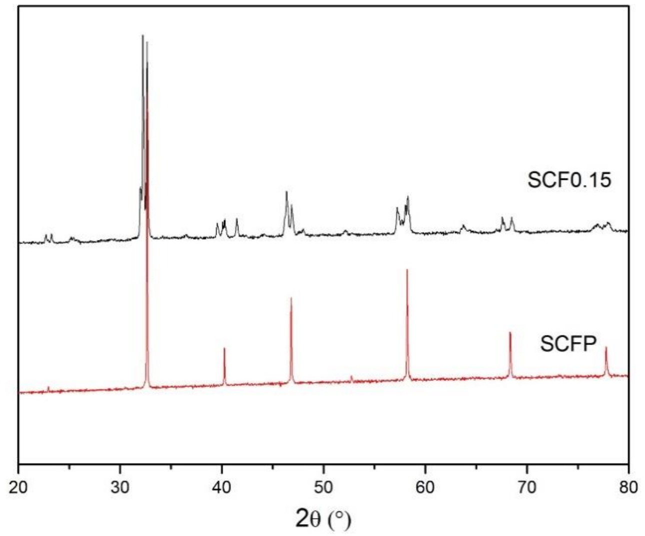

Figure S 4-1 XRD profiles of SCFP and SCF0.15 powders after TGA measurement at 600 °C first being in flowing air, and subsequently in N_2 and finally in air.

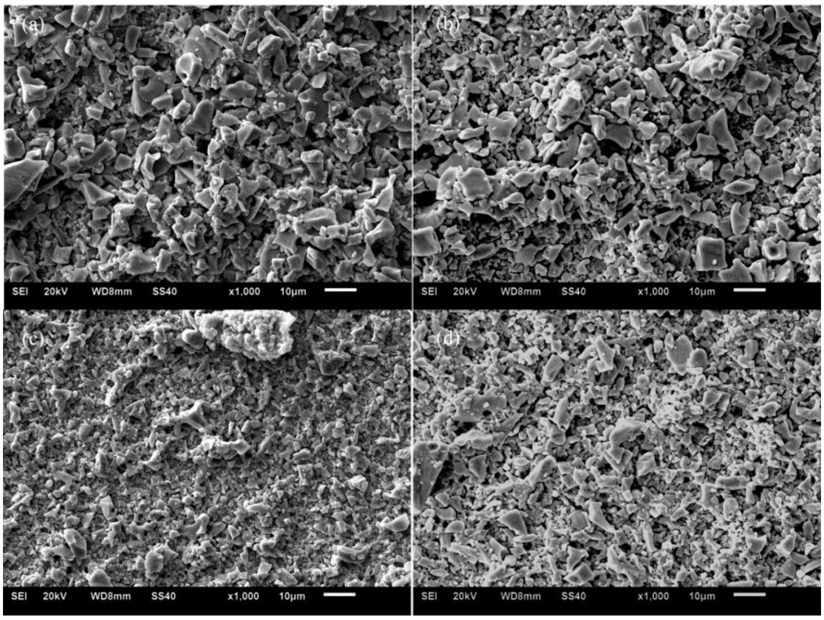

Figure S 4-2 SEM images of the microstructures of (a) SCF0.15 and (c) SCFP cathodes before and (b) SCF0.15 (d) SCFP cathodes after annealing at 600 °C for 40 h in air.

4.6 References

1. Steele, B. C. H., Material Science and Engineering: The Enabling Technology for the Commercialisation of Fuel Cell Systems. *Journal of Materials Science* **2001,** 36, (5), 1053-1068.

2. Minh, N. Q., Ceramic Fuel Cells. *Journal of the American Ceramic Society* **1993,** 76, (3), 563-588.

3. Steele, B. C.; Heinzel, A., Materials for Fuel-Cell Technologies. *Nature* **2001,** 414, (6861), 345-352.

4. Jacobson, A. J., Materials for Solid Oxide Fuel Cells. *Chemistry of Materials* **2009,** 22, (3), 660-674.

5. Orera, A.; Slater, P., New Chemical Systems for Solid Oxide Fuel Cells. *Chemistry of Materials* **2009,** 22, (3), 675-690.

6. Tarancón, A.; Burriel, M.; Santiso, J.; Skinner, S. J.; Kilner, J. A., Advances in layered oxide cathodes for intermediate temperature solid oxide fuel cells. *Journal of Materials Chemistry* **2010,** 20, (19), 3799-3813.

7. Zhou, W.; Ran, R.; Shao, Z., Progress in Understanding and Development of $Ba_{0.5}Sr_{0.5}Co_{0.8}Fe_{0.2}O_{3-\delta}$ -Based Cathodes for Intermediate-Temperature Solid-Oxide Fuel Cells: A Review. *Journal of Power Sources* **2009,** 192, (2), 231-246.

8. Aricò, A. S.; Bruce, P.; Scrosati, B.; Tarascon, J.-M.; Van Schalkwijk, W., Nanostructured Materials for Advanced Energy Conversion and Storage Devices. *Nature materials* **2005,** 4, (5), 366-377.

9. Kharton, V.; Yaremchenko, A.; Kovalevsky, A.; Viskup, A.; Naumovich, E.; Kerko, P., Perovskite-type Oxides for High-temperature Oxygen Separation Membranes. *Journal of Membrane Science* **1999,** 163, (2), 307-317.

10. Deng, Z.; Yang, W.; Liu, W.; Chen, C., Relationship between Transport Properties and Phase Transformations in Mixed-conducting Oxides. *Journal of Solid State Chemistry* **2006,** 179, (2), 362-369.

11. Rodriguez, J.; Gonzalez-Calbet, J.; Grenier, J.; Pannetier, J.; Anne, M., Phase Transitions in $Sr_2Co_2O_5$: A Neutron Thermodiffractometry Study. *Solid state communications* **1987,** 62, (4), 231-234.

12. Rodriguez, J.; Gonzalez-Calbet, J., Rhombohedral $Sr_2Co_2O_5$: A New $A_2M_2O_5$ Phase. *Materials research bulletin* **1986,** 21, (4), 429-439.

13. Grenier, J.-C.; Fournès, L.; Pouchard, M.; Hagenmuller, P., A Mössbauer Resonance Investigation of ^{57}Fe Doped $Sr_2Co_2O_5$. *Materials research bulletin* **1986,** 21, (4), 441-449.

14. Lei, Y.; Ito, Y.; Browning, N. D.; Mazanec, T. J., Segregation Effects at Grain Boundaries in Fluorite‐Structured Ceramics. *Journal of the American Ceramic Society* **2002,** 85, (9), 2359-2363.

15. Raza, R.; Wang, X.; Ma, Y.; Liu, X.; Zhu, B., Improved Ceria–carbonate Composite Electrolytes. *International Journal of Hydrogen Energy* **2010,** 35, (7), 2684-2688.

16. Qiu, L.; Lee, T. H.; Liu, L. M.; Yang, Y. L.; Jacobson, A. J., Oxygen Permeation Studies of $SrCo_{0.8}Fe_{0.2}O_{3-\delta}$. *Solid State Ionics* **1995,** 76, (3–4), 321-329.

17. Kruidhof, H.; Bouwmeester, H.; Burggraaf, A., Influence of order-disorder transitions on oxygen permeability through selected nonstoichiometric perovskite-type oxides. *Solid State Ionics* **1993,** 63, 816-822.

18. Grunbaum, N.; Mogni, L.; Prado, F.; Caneiro, A., Phase equilibrium and electrical conductivity of SrCo< sub> 0.8</sub> Fe< sub> 0.2</sub> O< sub> 3− δ</sub>. *Journal of Solid State Chemistry* **2004,** 177, (7), 2350-2357.

19. Liu, L.; Lee, T.; Qiu, L.; Yang, Y.; Jacobson, A., A Thermogravimetric Study of the Phase Diagram of Strontium Cobalt Iron Oxide, $SrCo_{0.8}Fe_{0.2}O_{3-\delta}$. *Materials research bulletin* **1996,** 31, (1), 29-35.

20. Harrison, W.; Lee, T.; Yang, Y.; Scarfe, D.; Liu, L.; Jacobson, A., A Neutron Diffraction Study of Two Strontium Cobalt Iron Oxides. *Materials research bulletin* **1995,** 30, (5), 621-630.

21. Tikhonovich, V.; Zharkovskaya, O.; Naumovich, E.; Bashmakov, I.; Kharton, V.; Vecher, A., Oxygen nonstoichiometry of Sr (Co, Fe) O< sub> 3− δ</sub>-based perovskites: I. Coulometric titration of SrCo0. 85Fe0. 10Cr0. 05O3− δ by the two-electrode technique. *Solid State Ionics* **2003,** 160, (3), 259-270.

22. Yang, L.; Tan, L.; Gu, X.; Jin, W.; Zhang, L.; Xu, N., A New Series of Sr (Co, Fe, Zr) $O_{3-\delta}$ Perovskite-Type Membrane Materials for Oxygen Permeation. *Industrial & Engineering Chemistry Research* **2003,** 42, (11), 2299-2305.

23. Shao, Z.; Haile, S. M., A High-Performance Cathode for the Next Generation of Solid-Oxide Fuel Cells. *Nature* **2004,** 431, (7005), 170-173.

24. Porras‐Vazquez, J. M.; Slater, P. R., Synthesis and Characterization of Oxyanion‐Doped Cobalt Containing Perovskites. *Fuel Cells* **2012,** 12, (6), 1056-1063.

25. Hancock, C. A.; Slade, R. C. T.; Varcoe, J. R.; Slater, P. R., Synthesis, Structure and Conductivity of Sulfate and Phosphate Doped $SrCoO_3$. *Journal of Solid State Chemistry* **2011,** 184, (11), 2972-2977.

26. Porras-Vazquez, J. M.; Kemp, T. F.; Hanna, J. V.; Slater, P. R., Synthesis and Characterisation of Oxyanion-doped Manganites for Potential Application as SOFC Cathodes. *Journal of Materials Chemistry* **2012,** 22, (17), 8287-8293.

27. Shin, J. F.; Hussey, L.; Orera, A.; Slater, P. R., Enhancement of the Conductivity of $Ba_2In_2O_5$ Through Phosphate Doping. *Chemical Communications* **2010,** 46, (25), 4613-4615.

28. Shin, J. F.; Orera, A.; Apperley, D.; Slater, P., Oxyanion Doping Strategies to Enhance the Ionic Conductivity in $Ba_2In_2O_5$. *Journal of Materials Chemistry* **2011,** 21, (3), 874-879.

29. McIntosh, S.; Vente, J. F.; Haije, W. G.; Blank, D. H.; Bouwmeester, H. J., Oxygen Stoichiometry and Chemical Expansion of $Ba_{0.5}Sr_{0.5}Co_{0.8}Fe_{0.2}O_{3-\delta}$ Measured by in Situ Neutron Diffraction. *Chemistry of Materials* **2006,** 18, (8), 2187-2193.

30. Zhou, W.; Jin, W. Q.; Zhu, Z. H.; Shao, Z. P., Structural, Electrical and Electrochemical Characterizations of $SrNb_{0.1}Co_{0.9}O_{3-\delta}$ as a Cathode of Solid Oxide Fuel Cells Operating Below 600°C *International Journal of Hydrogen Energy* **2010,** 35, (3), 1356-1366.

31. Aguadero, A.; Alonso, J. A.; Pérez-Coll, D.; de la Calle, C.; Fernández-Díaz, M. a. T.; Goodenough, J. B., $SrCo_{0.95}Sb_{0.05}O_{3-\delta}$ as Cathode Material for High Power Density Solid Oxide Fuel Cells. *Chemistry of Materials* **2009,** 22, (3), 789-798.

32. McIntosh, S.; Vente, J. F.; Haije, W. G.; Blank, D. H. A.; Bouwmeester, H. J. M., Structure and Oxygen Stoichiometry of $SrCo_{0.8}Fe_{0.2}O_{3-\delta}$ and $Ba_{0.5}Sr_{0.5}Co_{0.8}Fe_{0.2}O_{3-\delta}$. *Solid State Ionics* **2006,** 177, (19–25), 1737-1742.

33. Jung, J.-I.; Misture, S.; Edwards, D., The Electronic Conductivity of $Ba_{0.5}Sr_{0.5}Co_xFe_{1-x}O_{3-\delta}$ (BSCF: $x = 0 \sim 1.0$) under Different Oxygen Partial Pressures. *Journal of Electroceramics* **2010,** 24, (4), 261-269.

34. Aguadero, A.; Pérez-Coll, D.; Alonso, J. A.; Skinner, S. J.; Kilner, J., A New Family of Mo-Doped $SrCoO_{3-\delta}$ Perovskites for Application in Reversible Solid State Electrochemical Cells. *Chemistry of Materials* **2012,** 24, (14), 2655-2663.

35. Yang, W.; Hong, T.; Li, S.; Ma, Z.; Sun, C.; Xia, C.; Chen, L., Perovskite $Sr_{1-x}Ce_{x}CoO_{3-\delta}$ ($0.05 \leqslant x \leqslant 0.15$) as Superior Cathodes for Intermediate Temperature Solid Oxide Fuel Cells. *ACS Applied Materials & Interfaces* **2013,** 5, (3), 1143-1148.

Chapter 5 The comparative studies on Ta-doped SC perovskite cathode with different doping levels

Introduction

In Chapter 4, we found that high valence of dopant can improve cathode's ORR activity and stability at intermediate temperature. As a B-site dopant in high valence, Nb^{5+} is widely incorporated into perovskite oxides (Section 2.4.2) and reported beneficial for perovskite cathode of IT-SOFC. However, Ta^{5+} still remains unexplored as dopant for IT-SOFC cathode, though Ta has very similar ionic radius and valence to Nb^{5+}. For this reason, this chapter tends to develop perovskite cathodes based on $Sr(Co, Ta)O_{3-\delta}$, and to study the effects of Ta on cathode electroactivity and stability.

Contribution

In this chapter, we successfully synthesized $SrCoO_{3-\delta}$ perovskite oxides doped with different content of Ta, and evaluated them as cathode for IT-SOFCs. Ta can stabilize the cubic perovskite structure of $SrCoO_{3-\delta}$, but doping < 5 mol% of Ta can result in a tetragonal structure at room temperature. The Ta content is found to influence the electrical conductivity: small content (5 mol%) of Ta increases electrical conductivity, which is similar to effect of P; Ta content higher than 5 mol% degrades the electrical conductivity likely by blocking the hopping process. Besides, the high valence of Ta increases overall positive charge of cations, thereby decreasing the content of oxygen vacancies. Containing 5mol% ~20 mol% of Ta, the doped $SrCoO_{3-\delta}$ cathodes show stable and promising ORR activity that can be comparable to some of the state-of-the-art cathodes. The remarkably improved cathode performance can be explained by the enhanced oxygen surface exchange kinetics. This work has been published in the ChemElectroChem: Li, M.; Zhou, W.; Zhu, Z., Comparative Studies of $SrCo_{1-x}Ta_xO_{3-\delta}$ ($x=0.05$–0.4) Oxides as Cathodes for Low-Temperature Solid-Oxide Fuel Cells. *ChemElectroChem* **2015,** 2, (9), 1331-1338.

The Comparative Studies of $SrCo_{1-x}Ta_xO_{3-\delta}$ (x=0.05-0.4) Oxides as Cathodes of Low-temperature Solid Oxide Fuel Cells

Mengran Li, Wei Zhou, and Zhonghua Zhu**

Abstract: To address the sluggish ORR kinetics of cathodes has become of great interest and significance for the deployment of the solid oxide fuel cells (SOFCs) operated at lower temperatures. A series of Sr (Co, Ta) $O_{3-\delta}$ oxides with multi-level substitutions of tantalum ions have been studied as cathodes of SOFCs, in terms of their crystal structures, electrochemical properties and durability. The effects of doping tantalum on oxygen reduction reaction (ORR) have been explored and discussed. Not only can the crystallite structures of $SrCoO_{3-\delta}$ be stabilized by incorporating Ta^{5+} at elevated temperatures, but also the activities towards ORR are significantly enhanced by doping relatively small amounts of Ta^{5+} (≤ 20%mol), which is probably due to the improved oxygen surface exchange by the positive effects of Ta^{5+} dopants on oxidation states of cobalt ions.

Keywords: Cathode; Perovskite; LT-SOFC; Tantalum; Oxygen reduction reaction

5.1 Introduction

Solid oxide fuel cells (SOFCs) are the unique devices that are capable of converting chemical energy of nearly all types of fuels directly into electricity with very high efficiency.[1, 2] However, its high operating temperature is the key issue that prohibits the widespread deployment of this technology, because high operating temperature results in poor stability, high system and operational costs and lower theoretical fuel cell efficiencies.[3] Therefore, lowering the operating temperature of SOFCs is of great interest and significance in recent years. The main challenge for low-temperature SOFCs (LT-SOFCs) is to address the polarization losses of the components of SOFCs at low temperatures, especially of the cathodes which are responsible for catalyzing the oxygen reduction reaction (ORR).[4-6]

Intensive research has been conducted over the last two decades exploring cathode materials with high activities and stabilities.[7-14] It is widely accepted that the materials with mixed electronic and ionic conductivities (MIECs) are one of the most promising candidates for the next generation of cathodes of LT-SOFCs.[6, 15] Among these MIEC materials, $SrCoO_{3-\delta}$ (SC) with cubic perovskite structure has been reported to exhibit relatively high ORR activities at intermediate temperature range (600-800ºC) because of its high mixed conductivities.[16] Unfortunately, undesired phases were reported to exist in SC below 800ºC and varying ambient atmospheres.[17-20] Several studies demonstrate that the substitution of cations with high valence states into B-sites (where Co cations stay) is an effective way to stabilize SC's cubic perovskite structure[21-26]. What is more, low level of dopants with high valence states can also enhance SC's cathode performance by enhancing its electrical conductivities.[21, 25]

Recently, Nb^{5+} is widely doped into different parent perovskite cathode materials to stabilize the cathode-favoured cubic structure and even give a boost to the ORR activities of the cathodes.[9, 26-30] For example, Zhou *et. al.*[13] reported a highly active cathode of SOFC at temperatures below 600ºC by substituting Nb^{5+} into $Sr(Sc,Co)O_{3-\delta}$ perovskite oxide, and many researchers also substituted Nb^{5+} into the milestone cathodes such as $(La,Sr)(Co,Fe)O_{3-\delta}$[28] and $(Ba,Sr)(Co,Fe)O_{3-\delta}$[27]. What is more, a few researchers also studied the cathode materials substituted by Ta^{5+} cations, which share very similar ionic radii and oxidation state with Nb^{5+}.[25] It is also reported that doping 10% mol of Ta^{5+} into SC can suppress the crystal structure deformation, and increase the electrical conductivities.[25, 31] However, it remains unknown to date about the effects of incorporating Ta^{5+} ions into SC as a cathode of SOFCs. Therefore, we aim to evaluate the potential of $SrCo_{1-x}Ta_xO_{3-\delta}$ (x=0.05, 0.1, 0.15, 0.2, 0.4) (SCT5-SCT40) as cathodes for LT-SOFCs and the effects of Ta^{5+} by varying its substitution levels on the activity over ORR.

Herein, the incorporation of Ta^{5+} cations into SC perovskite oxides with different concentrations was demonstrated as cathodes of SOFCs. The effects of Ta^{5+} on the cathode performance were evaluated mainly regarding the oxygen vacancies, electrical conductivities, structure stabilities and the activities towards ORR of the doped SC perovskite cathodes.

5.2 Experimental

The syntheses of SCT5-40 were performed via conventional solid state reaction. For this purpose, stoichiometric amounts of $SrCO_3$ (≥99.9%, Aldrich), Co_3O_4 (≤10μm, Aldrich) and Ta_2O_5 (>99.9%, Aldrich) were ball milled for 24 hours, followed by pelletizing and sintering in stagnant air at 1200ºC for 10 hours. Thereafter, the sintered pellets were well ground and then sintered at 1200ºC for another 10 hours.

The electrical conductivities of the samples were measured in the flowing air (~200 ml/min) by the DC four-probe method. The dense bars of the materials were prepared by pressing the cathode powders into bars, followed by sintering at 1200ºC in air for 5 hours and subsequently polishing the bar into similar dimensions. Silver paste was used as the current and voltage electrodes. The measurement of the electrical conductivities was carried out by an Autolab PGSTAT30 electrical workstation.

The concentration of oxygen vacancies and the average cobalt oxidation states of SCT5-40 at room temperature were obtained by iodometric titration method[32] according to the principles as briefly introduced below:

The $SrCo_{1-x}Ta_xO_{3-\delta}$ system only contains Co^{Z+} ions that can be reduced by I^- ions. When the m g sample is dissolved in hydrochloric acid solution with excess KI, a reaction occurs:

$$Co^{Z+} + \left(Z-2\right)I^- = Co^{2+} + \left(0.5Z-1\right)I_2 \tag{5.1}$$

Z represents the average oxidation states of Co ions in the sample. Ta^{5+} cannot be dissolved in hydrochloric acid, so it will come out of the solution system in the form of Ta_2O_5. The liberated I_2 can be titrated by a solution of sodium thiosulfate with a known concentration C:

$$I_2 + 2Na_2S_2O_3 \rightarrow 2NaI + Na_2S_4O_6 \tag{5.2}$$

If V mL of sodium thiosulfate is consumed for the titration, the average oxidation state of cobalt ions can be determined by the following equations:

The molecular weight of the sample is given by:

$$M\left(SrCo_{1-x}Ta_xO_{3-\delta}\right) = M\left(Sr\right) + \left(1-x\right)M\left(Co\right) + xM\left(Ta\right) + \left(3-\delta\right)M\left(O\right) \tag{5.3}$$

δ can be determined according to charge neutrality:

$$2\left(3-\delta\right) = 2 + \left(1-x\right)Z + 5x \tag{5.4}$$

$$\delta = 2 - 2.5x - 0.5\left(1-x\right)Z \tag{5.5}$$

Therefore, the molecular weight and the oxygen vacancies of the sample are only a function of Z. Z can be determined by equation provided below:

$$\frac{m}{M\left(SrCo_{1-x}Ta_xO_{3-\delta}\right)\left(1-x\right)\left(Z-2\right)} = CV \tag{5.6}$$

In the Eq.4, the only variable unknown is the value of Z (oxidation state of Co), and therefore Z can be calculated using this equation. Once the value of Z is determined, the oxygen vacancy content can be obtained using Eq. 3. So it can be seen that the equations will not only help determine the oxygen vacancy content of the sample, but also the average oxidation states of Co^{Z+} ions in the sample.

The titration experimental procedures are as described as follows:

First of all, 0.1 M sodium thiosulfate solution was prepared by weighing and dissolving $Na_2S_2O_3$ (≥99.99%, Sigma-Aldrich) in the boiled deionized water, which is followed by adding small amount of sodium carbonate to help keep the pH of the solution above 7 and therefore slow down thiosulfate decomposition. Subsequently, the solution was standardized against potassium iodate, and the standardization process was repeated over three times, and the concentration of prepared sodium thiosulfate is about 0.0999 M. The following step is to use the freshly prepared sodium thiosulfate solution, which has been standardized, for the titration of SCT5-40 samples. Every sample (~0.1 g) was exactly weighed and dissolved in 1 M HCl solution (100mL) containing an excess of KI (over 2g). As a result, the Co^{3+} and Co^{4+} will be reduced to Co^{2+} by I^-, and iodine was formed. Meanwhile, small amount of white substances will be precipitated from the solution because Ta_2O_5 cannot be dissolved into HCl solution. However, these precipitates are found insignificantly interfere the identification of titration end point because of their small content and white colour. The formed iodine was titrated by the prepared thiosulfate solution, using starch solution (1%) as the indicator. About 5mL of starch solution was added just before the end point. The end-point was detected visually as the blue colour disappeared and the solution turned to a pink colour. In order to prevent oxidation of the reductant by dissolved oxygen, the solvent of HCl solution was freed from dissolved solution by boiling the deionized water for several hours. The titration was carried out in an air-tight cell and repeated at least 3 times and the final oxygen content and the oxidation states of cobalt were the average of the test results.

Thermogravimetric (TG) was responsible for monitoring the oxygen vacancies changes of powderous specimens in a function of temperature in flowing air with a flow rate of 20ml/min. The powderous samples were first treated by pelletizing at high pressure in order to ensure similar grain sizes of the specimen. The samples were first held at 100°C for 2 hours to remove the moisture inside the samples, and then gradually heated up to 850°C. It can be easily observed from the TGA results that there is nearly no change of weight of all the samples at temperatures below 200ºC. Therefore, it is reasonable to assume that the oxygen vacancy level at room temperature, which is estimated using titration method, remains nearly the same at 100ºC. When the temperature is over 200ºC, the decreasing weight is a result of oxygen coming out from the lattice. Therefore, the corresponding oxygen vacancy at different temperature can be estimated using the following equation according to mole balance:

$$n(sample) = \frac{m_0}{M_0} = \frac{m_T}{M_0 - (\delta_T - \delta_0)M(O)} \tag{5.7}$$

Where n(sample), m_0, M_0 and δ_0 are the moles of sample, the initial mass, molecular weight and oxygen vacancy content as determined using titration respectively, and m_T and δ_T are the mass and oxygen vacancy content at T temperature respectively, and m_T is the mass monitored by TG. It can be seen from the equation that δ_T is the only variable unknown, so the δ_T can thereby be easily calculated.

The oxidation states can be obtained using the following equation derived from Eq.2 according to charge neutrality:

$$Z = \frac{4 - 2\delta - 5x}{1 - x} \tag{5.8}$$

The electrochemical impedance spectroscopy (EIS) was performed to test the activities of the specimen towards ORR in a configuration of symmetrical cells. The Autolab PGSTAT30 is responsible for the EIS test, and the flow rate of the air that the symmetrical cells are exposed to during the test is around 200mL/min. The symmetrical cells were fabricated by spraying the ink of cathode materials onto both sides of the dense $Sm_{0.2}Ce0_{.8}O_{1.9}$ (SDC) electrolyte disks on the hot plate.

The ink of the cathode material was prepared by well suspending the targeted cathode material in isopropyl alcohol. Subsequently, the sprayed symmetrical cells were calcined at 1000°C for 2 hours under an air atmosphere. Silver paste was used as current collector.

X-ray Diffractometer (XRD) was used to characterize the crystallite structures of the targeted materials. Le Bail refinement was used to determine the space group and lattice parameters of the SCT5-SCT40 using DIFFRACplus Topas 4.2 software. During the refinements, general parameters, such as the scale factor, background parameters, and the zero point of the counter, were optimized. The microstructures of the cathodes were studied by scanning electron microscopy (SEM).

5.3 Results and discussion

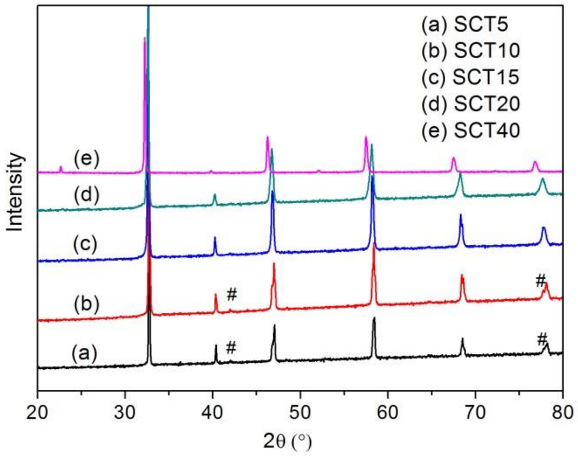

Figure 5-1 X-ray diffraction (XRD) patterns for SCT5-40 at room temperature. The small peaks indexed by # are peaks indicating the tetragonal phase.

The XRD patterns at room temperature as shown in Figure 5-1 suggest that the stabilization of a 3C perovskite phases is achieved in the SCTx system with substitution levels higher than 10 % mol, but SCT5 and SCT10 exhibit tetragonal structures belonging to P4/mmm space group. Similar crystal structure changes of SC were also reported with different B-site dopant concentrations, such as Mo^{4+} and Sb^{5+}: SC possessing low contents of Mo^{6+} or Sb^{5+} are in a tetragonal P4/mmm space group, but higher concentration of dopants leads to a cubic perovskite phase of SC at room temperature. [22, 33] Nagai *et al*[34] studied the effects of different dopants on the stability of SC-based perovskite structure, and pointed out that the structure stability can be improved by doping B-site cations with high valence states because higher valence state not only increases the electrostatic repulsion among B-site cations, but also suppress too much oxygen loss from the lattice.[34] Therefore, the stabilization of SC's structure is also likely to be ascribed to the high valence state of the substituted Ta (+5).

Table 5-1 Crystal structural constants of SCTx materials derived from refining XRD patterns at room temperature.

	a (Å)	b (Å)	c (Å)
SCT5	3.8657	3.8657	7.7652
SCT10	3.8711	3.8711	7.7779
SCT15	3.8856	3.8856	3.8856
SCT20	3.8927	3.8927	3.8927
SCT40	3.9231	3.9231	3.9231

Moreover, the substitution of Ta^{5+} is also found to affect the sizes of the unit cells of SC. Table 5-1 shows lattice constants of the SCTx, which were calculated by refining the XRD results at room temperature by using Le Bail method. We observed that the unit cell expands with the concentration of Ta^{5+}, which is also reflected by the shifts of all Bragg peaks of SC with more Ta^{5+} substituted to lower values of diffraction angle. This can be explained by the larger ionic radii of Ta^{5+} as compared to most cobalt ions in the oxides[35].

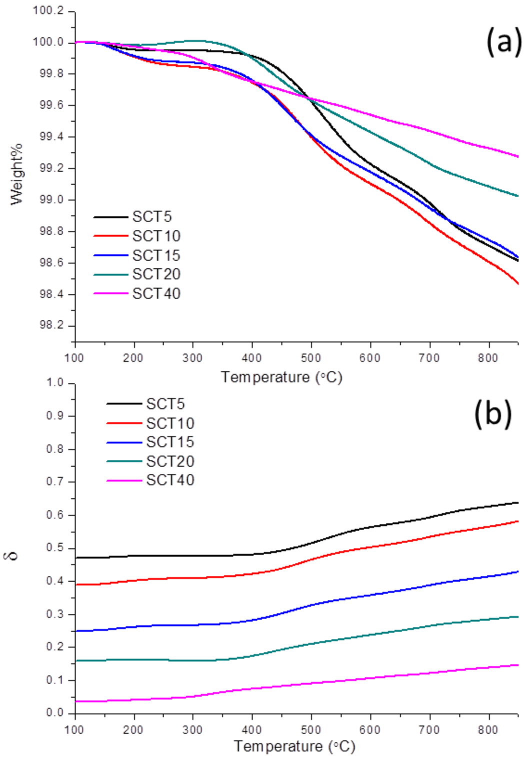

Figure 5-2 Changes of (a) weight percentages and (b) the oxygen vacancies (δ) of SCTx materials at different temperatures.

As aforementioned, high mixed conductivities of the materials is one of the requirements for the good potential cathodes of LT-SOFC. It is widely accepted that the ionic conduction in the perovskite occurs via vacancy mechanism. In general, the more disordered oxygen vacancies are, the higher the ionic conductivity will be. Hence, the Thermogravimetric Analysis was utilized to estimate the concentrations of the oxygen vacancies (oxygen non-stoichiometry δ) against temperature by measuring the weight changes of the specimens in flowing air. The initial oxygen vacancy concentrations of the samples at room temperature were obtained through iodometric titration method: the δs of SCT5-SCT40 are approximately 0.47, 0.39, 0.25, 0.16 and 0.04 respectively. It is noted that there is nearly no change of weight for SCT5-40 at temperature lower than 200 °C, indicating that there is negligible amount of oxygen released from the sample below 200 °C. Therefore, it is reasonable to assume that the oxygen vacancy content estimated at room temperature using iodometric titration can be used as the initial levels oxygen vacancy at 100 °C. At temperature over 200 °C, the oxygen vacancy concentration of the sample is obtained according to (5.5) provided in the experiment part. The results are presented in Figure 5-2(a) and (b). It is observed that more oxygen vacancies are formed at rising temperature because of its more reducing atmosphere, and the level of oxygen vacancies decreases with increasing doping concentrations of Ta^{5+}, illustrating that the incorporation of Ta^{5+} crimps the oxygen vacancy level in SC oxide. This can be explained by the high fixed oxidation state of Ta^{5+}, which increases the overall charges of the cations, and thus more oxygen ions are required to compensate the charge balance.

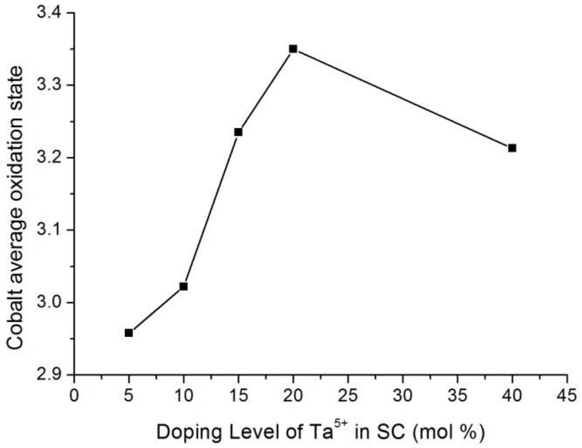

Figure 5-3 Estimated average oxidation states of cobalt ions in SCTx materials at room temperature against substituting concentrations of Ta^{5+} using iodometric titration method.

The effects of the tantalum dopants on cobalt cations were also investigated at room temperature. The average oxidation states of the cobalt in the oxides were also estimated through the same iodometric titration procedure. The average oxidation states of Co ions in SCT5-40 are estimated to be 2.96, 3.02, 3.24, 3.35 and 3.21 separately at room temperature. The results were shown in Figure 5-3. It is found that the average oxidation states of the cobalt ions increase with the incorporating levels of Ta^{5+} below 20% mol, while it drops to +3.21 for SCT40, which is even lower than that of SCT15. There are two main factors that affect the oxidation states of cobalt ions: one is the tendency to maintain their crystallite structures, and the other is the overall charge balance. For the low doping levels of Ta^{5+} (≤ 20% mol), the cobalt ions need to expand their size (lower down the oxidation state) to maintain their present structures: the lower concentration of Ta^{5+} is, the larger size of the cobalt will become. However, when the amount of dopants with larger ionic radii is enough to support the perovskite crystallite structure, the charge balance factor will dominate: the cobalt ions have to reduce its valence to ensure the overall charge balanced.

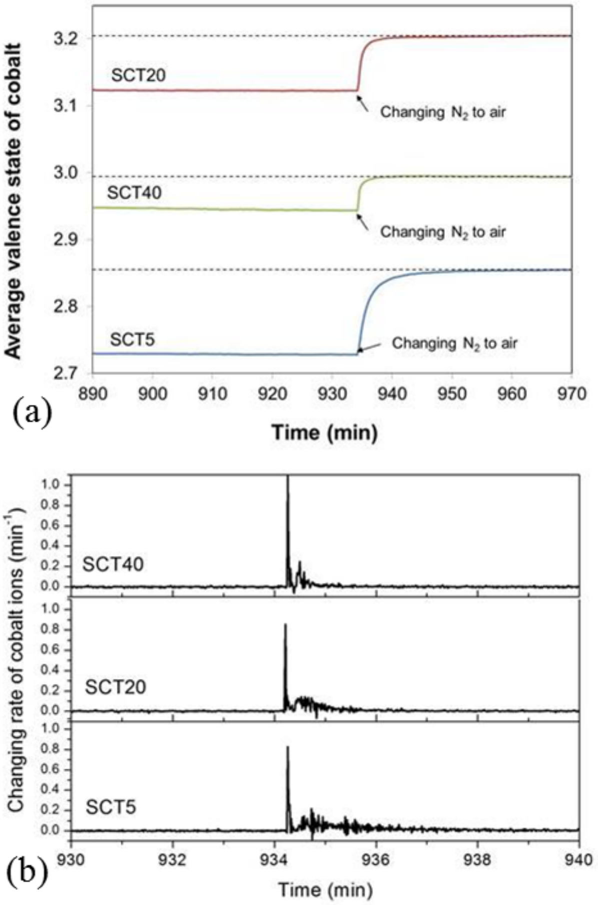

Figure 5-4 Changes of Co oxidation states of SCT5, SCT20 and SCT40 against time at 500°C in response of gas switch from N_2 to air. (b) The changing rates of the cobalt oxidation states, which are derived from results shown in (a).

In order to further investigate the effects of the dopants on the oxidations states of cobalt, we monitored the weight change of the specimen after quickly switching the flowing nitrogen to air at 500 °C. Figure 5-4a shows the changes of the oxidation states of cobalt ions, which are determined from the change of samples' weight. The weight change of the sample is a result of loss or intake of oxygen because of different oxygen partial pressures in the ambient atmosphere. Hence the oxygen vacancy content can be easily calculated from the weight change as compared to the weight of the original sample, and the initial levels of oxygen vacancies determined via iodometric titrations (5.5). Because there is a relationship existing between oxygen vacancy concentration and the oxidation states of Co ions as provided by the 5.6 in the experimental part, we can finally be capable of convert the weight change into the average oxidation states of the Co ions using 5.6. As shown in Figure 4a, the cobalt ions begin to be oxidized with time after the change of ambient atmosphere due to the rise of partial pressure of the oxygen. However, it is worth noting that the SC doped with more Ta^{5+} are faster to reach equilibrium in comparison to analogues with lower levels of Ta^{5+}. The changing rates as provided in Figure 5-4b also clearly show that the cobalt cations in SCT40 are the fastest to respond to the sudden change of oxygen partial pressure, and it takes the longest time (over 2 min) for the states of cobalt ions in SCT5 to become stable. The high changing rate of the materials is likely to be related to the fast oxygen exchange process. Therefore, it is concluded that incorporation of Ta^{5+} makes it faster for cobalt ions to change their states in response to oxygen level changes, and thus probably improve the kinetics of the oxygen surface exchange.

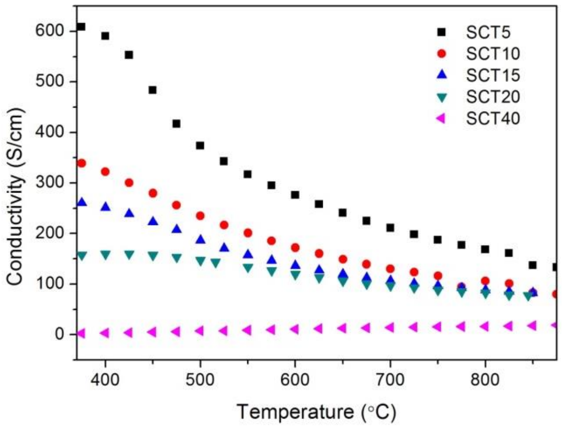

Figure 5-5 Electrical conductivities of SCT5-SCT40 specimen along temperatures studied by four-probe method.

Figure 5-5 presents the electrical conductivity of SCTx system at different temperatures. The electrical conductivity decreases with temperature for SCT5-SCT20, following a typical metallic behaviour at temperature higher than 400 °C. The SCT40 sample, however, shows semiconductor behaviour: the electrical conductivity becomes higher at higher temperature. In addition, it has been reported that the electrical conductivity of the un-doped SC is around 5-20 S/cm at temperature lower than 800 °C and ~200 S/cm at temperature above 800 °C.[36] In comparison to SC, small amounts of Ta^{5+} dopants have benign effects on the electrical conductivity, especially for SCT5, whose electrical conductivity reaches up to about 590 S/cm at 400 °C. The enhancement of the electrical conductivity can be explained by the increased concentration charge carriers provided by the dopants and the stabilised structure with high symmetry. Other researchers also reported the similar improvement of electrical conductivities of SC doped with low contents of cations with high oxidation states, such as

Sb[22], Ti[37], P[21], Nb[26] and Mo. This is probably due to their P4/mmm structures, which was also reported by Zhu. *et al*[38].

Moreover, it is worthy to be mentioned that the electrical conductivities of SCTx system drop with increasing Ta contents, indicating that more doped Ta^{5+} will reduce the electrical conductivities. The deterioration of the electrical conductivities with higher Ta doping level is probably because of the inhibition of the electrons hopping along the (Co, Ta)-O-(Co, Ta) bonds and the reduced concentration of the hopping sites (lower concentrations of cobalt cations). Similar phenomena were also observed for SC doped with Sb[33] and Mo[23].

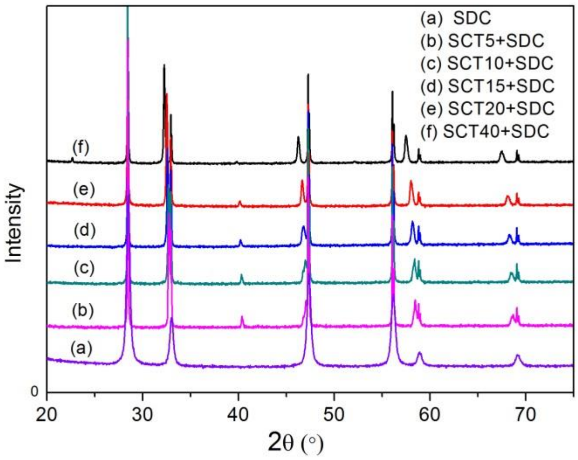

Figure 5-6 The XRD results of SCT5-40 powders well mixed with SDC electrolyte materials pre-treated at 1000°C for 2 hours.

We also checked the compatibility of the SCT5-SCT40 with electrolyte SDC by mixing the powderous SDC with the targeted specimen (1:1 wt%) followed by sintering at 1000 °C for 2 h in the stagnant air. The XRD was used to determine their crystallite structures. It is shown from Figure 5-6. that there are no extra peaks observed for the mixed powders, which implies that there are negligible chemical interactions between the SCT5-SCT40 cathode materials and SDC at 1000 ºC, which is the fabrication temperature for the symmetrical cells.

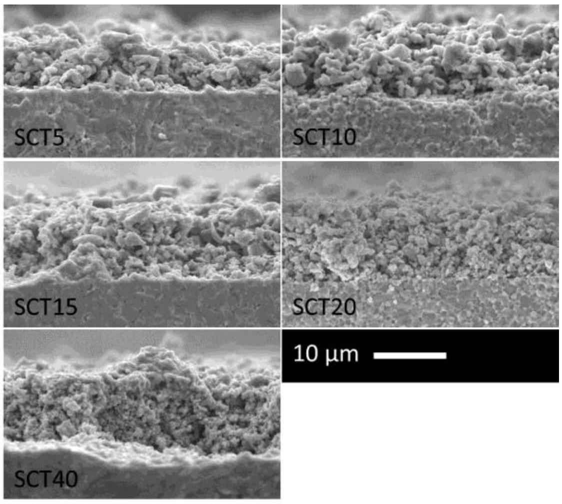

Figure 5-7 Scanning electron micrograph of cross sections of SCT5-SCT40 cathodes.

SEM images as presented in Figure 5-7 show that the porous cathodes of the all the samples are well attached to the surface of the SDC surface. Therefore, it is demonstrated that all the tantalum doped SC cathode materials all adhere well to the electrolyte. In addition, it is found from the SEM images that the particles of the samples with more Ta^{5+} are smaller than those with lower levels of tantalum, which will be beneficial to the ORR performance. Notably, similar thicknesses of the cathodes are achieved by controlling the fabrication processes.

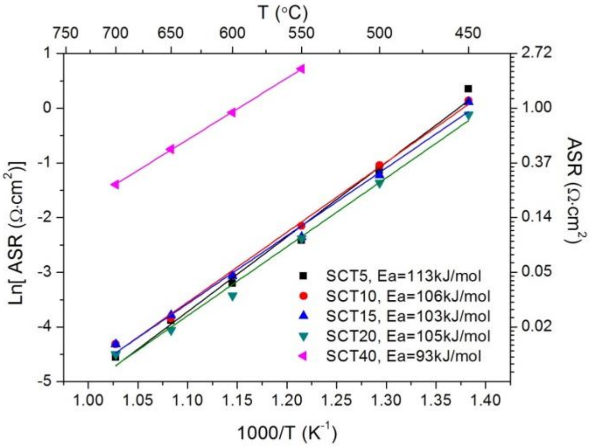

Figure 5-8 The ASR values of SCT5-SCT40 cathodes against temperature from 450°C to 700°C as determined by EIS in a configuration of cathode |SDC |cathode symmetrical cells under open circuit conditions.

EIS was used to study the ORR activity of the samples. Area specific resistance (ASR) was the parameter to describe the performance of SOFC cathodes: the lower is the value of the ASR, the more active the cathode will be over ORR. Figure 5-8 shows the ASR values of as-prepared cathodes as a function of temperature. We observed that the SCTx with low concentrations of Ta^{5+} exhibit similar outstanding cathode performance, which can be even comparable to some benchmark cathode materials, such as $Ba_{0.5}Sr_{0.5}Co_{0.8}Fe_{0.2}O_{3-\delta}$[12] and $PrBaCo_2O_{5+\delta}$[39]. For example, the SCT5 cathode reaches an ASR as low as 0.11-0.089 $\Omega\cdot cm^2$ at 550ºC, showing a quite similar ORR activity to the other Ta^{5+}-doped analogues. The very low ASR values of SCTx with low concentrations of Ta^{5+} are mainly attributed to their more oxygen vacancies and stabilized perovskite structures. Moreover, the cathodes of SCTx with relative high contents of Ta^{5+} ($\leq$ 20% mol) show slightly better performance compared to the ones with lower levels of Ta^{5+}, which can be explained by the smaller grain sizes of SC with more Ta^{5+} as shown in Figure 5-7 and the faster kinetics of oxygen surface exchange as determined by TGA results.

The SCT40, however, shows much higher ASR values in comparison to other tantalum analogues. The sluggish performance of SCT40 cathode can be ascribed to its significantly lower electrical conductivity and less oxygen vacancies for ionic conductions than others as proved, even though the particle sizes of SCT40 are much smaller than others as shown in the SEM images.

We also noted that the activation energies of the cathodes become smaller with increasing amount of Ta^{5+}, and the activation energy of SCT40 is as low as around 93 kJ/mol. The results indicate that the incorporation of Ta^{5+} can reduce the activation energy for oxygen reduction

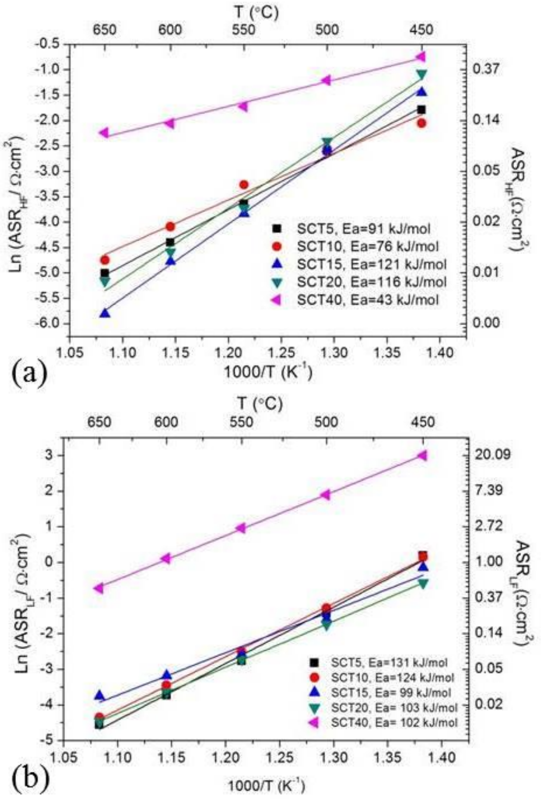

Figure 5-9 SCT5-SCT40 cathode ASR values of two processes at high frequencies (HF) presented in (a), and low frequencies (LF) shown in (b), which are obtained by fitting the cathode impedances from EIS to two-process equivalent circuits.

The impedance spectra of the SCTx cathodes were also fitted to the equivalent circuits including two dominant processes (Figure S 5-1): one is the process related to the charge transfer to the absorbed oxygen species, and the other corresponds to the process where atomic oxygen gets involved.[40] The observed impedance arcs of the cathodes consist of two main arcs, and the arc at high frequencies corresponds to the former process and the one at low frequencies represents the latter one. The ASR values for the two processes along the SCTx system are shown in Figure 5-9. It is observed that SCT5-SCT20 exhibit relatively low resistances, but SCT40 show much higher resistances than others on both processes. The poor activity of SCT40 is due to its relatively small concentrations of oxygen vacancies in the lattice and very low conductivities. Moreover, the Ta itself is inert for oxygen surface exchange processes, so it can be concluded that it is the tantalum that improve the redox ability of cobalt and therefore enhance their ORR activities.

The activation energies of all the cathodes were also calculated for the two processes. It is found that the SCT cathodes doped with higher contents of Ta (15-20% mol but not including 40%) generally show higher activation energies than those with less Ta (5-10% mol) for the process corresponding to charge transfer. However, lower activation energies, in terms of the process at low frequencies, are noted for SCT cathodes with high contents of Ta (15-40% mol). Providing much higher resistances are noted at low frequencies, the dominant step for ORR is the process getting atomic oxygen involved on the surface. Therefore, we believe that the incorporation of tantalum improves the ORR activity through enhancing the kinetics of the process where atomic oxygen is involved at lower temperatures.

It is also interesting to note that the SCT40 shows very low activation energies for both processes, which is likely to be a result of its fast oxygen surface exchange as determined by the aforementioned TGA results. It suggests that SCT40 could be a good decorator material for ORR. The related experiment is ongoing in our group.

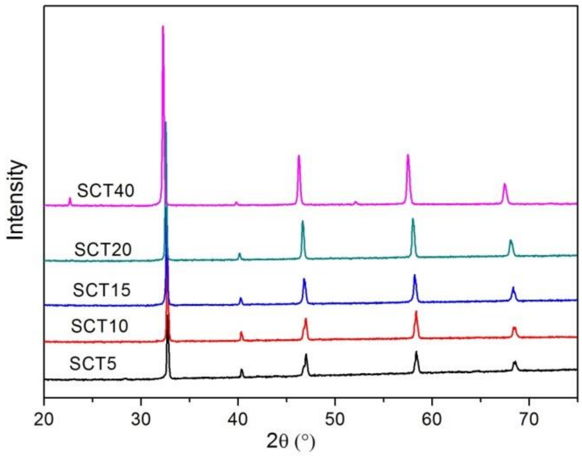

Figure 5-10 XRD results of SCT5-40 powders after treatment at 600°C for 45 hours, followed by cooling down to room temperature.

The crystallite structure stabilities of the SCTx were studied by treating the cathode powders at 600 ºC under stagnant air for 45 h, and then cooled down in air. The crystallite structures of these pre-treated cathode materials were characterized by XRD. It is observed from Figure 5-10 that SCT5-SCT40 still preserves their structures after 45-hour annealing at 600 °C. Thus it is demonstrated that the incorporation of Ta^{5+} can stabilize the structure of the SC after staying at 600 °C for 45 h.

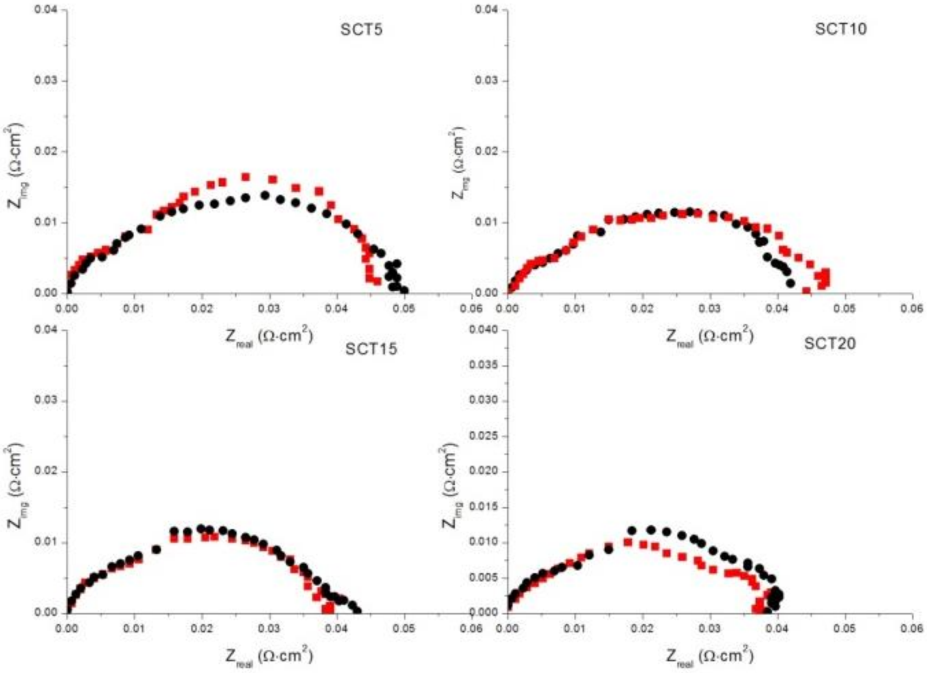

Figure 5-11 The impedances of SCT5-SCT20 cathodes of symmetrical cells before and after sintering at 600°C for 45 hours under open circuit conditions.

Further stability test was carried out by keeping the symmetrical cells at 600ºC for 45 h and measuring the ORR performance of the SCT5-SCT20 cathodes. The results are shown in Figure 5-11. We observed that there is nearly no performance change for SCT5-SCT20 cathodes. As discussed, the substitutions of Ta^{5+} help stabilize the crystallite structure of SC, and therefore improve the stabilities of SCT10-SCT20 cathodes.

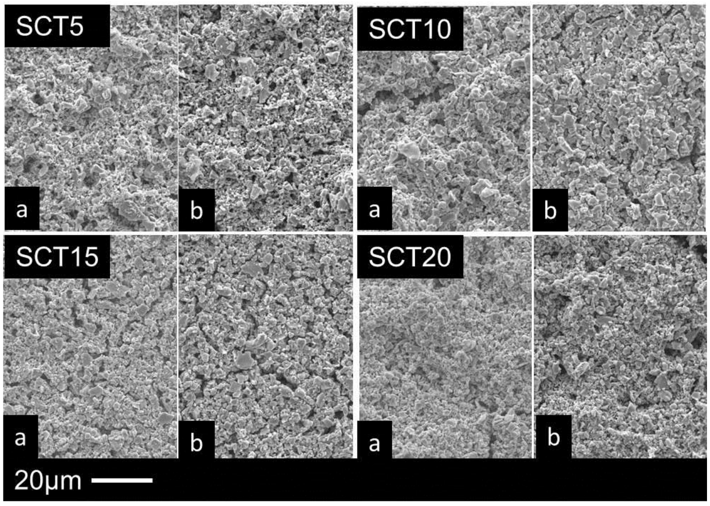

Figure 5-12 Topographies of SCT5-SCT20 cathodes before (a) and after (b) heating at 600°C for 45 h.

Furthermore, the particle coarsening was also checked by characterizing the topographies of the cathodes after annealing at 600 ºC for 40 h. The SEM images of the topographies of the cathodes are shown in Figure 5-12. There is nearly no change in the particle sizes of the cathodes of all the samples. Therefore, the crystallite phase deformation of SCT5 mainly contributes to the degradation of the cathode performance during the heat treatment.

5.4 Conclusions

To sum up, a series of Ta^{5+} doped SC with different contents (5%-40% mol) were prepared and evaluated as cathodes of SOFCs. Firstly, the incorporations of Ta^{5+} into SC oxides with slightly high contents (15-40% mol) are demonstrated to stabilize the cubic perovskite structure of SC at room temperature, and a tetragonal structure is observed for doped SC with less Ta^{5+} (5-10% mol). Secondly, the substitution of Ta^{5+} into SC reduces the concentrations of oxygen vacancies in the lattice, and high level of Ta (> 5mol %) deteriorates the electrical conductivities. Thirdly, the oxidation states of cobalt ions in SC doped with more Ta^{5+} are easier to change in response to a sudden change of oxygen partial pressure in ambient atmosphere, reflecting faster oxygen surface exchanges. Fourthly, SCT5-SCT20 cathodes exhibit similar high ORR activities at low temperatures because of their high mixed conductivities and enhanced kinetics of process where atomic oxygen is involved at the surface, but SCT40 cathode is far more sluggish than the rest of analogues due to its low conductivities. Finally, the tantalum doped SC shows high crystallite structural stability at elevated temperatures, and therefore no ORR performance degradation is observed for SCT5-SCT20 cathodes for at least 45 h.

Acknowledgement

The authors appreciate the technical support from Centre for Microscopy and Microanalysis at the University of Queensland.

This work is financially supported by Australian Research Council (DP130102151) and author Mengran Li acknowledges additional financial support from the top-up assistance program (TUAP) scholarship and the scholarship from China Scholarship Council.

5.5 Supplementary Information

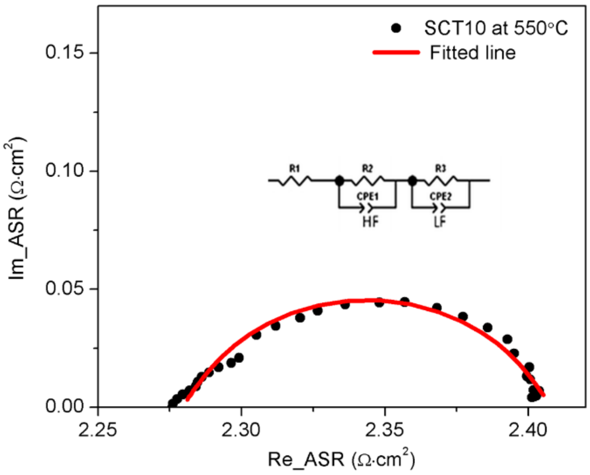

Figure S 5-1 The impedance pattern of SCT10 cathode at 550 °C in flowing air and the fitted pattern using an equivalent circuit model with two dominant processes.

5.6 References

1. Wachsman, E. D.; Lee, K. T., Lowering the Temperature of Solid Oxide Fuel Cells. *Science* **2011,** 334, (6058), 935-939.

2. Park, S.; Vohs, J. M.; Gorte, R. J., Direct Oxidation of Hydrocarbons in a Solid-oxide Fuel Cell. *Nature* **2000,** 404, (6775), 265-267.

3. Zhou, W.; Ran, R.; Shao, Z., Progress in understanding and development of Ba0.5Sr0.5Co0.8Fe0.2O3−δ-based cathodes for intermediate-temperature solid-oxide fuel cells: A review. *Journal of Power Sources* **2009,** 192, (2), 231-246.

4. Steele, B. C. H., Material Science and Engineering: The Enabling Technology for the Commercialisation of Fuel Cell Systems. *Journal of Materials Science* **2001,** 36, (5), 1053-1068.

5. Jacobson, A. J., Materials for Solid Oxide Fuel Cells. *Chemistry of Materials* **2009,** 22, (3), 660-674.

6. Adler, S. B., Factors Governing Oxygen Reduction in Solid Oxide Fuel Cell Cathodes†. *Chemical Reviews* **2004,** 104, (10), 4791-4844.

7. Lee, J. G.; Park, J. H.; Shul, Y. G., Tailoring gadolinium-doped ceria-based solid oxide fuel cells to achieve 2 W cm−2 at 550 °C. *Nat Commun* **2014,** 5.

8. Ding, H.; Xue, X., An Interfacial Nanospike-Structured Cathode for Low Temperature Solid Oxide Fuel Cells. *Advanced Materials Interfaces* **2014**, n/a-n/a.

9. Zhu, Y.; Chen, Z.-G.; Zhou, W.; Jiang, S.; Zou, J.; Shao, Z., An A-Site-Deficient Perovskite Offers High Activity and Stability for Low-Temperature Solid-Oxide Fuel Cells. *ChemSusChem* **2013,** 6, (12), 2249-2254.

10. Zhu, Y.; Sunarso, J.; Zhou, W.; Jiang, S.; Shao, Z., High-performance $SrNb_{0.1}Co_{0.9-x}Fe_xO_{3-\delta}$ Perovskite Cathodes for Low-temperature Solid Oxide Fuel Cells. *Journal of Materials Chemistry A* **2014,** 2, (37), 15454-15462.

11. Liang, F.; Zhou, W.; Zhu, Z., A Highly Stable and Active Hybrid Cathode for Low-Temperature Solid Oxide Fuel Cells. *ChemElectroChem* **2014,** 1, (10), 1627-1631.

12. Shao, Z.; Haile, S. M., A High-Performance Cathode for the Next Generation of Solid-Oxide Fuel Cells. *Nature* **2004,** 431, (7005), 170-173.

13. Zhou, W.; Sunarso, J.; Zhao, M.; Liang, F.; Klande, T.; Feldhoff, A., A Highly Active Perovskite Electrode for the Oxygen Reduction Reaction Below 600 °C. *Angewandte Chemie International Edition* **2013,** 52, (52), 14036-14040.

14. Lee, K. T.; Lidie, A. A.; Yoon, H. S.; Wachsman, E. D., Rational Design of Lower-Temperature Solid Oxide Fuel Cell Cathodes Via Nanotailoring of Co-Assembled Composite Structures. *Angewandte Chemie International Edition* **2014,** 53, (49), 13463-13467.

15. Sammells, A. F.; Cook, R. L.; White, J. H.; Osborne, J. J.; MacDuff, R. C., Rational Selection of Advanced Solid Electrolytes for Intermediate Temperature Fuel Cells. *Solid State Ionics* **1992,** 52, (1), 111-123.

16. Kharton, V.; Yaremchenko, A.; Kovalevsky, A.; Viskup, A.; Naumovich, E.; Kerko, P., Perovskite-type Oxides for High-temperature Oxygen Separation Membranes. *Journal of Membrane Science* **1999,** 163, (2), 307-317.

17. Deng, Z.; Yang, W.; Liu, W.; Chen, C., Relationship between Transport Properties and Phase Transformations in Mixed-conducting Oxides. *Journal of Solid State Chemistry* **2006,** 179, (2), 362-369.

18. Rodriguez, J.; Gonzalez-Calbet, J., Rhombohedral $Sr_2Co_2O_5$: A New $A_2M_2O_5$ Phase. *Materials research bulletin* **1986,** 21, (4), 429-439.

19. Rodriguez, J.; Gonzalez-Calbet, J.; Grenier, J.; Pannetier, J.; Anne, M., Phase Transitions in $Sr_2Co_2O_5$: A Neutron Thermodiffractometry Study. *Solid state communications* **1987,** 62, (4), 231-234.

20. Jeen, H.; Choi, W. S.; Biegalski, M. D.; Folkman, C. M.; Tung, I. C.; Fong, D. D.; Freeland, J. W.; Shin, D.; Ohta, H.; Chisholm, M. F.; Lee, H. N., Reversible Redox Reactions in An Epitaxially Stabilized $SrCoO_x$ Oxygen Sponge. *Nat Mater* **2013,** 12, (11), 1057-1063.

21. Li, M.; Zhou, W.; Xu, X.; Zhu, Z., $SrCo_{0.85}Fe_{0.1}P_{0.05}O_{3-\delta}$ Perovskite as a Cathode for Intermediate-Temperature Solid Oxide Fuel Cells. *Journal of Materials Chemistry A* **2013,** 1, (43), 13632-13639.

22. Aguadero, A.; Alonso, J. A.; Pérez-Coll, D.; de la Calle, C.; Fernández-Díaz, M. a. T.; Goodenough, J. B., SrCo0. 95Sb0. 05O3− δ as Cathode Material for High Power Density Solid Oxide Fuel Cells†. *Chemistry of Materials* **2009,** 22, (3), 789-798.

23. Aguadero, A.; Pérez-Coll, D.; Alonso, J. A.; Skinner, S. J.; Kilner, J., A New Family of Mo-Doped $SrCoO_{3-\delta}$ Perovskites for Application in Reversible Solid State Electrochemical Cells. *Chemistry of Materials* **2012,** 24, (14), 2655-2663.

24. Hancock, C. A.; Slade, R. C. T.; Varcoe, J. R.; Slater, P. R., Synthesis, Structure and Conductivity of Sulfate and Phosphate Doped $SrCoO_3$. *Journal of Solid State Chemistry* **2011,** 184, (11), 2972-2977.

25. Zhou, Q.; Wei, T.; Shi, Y.; Guo, S.; Li, Y.; Su, J.; Ren, H.; Zhu, Y., Evaluation and Optimization of $SrCo_{0.9}Ta_{0.1}O_{3-\delta}$ Perovskite as Cathode for Solid Oxide Fuel Cells. *Current Applied Physics* **2012,** 12, (4), 1092-1095.

26. Zhou, W.; Jin, W. Q.; Zhu, Z. H.; Shao, Z. P., Structural, Electrical and Electrochemical Characterizations of $SrNb_{0.1}Co_{0.9}O_{3-\delta}$ as a Cathode of Solid Oxide Fuel Cells Operating Below 600°C *International Journal of Hydrogen Energy* **2010,** 35, (3), 1356-1366.

27. Huang, S.; Wang, G.; Sun, X.; Lei, C.; Li, T.; Wang, C., Cobalt-free Perovskite $Ba_{0.5}Sr_{0.5}Fe_{0.9}Nb_{0.1}O_{3-\delta}$ as A Cathode Material for Intermediate Temperature Solid Oxide Fuel Cells. *Journal of Alloys and Compounds* **2012,** 543, (0), 26-30.

28. Chen, X.; Jiang, S. P., Highly Active and Stable $(La_{0.24}Sr_{0.16}Ba_{0.6})(Co_{0.5}Fe_{0.44}Nb_{0.06})O_{3-\delta}$ (LSBCFN) Cathodes for Solid Oxide Fuel Cells Prepared by A Novel Mixing Synthesis Method. *Journal of Materials Chemistry A* **2013,** 1, (15), 4871-4878.

29. Yoo, S.; Kim, J.; Song, S. Y.; Lee, D. W.; Shin, J.; Ok, K. M.; Kim, G., Structural, Electrical and Electrochemical Characteristics of $La_{0.1}Sr_{0.9}Co_{1-x}Nb_xO_{3-\delta}$ as A Cathode Material for Intermediate Temperature Solid Oxide Fuel Cells. *RSC Advances* **2014,** 4, (36), 18710-18717.

30. Deng, Z.; Smit, J.; Niu, H.; Evans, G.; Li, M.; Xu, Z.; Claridge, J.; Rosseinsky, M., B-Cation Ordered Double Perovskite $Ba_2CoMo_{0.5}Nb_{0.5}O_{6-\delta}$ as A Potential SOFC Cathode. *Chemistry of Materials* **2009,** 21, (21), 5154-5162.

31. Chen, X.; Huang, L.; Wei, Y.; Wang, H., Tantalum Stabilized $SrCoO_{3-\delta}$ Perovskite Membrane for Oxygen Separation. *Journal of Membrane Science* **2011,** 368, (1–2), 159-164.

32. Karppinen, M.; Matvejeff, M.; Salomaki, K.; Yamauchi, H., Oxygen content analysis of functional perovskite-derived cobalt oxides. *Journal of Materials Chemistry* **2002,** 12, (6), 1761-1764.

33. Aguadero, A.; Perez-Coll, D.; De la Calle, C.; Alonso, J.; Escudero, M.; Daza, L., $SrCo_{1-x}Sb_xO_{3-\delta}$ Perovskite Oxides as Cathode Materials in Solid Oxide Fuel Cells. *Journal of Power Sources* **2009,** 192, (1), 132-137.

34. Nagai, T.; Ito, W.; Sakon, T., Relationship between Cation Substitution and Stability of Perovskite Structure in $SrCoO_{3-\delta}$-Based Mixed Conductors. *Solid State Ionics* **2007,** 177, (39–40), 3433-3444.

35. Shannon, R.; Prewitt, C., Effective Ionic Radii and Crystal Chemistry. *Journal of Inorganic and Nuclear Chemistry* **1970,** 32, (5), 1427-1441.

36. De la Calle, C.; Aguadero, A.; Alonso, J.; Fernandez-Diaz, M., Correlation between Reconstructive Phase Transitions and Transport Properties from $SrCoO_{2.5}$ Brownmillerite: A Neutron Diffraction Study. *Solid State Sciences* **2008,** 10, (12), 1924-1935.

37. Shen, Y.; Wang, F.; Ma, X.; He, T., $SrCo_{1-y}Ti_yO_{3-\delta}$ as Potential Cathode Materials for Intermediate-Temperature Solid Oxide Fuel Cells. *Journal of Power Sources* **2011,** 196, (18), 7420-7425.

38. Zhu, Y.; Lin, Y.; Shen, X.; Sunarso, J.; Zhou, W.; Jiang, S.; Su, D.; Chen, F.; Shao, Z., Influence of Crystal Structure on the Electrochemical Performance of A-site-deficient $Sr_{1-s}Nb_{0.1}Co_{0.9}O_{3-\delta}$ Perovskite Cathodes. *RSC Advances* **2014,** 4, (77), 40865-40872.

39. Choi, S.; Yoo, S.; Kim, J.; Park, S.; Jun, A.; Sengodan, S.; Kim, J.; Shin, J.; Jeong, H. Y.; Choi, Y., Highly efficient and robust cathode materials for low-temperature solid oxide fuel cells: PrBa0. 5Sr0. 5Co2-xFexO5+ [dgr]. *Scientific reports* **2013,** 3.

40. Takeda, Y.; Kanno, R.; Noda, M.; Tomida, Y.; Yamamoto, O., Cathodic Polarization Phenomena of Perovskite Oxide Electrodes with Stabilized Zirconia. *Journal of the Electrochemical Society* **1987,** 134, (11), 2656-2661.

Chapter 6 Effect of non-geometry factors on ORR activity of Nb or Ta doped SC perovskite cathodes

Introduction

As discussed in Section 2.4.2, one of the challenges to study the effects of dopant on ORR is the complexity of oxygen reduction reaction that involves different factors such as crystal structure, lattice geometry and cation valence. Section 2.3 shows that lattice symmetry and structure is related to the ionic radii of cations, so similar structure and geometry can be achieved if the dopants have similar ionic radii and valence. Nb^{5+} and Ta^{5+} are such cations that are in the similar ionic radii and valence. As mentioned in the previous chapters, these two dopants can both stabilize the perovskite structure of $SrCoO_{3-\delta}$, and renders the doped cathodes more active on catalyzing oxygen reduction reaction at intermediate temperature. Accordingly, we developed $SrCoO_{3-\delta}$ doped with Nb and Ta separately, examined their lattice similarity, and studied the non-geometric effects of these dopants on oxygen reduction reaction.

Contribution

In this chapter, $SrCoO_{3-\delta}$ perovskite oxides doped with Nb and Ta separately were prepared and evaluated as cathode for IT-SOFC. Similar perovskite structure and lattice constants are confirmed for these two perovskite oxides. We observed that oxygen vacancy content is higher in Ta-doped oxides as compared to Nb-doped one due to the lower electronegativity of Ta. As a result, the ORR-related properties of Ta-doped cathode, such as surface exchange kinetics, oxygen diffusivity and cathode electroactivity, are both higher than those of the Nb-doped analogue. This is the first time to probe the enhancing mechanism of Ta by constraining the lattice geometric factors, and electronegativity is first demonstrated to be another factor affecting cathode performance of IT-SOFC. We published this work in the Journal of Material Chemistry A: Li, M.; Zhou, W.; Peterson, V. K.; Zhao, M.; Zhu, Z., A comparative study of $SrCo_{0.8}Nb_{0.2}O_{3-\delta}$ and $SrCo_{0.8}Ta_{0.2}O_{3-\delta}$ as low-temperature solid oxide fuel cell cathodes: effect of non-geometry factors on the oxygen reduction reaction. *Journal of Materials Chemistry A* **2015**, 3, 24064-24070.

A Comparative Study of $SrCo_{0.8}Nb_{0.2}O_{3-\delta}$ and $SrCo_{0.8}Ta_{0.2}O_{3-\delta}$ as Low-Temperature Solid Oxide Fuel Cell Cathodes: Effect of Non-Geometry Factors on the Oxygen Reduction Reaction

Mengran Li, Wei Zhou*, Vanessa K. Peterson, Mingwen Zhao and Zhonghua Zhu*

Abstract: The oxygen reduction reaction (ORR) activity of cathodes has to be improved to realize the low-temperature operation of solid-oxide fuel cells (SOFCs). Whilst geometric factors are conventionally accepted to influence the ORR activity of perovskite cathodes, other factors may also contribute and therefore need to be explored. Here, we substituted 20% niobium and tantalum which have similar ionic radii into strontium cobaltites to obtain the two perovskite oxides $SrCo_{0.8}Nb_{0.2}O_{3-\delta}$ (SCN20) and $SrCo_{0.8}Ta_{0.2}O_{3-\delta}$ (SCT20), respectively. Our study of the isostructural SCN20 and SCT20 allows geometric effects to be separated from other factors, and we observe better cathode performance of SCT20 cathode, which may be related to the lower electronegativity of Ta^{5+}, thus resulting in higher oxygen surface exchange kinetics and diffusivity as compared with Nb^{5+}.

6.1 Introduction

Solid-oxide fuel cells (SOFCs) are energy devices that convert various fuels into electricity with high efficiencies. Lowering the operating temperature of SOFCs is of importance and interest[1], because this facilitates the use of low-cost construction materials, accelerates start-up/shutdown procedures, and improves the long-term durability of the system.[2] However, the polarization losses of the SOFC electrodes, especially those arising from the slow kinetics of the oxygen reduction reaction (ORR) at the cathodes still remain as the major challenge for low temperature SOFC.[3-5]

It is widely accepted that the ORR occurs when oxygen is absorbed and diffuses towards the triple phase boundary (TPB), where the cathode (electronic conductor), electrolyte (ionic conductor), and gaseous phase meet, followed by charge gain and diffusion into the electrolyte.[6-8] Therefore, the oxygen surface-exchange coefficient (k) and oxygen bulk-diffusion coefficient (D) are regarded as key parameters affecting the ORR, with larger values promoting a faster ORR. The parameters k and D are enhanced by high mixed ionic and electronic conductivities (MIECs).[9] The mixed conductivities of a cathode will extend the active sites throughout the cathode surface, therefore enhancing the ORR.

Efforts have been devoted to develop cathode materials for low-temperature solid-oxide fuel cells (LT-SOFCs)[10-18], and perovskite oxides with high MIECs are regarded as one of the most promising candidates for catalyzing the ORR at low temperature.[19] It is well known that perovskite structures are stable to extensive compositional modification, with such strategy useful in tuning properties for target application.[20] Amongst the MIEC materials, perovskite-structure strontium cobaltites show high mixed conductivities[21], and are therefore of great interest for application as LT-SOFC cathodes. However, the perovskite phase of strontium cobaltite is unstable at the operating temperature of SOFCs.[22-24] Strategic doping with high valence-state cations such as P^{5+}, Nb^{5+} and Sb^{5+}, were found to be of benefit, i.e. stabilizing the perovskite structure at high temperature.[25-28]

Furthermore, researchers also explored the strategic design of next-generation LT-SOFC cathodes by examining approaches such as the use of the octahedral factor[29] or the Goldschmidt tolerance factor[30, 31] in an effort to predict perovskite structures with favourable electrochemical activities[9, 32]. For example, cathode performance is enhanced by disordered oxygen vacancies, increasing structural symmetry, critical radius[33] and lattice free volumes[32], as well as lowering metal-oxygen bonding energies. However, such factors may co-exist, and are usually affected by the crystal structural geometry. The determination of their independent contribution to cathode performance remains a challenge. To this end, geometric factors should be constrained in a study of other factors. It is well known that Nb^{5+} and Ta^{5+} share the same ionic radii (0.64 Å for both)[34, 35] and fixed high valence-states (5+) at high temperature in an oxidizing environment, but they are different in electronegativity. The Pauling electronegativity of Nb^{5+} (1.87) is larger than that of Ta^{5+} (1.8)[36, 37] Electronegativity is the tendency of an atom or group to attract electrons,[38] and is therefore expected to influence the electrochemical performance of SOFC cathodes.

Herein, we compared the properties of $SrCo_{0.8}Nb_{0.2}O_{3-\delta}$ (SCN20) and $SrCo_{0.8}Ta_{0.2}O_{3-\delta}$ (SCT20) including their crystal structures, conductivities, k and D values, as well as their ORR activities. The similar ionic radii of Nb and Ta are expected to promote similar geometry factors, enabling the contributions from non-geometry factors such as electronegativity on the ORR to be separated from that arising from geometrical factors.

6.2 Experimental

Phase-pure SCN20 and SCT20 powders were synthesized through solid-state methods. Stoichiometric mixtures of $SrCoO_3$ (≥ 99.9%, Aldrich), Co_3O_4((≥ 99.9%, ≤ 10μm, Aldrich), and Nb_2O_5 (≥ 99.9%, Aldrich) or Ta_2O_5 (≥ 99.9%, Aldrich) were ball-milled for 24 h, followed by pelletizing and sintering at 1200 °C for 20 h in stagnant air.

Thermogravimetric analysis (TGA) was performed to estimate the oxygen content of SCN20 and SCT20 at different temperatures by annealing powder samples from room temperature to 850 °C at 1 °C/min. The samples were pre-treated by pelletizing at the same pressure to ensure similar grain size and baking at 200 °C for 2 h to remove absorbed moisture. Weight changes of SCN20 and SCT20 were recorded when the flowing gas was changed from pure N_2 to air, and the samples were first heated at 460 °C (furnace temperature 500 °C) until the weight reach equilibrium in flowing pure N_2. The initial oxygen contents of samples were obtained from the Rietveld refinement results of NPD patterns, and double checked by the titration method as described in our previous work.[18] The oxidation state (Z) changes of Co were then estimated according to the change in oxygen non-stoichiometry (δ):

$$Z = \frac{3-2\delta}{0.8} \tag{6.1}$$

Symmetrical cells for impedance studies were fabricated by nitrogen-borne spraying the cathode powders, which were suspended in isopropyl alcohol, onto both sides of a $Sm_{0.2}Ce_{0.8}O_{1.9}$ (SDC) electrolyte disk, and then calcining at 1000 °C in stagnant air for 2 h. Silver mesh was used as current collectors of the symmetrical cells, which were attached to both sides of the cell using silver paste. The samples for electrical conductivity and electrical conductivity relaxation (ECR) tests were dense bars with dimension 0.65 cm x 0.2 cm x 0.1 cm. The cathode powder was ball milled at 400 rpm for 3 h, pelletized at 400 MPa, and then sintered at 1200 °C for 10 h. Both SCN20 and SCT20 have densities > 95% relative to their theoretical densities as confirmed by Archimedes method. The bars were well polished and attached with silver leads as electrodes using silver paste.

The anode-supported single cells were fabricated by co-pressing the anode and SDC electrolyte into pellets, and sintering at 1350 °C for 3 h. The anode material was prepared by ball milling commercial NiO, SDC, and Dextrin pore former in a weight ratio of 6:4:1, respectively, for 24 h in ethanol. The cathode material was sprayed onto the SDC electrolyte, followed by calcination at 1000 °C for 2 h.

The ORR performance of the target cathode materials was evaluated using electrochemical impedance spectroscopy (EIS) in a symmetrical-cell configuration. The mechanism of the ORR was analysed by using LEVM software. A four-probe dc method was used for electrical conductivity measurements. The surface-exchange coefficient (k) and oxygen bulk-chemical diffusivity (D) of the cathode materials were obtained using ECR performed by recording the changes of the electrical conductivity with time after a step change in the ambient atmosphere with O_2 from 0.21 to 0.0998 atm. The change of the electrical conductivities against time were fitted using ECRTOOL[39] to obtain k and D. A PGSTAT302 Autolab workstation was used for the electrochemical measurements including EIS, electrical conductivity, and ECR.

The crystal structures of the cathode materials were studied using X-ray powder diffraction (XRD) and neutron powder diffraction (NPD). X-ray photoelectron spectroscopy (XPS) was used to examine the binding energies of dopants in the sample at room temperature. High resolution NPD data were collected using ECHIDNA[40] at the ANSTO with a neutron wavelength of 1.6219(2) Å, determined using the La^{11}B$_6$ NIST standard reference material 660b. NPD data were collected from samples in a 6 mm vanadium can for 6 h over the angular range (2θ) 4 to 164°. GSAS-II[41] was employed to perform Rietveld analysis of the NPD data using a $Pm\bar{3}m$ cubic perovskite starting structure.[42] Scanning electron microscopy (SEM, Philips XL30) was also used to characterize the cathode microstructure.

The first-principles calculation were conducted with the Vienna ab inito simulation package (VASP)[43, 44] using density-functional theory (DFT). Ion-electron interactions were treated using projector-augmented-wave potentials[45] and a generalized gradient approximation (GGA) in the form of Perdew-Burke-Ernzerhof was adopted to describe electron-electron interactions.[46] The GGA+U calculations were performed with the simplified spherically-averaged approach, where the U_{eff} (U_{eff}=U - J) is applied to d electrons. Electron wave functions were expanded using plane waves with an energy cut off of 520 eV. The Kohn-Sham equation was solved self-consistently with a convergence of 10^{-5}. The stoichiometry of the simulated systems was set to $SrCo_{0.75}Nb_{0.25}O_3$, $SrCo_{0.75}Ta_{0.25}O_3$ due to computational limits.

6.3 Results and Discussions

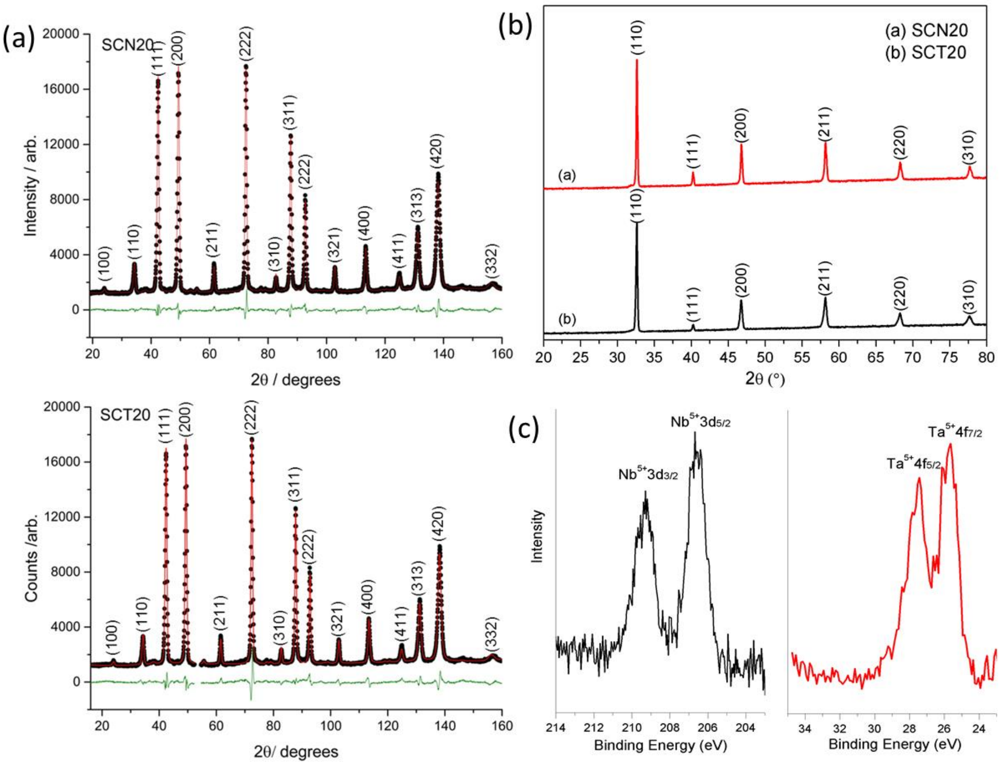

Figure 6-1 (a) Rietveld refinement plot of SCN20 (top) and SCT20 (bottom) powders at room temperature using NPD. Data are shown as black dots, the calculation as a red line, and the difference between the two as a green line. For SCN20 the weighted profile R-factor (R_{wp}) = 4.53%, the integrated intensity R-factor (R_F^2) = 3.46%, and goodness of fit ($\chi2$)= 2.48. For SCT20 R_{wp} = 5.29%, R_F^2 = 4.13%, and $\chi2$ = 3.42. (b) X-ray diffraction patterns of SCN20 and SCT20 at room temperature.

(c) X-ray photoelectron spectroscopy profile of Nb and Ta cation in SCN20 and SCT20 respectively at room temperature.

Table 6-1 Crystallographic details of SCN20 and SCT20 obtained from Rietveld refinement using NPD data at room temperature.

Samples	$Pm\bar{3}m$ space group Lattice parameter (Å)	Atom	Site	x	y	z	Occupancy
SCN20	3.8971(1)	Sr	1*b*	0.5	0.5	0.5	1.000
		Co	1*a*	0	0	0	0.79(1)
		Nb	1*a*	0	0	0	0.215(9)
		O	3*d*	0.5	0	0	0.966(6)
SCT20	3.8978(2)	Sr	1*b*	0.5	0.5	0.5	1.000
		Co	1*a*	0	0	0	0.79(1)
		Ta	1*a*	0	0	0	0.21(1)
		O	3*d*	0.5	0	0	0.947(5)

The NPD results reveal that SCN20 and SCT20 both exhibit cubic perovskite structures in $Pm\bar{3}m$ space-group symmetry at room temperature, with similar lattice parameters of a = 3.8971(1) Å for SCN20 and a = 3.8978(2) Å for SCT20 (Figure 6-1(a) and Table 6-1). Broad, small reflections were noted in the NPD data that were unindexed in $Pm\bar{3}m$ and these were excluded from the structure refinement. XPS results in Figure 6-1(c) shows that the binding energy (B.E.) of Nb 3d5/2 (206.69 eV) can be assigned to Nb^{5+} [ref. [47]], and B.E. of Ta 4f7/2 (25.64 eV) to Ta^{5+} [ref. [48]], indicating the same 5+ charge on both Nb and Ta cations in SCN20 and SCT20 respectively. The isostructural nature of the SCN20 and SCT20 is expected, given the similar ionic radii of Nb^{5+} and Ta^{5+}, which ensured similar-sized unit-cells. NPD results indicate a refined oxygen-stoichiometry (3-δ) of SCN20 of 2.898 (18), which is higher than that obtained for SCT20 of 2.843(15). The average valence state of cobalt in both samples can be obtained according to the charge balance: the average oxidation-state of cobalt cations in SCN20 is +3.44(6), which is larger overall but the same within 1 estimated standard deviation of the +3.33(6) for SCT20. Considering the similar lattice geometries and doping level of SCT20 and SCN20, the different cobalt oxidation-state may be explained by the different electronegativity of the dopants. A dopant with higher electronegativity will draw electron density from neighbouring cobalt, resulting in increased positive charge on the cobalt. Given the higher electronegativity of Nb^{5+} than Ta^{5+}, it is understandable that the average cobalt oxidation-state is slightly higher in SCN20 in comparison to SCT20.

Further, we studied the atomic-orbital-resolved electron density of states (PDOS) projected onto the Co close to Nb or Ta through first-principles calculations. From the PDOS results (Figure S6-1), Co-PDOS peak broadening is noticeable in SCT20 relative to SCN20, suggesting a weaker localisation of Co d states or less ionic character of Co in SCT20 than that in SCN20.[49, 50] Therefore, the Co surrounding Ta presents slightly lower charge, which leads to a higher level of oxygen vacancy as compared with Nb. Similar Co-PDOS peak broadening also occurs in $Ba_{0.5}Sr_{0.5}Co_{0.8}Fe_{0.2}O_{3-\delta}$ with relatively more oxygen vacancies[51], further confirming that the higher oxygen vacancy level in SCT20 is related to the relatively lower charge of neighbouring Co because of Ta's lower electronegativity.

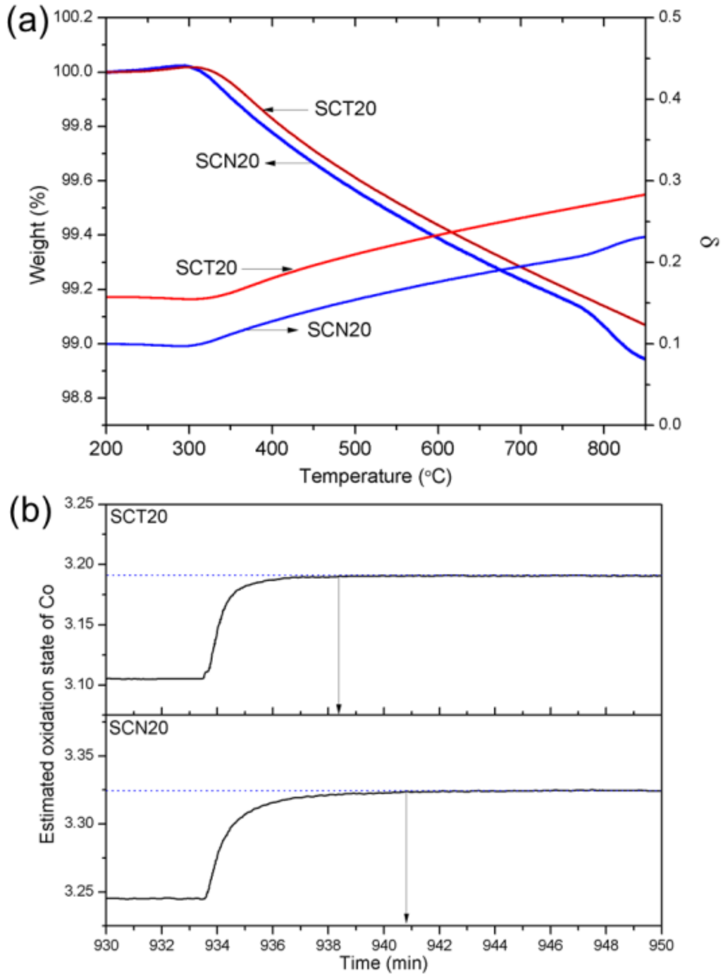

Figure 6-2 (a) Weight change (obtained from TGA) and oxygen vacancy content (δ) of SCN20 and SCT20 powders with temperature using a ramp rate of 1 °C/min and 2 h hold at 200 °C. (b) Change in the estimated oxidation-state of Co with time on exposure to pure N_2, then air, at 462 °C. Approximately 4.9 min is taken for the oxidation state of Co to reach equilibrium in SCT20 and 7.5 min in SCN20.

TGA was conducted to study the oxygen vacancy content (δ) in SCN20 and SCT20 at different temperatures in flowing air, based on the room-temperature oxygen vacancy content derived from the NPD results. The initial oxygen vacancy contents (δ), calculated from the Rietveld refinement results of NPD in Table 6-1, are around 0.102 in SCN20 and 0.157 in SCT20. While the δ values from titration method also confirms a lower oxygen vacancy level of SCN20 (0.14) than SCT20 (0.17). Figure 6-2(a) shows that both samples keep decreasing in mass with increasing temperature. These weight losses mainly stem from oxygen release, so the oxygen vacancy contents in both samples increase with temperature. More vacancies are observed in SCT20 than SCN20 at the same temperature. In addition, SCN20 decreases its weight slightly faster at temperature over ca. 780°C, implying that it is a little easier for SCN20 to form oxygen vacancies at high temperature.

Because Nb^{5+} and Ta^{5+} have fixed oxidation states, the intake or release of oxygen strongly relies on the change of the Co oxidation state. The Co oxidation states are therefore monitored to estimate how quickly the cobalt responds to the change of oxygen pressure. Both SCN20 and SCT20 powders were prepared for TGA by pressing and crushing in a procedure ensuring similar grain sizes (Figure S6-2) and BET surface area ($1.038 m^2/g$ for SCT20 and $1.186 m^2/g$ for SCN20). It is observed from Figure 6-2(b) that Co takes a shorter time (~4.9 min) in SCT20 to reach equilibrium than in SCN20 (~7.5 min). The quicker response of Co in SCT20 implies a faster oxygen surface-exchange process compared with SCN20.

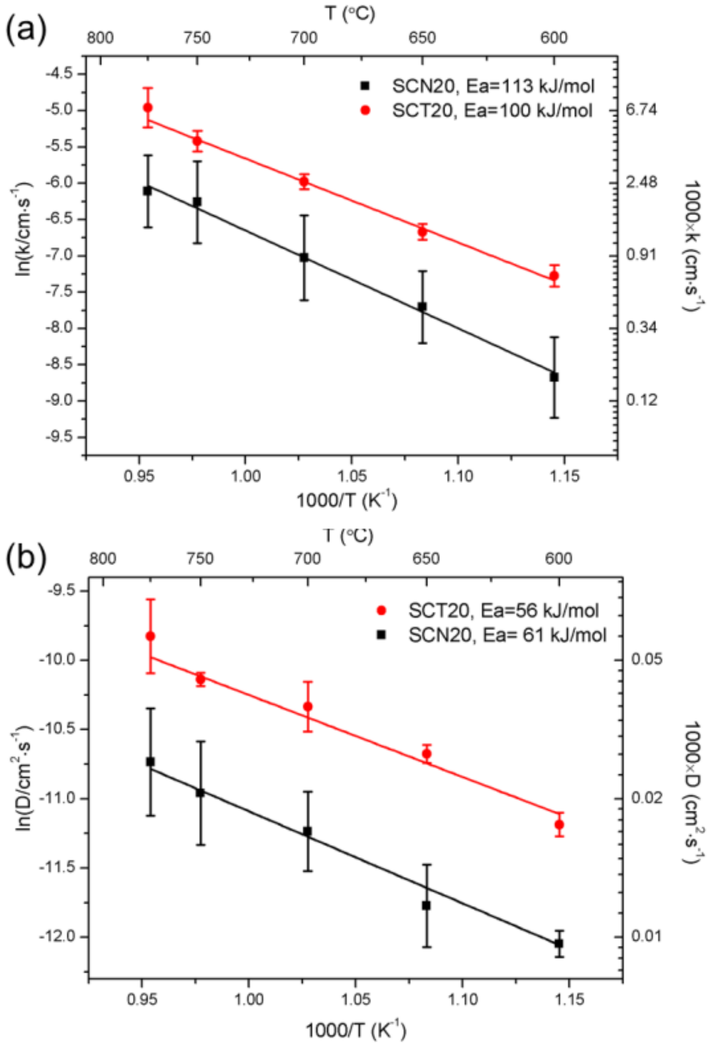

Figure 6-3 SCN20 and SCT20 (a) oxygen surface-exchange coefficient (k) and (b) oxygen diffusivity (D) as a function of temperature obtained from ECR.

The oxygen surface-exchange coefficient (k) and the bulk-chemical diffusivity (D) are key factors affecting the catalytic activity of a cathode to reduce oxygen. Electrical conductivity relaxation (ECR) was performed to study these two parameters as a function of temperature. Figure 6-3 compares k and D of SCN20 and SCT20. We note that oxygen diffuses slightly faster in bulk SCT20 than in SCN20. Further, SCT20 exhibits a higher activity in terms of the surface exchange of oxygen and has a lower activation energy than SCN20, resulting in a higher level surface-exchange coefficient at lower temperature. The faster oxygen intake of SCT20 than SCN20 at low temperature (462 °C) as discussed in Figure 6-2(b) is consistent with this observation.

Given the similar geometries and electrical conductivities of SCN20 and SCT20 (Figure S6-3), it is likely that the higher oxygen surface-exchange rate for SCT20 mainly result from the lower electronegativity of the tantalum, leading to increased oxygen vacancies.

To the best of our knowledge, studies on the effects of electronegativity on the ORR at room temperature have been very limited. Enhanced oxygen chemisorption onto ORR catalysts was achieved by Yang *et al.*[52] by doping boron with low electronegativity, into carbon nanotubes. The increased positive charge on boron was thought to play a significant role in the capture of oxygen. According to the electronegativity theory of Sanderson[53], the effective electronegativity of atoms is equal to the geometric mean of the initial atom electronegativity due to electron distribution. Therefore, the global electronegativity of SCN20 will be slightly higher than that of SCT20. Low electronegativity leads to a decrease in work function, which significantly affects charge exchange and represents a barrier for adding or removing electrons in a solid.[54] Therefore, the process of charge exchange with oxygen during the oxygen surface-exchange reaction is probably improved as a result of the relatively-lower level work function in SCT20. Of more significance to the ORR is the higher level of oxygen vacancies that arises from the lower-electronegativity of tantalum. To the best of our knowledge, electronegativity has never been considered to be a factor that may influence the concentrations of oxygen vacancies in perovskite oxides. Figure S6-6 further shows that SCT20 has a higher ionic conductivity than SCN20, with such difference increasing at lower temperature. The higher ionic conductivity of SCT20 arises from the higher oxygen vacancy content, which may be attributed to the lower electronegativity.

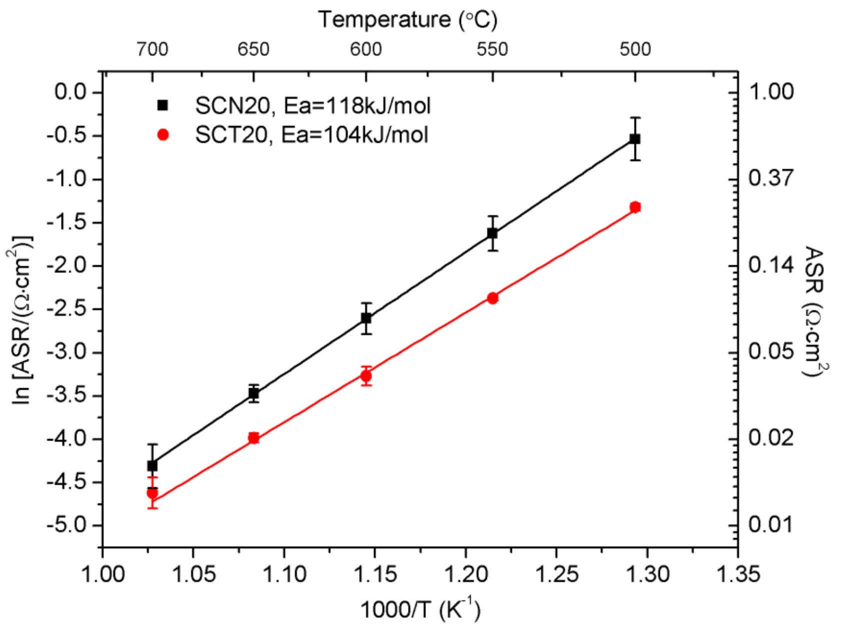

Figure 6-4 Average area-specific resistance (ASR) of SCN20 and SCT20 within a cathode | SDC |cathode symmetrical cell in flowing air.

The ORR electrochemical activities of SCN20 and SCT20 were investigated using EIS in symmetrical cells with SDC electrolyte. The area-specific resistance (ASR), derived from the impedance spectra, is the key variable characterizing the cathode performance, and a low ASR results in a high ORR activity. Figure 6-4 presents the ASR of SCN20 and SCT20 as a function of temperature between 500 and 700 °C. The ASR of SCT20 is lower than SCN20, being 0.092-0.097 $\Omega\cdot cm^2$ and 0.21-0.24 $\Omega\cdot cm^2$ at 550 °C, respectively. The lower ASR of SCT20 implies that the SCT20 cathode is more favourable for catalyzing the ORR. Additionally, SCT20 cathodes also exhibit a lower activation energy (104 kJ/mol) for the ORR than SCN20 (118 kJ/mol).

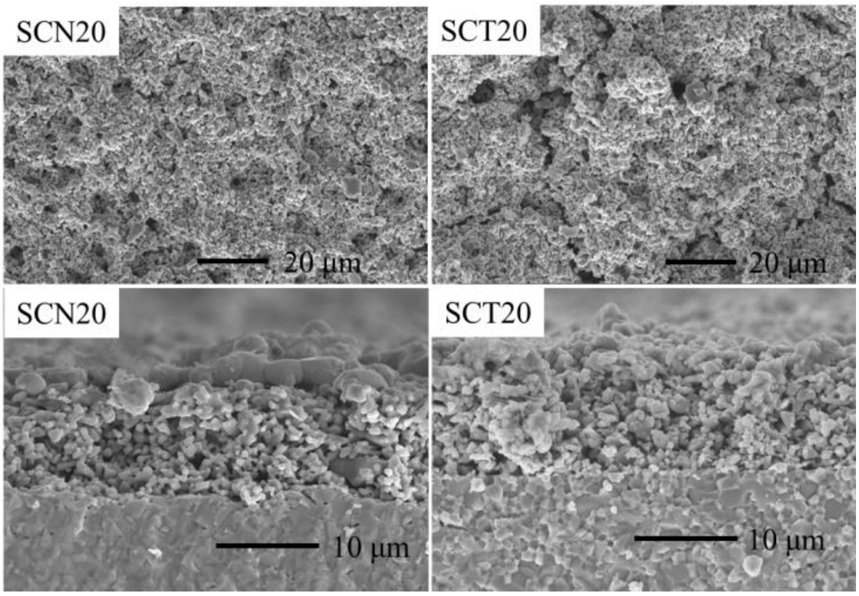

Figure 6-5 Scanning electron microscope (SEM) images of topography and cross sections of SCN20 and SCT20 cathodes in a configuration of symmetrical cell.

Given the similar microstructures as indicated by SEM (Figure 6-5) and good compatibility with electrolyte (Figure S6-4) of the two cathodes, the better ORR performance of SCT20 is likely attributable to the higher oxygen surface-exchange coefficient and faster bulk-oxygen diffusion. It is likely that the low electronegativity plays an important role in improving the ORR activity in the case of SCT20 and SCN20.

Impedance spectra of SCN20 and SCT20 were fitted to an equivalent circuit involving two processes: charge transfer and non-charge transfer (Figure S6-7-S6-11). The resistance of SCT20 corresponding to these processes are both lower than those of SCN20 (Table S6-1). The lower ASR of both processes in SCT20 compared with SCN20 indicates that low global electronegativity can significantly improve both charge transfer and non-charge transfer processes in the ORR. The observed improvement can be reconciled with the relatively-lower work functions of SCT20 as a result of lower global electronegativity.

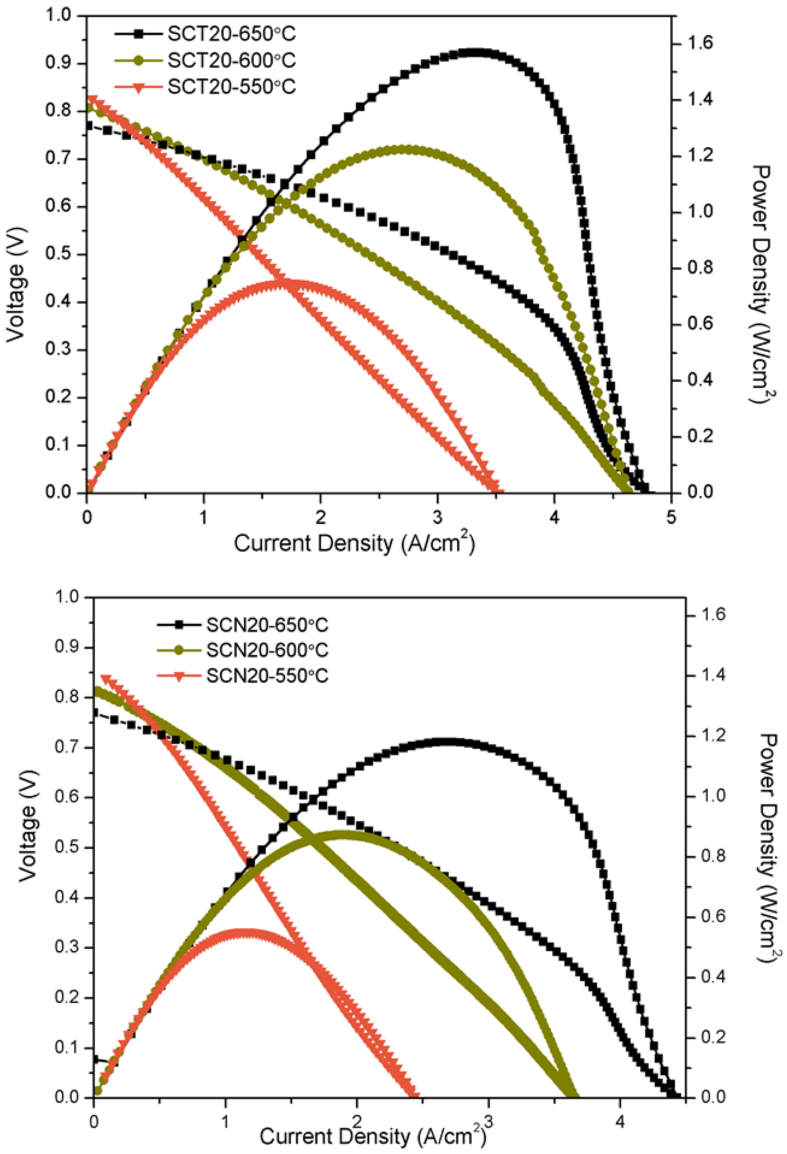

Figure 6-6 The power densities of anode-supported single cell with SCN20 and SCT20 as cathode respectively.

Accordingly, single-cell performance tests (Figure 6-6) show a peak power density of ~1.22 W/cm^2 for SCT20 at 600 °C, higher than that of ~0.95 W/cm^2 for SCN20. The better performance is a result of the higher ORR activity of SCT20 when compared with SCN20 as cathodes of the single cells.

6.4 Conclusions

The effects of non-geometry factors on the ORR activity of cathodes for SOFCs was investigated by comparing the SCN20 and SCT20 materials, where the two different dopants (Nb^{5+} and Ta^{5+}) share similar ionic radii but different electronegativity. Given the similar lattice geometries of the two materials, the lower electronegativity of Ta^{5+} in comparison to Nb^{5+} is revealed to induce a slightly lower valence of cobalt, resulting in a higher concentration of oxygen vacancies. Lower global electronegativity is also suggested to reduce the work function of the sample, enhancing the charge-transfer processes during the oxygen surface-exchange process. As a result, SCT20 was found to have a better ORR performance than SCN20 at lower temperature as SOFC cathode. Our findings indicate that electronegativity is another factor besides geometry affecting the ORR activity of the perovskite materials, and provide new effective strategies to design novel high-performance MIEC materials.

Acknowledgement

The authors appreciate the technical support from Centre for Microscopy and Microanalysis at the University of Queensland.

This work is financially supported by Australian Research Council (DP130102151) and author Mengran Li acknowledges additional financial support from the top-up assistance program (TUAP) scholarship and the scholarship from China Scholarship Council.

6.5 Supplementary Information

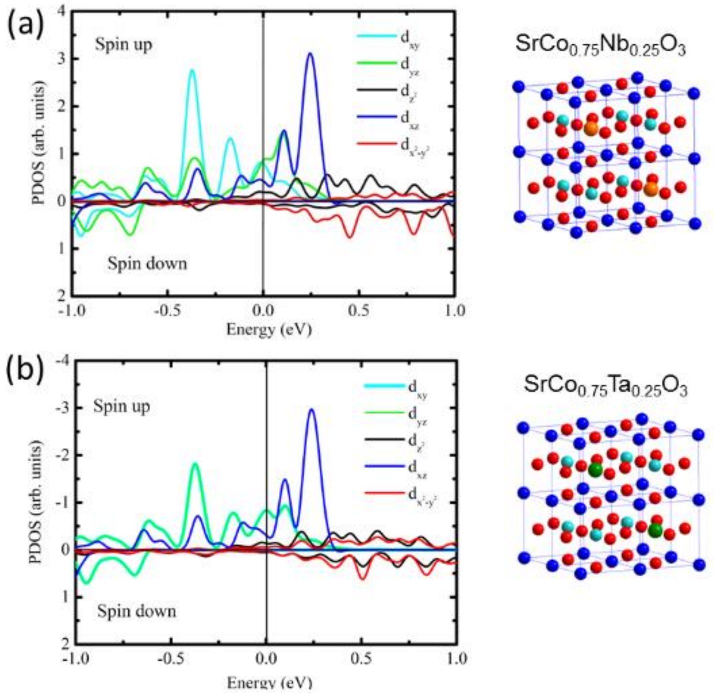

Figure S 6-1 Atomic orbital resolved electron density (PDOS) projected on the nearest Co atoms to Nb or Ta in (a) SCN20 and (b) Ta respectively.

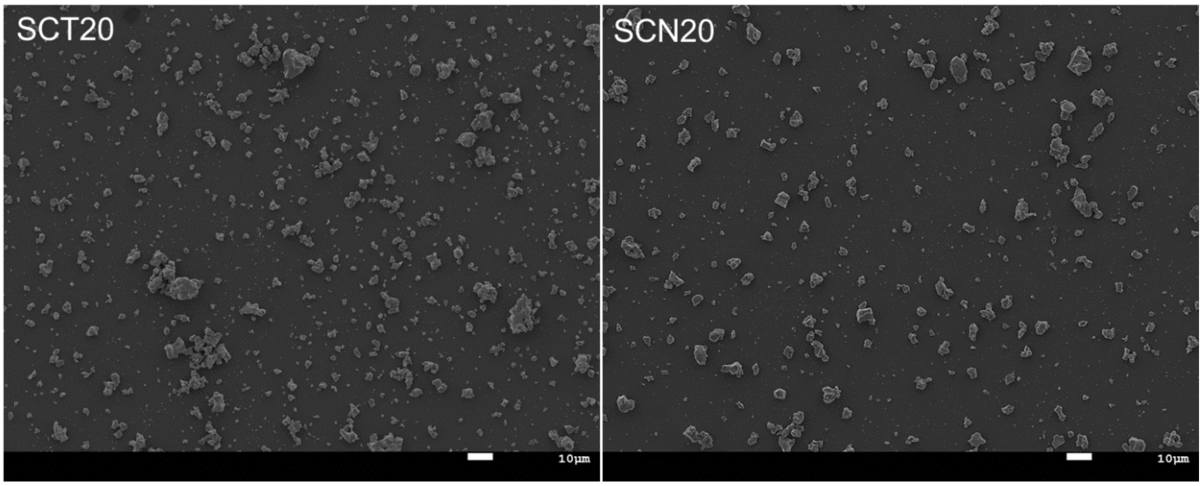

Figure S 6-2 SEM images of the SCT20 and SCN20 powders following TGA.

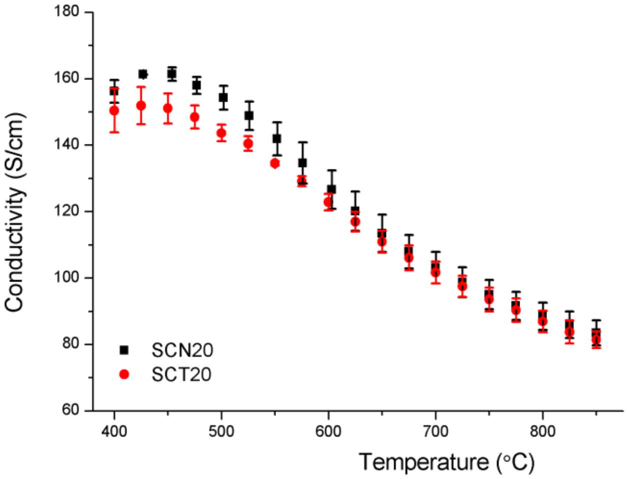

Figure S 6-3 Electrical conductivities of SCN20 and SCT20 as a function of temperature ranging from 375 to 850 °C.

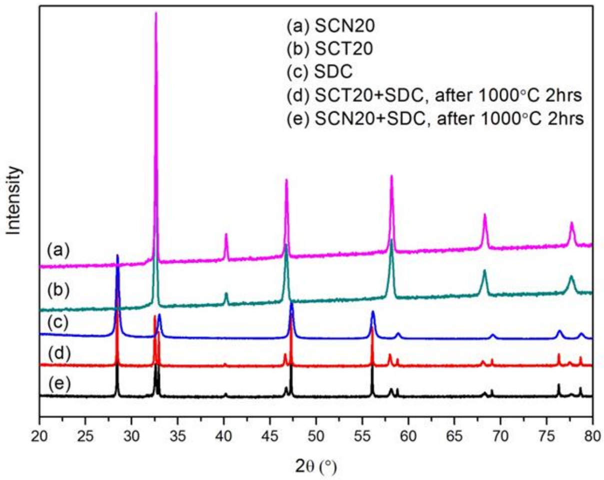

Figure S 6-4 XRD (Cu Kα) patterns of SCN20, SCT20, and SDC at room temperature, and SCT20 and SCN20 well mixed with SDC respectively followed by pelletising and sintering at 1000 °C for 2 hours.

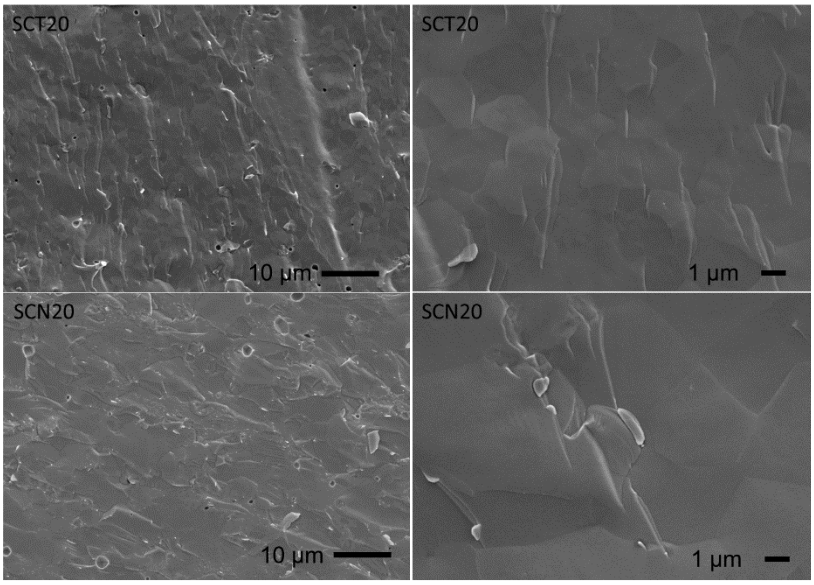

Figure S 6-5 SEM cross sectional images of membranes for oxygen permeability tests, showing relative dense samples for both SCN20 and SCT20, and slight larger grain size of SCN20 (~4µm) than SCT20(~3µm).

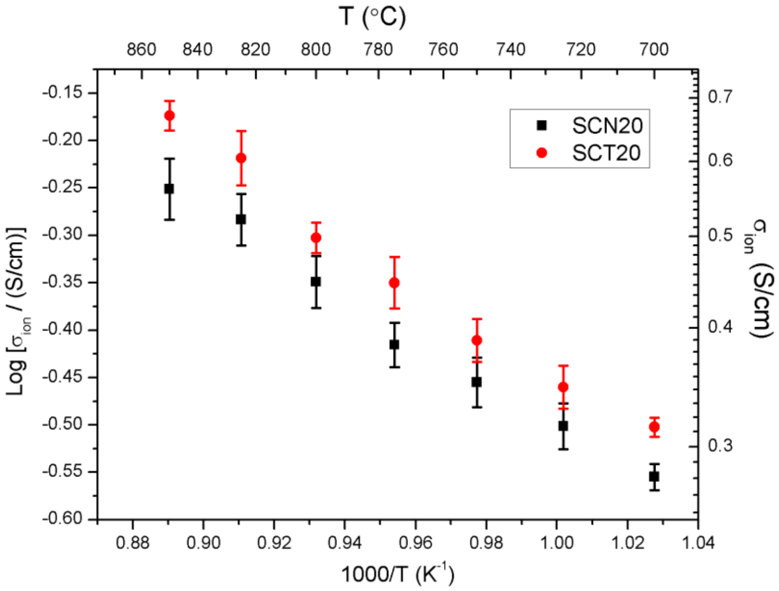

Figure S 6-6 Comparison of ionic conductivities for SCN20 and SCT20 estimated by studying the oxygen permeability against temperature.

The ionic conductivity of SCN20 and SCT20 was determined by studying the oxygen permeation of both materials as a function of temperature between 700 and 850 °C. The overall resistance to oxygen permeation through the ceramic membrane can be obtained from the following equation[55]:

$$R_{overall} = \frac{RT}{16F^2} \frac{1}{SJ_{O_2}} \left[\ln\left(\frac{P'_{O_2}}{P''_{O_2}} \right) \right] \tag{6.2}$$

R - the ideal gas constant

F - the Faraday constant

S - the valid area of the membrane

J_{O_2}- the oxygen permeation flux

P'_{O_2} - The oxygen partial pressure at the side of membrane exposed to air

P''_{O_2} - the oxygen partial pressure at the sweep side

If the oxygen permeation process is dominated by the bulk diffusion, the resistance from ionic conduction will become the major contribution to the overall permeation resistance. Therefore, the overall resistance is controlled by ionic conduction and ionic conductivity can be estimated by the following equation:

$$\sigma_{ionic} = \frac{1}{R_{ionic}} \times \frac{S}{L} \approx \frac{1}{R_{overall}} \times \frac{S}{L} \qquad (6.3)$$

Where L is the thickness of the membrane.

The thickness of the membrane is far larger than the characteristic length L_c, which is the ratio between the oxygen diffusivity and the surface exchange coefficient. L_c, obtained from the results of ECR experiments, is around 0.0084-0.0178 cm for SCN20 and 0.016-0.022 cm for SCT20, while the thickness of both membranes is 0.069 cm. Therefore, it is reasonable to assume that bulk diffusion is the predominate process of the oxygen permeation.

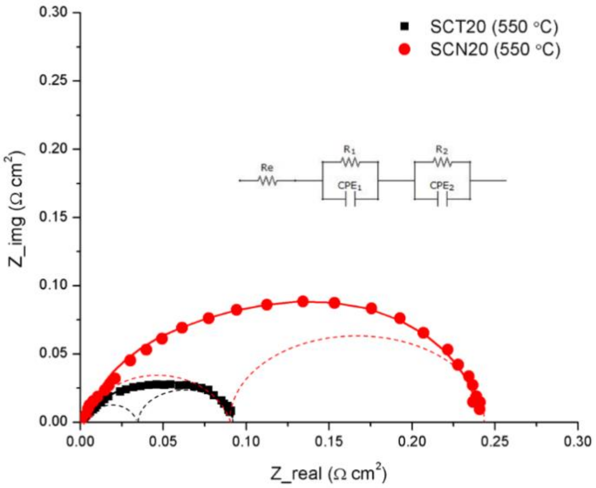

Figure S 6-7 An example of equivalent circuit fitting of EIS data for SCN20 and SCT20 cathodes at 550 °C.

Table S 6-1 ASR values corresponding to different processes (low frequency = LF, high frequency = HF).

Temperature(°C)	SCN20 ($\Omega\cdot cm^2$)		SCT20($\Omega\cdot cm^2$)	
	ASR-HF	ASR-LF	ASR-HF	ASR-LF
500	0.36	0.41	0.12	0.14
550	0.092	0.15	0.036	0.057
600	0.017	0.07	0.014	0.021
650	0.0065	0.029	0.006	0.011

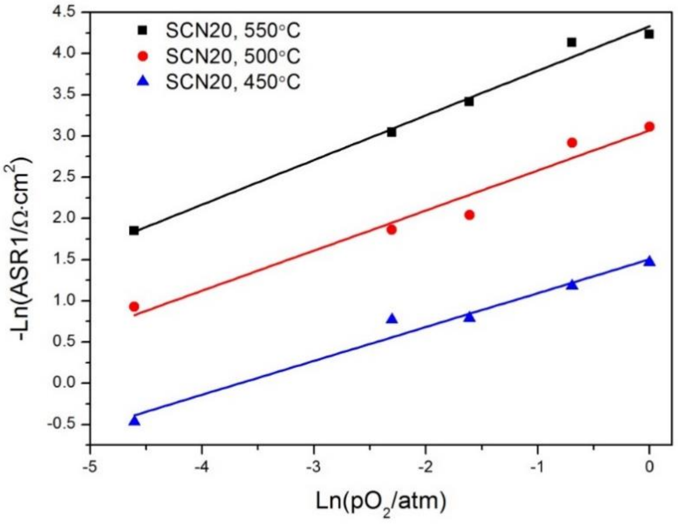

Figure S 6-8 . ASR values of the SCN20 cathode corresponding to the process at low frequencies at different temperatures against the oxygen partial pressure.

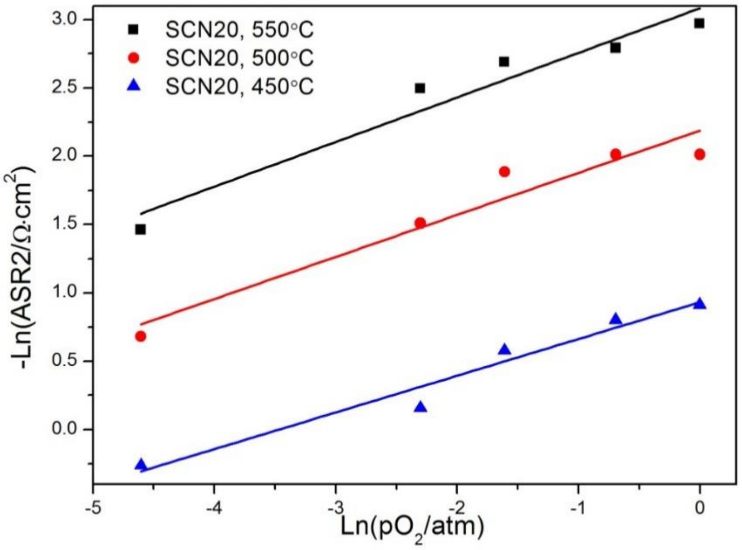

Figure S 6-9 ASR values for the SCN20 cathode corresponding to the process at high frequencies at different temperatures against the oxygen partial pressure.

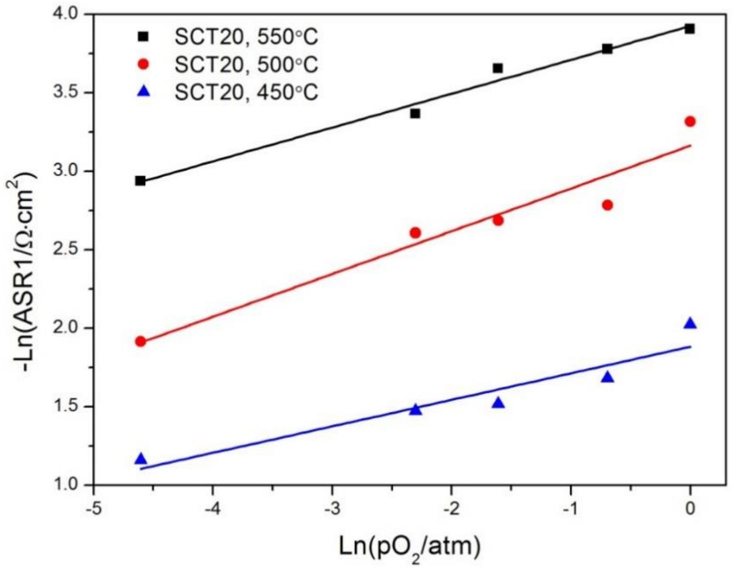

Figure S 6-10 ASR values for the SCT20 cathode corresponding to the process at low frequencies at different temperatures against the oxygen partial pressure.

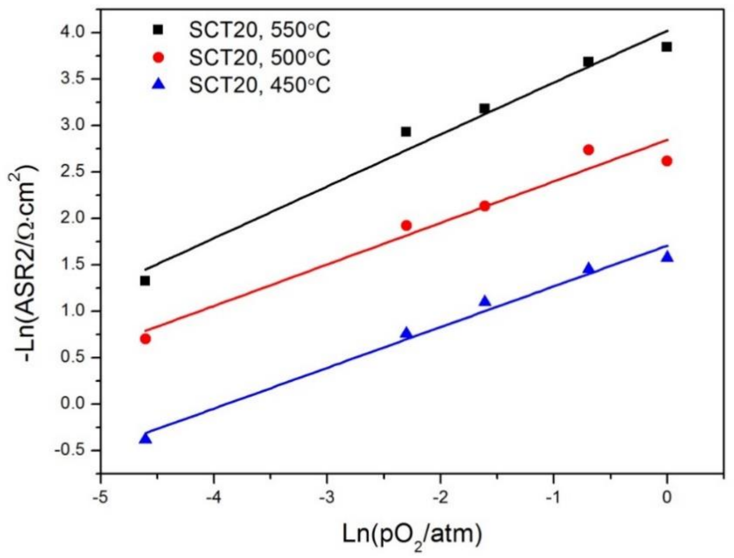

Figure S 6-11 ASR values for the SCT20 cathode corresponding to the process at high frequencies at different temperatures against the oxygen partial pressure.

The mechanism of ORR was studied by measuring the resistances of target cathode materials at different oxygen partial pressures over the temperature range 450 -550 °C. Electrical impedance spectra were fitted to the Re(R1Q1) (R2Q2) equivalent circuit model using LEVM software, where Re represents the ohmic resistance of the SDC electrolyte, and the two series connected elements (RQ) correspond to two ORR processes: the R is the resistance and Q is the constant phase element.

The parameter that usually determines the ORR is the slope of electrode resistance against the temperature as provide by the following relationship[56]:

$$\frac{1}{R_p} \propto P_{O_2}^{m} \tag{6.4}$$

As shown in the above figures, the slope of ASR at low frequencies (ASR-LF) is 0.14-0.19 for SCN20 and 0.17-0.22 for SCT20, while the slope of ASR at high frequencies (ASR-HF) is 0.35-0.4 for SCN20 and 0.44-0.56 for SCT20. The slope of the ASR-HF for both of SCN20 and SCT20 is close to 0.25, implying that the first step was limited by the following process[56]:

$$O_{2,\mathrm{ads}} + 2e' + V_O'' \leftrightarrow O_O^{\times} \tag{6.5}$$

$O_{2,\mathrm{ads}}$ denotes an oxygen molecule absorbed onto the cathode surface;

e' is an electron;

V_O'' represents an oxygen vacancy with a double positive charge;

$O_O^{\times}$ is an oxygen occupying an oxygen lattice site with a neutral charge.

The slope for the second process for both of cathodes is close to 0.5, which indicates that non-charge transfer dominates.

6.6 References

1. Wachsman, E. D.; Lee, K. T., Lowering the Temperature of Solid Oxide Fuel Cells. *Science* **2011,** 334, (6058), 935-939.

2. Minh, N. Q., Ceramic Fuel Cells. *Journal of the American Ceramic Society* **1993,** 76, (3), 563-588.

3. Steele, B. C.; Heinzel, A., Materials for Fuel-Cell Technologies. *Nature* **2001,** 414, (6861), 345-352.

4. Jacobson, A. J., Materials for Solid Oxide Fuel Cells. *Chemistry of Materials* **2009,** 22, (3), 660-674.

5. Orera, A.; Slater, P., New Chemical Systems for Solid Oxide Fuel Cells. *Chemistry of Materials* **2009,** 22, (3), 675-690.

6. Adler, S. B., Factors governing oxygen reduction in solid oxide fuel cell cathodes. *Chemical reviews* **2004,** 104, (10), 4791-4844.

7. Wang, J.-H.; Liu, M.; Lin, M., Oxygen reduction reactions in the SOFC cathode of Ag/CeO< sub> 2</sub>. *Solid State Ionics* **2006,** 177, (9), 939-947.

8. Yoo, S.; Jun, A.; Ju, Y.-W.; Odkhuu, D.; Hyodo, J.; Jeong, H. Y.; Park, N.; Shin, J.; Ishihara, T.; Kim, G., Development of Double-Perovskite Compounds as Cathode Materials for Low-Temperature Solid Oxide Fuel Cells. *Angewandte Chemie International Edition* **2014,** 53, (48), 13064-13067.

9. Richter, J.; Holtappels, P.; Graule, T.; Nakamura, T.; Gauckler, L., Materials Design for Perovskite SOFC Cathodes. *Monatshefte für Chemie - Chemical Monthly* **2009,** 140, (9), 985-999.

10. Zhou, W.; Shao, Z.; Ran, R.; Jin, W.; Xu, N., A novel efficient oxide electrode for electrocatalytic oxygen reduction at 400–600 C. *Chemical Communications* **2008**, (44), 5791-5793.

11. Zhou, W.; Sunarso, J.; Zhao, M.; Liang, F.; Klande, T.; Feldhoff, A., A Highly Active Perovskite Electrode for the Oxygen Reduction Reaction Below 600 °C. *Angewandte Chemie International Edition* **2013,** 52, (52), 14036-14040.

12. Lee, J. G.; Park, J. H.; Shul, Y. G., Tailoring Gadolinium-Doped Ceria-Based Solid Oxide Fuel Cells to Achieve 2 W Cm^{-2} at 550 °C. *Nature Communications* **2014,** 5.

13. Shao, Z.; Haile, S. M., A High-Performance Cathode for the Next Generation of Solid-Oxide Fuel Cells. *Nature* **2004,** 431, (7005), 170-173.

14. Choi, S.; Yoo, S.; Kim, J.; Park, S.; Jun, A.; Sengodan, S.; Kim, J.; Shin, J.; Jeong, H. Y.; Choi, Y., Highly Efficient and Robust Cathode Materials for Low-Temperature Solid Oxide Fuel Cells: $PrBa_{0.5}Sr_{0.5}Co_{2-X}Fe_xO_{5+\delta}$. *Scientific reports* **2013,** 3.

15. Simner, S. P.; Bonnett, J. F.; Canfield, N. L.; Meinhardt, K. D.; Shelton, J. P.; Sprenkle, V. L.; Stevenson, J. W., Development of lanthanum ferrite SOFC cathodes. *Journal of Power Sources* **2003,** 113, (1), 1-10.

16. Zhang, X.; Liu, L.; Zhao, Z.; Tu, B.; Ou, D.; Cui, D.; Wei, X.; Chen, X.; Cheng, M., Enhanced Oxygen Reduction Activity and Solid Oxide Fuel Cell Performance with a Nanoparticles-Loaded Cathode. *Nano Letters* **2015,** 15, (3), 1703-1709.

17. Zhu, Y.; Sunarso, J.; Zhou, W.; Jiang, S.; Shao, Z., High-performance $SrNb_{0.1}Co_{0.9-x}Fe_xO_{3-\delta}$ Perovskite Cathodes for Low-temperature Solid Oxide Fuel Cells. *Journal of Materials Chemistry A* **2014,** 2, (37), 15454-15462.

18. Li, M.; Zhou, W.; Zhu, Z., Comparative Studies of $SrCo_{1-X}Ta_xo_{3-\delta}$ (X=0.05–0.4) Oxides as Cathodes for Low-Temperature Solid-Oxide Fuel Cells. *ChemElectroChem* **2015,** 2, (9), 1331-1338.

19. Zhou, W.; Ran, R.; Shao, Z., Progress in understanding and development of Ba0. 5Sr0. 5Co0. 8Fe0. 2O3Àd-based cathodes for intermediate-temperature solid-oxide fuel cells: a review. *J. Power Sources* **2009,** 192, (2), 231-246.

20. Pena, M.; Fierro, J., Chemical structures and performance of perovskite oxides. *Chemical Reviews* **2001,** 101, (7), 1981-2018.

21. Kharton, V.; Yaremchenko, A.; Kovalevsky, A.; Viskup, A.; Naumovich, E.; Kerko, P., Perovskite-type Oxides for High-temperature Oxygen Separation Membranes. *Journal of Membrane Science* **1999,** 163, (2), 307-317.

22. Deng, Z.; Yang, W.; Liu, W.; Chen, C., Relationship between Transport Properties and Phase Transformations in Mixed-conducting Oxides. *Journal of Solid State Chemistry* **2006,** 179, (2), 362-369.

23. Rodriguez, J.; Gonzalez-Calbet, J.; Grenier, J.; Pannetier, J.; Anne, M., Phase Transitions in Sr_2Co_2 O_5: A Neutron Thermodiffractometry Study. *Solid state communications* **1987,** 62, (4), 231-234.

24. Rodriguez, J.; Gonzalez-Calbet, J., Rhombohedral Sr< sub> 2</sub> Co< sub> 2</sub> O< sub> 5</sub>: A new A< sub> 2</sub> M< sub> 2</sub> O< sub> 5</sub> phase. *Materials research bulletin* **1986,** 21, (4), 429-439.

25. Aguadero, A.; Alonso, J. A.; Pérez-Coll, D.; de la Calle, C.; Fernández-Díaz, M. a. T.; Goodenough, J. B., $SrCo_{0.95}Sb_{0.05}O_{3-\delta}$ as Cathode Material for High Power Density Solid Oxide Fuel Cells. *Chemistry of Materials* **2009,** 22, (3), 789-798.

26. Hancock, C. A.; Slade, R. C. T.; Varcoe, J. R.; Slater, P. R., Synthesis, Structure and Conductivity of Sulfate and Phosphate Doped $SrCoO_3$. *Journal of Solid State Chemistry* **2011,** 184, (11), 2972-2977.

27. Li, M.; Zhou, W.; Xu, X.; Zhu, Z., SrCo 0.85 Fe 0.1 P 0.05 O 3− δ perovskite as a cathode for intermediate-temperature solid oxide fuel cells. *Journal of Materials Chemistry A* **2013,** 1, (43), 13632-13639.

28. Zhou, W.; Jin, W. Q.; Zhu, Z. H.; Shao, Z. P., Structural, Electrical and Electrochemical Characterizations of $SrNb_{0.1}Co_{0.9}O_{3-\delta}$ as a Cathode of Solid Oxide Fuel Cells Operating Below 600°C *International Journal of Hydrogen Energy* **2010,** 35, (3), 1356-1366.

29. Li, C.; Soh, K. C. K.; Wu, P., Formability of ABO3 perovskites. *Journal of Alloys and Compounds* **2004,** 372, (1–2), 40-48.

30. Muller, O.; Roy, R., *The Major Ternary Structural Families*. Springer-Verlag New York: 1974.

31. Vyshatko, N. P.; Kharton, V.; Shaula, A. L.; Naumovich, E. N.; Marques, F. M. B., Structural characterization of mixed conducting perovskites La(Ga,M)O3−δ (M=Mn, Fe, Co, Ni). *Materials Research Bulletin* **2003,** 38, (2), 185-193.

32. Sammells, A. F.; Cook, R. L.; White, J. H.; Osborne, J. J.; MacDuff, R. C., Rational selection of advanced solid electrolytes for intermediate temperature fuel cells. *Solid State Ionics* **1992,** 52, (1), 111-123.

33. Kilner, J.; Brook, R., A study of oxygen ion conductivity in doped non-stoichiometric oxides. *Solid State Ionics* **1982,** 6, (3), 237-252.

34. Shannon, R. t.; Prewitt, C. T., Effective Ionic Radii in Oxides and Fluorides. *Acta Crystallographica Section B: Structural Crystallography and Crystal Chemistry* **1969,** 25, (5), 925-946.

35. Shannon, R. t.; Prewitt, C., Revised values of effective ionic radii. *Acta Crystallographica Section B: Structural Crystallography and Crystal Chemistry* **1970,** 26, (7), 1046-1048.

36. Klixbüll Jørgensen, C., Electron Transfer Spectra. In *Progress in Inorganic Chemistry*, John Wiley & Sons, Inc.: 2007; pp 101-158.

37. Matar, S. F.; Campet, G.; Subramanian, M. A., Electronic Properties of Oxides: Chemical and Theoretical Approaches. *Progress in Solid State Chemistry* **2011,** 39, (2), 70-95.

38. Parr, R. G.; Donnelly, R. A.; Levy, M.; Palke, W. E., Electronegativity: the density functional viewpoint. *The Journal of Chemical Physics* **1978,** 68, (8), 3801-3807.

39. Ciucci, F., Electrical conductivity relaxation measurements: Statistical investigations using sensitivity analysis, optimal experimental design and ECRTOOLS. *Solid State Ionics* **2013,** 239, (0), 28-40.

40. Liss, K.-D.; Hunter, B.; Hagen, M.; Noakes, T.; Kennedy, S., Echidna—the new high-resolution powder diffractometer being built at OPAL. *Physica B: Condensed Matter* **2006,** 385, 1010-1012.

41. Toby, B. H.; Von Dreele, R. B., GSAS-II: the Genesis of a Modern Open-source All Purpose Crystallography Software Package. *Journal of Applied Crystallography* **2013,** 46, (2), 544-549.

42. Aguadero, A.; Calle, C. d. l.; Alonso, J. A.; Escudero, M. J.; Fernández-Díaz, M. T.; Daza, L., Structural and Electrical Characterization of the Novel $Srco_{0.9}Sb_{0.1}O_{3-\delta}$ Perovskite: Evaluation as a Solid Oxide Fuel Cell Cathode Material. *Chemistry of Materials* **2007,** 19, (26), 6437-6444.

43. Kresse, G.; Hafner, J., *Ab initio* molecular dynamics for liquid metals. *Physical Review B* **1993,** 47, (1), 558-561.

44. Kresse, G.; Furthmüller, J., Efficient Iterative Schemes for *ab initio* Total-energy Calculations using A Plane-wave Basis Set. *Physical Review B* **1996,** 54, (16), 11169-11186.

45. Kresse, G.; Joubert, D., From Ultrasoft Pseudopotentials to the Projector Augmented-wave Method. *Physical Review B* **1999,** 59, (3), 1758-1775.

46. Perdew, J. P.; Burke, K.; Ernzerhof, M., Generalized Gradient Approximation Made Simple. *Physical Review Letters* **1996,** 77, (18), 3865-3868.

47. McGuire, G. E.; Schweitzer, G. K.; Carlson, T. A., Core Electron Binding Energies in some Group IIIA, VB, and VIB Compounds. *Inorganic Chemistry* **1973,** 12, (10), 2450-2453.

48. Ho, S. F.; Contarini, S.; Rabalais, J. W., Ion-beam-induced Chemical Changes in the Oxyanions (Moyn-) and Oxides (Mox) where M = Chromium, Molybdenum, Tungsten, Vanadium, Niobium and Tantalum. *The Journal of Physical Chemistry* **1987,** 91, (18), 4779-4788.

49. Ramos, M.; Batista, M. N.; Martínez, A.; Busnengo, H. F., Dynamics of H2 Interacting with Substitutional Bimetallic Surface Alloys. In *Dynamics of Gas-Surface Interactions*, Díez Muiño, R.; Busnengo, H. F., Eds. Springer Berlin Heidelberg: 2013; Vol. 50, pp 131-155.

50. Singh, U. G.; Li, J.; Bennett, J. W.; Rappe, A. M.; Seshadri, R.; Scott, S. L., A Pd-doped Perovskite Catalyst, , for CO Oxidation. *Journal of Catalysis* **2007,** 249, (2), 349-358.

51. Kotomin, E. A.; Mastrikov, Y. A.; Kuklja, M. M.; Merkle, R.; Roytburd, A.; Maier, J., First Principles Calculations of Oxygen Vacancy Formation and Migration in Mixed Conducting $Ba_{0.5}Sr_{0.5}Co_{1-y}Fe_yO_{3-\delta}$ Perovskites. *Solid State Ionics* **2011,** 188, (1), 1-5.

52. Yang, L.; Jiang, S.; Zhao, Y.; Zhu, L.; Chen, S.; Wang, X.; Wu, Q.; Ma, J.; Ma, Y.; Hu, Z., Boron - Doped Carbon Nanotubes as Metal - Free Electrocatalysts for the Oxygen Reduction Reaction. *Angewandte Chemie* **2011,** 123, (31), 7270-7273.

53. Sanderson, R. T., Electronegativity and Bond Energy. *Journal of the American Chemical Society* **1983,** 105, (8), 2259-2261.

54. Greiner, M. T.; Chai, L.; Helander, M. G.; Tang, W.-M.; Lu, Z.-H., Transition Metal Oxide Work Functions: The Influence of Cation Oxidation State and Oxygen Vacancies. *Advanced Functional Materials* **2012,** 22, (21), 4557-4568.

55. Zeng, P.; Chen, Z.; Zhou, W.; Gu, H.; Shao, Z.; Liu, S., Re-evaluation of $Ba_{0.5}Sr_{0.5}Co_{0.8}Fe_{0.2}O_{3-\delta}$ Perovskite as Oxygen Semi-permeable Membrane. *Journal of Membrane Science* **2007,** 291, (1–2), 148-156.

56. Takeda, Y.; Kanno, R.; Noda, M.; Tomida, Y.; Yamamoto, O., Cathodic polarization phenomena of perovskite oxide electrodes with stabilized zirconia. *Journal of The Electrochemical Society* **1987,** 134, (11), 2656-2661.

Chapter 7 A Nb and Ta co-doped perovskite cathode for IT-SOFC

Introduction

The sluggish kinetics of cathode on reducing oxygen at lower temperature is one of the major challenges for the deployment of IT-SOFC technology. As reviewed in Section 2.4.2, co-doping dopants is possible to synergistically improve the cathode performance by optimising the oxygen migration in the lattice. In Chapter 5 and 6, we found that doping Ta can significantly lower the cathode polarisation resistance at reduced temperature. Nb is also an effective dopant for cathode performance enhancement. Besides, Ta and Nb ions have very similar ionic size and valence, so they should be compatible well with each other when doping into $SrCoO_{3-\delta}$, and the possible synergistic effects of co-doping could be easily studied through restraining the geometric differences of single-doped and co-doped samples. Therefore, we prepared a novel cathode material by co-doping Nb and Ta into $SrCoO_{3-\delta}$, and investigated the possible synergistic effects on oxygen reduction.

Contribution

In this chapter, we designed a novel perovskite composition based on $SrCoO_{3-\delta}$ by co-doping Nb and Ta. This cathode shows remarkably high electroactivity on ORR especially below 500 °C, with an area specific resistance as low as $0.16\ \Omega\cdot cm^2$ at 500 °C, which is lower than other highly active single-phase ORR catalysts reported by far. More importantly, a synergistic effect of Nb and Ta was found to improve the surface exchange process, ionic conduction and the ORR activity at low temperature. This work has been submitted to Nature Communications.

A Niobium and Tantalum Co-Doped Perovskite Cathode for Solid Oxide Fuel Cells Operating Below 500 °C

Mengran Li, Mingwen Zhao, Feng Li, Wei Zhou*, Vanessa K. Peterson, Xiaoyong Xu, Zongping Shao, Ian Gentle, Zhonghua Zhu*

Abstract: The slow activity of the cathode is one of the most significant barriers to realizing the operation of low-temperature solid oxide fuel cells (LT-SOFCs) below 500 °C. Here, we report the novel niobium and tantalum co-substituted perovskite $SrCo_{0.8}Nb_{0.1}Ta_{0.1}O_{3-\delta}$ (SCNT) as a LT-SOFC cathode which exhibits notably high oxygen reduction reaction (ORR) activity at low temperature. This cathode has an area specific resistance as low as ~ 0.16 and ~ 0.68 $\Omega{\cdot}cm^2$ in a symmetrical cell and peak power densities of 1.2 and 0.7 W cm^{-2} in a $Gd_{0.1}Ce_{0.9}O_{1.95}$ (GDC)-based anode-supported fuel-cell at 500 and 450 °C, respectively. The high performance of the SCNT cathode is attributed to an optimal balance of oxygen vacancies, ionic mobility and surface electron transfer ability as promoted by the synergistic effects of the niobium and tantalum. Therefore, we demonstrate that the SOFC operating temperature can be reduced to 450 °C by simply using this new $SrCo_{0.8}Nb_{0.1}Ta_{0.1}O_{3-\delta}$ perovskite cathode, which also points to an effective strategy in the design of LT-SOFC cathodes.

7.1 Introduction

A low-temperature solid oxide fuel cell (LT-SOFC) is a durable energy device that can be deployed to convert the chemical energy stored in various types of fuels into electricity with high efficiency, ease of sealing and reduced system and operational costs.[1-3] However, the low operating temperature (450-600 ºC) typically leads to sluggish kinetics of the oxygen reduction reaction (ORR) at the cathode, with this being a major limitation to LT-SOFC performance.[4-9]

Intensive research has been carried out in an effort to explore novel cathode compositions suitable for operation at low temperature.[4, 6, 7, 10-15] Oxides offering high mixed ionic and electronic conductivities (MIECs) are considered to be some of the most promising candidates for the next generation of SOFC cathodes due to their extended active sites for the ORR compared with purely electronic conducting materials.[16, 17] Several cathodes with high MIECs that exhibited relatively low cathode polarization resistance below 600 ºC have been reported recently.[11] For example, the in-situ co-assembly of $La_{0.8}Sr_{0.2}MnO_3$ (with a very low O_2 dissociative energy barrier) and $Bi_{1.6}Er_{0.4}O_3$ (with fast O_2 incorporation kinetics) leads to a high-performance cathode with a low polarisation resistance of ~0.078 $\Omega\cdot cm^2$ at 600 °C.[11] Choi *et al.*[12] developed the novel MIEC cathode $PrBa_{0.5}Sr_{0.5}Co_{1.5}Fe_{0.5}O_{5+\delta}$, which exhibits polarization resistance as low as ~0.056 $\Omega\cdot cm^2$ at 600 °C under open circuit conditions, and the $NdBa_{0.75}Ca_{0.25}Co_2O_{5+\delta}$ material also exhibits outstanding ORR activity at reduced temperature.[7] Another MIEC cathode composition, $Ba_{0.9}Co_{0.7}Fe_{0.2}Mo_{0.1}O_{3-\delta}$, was also reported to have enhanced cathode performance showing a polarization resistance of ~0.28 $\Omega\cdot cm^2$ at 500 °C.[18]

Some of the most popular MIEC cathode materials currently under investigation are the stabilized $SrCoO_{3-\delta}$ (SC) perovskite oxides, such as $Sm_{0.5}Sr_{0.5}CoO_{3-\delta}$[19], (La,Sr)(Co,Fe)$O_{3-\delta}$,[20, 21] and $Ba_{0.5}Sr_{0.5}Co_{0.8}Fe_{0.2}O_{3-\delta}$[4, 22], which are claimed to exhibit high ORR activity in the intermediate temperature range 600 -750 ºC due to their relatively high mixed conductivities.[23, 24] The perovskite structure favoured for LT-SOFC cathodes is usually stabilized by partial *B*-site substitution with high oxidation-state cations[25], such as Nb,[26, 27] Mo,[28] Sb,[29, 30] and P[31, 32], which lead to a low area specific resistance (ASR) for the ORR.[27-29, 31, 33, 34] Further, Zhou *et al.*[10] developed a highly active perovskite cathode material for operation below 550 ºC featuring partial replacement of Co ions with both Sc^{3+}

and Nb^{5+}, where these dopants induce a remarkably-high ORR activity at 550 °C. To the best of our knowledge, few studies report the possible synergistic effects of co-doping highly charged dopants on catalyzing the ORR in LT-SOFC cathodes.

Herein, we report studies of the synergistic effects of two highly-charged *B*-site dopants on the performance of our novel perovskite LT-SOFC cathode $SrCo_{0.8}Nb_{0.1}Ta_{0.1}O_{3-\delta}$ (SCNT), with this cathode exhibiting outstanding and stable electrochemical performance below 500 ºC. A very low ASR of ~ 0.16 and ~0.68 $\Omega \cdot cm^2$ was achieved at 500 °C and 450 °C, respectively, by the SCNT cathode in a symmetrical cell configuration under open circuit conditions. A LT-SOFC with a pure SCNT cathode exhibited exceptionally good performance of ~1.2 and ~0.7 W/cm^2 at 500 and 450 °C, respectively. Our results show that through the co-substitution of Nb^{5+} and Ta^{5+} can lead to an optimised balance of the oxygen vacancies, ionic mobility and efficient surface electron transfer ability, which are potentially related to beneficial effects on ORR catalysis.

7.2Experimental

7.2.1 Sample syntheses

The SCNT material was synthesized through a solid state reaction route by ball milling stoichiometric amounts of $SrCO_3$ (≥ 99.9%, Aldrich), Co_3O_4 (≥ 99.9%, Aldrich), Nb_2O_5 (≥ 99.9%, Aldrich), and Ta_2O_5 (≥ 99.9%, Aldrich) for 24 h, before pelletizing and sintering the mixture in stagnant air at 1200 ºC for 10 h. Subsequently, the sintered pellets were well ground and re-sintered for another 10 h at 1200 ºC. $SrCo_{0.9}Nb_{0.1}O_{3-\delta}$ (SCN10), $SrCo_{0.8}Nb_{0.2}O_{3-\delta}$ (SCN20), $SrCo_{0.9}Ta_{0.1}O_{3-\delta}$ (SCT10), $SrCo_{0.8}Ta_{0.2}O_{3-\delta}$ (SCT20), and $Ba_{0.5}Sr_{0.5}Co_{0.8}Fe_{0.2}O_{3-\delta}$ (BSCF) were also prepared through a similar synthesis route.

7.2.2 Structure characterization

The crystal structures of cathode materials were studied by X-ray powder diffraction (XRD) and neutron powder diffraction (NPD). High-resolution NPD data were collected using ECHIDNA, the high-resolution neutron powder diffractometer at the Australian Nuclear Science and Technology Organization (ANSTO),[35] with a neutron wavelength of 1.6219(2) Å, determined using the $La^{11}B_6$ NIST standard reference material 660b. NPD data were obtained from SCNT within a 6 mm vanadium can for 6 h in the 2θ angular range 4 to 164° with a step size of 0.125°. GSAS-II[36] was employed to perform Rietveld analysis of the high-resolution NPD data, using $Pm\bar{3}m$ cubic perovskite[33] as the starting structure. The structure was refined against both the XRD and NPD data, with atomic displacement parameters for the Co, Nb, and Ta, fixed to 0.01. High-resolution electron transmission microscopy (HR-TEM, Tecnai F20) in conjunction with selected area electron diffraction was also used for phase identification.

7.2.3 Conductivity and thermogravimetric analysis

A DC 4-probe method was used to measure electrical conductivity of the specimen in flowing air (200 mL/min). The samples for the conductivity measurement were dense bars, which were prepared by pressing the cathode powders followed by sintering at 1200 ºC for 5 h. Following this, samples were polished and silver leads were attached as the current and voltage electrodes. Electrical conductivity was measured using an Autolab PGSTAT20 workstation.

Ionic conductivities were estimated from oxygen permeability tests carried out by gas chromatography (GC).[37] Membranes were fabricated by pelletizing cathode powders (milled for 2 h in alcohol at 400 rpm), followed by sintering at 1200 °C for 10 h and polishing. The relative densities of all samples were over 95%. Subsequently, the dense pellets were sealed in an alumina tube using silver paste. The effective areas of membranes were ~ 65 mm^2 with thicknesses of 0.07 cm. Helium was applied at one side as the sweep gas with a rate of 100 mL/min and the other side was exposed to air. The overall resistance to oxygen permeation was calculated from the following equation:

$$R_{overall} = \frac{RT}{16F^2}\frac{1}{SJ_{O_2}}\left[\ln\left(\frac{P'_{O_2}}{P''_{O_2}}\right)\right] \tag{7.1}$$

R - ideal gas constant

F - Faraday constant

S - valid area of the membrane

J_{O_2} - oxygen permeation flux

P'_{O_2} - oxygen partial pressure at the side of membrane exposed to air

P''_{O_2} - oxygen partial pressure at the sweep side

It was assumed that bulk ionic conduction dominated the oxygen permeation process because of the relative thickness of the membranes, and therefore $R_{overall}$ is roughly equal to R_{ionic}. Hence, the ionic conductivity of the sample was estimated according the following equation:

$$\sigma_{ionic} = \frac{1}{R_{ionic}} \times \frac{S}{L} \approx \frac{1}{R_{overall}} \times \frac{S}{L} \tag{7.2}$$

Where L is the thickness of the membrane

Thermal gravimetric analysis was performed to monitor the weight change of SCNT, SCT20, and SCN20 during the abrupt change of atmosphere from flowing air to nitrogen to instrumental air at 500 ºC. Specimen were pelletized and ground using mortar and pestle to ensure similar grain sizes before the test. Samples were first gradually heated to 200 °C and held for 1 h to remove absorbed moisture. The temperature was then increased at a rate of 1 °C/min to 500 °C in flowing air (20 mL/min). Subsequently, the flowing gas was abruptly switched to nitrogen, and this condition remained for 2 h until the sample weight stabilized. Then, the atmosphere was switched back to air and the weight change recorded until equilibrium was reached. The rate of weight change was estimated by:

$$rateofweightchange = \frac{m_{t+\Delta t} - m_t}{\Delta t} \tag{7.3}$$

Where m_t is the weight of the sample at time t, and Δt is the time interval between two recorded adjacent points.

7.2.4 ORR characterization

Cathode polarization resistance was characterized in a cathode | $Sm_{0.2}Ce_{0.8}O_{1.9}$ (SDC, from Fuel Cell Materials) |cathode symmetrical cell configuration using electrochemical impedance spectroscopy (EIS) carried out using an Autolab PGSTAT20. The symmetrical cells were fabricated by spraying nitrogen-borne cathode slurries onto both sides of SDC dense disks, followed by calcination at

1000 °C for 2 h in stagnant air. Cathode slurries were prepared by suspending powder cathodes in isopropyl alcohol. The thicknesses of cathodes were controlled to be around 10 μm, and the active area of each cathode was ~ 1.15 cm^2. Silver paste was subsequently painted onto both cathode sides as current collector.

We evaluated the performance of the LT-SOFC using anode-supported button-like single cells. The anode powders were prepared by ball milling the NiO, $Ga_{0.1}Ce_{0.9}O_{1.95}$ (GDC, Aldrich) or SDC, and dextrin (pore former) with a weight ratio of 6:4:1 for 20 h in ethanol. The anode-supported single cells were fabricated by spin coating the GDC slurry onto the surface of the anode disks, which were fabricated by pressing anode powders into disks and sintering at 900 °C for 5 h. The GDC slurry for drop coating was prepared by suspending the GDC powders in terpineol and ethanol. The coated disks were subsequently sintered at 1400 °C for 5 h. The fuel cell for SDC-based cell stability test was fabricated using co-press method[4]. The cathode fabrication was carried out following similar steps to those for producing the symmetrical cell. The mechanism of the SCNT ORR was studied by fitting the EIS impedance spectra at different pO_2 to the R_e (R_1CPE_1) (R_2CPE_2) equivalent circuit model by using the LEVM software. The results are presented in the Figure S 7-13. Re represents the ohmic resistance of the electrolyte; (R_1CPE_1) and (R_2CPE_2) stand for the two ORR processes at high frequency and low frequency respectively. The physical meaning of the ORR processes are determined by a parameter m given as follows[38]:

$$\frac{1}{R_p} \propto P_{O_2}^{m} \tag{7.4}$$

R_p is the polarisation resistance of the corresponding ORR processes.

7.2.5 First-principles calculations

The first-principles calculations were performed with the Vienna ab initio simulation package (VASP)[39, 40] using density-functional theory (DFT). Ion-electron interactions were treated using projector-augmented-wave potentials[41] and a generalized gradient approximation (GGA) in the form of Perdew-Burke-Ernzerhof was adopted to describe electron-electron interactions.[42] The GGA+U calculations were performed with the simplified spherically-averaged approach applied to d electrons, where the coulomb (U) and exchange (J) parameters are combined into the single parameter U_{eff} ($U_{eff} = U - J$) which was set to 0.8 eV in these calculations. Electron wave functions were expanded using plane waves with an energy cut-off of 520 eV. The Kohn-Sham equation was solved self-consistently with a convergence of 10^{-5}. The stoichiometry of the simulated systems was set to $SrCo_{0.75}Nb_{0.25}O_3$, $SrCo_{0.75}Ta_{0.25}O_3$, and $SrCo_{0.75}Nb_{0.125}Ta_{0.125}O_3$ respectively due to computational limitation, and the Nb and Ta in SCNT are regarded as ordered instead of randomly distributed for simplification. The Brillouin zone was sampled using a 3×3×3 k-point grid. The minimum energy pathway for V_O migration was determined using a climbing image nudged band method.[43, 44]

7.3 Results & discussion

7.3.1 Structure and cation arrangement of SCNT

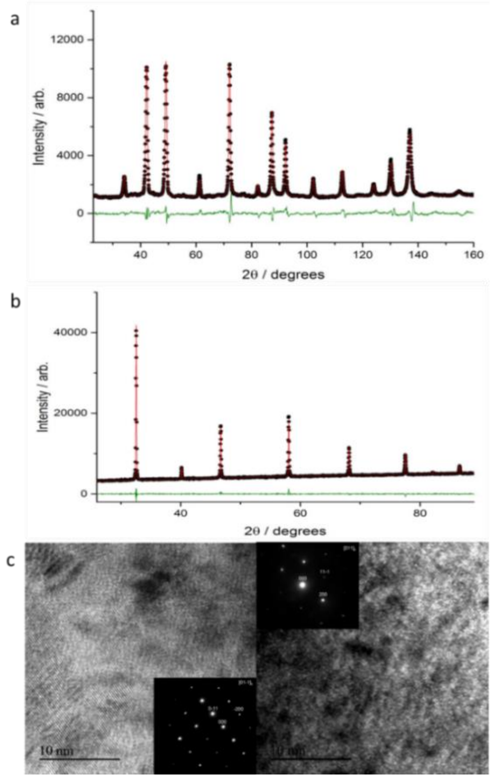

Figure 7-1 Joint Rietveld refinement plot of SCNT powders at room temperature using both neutron powder diffraction (a) and X-ray powder diffraction (b). Data are shown as black dots, the calculation as a red line, and the difference between these two as a green line. (c) High-resolution transmission electron microscopy bright field images of SCNT with selected area electron diffraction patterns shown as insets, in the [01-1] direction on the left and the [011] direction on the right.

Table 7-1 Crystallographic details of SCNT obtained from joint Rietveld refinement against both neutron and X-ray powder diffraction data.

Atom	**Site**	***x***	***y***	***z***	**Occupancy**	**U_{iso} (Å^2)**
Sr	1*b*	0.5	0.5	0.5	1.000	0.012(7)
Co	1*a*	0	0	0	0.831(4)	0.01
Nb	1*a*	0	0	0	0.097(5)	0.01
Ta	1*a*	0	0	0	0.069(5)	0.01
O	3*d*	0.5	0	0	0.944(5)	0.0278(3)
***a* = 3.9066(1) Å, *wR* = 2.44% , Reduced chi squared = 1.76**						

Joint Rietveld analysis of neutron and X-ray powder diffraction data (Figure 7-1(a) and (b)) revealed that the SCNT at room temperature exhibits a cubic perovskite structure with $Pm\bar{3}m$ space-group symmetry and a lattice constant of 3.9066(1) Å (Table 7-1). High-resolution transmission electron microscopy (HRTEM) combined with selected area electron diffraction (SAED) (Figure 7-1(c)) confirms this structure. Moreover, the binding energy of Nb 3d5/2 (206.76 eV) and Ta 4f 7/2 (25.58 eV) in SCNT, as shown in X-ray photoelectron spectroscopy (XPS) profile, indicates that the dopants are both in 5+ valence.[45, 46](Figure S 7-2) The cubic structure of SC is maintained by the co-doping of Nb^{5+} and Ta^{5+} at the Co-site because of their high oxidation states.[25] Rietveld refinement results show Nb and Ta cation doping levels of 9.7(5) and 6.9(5) mol % respectively in SCNT and an oxygen site that is 5.6(5) mol % deficient. Both the cubic perovskite structure and oxygen deficiency are beneficial for oxygen-ion conduction, which is critical for the cathode especially for LT-SOFC application. The former makes oxygen vacancies migrate freely among lattice equivalent oxygen sites[47], while the latter facilitates ionic conduction[48, 49].

ORR activity in symmetrical and single cells

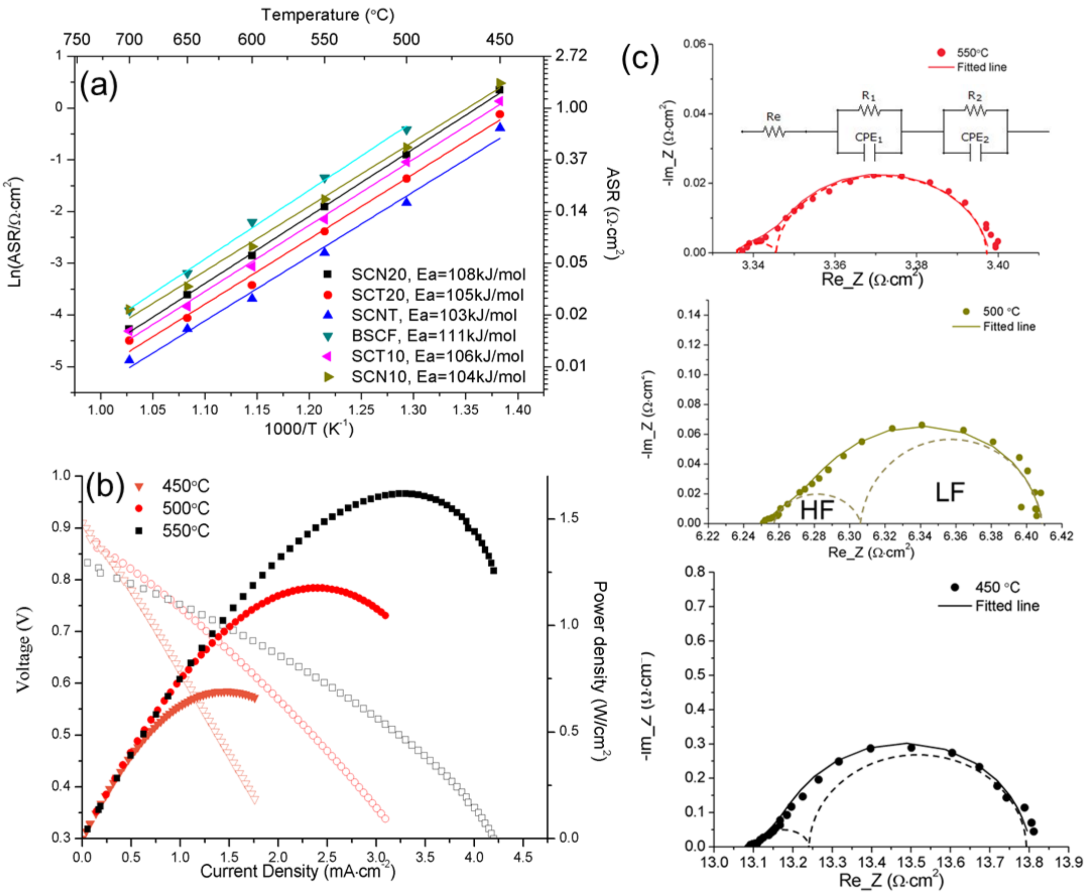

Figure 7-2 (a) Thermal evolution of the ASR of SCNT, $SrCo_{0.9}Nb_{0.1}O_{3-\delta}$ (SCN10), $SrCo_{0.9}Ta_{0.1}O_{3-\delta}$ (SCT10), $SrCo_{0.8}Nb_{0.2}O_{3-\delta}$ (SCN20), $SrCo_{0.8}Ta_{0.2}O_{3-\delta}$ (SCT20), and $Ba_{0.5}Sr_{0.5}Co_{0.8}Fe_{0.2}O_{3-\delta}$ (BSCF) cathodes as prepared and studied under the same conditions. Electrochemical impedance spectroscopy (EIS) results using a $Sm_{0.2}Ce_{0.8}O_{1.9}$ (SDC)-based symmetrical cell. (b) Performance of an anode-supported SCNT | GDC(~14µm) | GDC+Ni single cell at 450, 500, and 550 ºC with H_2 at the anode and flowing air at the cathode. (c) Example Nyquist plots for the SCNT symmetrical cell and the corresponding fitted impedance spectra using a two-process equivalent circuit model.

We determined the ORR activity of SCNT in a symmetrical cell configuration between 450 and 700 ºC using electrochemical impedance spectroscopy (EIS). The ASR, calculated from the intercept difference of EIS impedance with the real axis, is the key variable characterizing the ORR activity, with low ASR indicating high activity. The compatibility of SCNT with $Sm_{0.2}Ce_{0.8}O_{1.9}$ (SDC) and $Gd_{0.1}Ce_{0.9}O_{1.95}$ (GDC) electrolytes was examined by comparing the X-ray diffraction patterns of a 50:50 wt.% powder mixture of the SCNT and electrolyte after heated at the cathode fabrication temperature of 1000 ºC for 2 h (Figure S 7-3(a)). The results revealed no obvious changes to the SCNT after heating with electrolyte, indicating good chemical compatibility between the two. Since the silver current collector does not significantly affect cathode performance[50] and the cathode thickness (~10 μm) proves to be sufficient (Figure S 7-5 (b)), our measured ASRs reflect the ORR activity of the SCNT. Figure 7-2(a) shows that the SCNT cathode exhibits notably high ORR activity at low temperature, with an ASR as low as 0.061-0.086, 0.16-0.23, and 0.68-0.80 $\Omega\cdot cm^2$ at 550, 500, and 450 ºC, respectively. The SCNT cathode outperforms the other reported cathode compositions at below 500 °C.(Table S 7-1)[7, 10, 18, 50-52] For example, the ORR activity of SCNT cathode is nearly twice that of the highly active $SrSc_{0.175}Nb_{0.025}Co_{0.8}O_{3-\delta}$ [10] at 500°C, and is also higher than that of $Ba_{0.9}Co_{0.7}Fe_{0.2}Mo_{0.1}O_{3-\delta}$ [18] at 450 °C.

When examined against other cathodes under our investigation, the SCNT cathode performance was also found to be higher than that of the $SrCo_{0.9}Nb_{0.1}O_{3-\delta}$ (SCN10), $SrCo_{0.9}Ta_{0.1}O_{3-\delta}$ (SCT10), $SrCo_{0.8}Nb_{0.2}O_{3-\delta}$ (SCN20), and $SrCo_{0.8}Ta_{0.2}O_{3-\delta}$ (SCT20) cathode materials having ASRs of 0.476 ± 0.009, 0.353 ± 0.001, 0.63 ± 0.08[53], and 0.25 ± 0.021[53] $\Omega\cdot cm^2$ respectively at 500 °C. Additionally, a lower activation energy (103.1 ± 0.8 kJ/mol) of SCNT was observed relative to that of SCN10 (105.3 ± 1.6 kJ/mol), SCT10 (105.3 ± 0.5 kJ/mol), SCN20 (108.5 ± 0.3 kJ/mol), and SCT20 (105.8±1.5kJ/mol), implying its suitability for catalyzing oxygen reduction at low temperature.

The performance of the SCNT cathode in an LT-SOFC was examined using Ni-SDC|SDC (~ 20 μm) |SCNT (~ 10 μm) (Figure S 7-6) and Ni-GDC|GDC (~ 14 μm)| SCNT (~ 10 μm) fuel cells (Figure 7-2(b)). At 550, 500, and 450 °C, power densities of 1.13, 0.77, and 0.37 W/cm^2 were achieved respectively in the former single cell with ohmic resistances of ~ 0.072, 0.113, and 0.193 $\Omega\cdot cm^2$, which mainly arise from the electrolyte. An electrode polarization resistance (the sum of cathode and anode ASRs) of ~ 0.059, 0.132, and 0.271 $\Omega\cdot cm^2$ was achieved at the respective temperature. Given that SCNT has reasonable chemical compatibility with GDC (Figure S 7-3(b)) and a similar ORR activity with both GDC and SDC electrolyte (Figure S 7-5), GDC was also used in button single cells due to its ease of coating. The button cell was found to generate a peak power density as high as 1.75, 1.22, and 0.7 W/cm^2 at 550, 500, and 450 ºC, respectively, this being significantly higher than that of $Ba_{0.5}Sr_{0.5}Co_{0.8}Fe_{0.2}O_{3-\delta}$ (BSCF) of ~ 0.97, 0.52, and 0.316 W/cm^2 separately (Figure S 7-7). With a thinner GDC electrolyte, the fuel cell ohmic resistance is reduced to 0.033, 0.049, and 0.083 $\Omega\cdot cm^2$ at these temperatures, less than half of that for the SDC (~ 20 μm)-based fuel cell. However, the electrode resistance of the GDC cell is only slightly lower than that of the SDC-based cell, being

0.056, 0.116, and 0.242 Ω·cm^2 at these respective temperatures. Taking into consideration the ease and low-cost of the ceramic fabrication processes involved in the necessary scale-up[5], GDC electrolyte fuel cells were fabricated to a thickness of ~10-14 μm, though further reduction in GDC thickness is expected to boost the single cell performance by lowering its ohmic resistance.[6, 9] Overall, the performance of the SCNT-based fuel cell surpasses the target of 500 mW/cm^2 for SOFCs[54], suggesting the possibility of practical operation even below 450 °C.

7.3.2 Synergistic effects of Nb and Ta on the ORR

Notably, SCNT shows higher ORR activity when compared with the iso-structural SCN20 and SCT20 materials sharing similar lattice constants, with values of 3.9066(1) Å for SCNT (Table 7-1) , 3.8978(2) Å for SCT20, and 3.8971(1) Å for SCN20 obtained from the analysis of the NPD in our previous work[53]. The oxygen vacancy content of SCN20, SCT20 and SCNT as determined from NPD refinement at room temperature is 0.102±0.02, 0.159±0.15 and 0.168±0.15, respectively, reflecting that SCNT and SCT20 have similar oxygen vacancy contents, which are both significantly higher content of oxygen vacancies than that of SCN20. Thermal gravimetric analysis also shows higher oxygen vacancy contents in SCNT and SCT20 than SCN20 at elevated temperature. (Supplementary Fig. S9) Provided the fixed valence of dopants, the valence of reducible Co is likely the main reason for oxygen vacancy concentration difference, so we calculated average valence of cobalt of samples from element contents as determined by the refinement. The average valence of Co is 3.44, 3.33 and 3.41 for SCN20, SCT20 and SCNT, respectively. The lower Co valence in Ta-doped samples can be ascribed to the lower electronegativity of Ta than Nb.[55] In addition, our first-principles calculation result also show that oxygen formation energy are 1.539 eV, 1.456 eV, and 1.512 eV for the Nb-, Ta-, and Nb/Ta-doped models, respectively, which further supports the observed higher oxygen deficiency in SCNT as induced by Ta. Therefore, we can conclude that doping Ta into Nb-doped oxide can lower the average valence of Co, thereby creating more oxygen vacancies. However, it seems insufficient to explain the better performance of SCNT than SCT20 by their oxygen vacancy content difference.

Given the similar particle size (Figure S 7-4) but slightly less electrical conductivity (Figure S 7-10) of SCNT relative to SCN20 and SCT20, the outstanding performance of SCNT as an LT-SOFC cathode is likely go arise from the enhanced ORR-related properties such as bulk oxygen ionic conductivity and oxygen exchange kinetics.

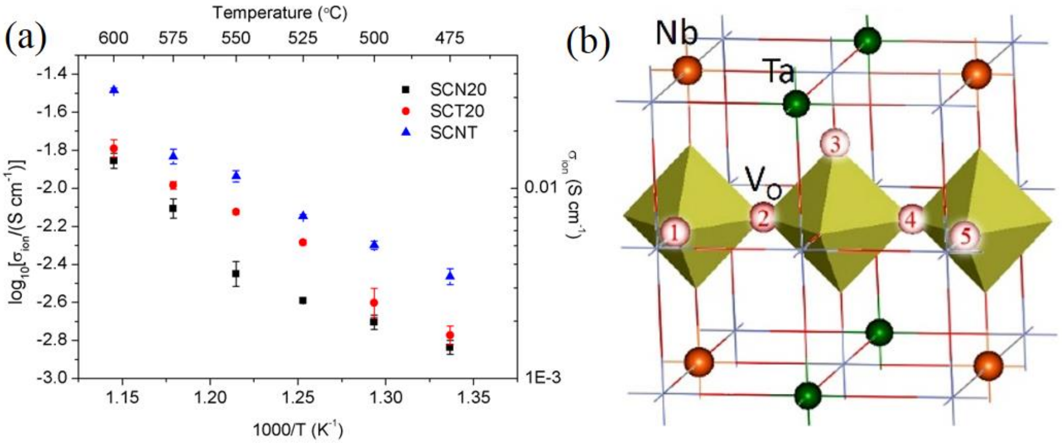

Figure 7-3 (a) Estimated ionic conductivities of SCN20, SCT20, and SCNT membranes with similar dimensions determined by oxygen permeability testing.(b) A schematic of the minimum energy migration pathway for an oxygen vacancy (V_O) in $SrCo_{0.75}Nb_{0.125}Ta_{0.125}O_{3-\delta}$, where dopants are shown by coloured balls and Co along the pathway are inside the octahedrons. Other Co and Sr ions are not drawn in the schematic for clarity

Hence, we estimated ionic conductivity of the SCN20, SCT20, and SCNT by studying the oxygen permeability of dense membranes with similar dimensions from 600 to 475 °C. The higher ionic conductivity (Figure 7-3(a)) of SCNT over SCN20 and SCT20 can be explained by the more oxygen vacancies in SCNT relative to SCN20. Ionic conductivity is known to be significantly affected by lattice geometry, critical radius,[56] and lattice free-volume available for oxygen ions to pass through.[57] Because these three materials have similar lattice dimensions, the faster ionic conduction in SCNT stems from the synergistic effects of Nb and Ta co-doping at the Co site, which potentially decreases the energy barrier for oxygen migration between neighbouring octahedral CoO_6 vacancies, as reported for Sc^{3+} and Nb^{5+} by Zhou *et al.*[10] In order to confirm this hypothesis, we investigated the pathways for an oxygen vacancy migration through first-principles calculations. It is found that the three models have the same minimum energy pathways, as shown in Figure 7-3(b), but different energy barriers. The highest energy barriers along the pathway are 0.433 eV, 0.638 eV, and 0.572 eV for Nb-, Ta-, and co-doped models, respectively, (Table S 7-2), indicating a higher vacancy mobility of Nb/Ta co-doped model as compared to Ta-doped one. Although SCNT and SCT20 have similar oxygen vacancy levels, the higher ionic conductivity of SCNT than SCT20 is likely a result of the incorporation of Nb dopant that can enhance ionic mobility in the lattice.

Additionally, slightly lower electrical conductivity, including both electronic and ionic conductivity with the electronic one dominating, is observed for SCNT compared to SCN20 and SCT20 (Figure S 7-10). The lower electrical conductivity is caused by more oxygen vacancies in SCNT that can diminish the charge carriers for hopping process. By extending the oxygen reduction active region and enhancing the ORR kinetics[49, 58], the higher oxygen vacancy content and improved mobility of SCNT imparted by the co-doping are likely to be more significant factor than electronic conductivity for the outstanding ORR performance of SCNT.

The oxygen surface exchange kinetics were investigated by comparing the O_2-intake time of each sample in response to the atmosphere change from N_2 to air at 500 °C. The SCNT mass equilibrates faster (~ 188 s) in than SCN20 (~ 245 s) and SCT20 (~ 217 s), suggesting a faster oxygen surface exchange of SCNT at lower temperature (Figure S 7-11). Therefore, the Nb and Ta together could also synergistically enhance the surface exchange process by creating more oxygen vacancies and improving ionic mobility.

Table 7-2 Comparison of the ASR at both low frequency (LF) and high frequency (HF) for SCNT, SCT20, and SCN20, and those estimated from impedance spectra in a symmetrical cell in flowing air using an equivalent circuit model with two processes.

Temperature (°C)	ASR_{HF} ($\Omega\cdot cm^2$)			ASR_{LF} ($\Omega\cdot cm^2$)		
	SCNT	**SCT20**	**SCN20**	**SCNT**	**SCT20**	**SCN20**
450	0.14(7)	0.40(4)	0.62(1)	0.53(7)	0.50(4)	1.57(1)
500	0.05(3)	0.12(1)	0.149(2)	0.11(2)	0.13(1)	0.400(2)
550	0.007(7)	0.036(8)	0.057(1)	0.054(1)	0.057(1)	0.123(1)
600	0.003(2)	0.014(6)	0.021(1)	0.022(3)	0.020(8)	0.063(1)
650	0.002(2)	0.007(3)	0.016(1)	0.012(5)	0.010(4)	0.021(1)

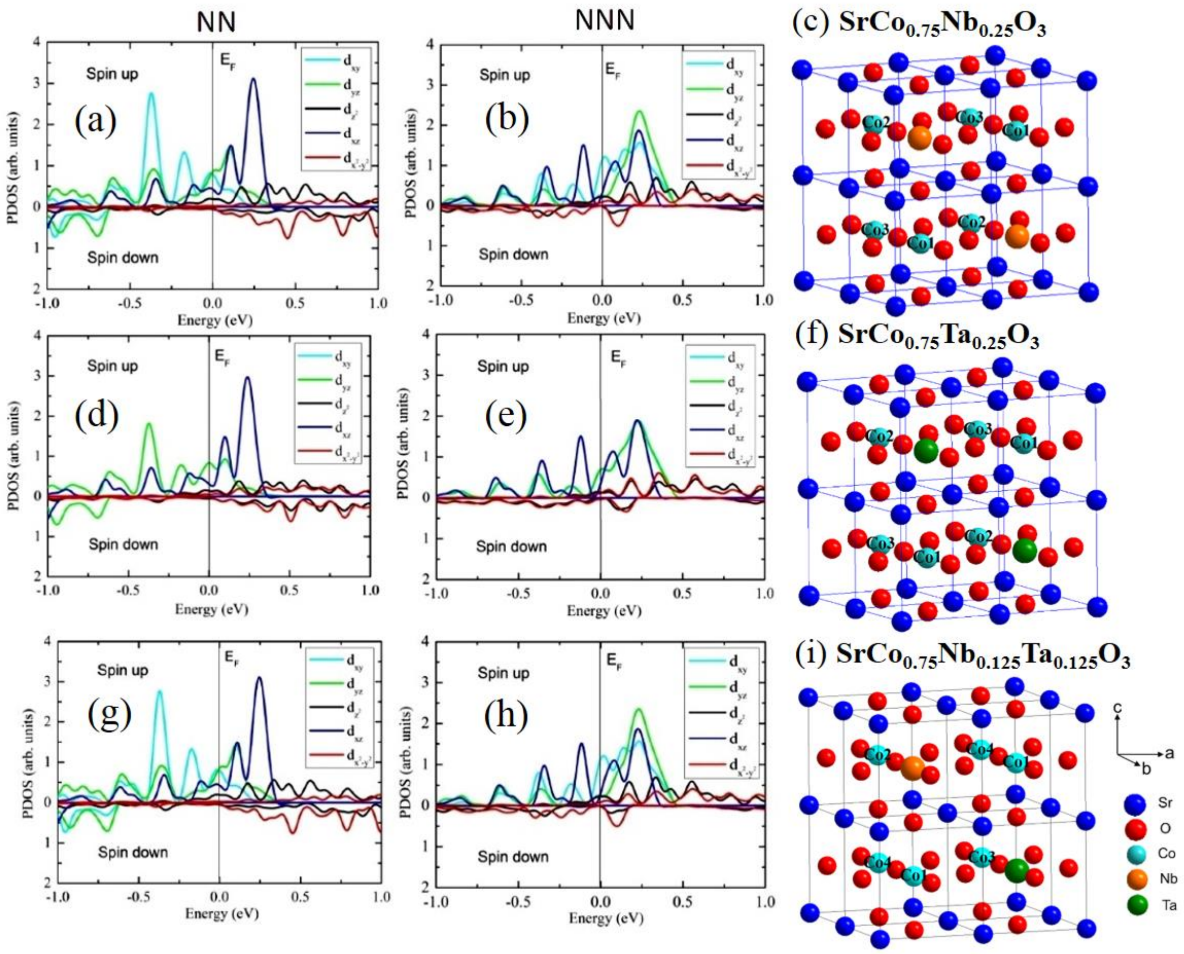

Figure 7-4 Atomic-orbital-resolved electron density of states (PDOS) projected onto the nearest neighbouring (NN) Co atoms (left column) and the next nearest neighbouring (NNN) of Co atoms (middle column) of (a), (b) $SrCo_{0.75}Nb_{0.25}O_{3-\delta}$, (d), (e) $SrCo_{0.75}Ta_{0.25}O_{3-\delta}$ and (g),(h) $SrCo_{0.75}Nb_{0.125}Ta_{0.125}O_{3-\delta}$ perovskite oxides, and the corresponding schematic of unit cells (right column). The energy at the fermi level is set to zero.

We also fitted the impedance spectra of SCNT, SCN20, and SCT20 cathodes to an equivalent circuit model consisting of two dominant reaction processes in order to further probe the mechanisms. An example of the fitting result is presented in Figure 2(c). The arc at high frequencies (HF) is related to the charge transfer and the one at low-frequencies (LF) to non-charge transfer according to Supplementary Fig. S13 and our previous work[53].

$$O_{2,ads} + 2e' + V_{O}^{\bullet\bullet} \Leftrightarrow O_{o}^{\times} \qquad (7.5)$$

Where $O_{2,ads}$ stands for an adsorbed oxygen molecule on cathode surface, e' for an electron, $V_{O}^{\bullet\bullet}$ for an oxygen vacancy and $O_{o}^{\times}$ for an oxygen occupying an oxygen lattice. Table 7-2 summarizes the polarization resistance of these two processes. SCNT exhibits significantly lower ASRs for the charge-transfer process than either SCN20 or SCT20, and nearly half of the resistance of SCN20 but with similar activity for the non-charge transfer process. The fast kinetics for charge transfer can be partly attributed to the proved high oxygen content of SCNT brought by Ta, since oxygen vacancy plays an important role in the charge-transfer process as shown in (7.5).

On the other hand, since Nb^{5+} and $Ta^{5+}$are inert to oxygen surface redox processes due to their fixed valence, Co atom plays a vital role in catalysing oxygen reduction. Therefore, we calculated the atomic-orbital-resolved electron density of states (PDOS) projected onto the Co atom in Nb, Ta, and Nb/Ta co-doped strontium cobalt oxides using first-principles calculations. As shown in schematic models (Figure 7-4 (c), (f) for Nb or Ta single-doped models and Figure 4(i) for co-doped model), There are two categories of cobalt atoms: one is the nearest neighbour (NN) Co to the dopant, including Co1, Co2 for single-doped model and Co1, Co2, Co3 for co-doped model; the other is the next nearest neighbour (NNN) Co to the dopants, including Co3 for single-doped model and Co4 for co-doped one. The NN-Co atoms have very similar density of states (DOS) near the Fermi level for these three models. For the NNN-Co atoms, Ta-doped model exhibits only 60% of DOS of Nb-doped model near the Fermi level, indicating that Nb is more favourable to increase the DOS of the NNN-Co near the Fermi level. Due to the beneficial effect from Nb, the DOS of NNN-Co near Fermi level for the co-doped model shows ~ 98% that of Nb-doped model. The enhanced DOS at Fermi level can make electron transfer more efficient,[59] and thereby contribute to an improved charge-transfer process. Therefore, it is likely that the higher DOS of NNN-Co ions near Fermi level as induced by Nb is the reason for the higher kinetics of charge-transfer steps of SCNT than that of SCT20, in spite of their similar concentration of oxygen vacancies.

Our experimental and calculation results reveal that the superior electroactivity of SCNT is a result of optimised balance of oxygen vacancy content, oxygen ion mobility and enhanced electron transfer processes, which are imparted by co-doping Nb and Ta.

7.3.3 Stability tests

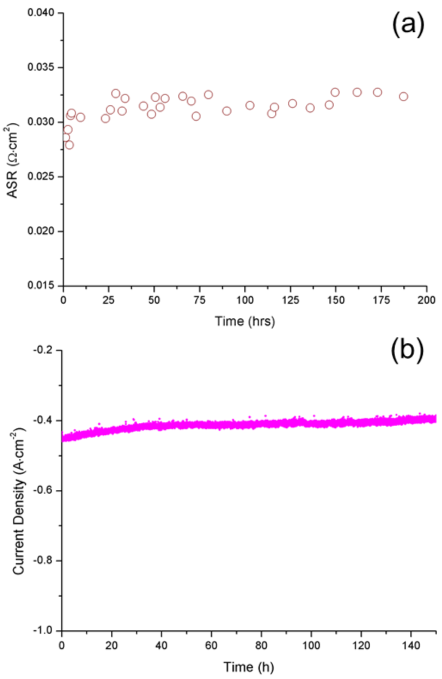

Figure 7-5 (a) ASRs of SCNT in a symmetrical cell under open circuit conditions at 600 ºC for 200 h (b) current density of a SCNT | SDC (~ 20 µm) | Ni + SDC single cell under 0.7 V polarization in air at 450 °C for 150 h.

The durability of the cathode was investigated in both symmetrical and single cell configurations, as shown in Figure 7-5. The ASR of SCNT within a symmetrical cell was tested under the open circuit condition for approximately 200 h. The ORR activity was relatively stable at ~ 0.033 Ω·cm^2 with an ASR increase of ~0.06% /h during the testing period. The slight increase of ASR during the stability test is likely to arise from the densification and the reduced porosity of the silver current collector, which degrades the overall cathode performance during this testing timeframe.[60-62] Another short-term stability evaluation of the SCNT cathode in a single cell configuration with ~ 20 µm thick SDC electrolyte also showed that the SCNT is stable under 0.7 V polarization for at least 150 h at 450 ºC in air. The low current density noted in the stability testing arises from the electrolyte thickness, which leads to high ohmic resistance. The stable ORR activity of SCNT is expected given its stable perovskite lattice (Figure S 7-12).

7.4 Conclusions

In summary, the novel perovskite composition $SrCo_{0.8}Nb_{0.1}Ta_{0.1}O_{3-\delta}$ (SCNT) has been synthesized and exhibits the highest reported activity for the reduction of oxygen in an LT-SOFC by far, with an ASR of only ~ 0.16 and ~0.68 $\Omega\cdot cm^2$ at 500 and 450 ºC respectively in a symmetrical cell configuration. High power density is therefore achieved using a pure SCNT cathode as a result of its outstanding ORR performance. A performance comparison amongst iso-structural SCNT, $SrCo_{0.8}Nb_{0.2}O_{3-\delta}$ (SCN20), and $SrCo_{0.8}Ta_{0.2}O_{3-\delta}$ (SCT20) cathodes reveals enhancement of the bulk oxygen ionic-conductivity achieved through co-doping of Nb^{5+} and Ta^{5+}. Our experimental results and density functional theory calculations both show that co-doping can result in an optimised balance of oxygen vacancy content, ion mobility and surface electron transfer ability, which is consistent with the higher performance of the co-doped SCNT cathode at lower temperature. Therefore, our highly active perovskite cathode not only presents a simple solution to address sluggish cathode kinetics below 500 °C, but also provides an effective doping strategy for the design of mixed-conducting materials for SOFC and oxygen-ion transport membrane applications at low temperature.

Acknowledgement

The authors appreciate the technical support from the Centre for Microscopy and Microanalysis at the University of Queensland, and neutron scattering study at ANSTO.

This work is financially supported by Australian Research Council (DP130102151) and author Mengran Li acknowledges additional financial support from the scholarship from China Scholarship Council. Prof. Zhu acknowledges the Open Funding from State Key Laboratory of Material – oriented Chemical Engineering (No. KL15-04).

7.5 Supplementary Information

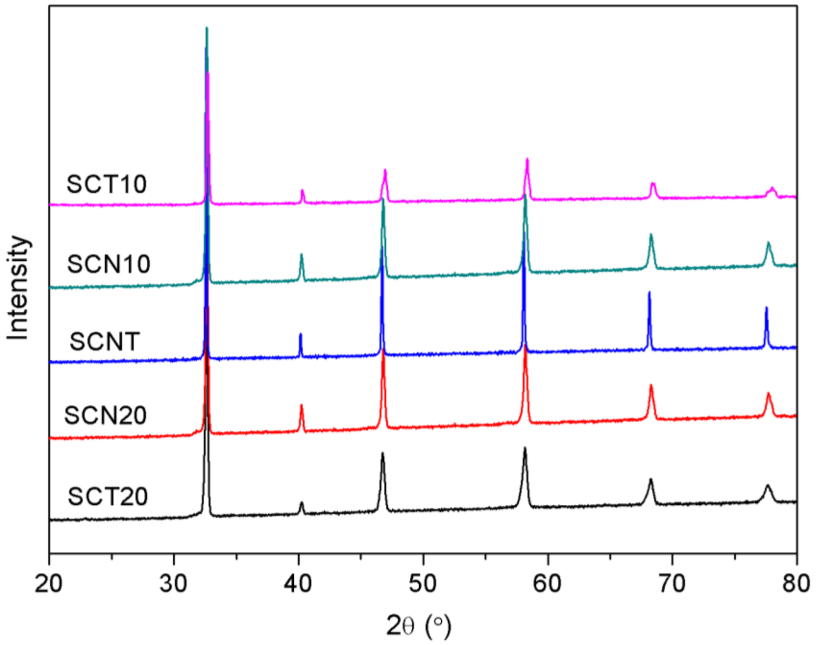

Figure S 7-1 X-ray (CuK$_\alpha$) diffraction patterns of SCNT, SCN20, SCT20, SCN10 and SCT10 at room temperature.

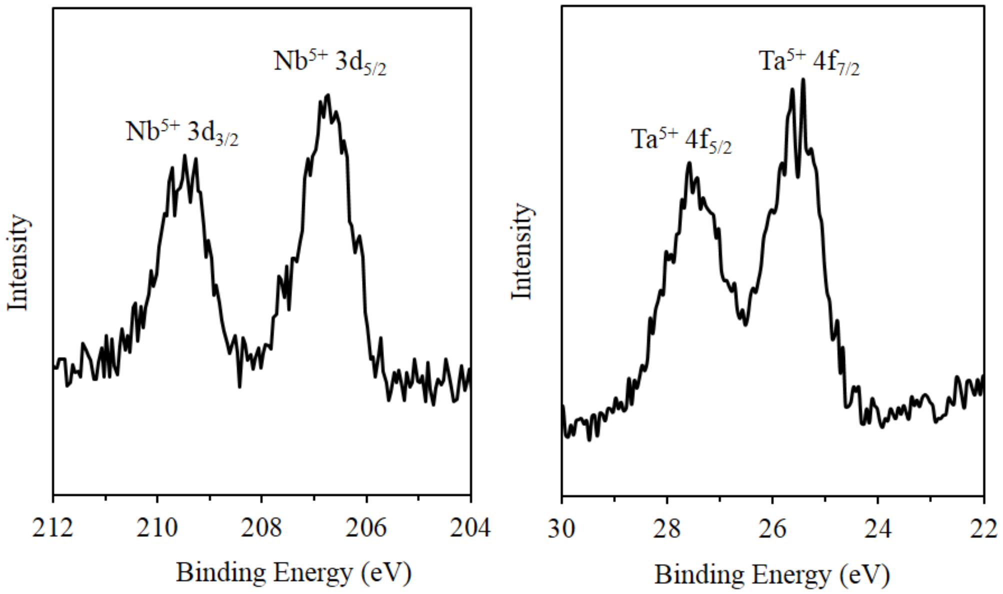

Figure S 7-2 X-ray photoelectron spectroscopy profile of Nb and Ta of SCNT at room temperature.

Table S 7-1 Comparison of ASR values between SCNT and other highly active cathode compositions in literatures.

Cathode Material Compositions	Area specific resistance ($\Omega\cdot cm^2$)	Reference
$SrCo_{0.8}Nb_{0.1}Ta_{0.1}O_{3-\delta}$	~0.16 @500°C ~0.68 @450°C	This work
$Ba_2Bi_{0.1}Sc_{0.2}Co_{1.7}O_{6-\delta}$	~1.50 @ 500°C	51
$SrSc_{0.175}Nb_{0.025}Co_{0.8}O_{3-\delta}$	~0.32 @500°C	10
$NdBa_{0.75}Ca_{0.25}Co_{0.25}Co_2O_{5+\delta}$	~0.67 @500°C	7
$Ba_{0.9}Co_{0.7}Fe_{0.2}Mo_{0.1}O_{3-\delta}$	~0.28 @500°C ~1.09 @450°C	18
$Ba_{0.5}Sr_{0.5}Co_{0.8}Fe_{0.2}O_{3-\delta}$	~0.50 @500°C	50
$SrSc_{0.2}Co_{0.8}O_{3-\delta}$	~0.45 @500°C	52

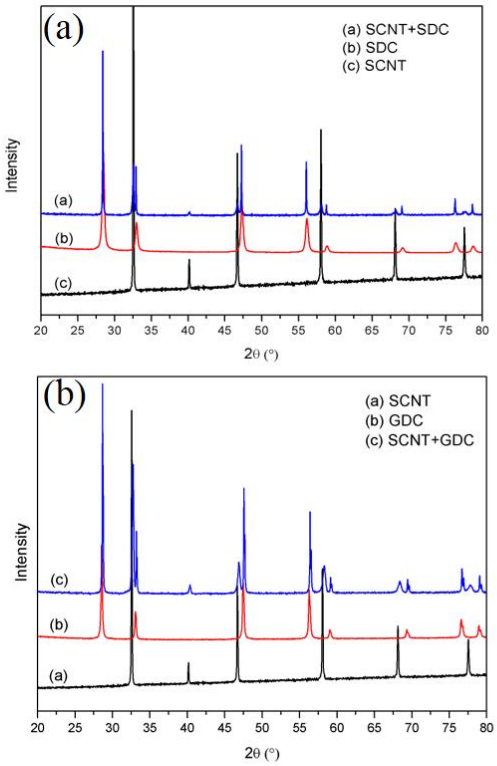

Figure S 7-3 X-ray diffraction data of (a) pure SCNT, SDC, and a 50:50 wt% SCNT/SDC mixture after 2 h sintering at 1000 ºC; (b) pure SCNT, GDC, and a 50:50 wt% SCNT/GDC mixture after 2 h sintering at 1000 ºC. The mixture was made by mechanically mixing the powders SCNT and SDC (or GDC) at room temperature.

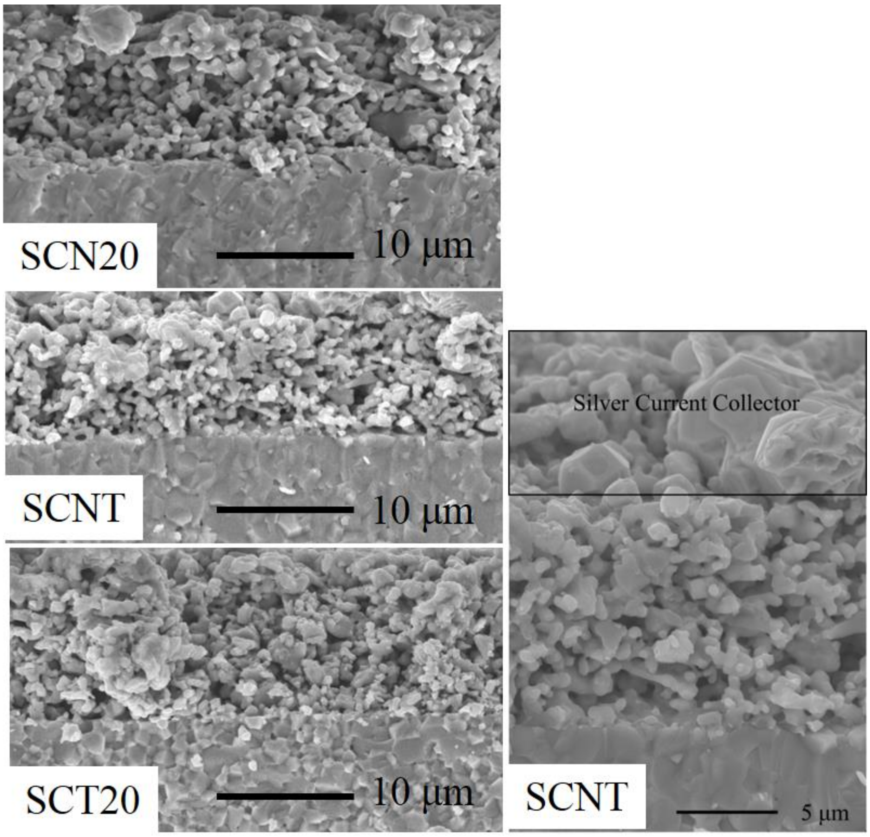

Figure S 7-4 Cross sectional SEM images of SCNT, SCN20, and SCT20 cathodes in a symmetrical cell configuration.

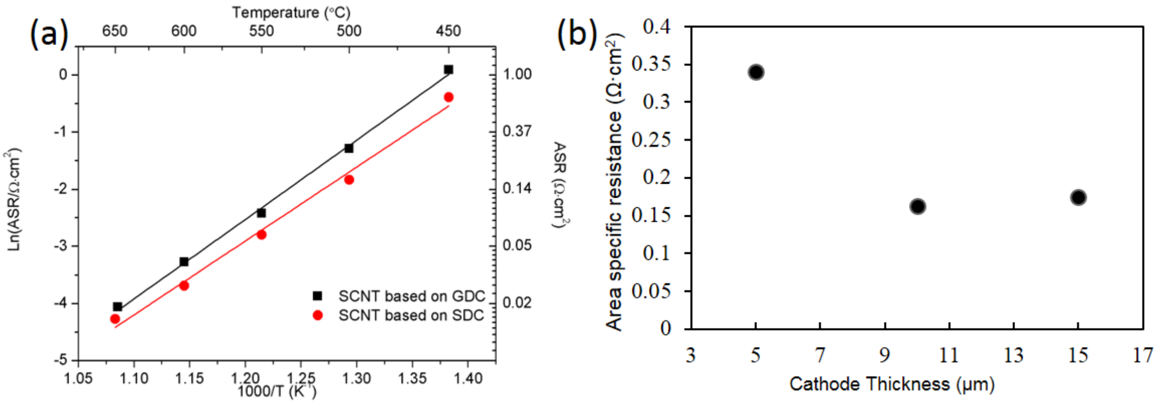

Figure S 7-5 ASRs of the SCNT cathode in SDC and GDC-based symmetrical cells as a function of temperature. (b) ASRs of SCNT cathodes with different cathode thicknesses based on SDC electrolyte

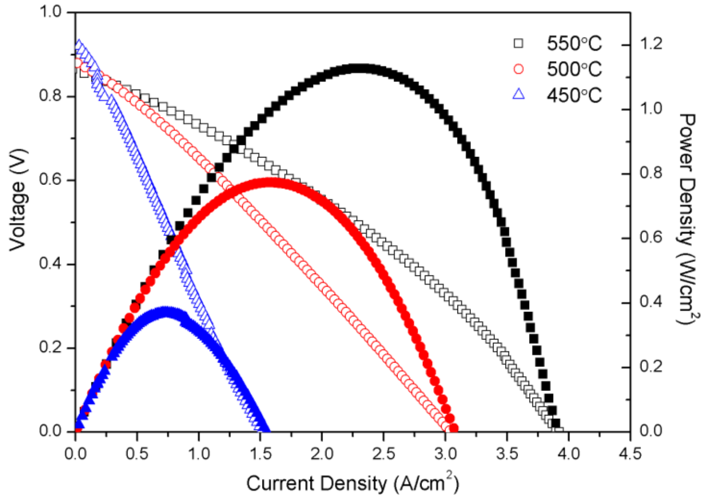

Figure S 7-6 Single-cell performance of a SCNT| SDC (~20µm)| Ni+SDC cell.

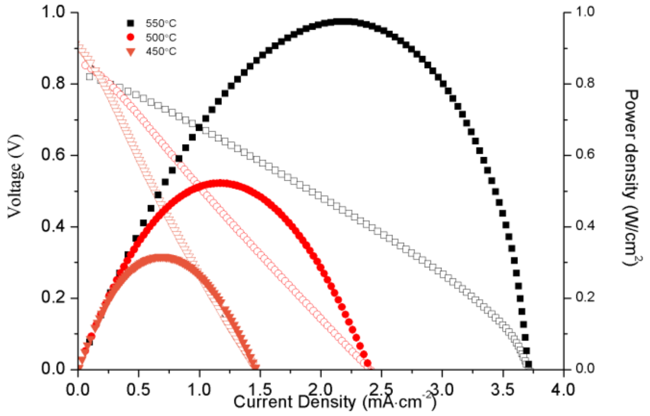

Figure S 7-7 Single cell performance of a BSCF|GDC(~14µm) | Ni+GDC cells showing a performance that is similar to that reported for BSCF-based SOFCs.[50, 63]

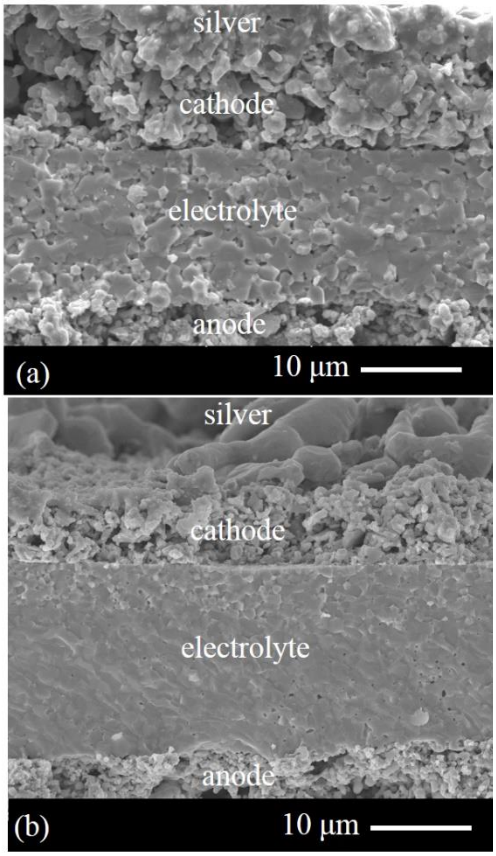

Figure S 7-8 SEM image of (a) an anode-supported single cell with GDC electrolyte (~ 14 µm) and SCNT cathode and (b) the SCNT-based single cell after stability testing (electrolyte thickness ~ 20 µm).

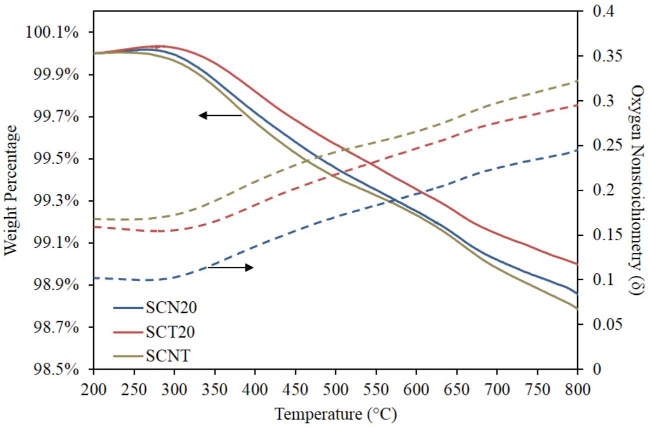

Figure S 7-9 Mass and oxygen nonstoichiometry change of $SrCo_{0.8}Nb_{0.2}O_{3-\delta}$ (SCN20), $SrCo_{0.8}Ta_{0.2}O_{3-\delta}$ (SCT20) and $SrCo_{0.8}Nb_{0.1}Ta_{0.1}O_{3-\delta}$ (SCNT) as a function of temperature in the flowing air with a flow rate of 20mL/min

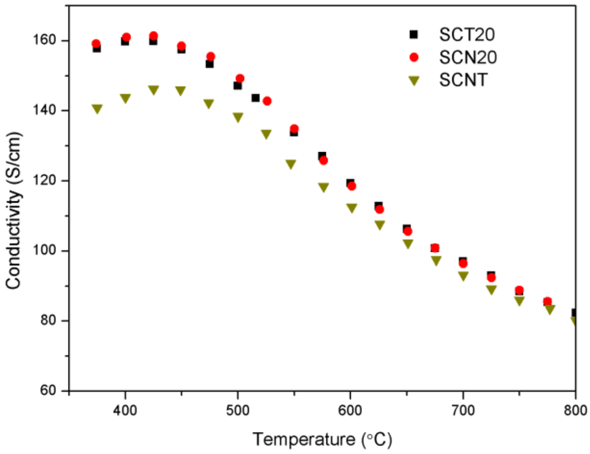

Figure S 7-10 Electrical conductivity of SCN20, SCT20, and SCNT samples using 4-probe DC method as a function of temperature.

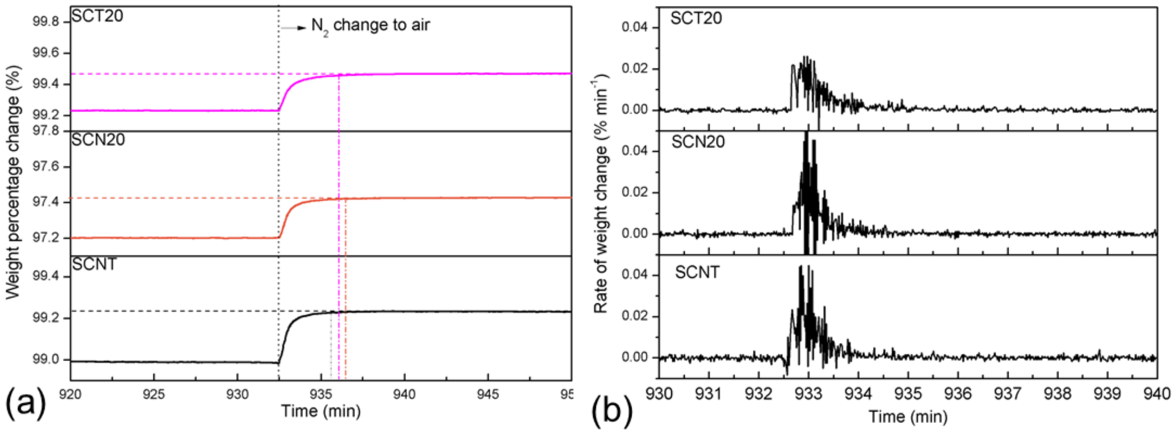

Figure S 7-11(a) Percentage weight change and (b) the corresponding rate of weight change, of SCN20, SCT20, and SCNT heated to 500 °C during a change of atmosphere from flowing nitrogen to flowing air . The weight change is a result of the intake of oxygen into the sample from the ambient air, with SCNT reaching equilibrium in the shortest time (~ 188 s) compared with SCN20 (~ 245 s) and SCT20 (~ 217s).

Table S 7-2 The energy barriers of an oxygen vacancy migrating along the pathway with minimum energy barriers

	①-②	②-③	③-④	④-⑤
$SrCo_{0.75}Nb_{0.25}O_{3-\delta}$	**0.433**	0.322	0.406	**0.433**
$SrCo_{0.75}Ta_{0.25}O_{3-\delta}$	**0.638**	0.442	0.525	**0.638**
$SrCo_{0.75}Nb_{0.125}Ta_{0.125}O_{3-\delta}$	**0.572**	0.323	0.437	0.228

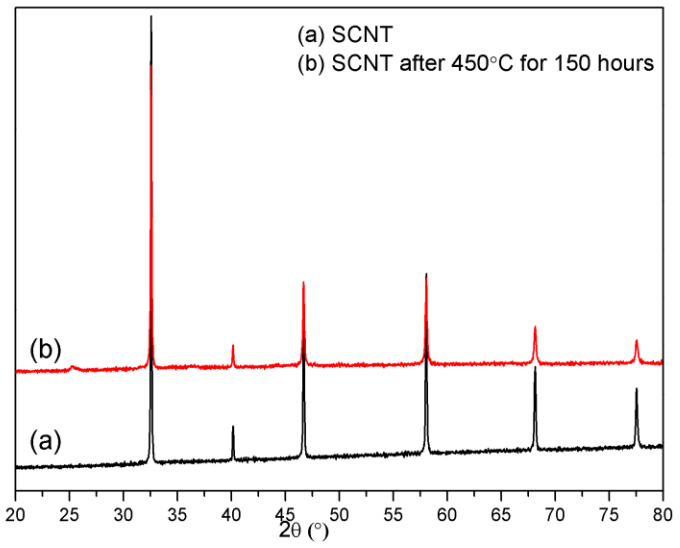

Figure S 7-12 XRD patterns of SCNT before and after heat treatment at 450 °C for 150 h.

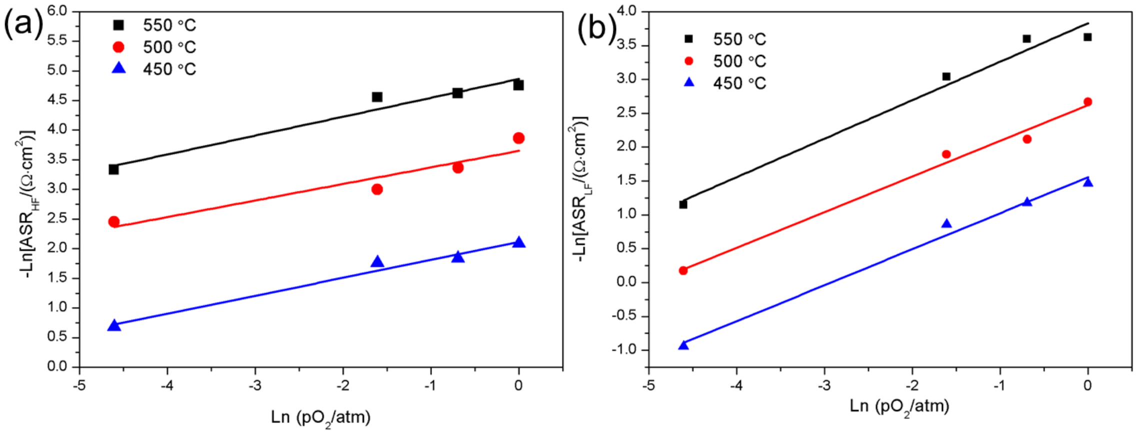

Figure S 7-13 ASR values of SCNT cathode corresponding to processes at (a) high frequencies and (b) frequencies as a function of pO_2 from 550°C to 450 °C. The slope m for $-\ln(ASR_{HF})\sim\ln(pO_2)$ is 0.28-0.32, which is close to 0.25, indicating that the process at high frequencies is related to charge-transfer process to the absorbed oxygen species. The slope for low frequencies is 0.53-0.57, suggesting non-charge-transfer process.[38]

7.6 References

1. Wachsman, E. D.; Lee, K. T., Lowering the Temperature of Solid Oxide Fuel Cells. *Science* **2011,** 334, (6058), 935-939.

2. Minh, N. Q., Ceramic Fuel Cells. *Journal of the American Ceramic Society* **1993,** 76, (3), 563-588.

3. Hibino, T.; Hashimoto, A.; Inoue, T.; Tokuno, J.-i.; Yoshida, S.-i.; Sano, M., A Low-Operating-Temperature Solid Oxide Fuel Cell in Hydrocarbon-Air Mixtures. *Science* **2000,** 288, (5473), 2031-2033.

4. Shao, Z. P.; Haile, S. M., A High-performance Cathode for the Next Generation of Solid-oxide Fuel Cells. *Nature* **2004,** 431, (7005), 170-173.

5. Steele, B. C.; Heinzel, A., Materials for Fuel-Cell Technologies. *Nature* **2001,** 414, (6861), 345-352.

6. Lee, J. G.; Park, J. H.; Shul, Y. G., Tailoring Gadolinium-Doped Ceria-Based Solid Oxide Fuel Cells to Achieve 2 W Cm^{-2} at 550 °C. *Nature Communications* **2014,** 5.

7. Yoo, S.; Jun, A.; Ju, Y.-W.; Odkhuu, D.; Hyodo, J.; Jeong, H. Y.; Park, N.; Shin, J.; Ishihara, T.; Kim, G., Development of Double-Perovskite Compounds as Cathode Materials for Low-Temperature Solid Oxide Fuel Cells. *Angewandte Chemie International Edition* **2014,** 53, (48), 13064-13067.

8. Zhang, X.; Liu, L.; Zhao, Z.; Tu, B.; Ou, D.; Cui, D.; Wei, X.; Chen, X.; Cheng, M., Enhanced Oxygen Reduction Activity and Solid Oxide Fuel Cell Performance with a Nanoparticles-Loaded Cathode. *Nano Letters* **2015,** 15, (3), 1703-1709.

9. An, J.; Kim, Y.-B.; Park, J.; Gür, T. M.; Prinz, F. B., Three-Dimensional Nanostructured Bilayer Solid Oxide Fuel Cell with 1.3 W/cm^2 at 450 °C. *Nano Letters* **2013,** 13, (9), 4551-4555.

10. Zhou, W.; Sunarso, J.; Zhao, M.; Liang, F.; Klande, T.; Feldhoff, A., A Highly Active Perovskite Electrode for the Oxygen Reduction Reaction Below 600 °C. *Angewandte Chemie International Edition* **2013,** 52, (52), 14036-14040.

11. Lee, K. T.; Lidie, A. A.; Yoon, H. S.; Wachsman, E. D., Rational Design of Lower-Temperature Solid Oxide Fuel Cell Cathodes Via Nanotailoring of Co-Assembled Composite Structures. *Angewandte Chemie International Edition* **2014,** 53, (49), 13463-13467.

12. Choi, S.; Yoo, S.; Kim, J.; Park, S.; Jun, A.; Sengodan, S.; Kim, J.; Shin, J.; Jeong, H. Y.; Choi, Y., Highly Efficient and Robust Cathode Materials for Low-Temperature Solid Oxide Fuel Cells: $PrBa_{0.5}Sr_{0.5}Co_{2-x}Fe_xO_{5+\delta}$. *Scientific reports* **2013,** 3.

13. Choi, S.; Park, S.; Shin, J.; Kim, G., The Effect of Calcium Doping on the Improvement of Performance and Durability in a Layered Perovskite Cathode for Intermediate-Temperature Solid Oxide Fuel Cells. *Journal of Materials Chemistry A* **2015,** 3, (11), 6088-6095.

14. Chen, D.; Chen, C.; Zhang, Z.; Baiyee, Z. M.; Ciucci, F.; Shao, Z., Compositional Engineering of Perovskite Oxides for Highly Efficient Oxygen Reduction Reactions. *ACS Applied Materials & Interfaces* **2015,** 7, (16), 8562-8571.

15. Chiba, R.; Yoshimura, F.; Sakurai, Y., An investigation of LaNi1-xFexO3 as a cathode material for solid oxide fuel cells. *Solid State Ionics* **1999,** 124, (3-4), 281-288.

16. Adler, S. B., Factors Governing Oxygen Reduction in Solid Oxide Fuel Cell Cathodes†. *Chemical Reviews* **2004,** 104, (10), 4791-4844.

17. Richter, J.; Holtappels, P.; Graule, T.; Nakamura, T.; Gauckler, L., Materials Design for Perovskite SOFC Cathodes. *Monatshefte für Chemie - Chemical Monthly* **2009,** 140, (9), 985-999.

18. Huang, S.; Lu, Q.; Feng, S.; Li, G.; Wang, C., $Ba_{0.9}Co_{0.7}Fe_{0.2}Mo_{0.1}O_{3-\delta}$: A Promising Single-Phase Cathode for Low Temperature Solid Oxide Fuel Cells. *Advanced Energy Materials* **2011,** 1, (6), 1094-1096.

19. Xia, C.; Rauch, W.; Chen, F.; Liu, M., $Sm_{0.5}Sr_{0.5}CoO_3$ Cathodes for Low-Temperature SOFCs. *Solid State Ionics* **2002,** 149, (1–2), 11-19.

20. Esquirol, A.; Brandon, N. P.; Kilner, J. A.; Mogensen, M., Electrochemical Characterization of $La_{0.6}Sr_{0.4}Co_{0.2}Fe_{0.8}O_3$ Cathodes for Intermediate-Temperature SOFCs. *Journal of the Electrochemical Society* **2004,** 151, (11), A1847-A1855.

21. Wang, W. G.; Mogensen, M., High-performance Lanthanum-ferrite-based Cathode for SOFC. *Solid State Ionics* **2005,** 176, (5-6), 457-462.

22. Zhou, W.; Ran, R.; Shao, Z., Progress in understanding and development of Ba0.5Sr0.5Co0.8Fe0.2O3−δ-based cathodes for intermediate-temperature solid-oxide fuel cells: A review. *Journal of Power Sources* **2009,** 192, (2), 231-246.

23. Jeen, H.; Choi, W. S.; Biegalski, M. D.; Folkman, C. M.; Tung, I. C.; Fong, D. D.; Freeland, J. W.; Shin, D.; Ohta, H.; Chisholm, M. F.; Lee, H. N., Reversible Redox Reactions in An Epitaxially Stabilized $SrCoO_x$ Oxygen Sponge. *Nat Mater* **2013,** 12, (11), 1057-1063.

24. Kharton, V.; Yaremchenko, A.; Kovalevsky, A.; Viskup, A.; Naumovich, E.; Kerko, P., Perovskite-type Oxides for High-temperature Oxygen Separation Membranes. *Journal of Membrane Science* **1999,** 163, (2), 307-317.

25. Nagai, T.; Ito, W.; Sakon, T., Relationship between Cation Substitution and Stability of Perovskite Structure in $SrCoO_{3-\delta}$-Based Mixed Conductors. *Solid State Ionics* **2007,** 177, (39–40), 3433-3444.

26. Cascos, V.; Martínez-Coronado, R.; Alonso, J. A., New Nb-doped $SrCo_{1-x}Nb_xO_{3-\delta}$ Perovskites Performing as Cathodes in Solid-oxide Fuel Cells. *International Journal of Hydrogen Energy*, (0).

27. Zhou, W.; Jin, W. Q.; Zhu, Z. H.; Shao, Z. P., Structural, Electrical and Electrochemical Characterizations of $SrNb_{0.1}Co_{0.9}O_{3-\delta}$ as a Cathode of Solid Oxide Fuel Cells Operating Below 600°C *International Journal of Hydrogen Energy* **2010,** 35, (3), 1356-1366.

28. Aguadero, A.; Pérez-Coll, D.; Alonso, J. A.; Skinner, S. J.; Kilner, J., A New Family of Mo-Doped $SrCoO_{3-\delta}$ Perovskites for Application in Reversible Solid State Electrochemical Cells. *Chemistry of Materials* **2012,** 24, (14), 2655-2663.

29. Aguadero, A.; Alonso, J. A.; Pérez-Coll, D.; de la Calle, C.; Fernández-Díaz, M. a. T.; Goodenough, J. B., $SrCo_{0.95}Sb_{0.05}O_{3-\delta}$ as Cathode Material for High Power Density Solid Oxide Fuel Cells. *Chemistry of Materials* **2009,** 22, (3), 789-798.

30. Aguadero, A.; Perez-Coll, D.; De la Calle, C.; Alonso, J.; Escudero, M.; Daza, L., $SrCo_{1-x}Sb_x O_{3-\delta}$ Perovskite Oxides as Cathode Materials in Solid Oxide Fuel Cells. *Journal of Power Sources* **2009,** 192, (1), 132-137.

31. Li, M.; Zhou, W.; Xu, X.; Zhu, Z., $SrCo_{0.85}Fe_{0.1}P_{0.05}O_{3-\delta}$ Perovskite as a Cathode for Intermediate-Temperature Solid Oxide Fuel Cells. *Journal of Materials Chemistry A* **2013,** 1, (43), 13632-13639.

32. Hancock, C. A.; Slade, R. C. T.; Varcoe, J. R.; Slater, P. R., Synthesis, Structure and Conductivity of Sulfate and Phosphate Doped $SrCoO_3$. *Journal of Solid State Chemistry* **2011,** 184, (11), 2972-2977.

33. Aguadero, A.; Calle, C. d. l.; Alonso, J. A.; Escudero, M. J.; Fernández-Díaz, M. T.; Daza, L., Structural and Electrical Characterization of the Novel $Srco_{0.9}Sb_{0.1}O_{3-\delta}$ Perovskite: Evaluation as a Solid Oxide Fuel Cell Cathode Material. *Chemistry of Materials* **2007,** 19, (26), 6437-6444.

34. Zhu, Y.; Sunarso, J.; Zhou, W.; Jiang, S.; Shao, Z., High-performance $SrNb_{0.1}Co_{0.9-x}Fe_xO_{3-\delta}$ Perovskite Cathodes for Low-temperature Solid Oxide Fuel Cells. *Journal of Materials Chemistry A* **2014,** 2, (37), 15454-15462.

35. Liss, K.-D.; Hunter, B.; Hagen, M.; Noakes, T.; Kennedy, S., Echidna—the new high-resolution powder diffractometer being built at OPAL. *Physica B: Condensed Matter* **2006,** 385–386, Part 2, (0), 1010-1012.

36. Toby, B. H.; Von Dreele, R. B., GSAS-II: the Genesis of a Modern Open-source All Purpose Crystallography Software Package. *Journal of Applied Crystallography* **2013,** 46, (2), 544-549.

37. Zeng, P.; Chen, Z.; Zhou, W.; Gu, H.; Shao, Z.; Liu, S., Re-evaluation of $Ba_{0.5}Sr_{0.5}Co_{0.8}Fe_{0.2}O_{3-\delta}$ Perovskite as Oxygen Semi-permeable Membrane. *Journal of Membrane Science* **2007,** 291, (1–2), 148-156.

38. Takeda, Y.; Kanno, R.; Noda, M.; Tomida, Y.; Yamamoto, O., Cathodic polarization phenomena of perovskite oxide electrodes with stabilized zirconia. *Journal of The Electrochemical Society* **1987,** 134, (11), 2656-2661.

39. Kresse, G.; Hafner, J., *Ab initio* molecular dynamics for liquid metals. *Physical Review B* **1993,** 47, (1), 558-561.

40. Kresse, G.; Furthmüller, J., Efficient Iterative Schemes for *ab initio* Total-energy Calculations using A Plane-wave Basis Set. *Physical Review B* **1996,** 54, (16), 11169-11186.

41. Kresse, G.; Joubert, D., From Ultrasoft Pseudopotentials to the Projector Augmented-wave Method. *Physical Review B* **1999,** 59, (3), 1758-1775.

42. Perdew, J. P.; Burke, K.; Ernzerhof, M., Generalized Gradient Approximation Made Simple. *Physical Review Letters* **1996,** 77, (18), 3865-3868.

43. Henkelman, G.; Uberuaga, B. P.; Jónsson, H., A Climbing Image Nudged Elastic Band Method for Finding Saddle Points and Minimum Energy Paths. *The Journal of Chemical Physics* **2000,** 113, (22), 9901-9904.

44. Henkelman, G.; Jónsson, H., Improved Tangent Estimate in the Nudged Elastic Band Method for Finding Minimum Energy Paths and Saddle Points. *The Journal of Chemical Physics* **2000,** 113, (22), 9978-9985.

45. Bahl, M., ESCA studies of some niobium compounds. *Journal of Physics and Chemistry of Solids* **1975,** 36, (6), 485-491.

46. Ho, S.-F.; Contarini, S.; Rabalais, J., Ion-beam-induced chemical changes in the oxyanions (Moyn-) and oxides (Mox) where M= chromium, molybdenum, tungsten, vanadium, niobium and tantalum. *Journal of Physical Chemistry* **1987,** 91, (18), 4779-4788.

47. Adler, S.; Russek, S.; Reimer, J.; Fendorf, M.; Stacy, A.; Huang, Q.; Santoro, A.; Lynn, J.; Baltisberger, J.; Werner, U., Local structure and oxide-ion motion in defective perovskites. *Solid State Ionics* **1994,** 68, (3), 193-211.

48. Iwahara, H., Ionic Conduction in Perovskite-Type Compounds. In *Perovskite Oxide for Solid Oxide Fuel Cells*, Ishihara, T., Ed. Springer US: 2009; pp 45-63.

49. Adler, S. B., Factors Governing Oxygen Reduction in Solid Oxide Fuel Cell Cathodes. *Chemical Reviews* **2004,** 104, (10), 4791-4844.

50. Shao, Z.; Haile, S. M., A High-Performance Cathode for the Next Generation of Solid-Oxide Fuel Cells. *Nature* **2004,** 431, (7005), 170-173.

51. Zhou, W.; Sunarso, J.; Chen, Z.-G.; Ge, L.; Motuzas, J.; Zou, J.; Wang, G.; Julbe, A.; Zhu, Z., Novel B-site ordered double perovskite Ba2Bi0.1Sc0.2Co1.7O6-x for highly efficient oxygen reduction reaction. *Energy & Environmental Science* **2011,** 4, (3), 872-875.

52. Zhou, W.; Shao, Z.; Ran, R.; Cai, R., Novel $SrSc_{0.2}Co_{0.8}O_{3-\delta}$ as a Cathode Material for Low Temperature Solid-Oxide Fuel Cell. *Electrochemistry Communications* **2008,** 10, (10), 1647-1651.

53. Li, M.; Zhou, W.; Peterson, V. K.; Zhao, M.; Zhu, Z., A comparative study of SrCo0.8Nb0.2O3-[small delta] and SrCo0.8Ta0.2O3-[small delta] as low-temperature solid oxide fuel cell cathodes: effect of non-geometry factors on the oxygen reduction reaction. *Journal of Materials Chemistry A* **2015,** 3, (47), 24064-24070.

54. Brandon, N. P.; Skinner, S.; Steele, B. C. H., Recent Advances in Materials for Fuel Cells. *Annual Review of Materials Research* **2003,** 33, (1), 183-213.

55. Li, M.; Zhou, W.; Peterson, V. K.; Zhao, M.; Zhu, Z., A Comparative Study of $SrCo_{0.8}Nb_{0.2}O_{3-\delta}$ and $SrCo_{0.8}Ta_{0.2}O_{3-\delta}$ as Low-Temperature Solid Oxide Fuel Cell Cathodes: Effect of Non-Geometry Factors on the Oxygen Reduction Reaction. *Journal of Materials Chemistry A* **2015**.

56. Kilner, J. A.; Brook, R. J., A Study of Oxygen Ion Conductivity in Doped Non-stoichiometric Oxides. *Solid State Ionics* **1982,** 6, (3), 237-252.

57. Sammells, A. F.; Cook, R. L.; White, J. H.; Osborne, J. J.; MacDuff, R. C., Rational selection of advanced solid electrolytes for intermediate temperature fuel cells. *Solid State Ionics* **1992,** 52, (1), 111-123.

58. Wang, L.; Merkle, R.; Maier, J., Surface Kinetics and Mechanism of Oxygen Incorporation Into $Ba_{1-x}Sr_{x}Co_{y}Fe_{1-y}O_{3-\delta}$ SOFC Microelectrodes. *Journal of The Electrochemical Society* **2010,** 157, (12), B1802-B1808.

59. Cai, Z.; Kuru, Y.; Han, J. W.; Chen, Y.; Yildiz, B., Surface Electronic Structure Transitions at High Temperature on Perovskite Oxides: The Case of Strained La0.8Sr0.2CoO3 Thin Films. *Journal of the American Chemical Society* **2011,** 133, (44), 17696-17704.

60. Camaratta, M.; Wachsman, E., Silver–bismuth oxide cathodes for IT-SOFCs; Part I — Microstructural instability. *Solid State Ionics* **2007,** 178, (19–20), 1242-1247.

61. Sarikaya, A.; Petrovsky, V.; Dogan, F., Silver composites as highly stable cathode current collectors for solid oxide fuel cells. *Journal of Materials Research* **2006,** 27, (15), 1-6.

62. Chen, Y.; Wang, F.; Chen, D.; Dong, F.; Park, H. J.; Kwak, C.; Shao, Z., Role of silver current collector on the operational stability of selected cobalt-containing oxide electrodes for oxygen reduction reaction. *Journal of Power Sources* **2012,** 210, 146-153.

63. Liu, Q. L.; Khor, K. A.; Chan, S. H., High-performance Low-temperature Solid Oxide Fuel Cell with Novel BSCF Cathode. *Journal of Power Sources* **2006,** 161, (1), 123-128.

Chapter 8 Improvement on CO_2 tolerance of Ta-doped SC cathode by incorporating Sm-doped ceria

Introduction

Despite the potential high ORR electroactivity of $SrCoO_{3-\delta}$-based perovskite cathodes, their susceptibility to CO_2 impedes practical application of these highly active cathodes onto IT-SOFCs. As discussed in Section 2.5, there are only a few research studying CO_2 poisoning mechanism and exploring the strategies to make them more tolerant against CO_2 poisoning. Among these strategies, what proves effective to improve CO_2 resistivity is to introduce an additional CO_2 resistant material to protect the pristine $SrCoO_{3-\delta}$-based cathode. In Section 2.4.3, researchers have incorporated electrolyte materials into cobalt-containing perovskite to mitigate the thermal expansion mismatch. Consequently, we developed a Sr (Co, Ta)$O_{3-\delta}$ perovskite cathode hybrid with SDC protective layer in order to improve cathode stability in the presence of CO_2. The reason we used Sr(Co, Ta)$O_{3-\delta}$ as pristine cathode is because of its high ORR activity and good compatibility with SDC as demonstrated in Chapter 5.

Contribution

In this chapter, we found that incorporating SDC into Sr(Co, Ta)$O_{3-\delta}$ cathode by mechanically mixing or/and wet impregnation can significantly improve cathode tolerance against CO_2. The stability improvement of cathode in the presence of CO_2 is likely attributed to the SDC's low CO_2 adsorption, low reactivity with CO_2, and stable ionic conduction in the CO_2 containing atmosphere. Additionally, our experiment results show that this simple strategy is also effective in increasing CO_2 tolerance of other alkaline-earth-containing perovskite cathode materials. This work is in preparation for ACS Applied Materials & Interfaces.

A Highly CO_2 Tolerant Cathode for Intermediate Temperature Solid Oxide Fuel Cells: Sm-doped Ceria Protected $SrCo_{0.85}Ta_{0.15}O_{3-\delta}$ Hybrid

Mengran Li, Wei Zhou*, Zhonghua Zhu*

Abstract

Susceptibility to CO_2 is one of the major challenges for long-term stability of most of the alkaline-earth containing cathodes in intermediate-temperature solid oxide fuel cells. In this work, we incorporated Sm stabilized ceria (SDC) into $SrCo_{0.85}Ta_{0.15}O_{3-\delta}$ cathode by either mechanical mixing or wet impregnation method, and evaluated their cathode performance stability in the presence of 10% CO_2 air with 21% O_2. We found that such hybrid cathode shows an enhancement of CO_2 tolerance by nearly over 5 times as compared to pure SCT15 at 550 °C, which likely arises from low CO_2 adsorption and reactivity of SDC protective layer as demonstrated by thermogravimetric analysis, energy dispersive spectroscopy and four probe electrical conductivity measurement.

8.1 Introduction

A solid oxide fuel cell (SOFC) is a promising energy option for the future due to its direct conversion from hydrogen and hydrocarbons into electricity in a clean and very efficient way. Lowering down the operating temperature is of great significance for the SOFC commercialization because low temperatures (<600°C) will lead to significant cost reduction, easier sealing, prolonged system lifetime and etc.[1, 2] However, the electrodes, especially the cathode, become very inactive at low temperatures, which is one of the demanding issues for the low-temperature SOFC (LT-SOFC) development.[3, 4] Consequently, efforts were devoted to explore novel materials to enhance the activity over oxygen reduction reaction (ORR) at low temperature.[5-8] $SrCoO_{3-\delta}$ (SC)– based perovskite oxides, including some milestone cathodes such as $Ba_{0.5}Sr_{0.5}Co_{0.8}Fe_{0.2}O_{3-\delta}$ (BSCF)[3] and $SrSc_{0.175}Nb_{0.025}Co_{0.8}O_{3-\delta}$ [8], are regarded as one of the most promising candidates as the LT-SOFC cathode and under wide investigation in recent years. For example, the Ta-stabilized SC were also recently evaluated, and exhibit very low polarization resistances (~ 0.1 Ω·cm² at 550 °C) at low temperature.[9, 10]

However, one of the drawbacks for these SC-based perovskite oxides is their susceptibility to the CO_2 attack due to the alkaline-earth metal ions (Sr^{2+} or Ba^{2+}) compositions[11-16], which are easy to adsorb and interact with CO_2 especially at low temperature (below 700°C), resulting in slow oxygen surface exchange kinetics and therefore degraded cathode performance[17, 18]. CO_2 will compete against O_2 for the limited active oxygen vacancies on the cathode surface[19], and prolonged exposure to CO_2 also prompts carbonate formation and cathode structure deformation starting from the surface down to the bulk, resulting in unrecoverable structural damage.[20] One example is the $SrCo_{0.8}Sc_{0.2}O_{3-\delta}$ high-performance ORR catalyst, which degraded by ~ 12 times after only 5 min exposure to 10 vol% CO_2 atmosphere at 600°C.[15] The CO_2 poisoning effect is plausibly related to the cathode basic surface contributed from the basic alkaline-earth cations and surface defects[21], such as the oxygen vacancies. The interaction between cathode and CO_2 is regarded as a reaction between a basic and acid according to the Lewis acid-base theory. Therefore, a trade-off normally exists between the ORR activity and the CO_2 resistivity because the alkaline earth species and oxygen vacancies play an important role in efficient oxygen reduction.[15, 22]

To enhance the cathode CO_2 resistance, one of the effective strategies is to protect the highly active ORR cathodes from CO_2 by covering a protective layer that is at least oxygen conductive and has to be inert to CO_2. By adopting this strategy, a BSCF cathode structured with densified $La_2NiO_{4+\delta}$ (LN)-coned shell has been developed, which significantly improves the ORR activity under CO_2 exposure thanks to the MIEC and high CO_2 resistance of LN[15], but unconventional treatment microwave-induced plasma has to be used to prevent unwanted phase interaction between BSCF and LN.

On the other hand, most SC-based perovskite cathodes are chemical compatible with doped ceria electrolyte materials such as Sm-doped ceria (SDC), exhibiting a high ionic conductivity at lower temperature.[23] The SDC also shows stable oxygen permeability when exposed to CO_2.[24, 25] Moreover, the thermal expansion mismatch of SC-based cathodes can also be minimized by mixing the cathode with SDC to form composite cathode. Herein, the $SrCo_{0.85}Ta_{0.15}O_{3-\delta}$ (SCT15) – SDC composite cathodes were evaluated with respect to their tolerance to 10% CO_2 – containing gas mixtures with 21% O_2, and a systematic investigation was also presented on the influence of SDC on the cathode ORR activity and stability when exposed to 10% CO_2.

8.2 Experimental

The SCT15 was synthesized through the solid-state route: stoichiometric mixtures of $SrCoO_{3-\delta}$ (≥ 99.9%, Aldrich), Co_3O_4 (≥ 99.9%, Aldrich) and Ta_2O_5 (≥ 99.9%, Aldrich) were wet ball milled for 24 h, followed by pelletizing and sintering at 1200 °C for 20 h in stagnant air. The SDC (~30m^2/g) is a commercial product of the Fuelcellmaterials. $Ba_{0.5}Sr_{0.5}Co_{0.8}Fe_{0.2}O_{3-\delta}$ was prepared through EDTA-citric acid route.[3]

Symmetrical cells for electrochemical impedance studies were fabricated by nitrogen-borne spraying the cathode ink, which was prepared by ball milling the cathode powders in isopropyl alcohol and terpineol, onto both sides of the $Sm_{0.2}Ce_{0.8}O_{1.9}$ (SDC, from Fuel Cell Materials) electrolyte dense disk, and subsequently calcined at 1000 °C in stagnant air for 2 h. The SCT15+SDC composite cathodes were prepared through two main routes. One is to mechanically mix SCT15 and SDC powders (60:40 wt %) using ball mill for 2 h to form ink, and the subsequent steps are same to those for single-phase cathode fabrication. The other is to infiltrate 10 μL (4.2 wt% SDC) or 20 μL (8.4 wt% SDC) of the Sm and Ce nitrates ethanol solution (0.001 mol/mL) with 10 wt% citric acid into the SCT15+SDC composite backbone before another calcination at 900 °C for 5 h. These two hybrid cathodes through infiltration are named as SCT15+SDC+4.2% loading and SCT15+SDC+8.4% loading, respectively. Silver paste was painted onto the cathode, serving as the current collector. The specimens for electrical conductivity test were fabricated by pressing the SCT15 and SDC powders into pellets, and sintering at 1200 °C and 1400 °C respectively until dense, and then polishing into similar shape, with a dimension of roughly 0.75 cm × 0.2 cm × 0.1 cm.

We performed thermogravimetric analysis (TGA) to probe the interactions between the specimen and gas mixture (10% CO_2, 69% N_2 and 21% O_2) from 500 to 650°C by monitoring the weight change of the TGA samples in response to the immediate gas change from instrumental air to 10% CO_2-containing air, as well as the weight change when the atmosphere changed back to air. The 10% CO_2 gas mixture contains 69% N_2, 21% Air and 10% CO_2, and is purchased from the Coregas. The TGA samples were first pelletized at the same pressure and crushed to ensure similar grain sizes before the TGA test.

Electrochemical impedance spectroscopy (EIS) was used to study ORR activity of the cathodes in a symmetrical cell configuration and also to evaluate the cathode polarization resistance stability under exposure to 10% CO_2. The electrical conductivity measurement was conducted in a 4-probe dc method. PGSTAT302 Autolab workstation was used for these electrochemical tests, including EIS, single cell measurement and the electrical conductivity test.

The crystal structures of the samples were characterized by using X-ray powder diffraction (XRD), and scanning electron microscopy (SEM, JEOL JSM-7100F) was used to study the microstructures of the samples. Tecnai 20 Feg transmission electron microscopy (TEM) was used to perform energy dispersive X-ray analysis on different spots of SCT15 particles before and after CO_2 treatment.

8.3 Results and discussion

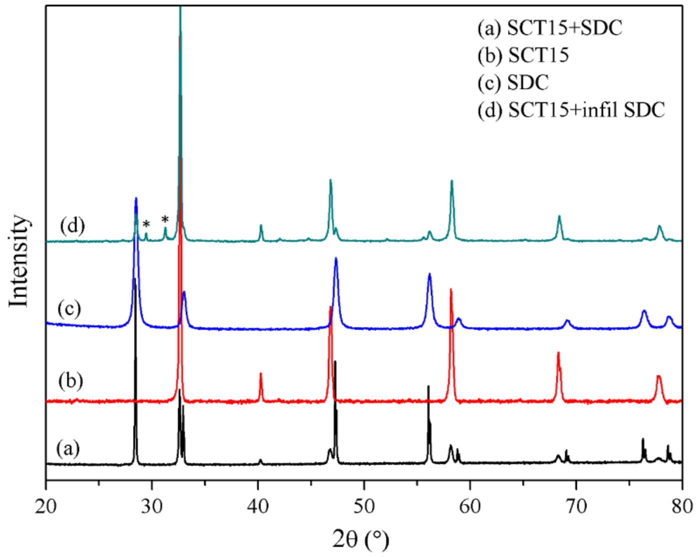

Figure 8-1 Room-temperature X-ray powder diffraction patterns of SCT15, SDC, the mixture of both treated at 1000 °C for 2 h, [9] and SCT15 infiltrated with SDC precursor followed by 5 h 900 °C treatment.

The compatibility of SCT15 with SDC has been studied from our previous work (Figure 8-1 (a)(b)(c)). SCT15 is proved to be chemically compatible with SDC below 1000 °C, as no apparent additional phases between SCT15 and SDC phases are detected from the X-ray diffraction (XRD) profiles of SCT15+SDC mixtures (50:50 wt %) after 1000°C treatment for 2h.[9] Besides, we also analyzed the crystal structures of the SCT15 powder infiltrated with 10 wt% of SDC. As presented in Figure 8-1(d), the major phases are similar to those of the SCT15+SDC mixture, implying that the SDC phase is formed, but some small additional peaks as indicated with asterisks suggest that small quantity of unknown phases were formed during the calcination.

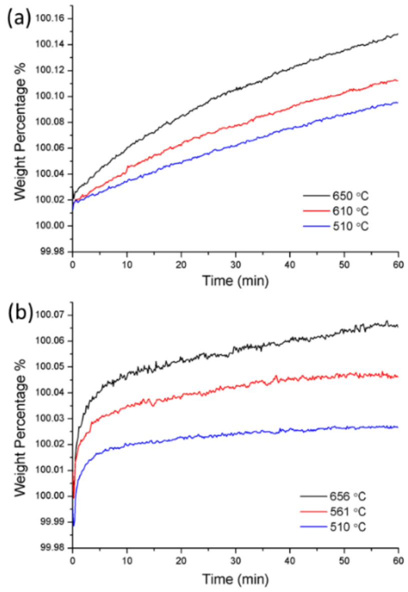

23

Figure 8-2 Weight percentage changes of (a) SCT15 and (b) SDC as a function of time when the atmosphere changed from air to 10% CO_2 gas at different temperatures.

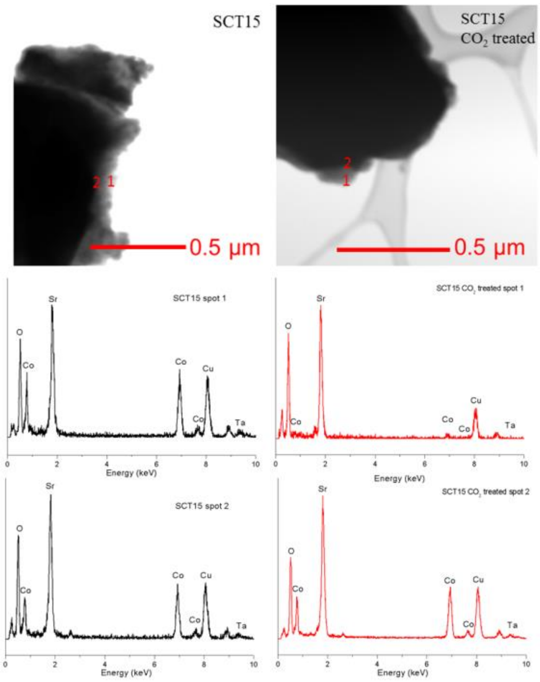

Figure 8-3 HADDF images of SCT15 before and after 10 h 10% CO_2 treatment at 510 °C and the corresponding energy dispersive X-ray analysis.

The effects of CO_2 on SCT15 and SDC materials are studied using thermal gravimetric analysis separately. Figure 8-2 shows that both the SCT15 and SDC mass increase in response to the feed of 10% CO_2 at different temperatures because of the CO_2 adsorption. These two samples adsorb more CO_2 in 10% CO_2 at higher temperature relative to lower temperature. Meanwhile, more oxygen vacancies are also formed at higher temperature in air.[9] As more oxygen vacancies are formed at higher temperature[9], it is likely that the higher levels of oxygen vacancies, which act as CO_2 effective adsorption sites, are responsible for the more CO_2 captured at temperature range 510 – 650 °C. Similar phenomenon was also observed for $Ba_{0.5}Sr_{0.5}Co_{0.8}Fe_{0.2}O_{3-\delta}$ material that exhibits higher interaction with CO_2 at rising temperature.[26]

However, SCT15 and SDC show different weight change profile reacting to CO_2. For example, SCT15 shows an almost linear behaviour in adsorbing CO_2 especially at 510 °C, but the CO_2 adsorption process is faster on SDC during the first 5 min but gradually slows down until nearly equilibrium. The continuous CO_2 adsorption process on SCT15 may arise from the Sr segregation from the bulk onto the surface to react with CO_2 due to its high basicity, which can be demonstrated by TEM-EDX results as shown in Figure 8-3. TEM-EDX was conducted to do the elemental analysis at the surface and bulk of SCT15 particles with and without treatment in 10% CO_2 for 10 h respectively. From the EDX analysis results, SCT15 free of CO_2 treatment has similar cation content levels at both spot 1 and spot 2, but the specimen with CO_2 treated exhibits a much higher level of Sr, which is likely in a form of carbonate, near the surface as compared with Co and Ta cations. Therefore, it can be concluded that the CO_2 is one of the major reasons for the Sr segregation, and the continuous weight increase of SCT15 in CO_2 is a result of the continuous diffusion of Sr to the surface to form carbonate. Similar Sr or other alkaline-earth elements segregation phenomena were also reported in previous work when exposed to CO_2 -containing air but with different oxygen content.[19, 20, 27] In the contrary, SDC nearly stops increasing its weight after 20 min at 510 °C, revealing a different CO_2 adsorption process: CO_2 is adsorbed on the SDC surface until reaching the equilibrium, where all the effective adsorption sites are saturated with CO_2. The difference may arise from the lack of basic elements such as Sr in SDC, so that no further increase of adsorbed CO_2 occurs.

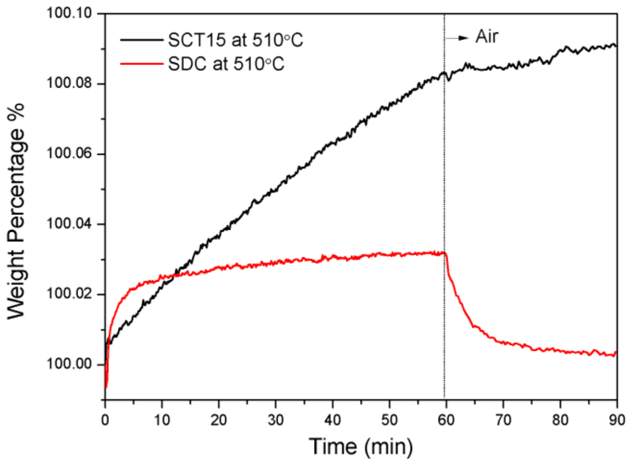

Figure 8-4 The weight percentage changes of SCT15 and SDC as a function of time when the atmosphere switched from 10% CO_2 to air at 60 min.

When the CO_2 is removed from the atmosphere at 510 °C, most of CO_2 desorbs from the SDC in the first 30 min, but SCT15 shows a different response to the CO_2 removal: nearly no CO_2 that is captured during the first 60 min CO_2 treatment escapes from SCT15. (Figure 8-4) This is a sign suggesting that the CO_2 adsorption process on SCT15 is irreversible at 510 °C and is not sensitive to the CO_2 concentration change. The slight weight gain after flowing gas switched in SCT15 is ascribed to the remained CO_2 in the furnace chamber. Meantime, part of CO_2 is becoming carbonate, which is also another main reason for the no release of CO_2 from SCT15 after the CO_2 partial pressure is significantly lowered. In contrast, however, SDC shows a reversible CO_2 adsorption probably and very low reactivity with CO_2 due to its relatively lower basic surface, so that the weight of SDC nearly decreases to the original weight level after CO_2 flux removed.

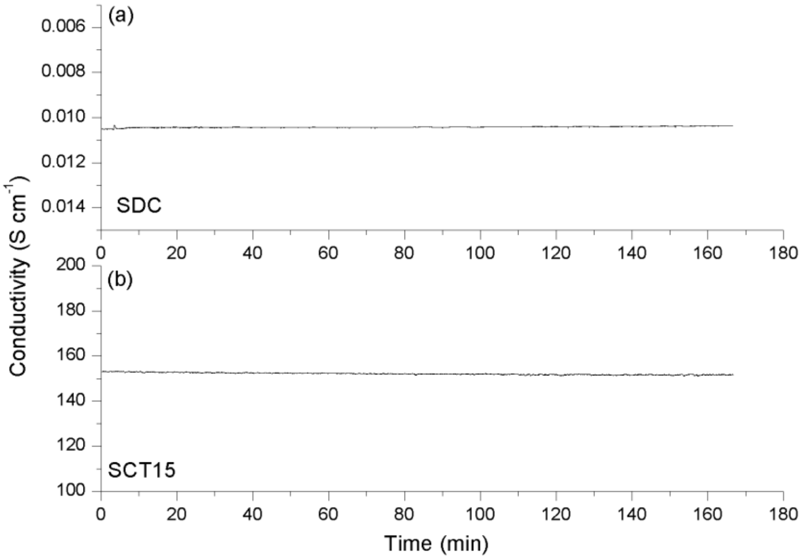

Figure 8-5 Electrical conductivities of SDC and SCT15 in exposure to 10% CO_2 at 500°C for 167 min after stabilized in air.

The electrical conductivity stability of SCT15 and SDC in the presence of 10% CO_2-containing air was studied using 4-probe dc method at 500 °C respectively. The electrical conductivity of these two materials consists of electronic and ionic conductivity: electronic conductivity dominates in SCT15, but ionic conductivity dominates in SDC. From Figure 8-5, negligible electrical conductivity changes are found for both SCT15 and SDC, indicating that 10% of CO_2 in the atmosphere does not have significant adverse effects on the electronic conductivity of SCT15 and the ionic conductivity of SDC.

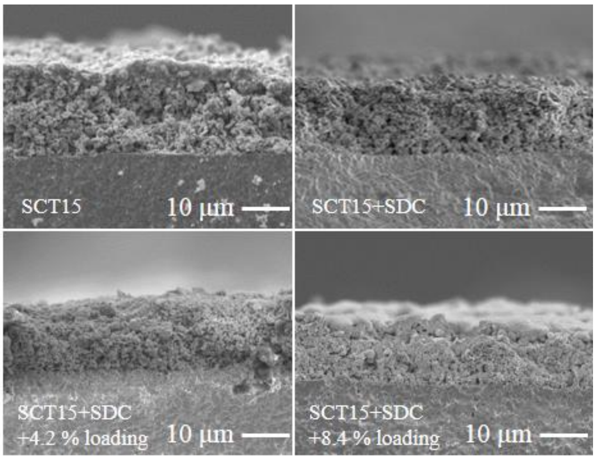

Figure 8-6 SEM micrographs of cross sections of SCT15, SCT15+SDC and SCT15+SDC with different SDC loadings cathodes under investigations.

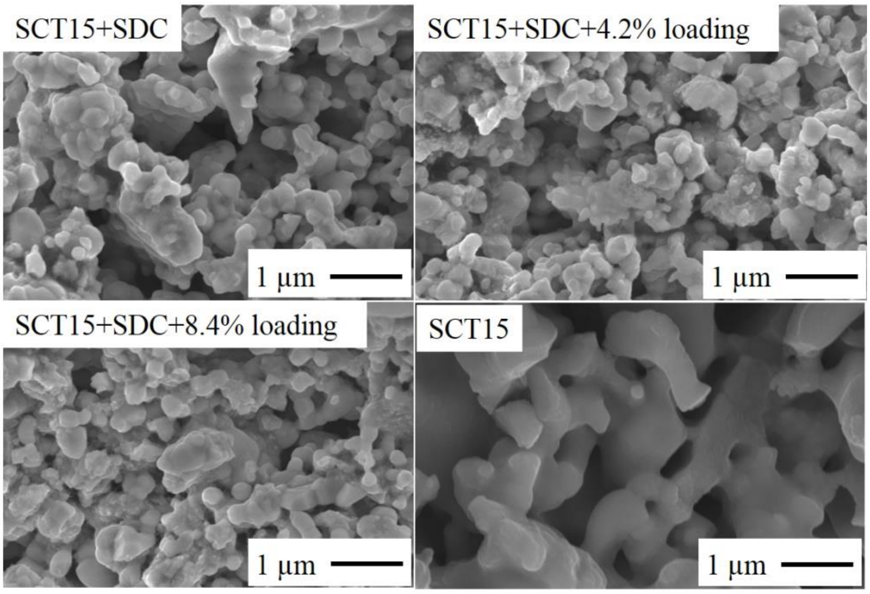

Figure 8-7 SEM micrographs of microstructures of SCT15, SCT15+SDC, SCT15+SDC with different SDC loadings cathodes under investigations.

The microstructures of the cathodes under investigation are studied using SEM. As shown in Figure 8-6, the cathodes all attach well with SDC surface, and are in a similar cathode thickness. Figure 8-7 shows that SCT15 cathode is covered by the small SDC particles with ~ 0.5 µm sizes for SCT15 + SDC cathode, and is additionally covered by nano-sized SDC particles for infiltration-loaded SCT15+SDC.

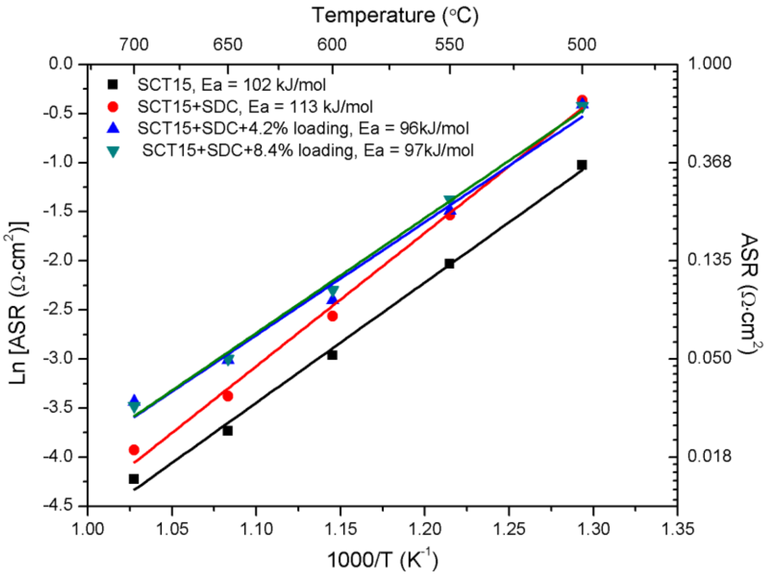

Figure 8-8 Area specific resistances (ASRs) of cathodes as a function of temperature in the flowing air.

The ORR activity of the cathodes in air is tested by electrochemical impedance analysis in a configuration of the SDC-based symmetrical cell from 500 °C to 700 °C. The area specific resistance (ASR), calculated from the impedance spectra, characterizes the cathode performance, with a lower value reflecting a higher activity over ORR. As shown in Figure 8-8, the pure SCT15 exhibits the lowest ASRs at the 500-700 °C temperature range among all the cathodes under study. The introduction of SDC will result in performance degradation of the pure SCT15 both in ASR values and the activation energy mainly because of the lower electrical conductivity of SDC in comparison to SCT15. Further additional infiltration of SDC also makes it slightly less active in oxygen reduction especially above 600 °C than SCT15+SDC cathode, but the activation energy is noticeably lowered down to 96-97 kJ/mol even comparable with the pure SCT15 cathode at ~102 kJ/mol. The enhanced activation energy may arise from the increase of three phase boundaries among SCT15, SDC and the air, which results from the additions of nano SDC particles by infiltrations as shown in Figure 8-7.

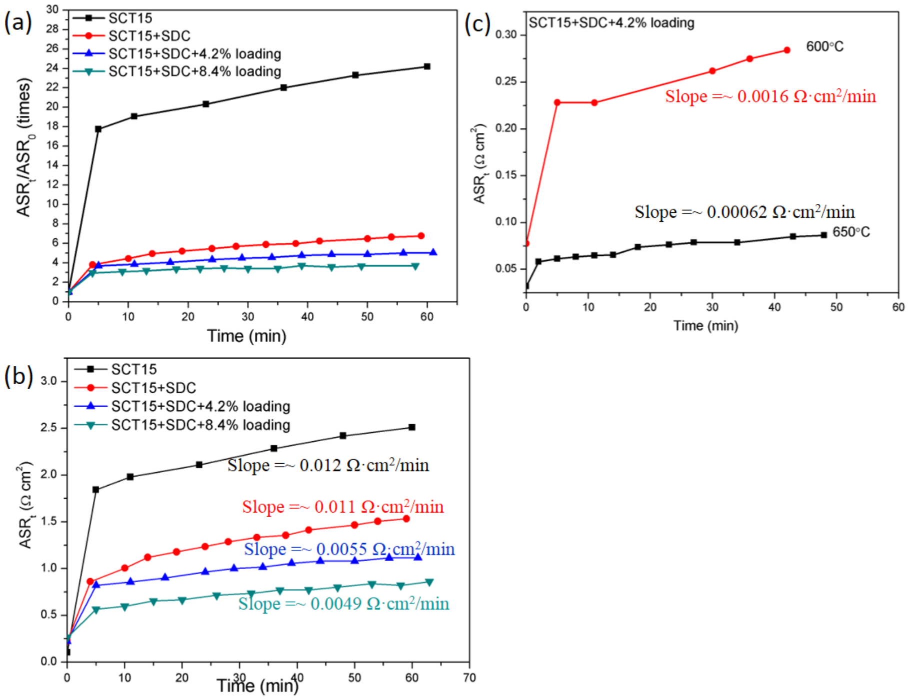

Figure 8-9 (a) Relative and (b) real ASR value changes with time for the studied cathodes when the flowing air is replaced by flowing 10% CO_2- containing air at 550 °C. (c) ASR change of SCT15+SDC+42% loading cathode as a function of time in the presence of 10% CO_2 at 600 °C and 650 °C. The slopes shown in the figure are the estimated slopes of linearly increasing ASR profile as a function of time, especially after 5 min exposure to 10% CO_2.

The cathode tolerance against CO_2 was evaluated in terms of ASR change in the presence of 10% CO_2, and Figure 8-9 (a) shows the relative ASR change as a function of time after 10% CO_2 is introduced. 0 min is the time when the 10% CO_2 gas mixture is fluxed in. We found that the electroactivity of SCT15 degrades dramatically by nearly 18 times in the first 5 min, and linearly degrades by 22 times after 1 h CO_2 exposure. The increasing rate of polarization resistance of SCT15 is about 0.012 $\Omega\cdot cm^2$/min after ~5 min exposure to 10% CO_2. The observed significant ORR deterioration as a result of CO_2 mainly arises from the competition for active adsorption sites between O_2 and CO_2[26, 28], as well as the formed carbonation that inhibits the oxygen exchange process on cathode surface.[18] However, for cathode hybrid with SDC the poisoning effect is significantly alleviated. For example, ASR of the SCT15+ SDC cathode increases by 5 times after 1 h exposure to 10% CO_2, and an ASR increase by only ~3 times occurs for SCT15+ SDC cathode with 8.4 wt% SDC loading at 550 °C. It is important to note from Figure 8-9(b) that the ASRs are also significantly decreased as compared to the pure SCT15 when the amount of SDC increases, though the ASRs of these composite cathodes are not as low as the pure SCT15 in the absence of CO_2. Moreover, the ASR increasing rate (time > 5min) is significantly reduced when the cathode is infiltrated with SDC: *e.g.* the SCT15+SDC+4.2% loading degrades at a rate of ~0.0055 $\Omega\cdot cm^2$/min, which is less than half the rate of pure SCT15 cathode. Additionally, the polarization resistance of cathode infiltrated with 4.2 wt% SDC remains below 0.1 $\Omega\cdot cm^2$ at 650 °C when exposed to 10% CO_2 for 48 min, showing an acceptable cathode performance in CO_2-containing atmosphere. (Figure 8-9(c)) Consequently, the incorporated SDC particles can serve as a discontinued protective layer against CO_2 for the SCT15 cathode mainly because of the aforementioned relatively low CO_2 adsorption and reactivity of SDC, as well as its unaffected ionic conductivity in the CO_2- containing atmosphere.

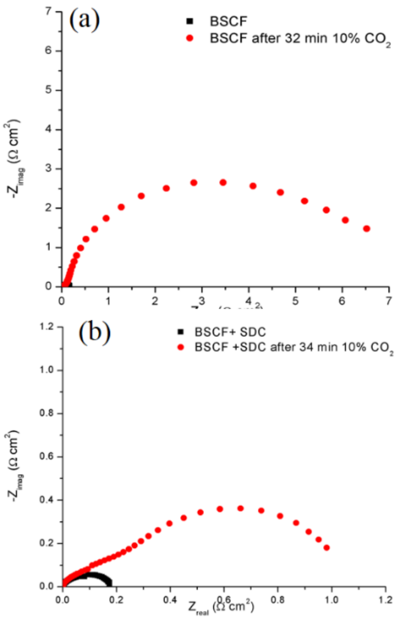

Figure 8-10 Comparisons of (a) BSCF and (b) BSCF+SDC cathode impedance profiles in response to ~30 min 10% CO_2 treatment.

Additionally, we also applied this strategy onto $Ba_{0.5}Sr_{0.5}Co_{0.8}Fe_{0.2}O_{3-\delta}$ (BSCF) cathode, which one of the benchmark cathodes for intermediate-temperature SOFCs but susceptible to CO_2, by simply mechanical mixing the BSCF cathode with SDC before fabricated onto the electrolyte. The CO_2 tolerance is also evaluated in a similar way with SCT15 at 550 °C. Figure 8-10 provides the impedance spectra of both BSCF and BSCF-SDC cathodes in a configuration of symmetrical cell before and after 30 min 10% CO_2 treatment. It is obvious that when the pure BSCF is exposed to 10% CO_2, the ASR increases by ~ 46 times after only 32 min exposure, but the ASR only goes up by 6 times for BSCF+ SDC cathode. Therefore, it can be concluded that the CO_2 tolerance of doped SC can be significantly enhanced by introducing SDC protective layer into the cathode.

8.4 Conclusions

Samarium doped ceria is introduced onto $SrCo_{0.85}Ta_{0.15}O_{3-\delta}$ cathode through both mixing and infiltration methods in order to enhance the resistivity of SCT15 cathode against CO_2 attack. Our study reveals different CO_2 adsorption mechanisms between SCT15 and SDC at SOFC operating temperatures, and that much higher reactivity of SCT15 with CO_2 as compared to SDC. Because of the stability of SDC in the CO_2 - containing atmosphere as a result of its low CO_2 reactivity and adsorption, the SCT15 with SDC protective layer is found to be far less susceptible when exposed to

10% CO_2 as compared to pure SCT15. This strategy is also found to be effective to improve the CO_2 tolerance of other promising cathode materials containing alkaline-earth metals.

Acknowledgement

The authors appreciate the technical support from Centre for Microscopy and Microanalysis at the University of Queensland.

This work is financially supported by Australian Research Council (DP130102151) and author Mengran Li acknowledges additional financial support from the top-up assistance program (TUAP) scholarship and the scholarship from China Scholarship Council.

8.5 References

1. Wachsman, E. D.; Lee, K. T., Lowering the Temperature of Solid Oxide Fuel Cells. *Science* **2011,** 334, (6058), 935-939.

2. Minh, N. Q., Ceramic Fuel Cells. *Journal of the American Ceramic Society* **1993,** 76, (3), 563-588.

3. Shao, Z.; Haile, S. M., A High-Performance Cathode for the Next Generation of Solid-Oxide Fuel Cells. *Nature* **2004,** 431, (7005), 170-173.

4. Steele, B. C.; Heinzel, A., Materials for Fuel-Cell Technologies. *Nature* **2001,** 414, (6861), 345-352.

5. Lee, J. G.; Park, J. H.; Shul, Y. G., Tailoring Gadolinium-Doped Ceria-Based Solid Oxide Fuel Cells to Achieve 2 W Cm^{-2} at 550 °C. *Nature Communications* **2014,** 5.

6. Yoo, S.; Jun, A.; Ju, Y.-W.; Odkhuu, D.; Hyodo, J.; Jeong, H. Y.; Park, N.; Shin, J.; Ishihara, T.; Kim, G., Development of Double-Perovskite Compounds as Cathode Materials for Low-Temperature Solid Oxide Fuel Cells. *Angewandte Chemie International Edition* **2014,** 53, (48), 13064-13067.

7. Zhang, X.; Liu, L.; Zhao, Z.; Tu, B.; Ou, D.; Cui, D.; Wei, X.; Chen, X.; Cheng, M., Enhanced Oxygen Reduction Activity and Solid Oxide Fuel Cell Performance with a Nanoparticles-Loaded Cathode. *Nano Letters* **2015,** 15, (3), 1703-1709.

8. Zhou, W.; Sunarso, J.; Zhao, M.; Liang, F.; Klande, T.; Feldhoff, A., A Highly Active Perovskite Electrode for the Oxygen Reduction Reaction Below 600 °C. *Angewandte Chemie International Edition* **2013,** 52, (52), 14036-14040.

9. Li, M.; Zhou, W.; Zhu, Z., Comparative Studies of $SrCo_{1-X}Ta_xo_{3-\delta}$ (X=0.05–0.4) Oxides as Cathodes for Low-Temperature Solid-Oxide Fuel Cells. *ChemElectroChem* **2015,** 2, (9), 1331-1338.

10. Li, M.; Zhou, W.; Peterson, V. K.; Zhao, M.; Zhu, Z., A Comparative Study of $SrCo_{0.8}Nb_{0.2}O_{3-\delta}$ and $SrCo_{0.8}Ta_{0.2}O_{3-\delta}$ as Low-Temperature Solid Oxide Fuel Cell Cathodes: Effect of Non-Geometry Factors on the Oxygen Reduction Reaction. *Journal of Materials Chemistry A* **2015**.

11. Chen, W.; Chen, C.-s.; Winnubst, L., Ta-Doped $SrCo_{0.8}Fe_{0.2}O_{3-\delta}$ Membranes: Phase Stability and Oxygen Permeation in CO_2 Atmosphere. *Solid State Ionics* **2011,** 196, (1), 30-33.

12. Zhu, Y.; Sunarso, J.; Zhou, W.; Shao, Z., Probing CO_2 Reaction Mechanisms and Effects on the $SrNb_{0.1}Co_{0.9-x}Fe_xO_{3-\delta}$ Cathodes for Solid Oxide Fuel Cells. *applied Catalysis, B: Environmental* **2015,** 172–173, 52-57.

13. Cetin, D.; Yu, Y.; Luo, H.; Lin, X.; Ludwig, K.; Basu, S. N.; Pal, U. B.; Gopalan, S., Effect of Carbon Dioxide on the Cathodic Performance of Solid Oxide Fuel Cells. *ECS Transactions* **2014,** 61, (1), 131-137.

14. Zhou, W.; Zhu, Z., The instability of solid oxide fuel cells in an intermediate temperature region. *Asia‐Pacific Journal of Chemical Engineering* **2011,** 6, (2), 199-203.

15. Zhou, W.; Liang, F.; Shao, Z.; Zhu, Z., Hierarchical CO_2-Protective Shell for Highly Efficient Oxygen Reduction Reaction. *Scientific Reports* **2012,** 2, 327.

16. Yi, J.; Feng, S.; Zuo, Y.; Liu, W.; Chen, C., Oxygen Permeability and Stability of $Sr_{0.95}Co_{0.8}Fe_{0.2}O_{3-\delta}$ in a CO_2- and H_2O-Containing Atmosphere. *Chemistry of Materials* **2005,** 17, (23), 5856-5861.

17. Yue, X.; Yan, A.; Zhang, M.; Liu, L.; Dong, Y.; Cheng, M., Investigation on Scandium-doped Manganate $La_{0.8}Sr_{0.2}Mn_{1-x}Sc_xO_{3-\delta}$ Cathode for Intermediate Temperaturesolid Oxide Fuel Cells. *Journal of Power Sources* **2008,** 185, (2), 691-697.

18. Bucher, E.; Egger, A.; Caraman, G. B.; Sitte, W., Stability of the Sofc Cathode Material $(Ba,Sr)(Co,Fe)O_{3-\delta}$ in CO_2-Containing Atmospheres. *Journal of the Electrochemical Society* **2008,** 155, (11), B1218-B1224.

19. Yáng, Z.; Harvey, A. S.; Gauckler, L. J., Influence of CO_2 on $Ba_{0.2}Sr_{0.8}Co_{0.8}Fe_{0.2}O_{3-\delta}$ at Elevated Temperatures. *Scripta Materialia* **2009,** 61, (11), 1083-1086.

20. Yi, J.; Weirich, T. E.; Schroeder, M., CO_2 Corrosion and Recovery of Perovskite-Type $BaCo_{1-x-y}Fe_xNb_yO_{3-\delta}$ Membranes. *Journal of Membrane Science* **2013,** 437, (0), 49-56.

21. Hammami, R.; Batis, H.; Minot, C., Combined Experimental and Theoretical Investigation of the CO_2 Adsorption on $LaMnO_{3+y}$ Perovskite Oxide. *Surface Science* **2009,** 603, (20), 3057-3067.

22. Sugiura, S.; Shibuta, Y.; Shimamura, K.; Misawa, M.; Shimojo, F.; Yamaguchi, S., Role of Oxygen Vacancy in Dissociation of Oxygen Molecule on SOFC Cathode: Ab Initio Molecular Dynamics Simulation. *Solid State Ionics*.

23. Eguchi, K.; Setoguchi, T.; Inoue, T.; Arai, H., Electrical Properties of Ceria-based Oxides and Their Application to Solid Oxide Fuel Cells. *Solid State Ionics* **1992,** 52, (1), 165-172.

24. Zhang, K.; Shao, Z.; Li, C.; Liu, S., Novel CO_2-tolerant Ion-transporting Ceramic Membranes with an External Short Circuit for Oxygen Separation at Intermediate Temperatures. *Energy & Environmental Science* **2012,** 5, (1), 5257-5264.

25. Zhang, K.; Meng, B.; Tan, X.; Liu, L.; Wang, S.; Liu, S., CO2-Tolerant Ceramic Membrane Driven by Electrical Current for Oxygen Production at Intermediate Temperatures. *Journal of the American Ceramic Society* **2014,** 97, (1), 120-126.

26. Yan, A.; Liu, B.; Dong, Y.; Tian, Z.; Wang, D.; Cheng, M., A Temperature Programmed Desorption Investigation on the Interaction of $Ba_{0.5}Sr_{0.5}Co_{0.8}Fe_{0.2}O_{3-\delta}$ Perovskite Oxides with CO_2 in the abence and presence of H_2O and O_2. *Applied Catalysis, B: Environmental* **2008,** 80, (1–2), 24-31.

27. Pfeiffer, H.; Vázquez, C.; Lara, V. H.; Bosch, P., Thermal Behavior and CO_2 Absorption of $Li_{2-x}Na_xZrO_3$ Solid Solutions. *Chemistry of Materials* **2007,** 19, (4), 922-926.

28. Arnold, M.; Wang, H.; Feldhoff, A., Influence of CO_2 on the Oxygen Permeation Performance and the Microstructure of Perovskite-type $(Ba_{0.5}Sr_{0.5})(Co_{0.8}Fe_{0.2})O_{3-\delta}$ Membranes. *Journal of Membrane Science* **2007,** 293, (1–2), 44-52.

Chapter 9 Conclusions and recommendations

9.1 Conclusions

In summary, this project tends to develop robust cathode materials based on $SrCoO_{3-\delta}$ perovskite oxide with high electroactivity on reducing oxygen at intermediate temperature (500 °C ~ 750 °C) even in the presence of CO_2, and to study factors that affect cathode performance and stability. From the studies presented in the thesis, conclusions can be drawn as follows.

Firstly, dopants in fixed high valence, such as P^{5+}, Ta^{5+} and Nb^{5+}, can be incorporated into $SrCoO_{3-\delta}$ oxide, and are helpful to stabilize the ORR beneficial perovskite structure ($Pm\bar{3}m$) of $SrCoO_{3-\delta}$ both at room temperature and intermediate temperature, which arises from their high valence state that prevents oxygen vacancy ordering and some phase distortions. Because of this phase stabilization effect, these dopants can significantly enhance cathode performance stability. The content of these dopants especially Ta^{5+} can influence the crystal structure of cathode material: less than 5 mol% Ta^{5+} doping makes $SrCoO_{3-\delta}$ a tetragonal structure ($I4/mmm$), but over 5 mol% doping results in cubic perovskite structure at room temperature. Moreover, the cubic perovskite structure of $SrCoO_{3-\delta}$ is still maintained when Ta^{5+} doping level reaches 40 mol%.

Secondly, the substitution level of Ta^{5+} has an impact on the mixed electronic and ionic conductivities of $SrCoO_{3-\delta}$. Low doping content (< 5 mol%) can increase the electronic conductivity, because dopants can both stabilize high-symmetry structure that is good for hopping and increase the concentration of charge carriers. However, high doping content (> 5 mol%) can deteriorate the electronic conductivity likely due to the increasing inhibition of (Co, dopant)-O- (Co, dopant) bonds onto the hopping process. Moreover, the high valence of dopants increases the overall charges of cations, so oxygen vacancies of these doped materials have to decrease to compensate the charge imbalance.

Thirdly, fixed valence dopants can influence the cathode electroactivity of $SrCoO_{3-\delta}$ in an indirect way. The valence of Co in $SrCoO_{3-\delta}$ doped with more Ta^{5+} is easier to change in response to change of oxygen partial pressure. As a result, doping Ta^{5+} can enhance the oxygen exchange processes, particularly the steps involving atomic oxygen, therefore significantly lowering the cathode polarization resistance down to 0.089 ~ 0.11 Ω·cm^2 at 550 °C ($SrCo_{0.95}Ta_{0.05}O_{3-\delta}$ for example). What also needs to mention is that low electronegativity of dopant is beneficial for improving cathode electroactivity by increasing oxygen vacancy content.

Fourthly, a new robust perovskite cathode has been developed with superior cathode performance by co-doping Nb^{5+} and Ta^{5+} into $SrCoO_{3-\delta}$ oxide. This cathode material exhibits an area specific resistance of ~ 0.16 Ω·cm^2 and ~ 0.64 Ω·cm^2 at 500 °C and 450 °C, respectively. The remarkably high cathode activity is likely ascribed to a synergist effect of Nb^{5+} and Ta^{5+} that leads to an optimized balance between oxygen vacancy content, ionic mobility and surface electron transfer process, which have a positive effect on ORR.

Finally, compositing Ta-doped $SrCoO_{3-\delta}$ cathodes with Sm-doped ceria can significantly improve cathode tolerance against CO_2 at intermediate temperature. The enhanced resistivity against CO_2 can be attributed to the chemical stability and low adsorption of SDC in exposure to CO_2. More importantly, this strategy is also effective for other alkaline-earth containing perovskite cathodes, such as BSCF, in alleviating deterioration of cathode performance due to CO_2 poisoning.

In summary, the $SrCoO_{3-\delta}$ perovskite oxide doped with high fixed valence dopants such as P, Nb, and Ta shows promising electroactivity and stability on electrochemically catalyzing oxygen reduction at intermediate temperature. The ORR activity enhancement can be achieved by these dopants in two main ways:

- fixed and high valence dopants can stabilize the beneficial cubic perovskite structure due to their high valence states;
- these dopants can also indirectly enhance the ionic conductivity and/or oxygen surface exchange processes by optimizing the neighboring Co ions.

Moreover, a simple compositing strategy has also been developed in this project to significantly alleviate the susceptibility of $SrCoO_{3-\delta}$-based perovskite cathodes against CO_2 at intermediate temperature.

9.2 Recommendations

Based upon the research that has been done, the following recommendations are made for the future work.

Cathode synthesis route needs to be optimised to further improve cathode performance. For the conventional solid-state reaction, high temperature (normally >1000 °C) is necessary to facilitate the reaction, but high temperature normally results in serious particle agglomeration and losses of catalyst surface area. Nevertheless, some novel material synthesis routes, such as in-situ co-assembly[1], exsolving process[2] and solid-state reactive sintering (SSRS)[3], could be possible to reduce particle sizes of cathodes through lowering the synthesis temperatures, thereby optimising cathodes' microstructures and improving cathode electroactivity towards ORR.

Designing novel cathode fabrication techniques is also important for IT-SOFC cathode development because the fabrication process can significantly affect the cathode microstructures and the sizes of TPBs. For example, the traditional high-temperature cathode fabrication process usually limits the choice of cathode compositions and microstructures. Therefore, lowering the cathode-fabrication temperature by using novel techniques, such as microwave-induced plasma technique[4], makes it possible for novel microstructures and reduced cathode particle size, which both could further exploit the electrocatalysis potential of existing cathodes.

The synergistic effects of co-doping on cathode electroactivity are still required to investigate for dopants in different valence, sizes, and doping contents. Understanding these mechanisms could contribute to doping strategies for cathode design, and is significant in understanding how dopants work in improving ORR activity.

Further improving CO_2 resistance without sacrificing ORR activity is still challenging, but is highly required for IT-SOFC cathodes. Incorporating protective phase into highly active cathode materials proves to be effective, but methods to further optimise the interfaces between protective phases and cathodes still need to be explored and studied. Besides, understanding the mechanisms behind adsorption of CO_2 on cathode surface could be very helpful in developing strategies to improve the cathode stability in the presence of CO_2.

9.3 References

1. Lee, K. T.; Lidie, A. A.; Yoon, H. S.; Wachsman, E. D., Rational Design of Lower-Temperature Solid Oxide Fuel Cell Cathodes Via Nanotailoring of Co-Assembled Composite Structures. *Angewandte Chemie International Edition* **2014,** 53, (49), 13463-13467.

2. Zhu, Y.; Zhou, W.; Ran, R.; Chen, Y.; Shao, Z.; Liu, M., Promotion of Oxygen Reduction by Exsolved Silver Nanoparticles on a Perovskite Scaffold for Low-Temperature Solid Oxide Fuel Cells. *Nano Letters* **2016,** 16, (1), 512-518.

3. Duan, C.; Tong, J.; Shang, M.; Nikodemski, S.; Sanders, M.; Ricote, S.; Almansoori, A.; O’Hayre, R., Readily Processed Protonic Ceramic Fuel Cells with High Performance at Low Temperatures. *Science* **2015,** 349, (6254), 1321-1326.

4. Zhou, W.; Liang, F.; Shao, Z.; Zhu, Z., Hierarchical CO_2-Protective Shell for Highly Efficient Oxygen Reduction Reaction. *Scientific Reports* **2012,** 2, 327.